POLYACRYLONITRILE / CARBON NANOTUBE COMPOSITE FIBERS: EFFECT OF VARIOUS PROCESSING PARAMETERS ON FIBER STRUCTURE AND PROPERTIES

A Dissertation
Presented to
The Academic Faculty

by

Young Ho Choi

In Partial Fulfillment
of the Requirements for the Degree
Doctor of Philosophy in the
School of Polymer, Textile, and Fiber Engineering

Georgia Institute of Technology
December 2010

POLYACRYLONITRILE / CARBON NANOTUBE COMPOSITE FIBERS: EFFECT OF VARIOUS PROCESSING PARAMETERS ON FIBER STRUCTURE AND PROPERTIES

Approved by:

Dr. Satish Kumar, Advisor
School of Materials Science and Engineering
Georgia Institute of Technology

Dr. Seung Soon Jang
School of Materials Science and Engineering
Georgia Institute of Technology

Dr. Anselm Griffin
School of Materials Science and Engineering
Georgia Institute of Technology

Dr. Kyriaki Kalaitzidou
School of Mechanical Engineering
Georgia Institute of Technology

Dr. Donggang Yao
School of Materials Science and Engineering
Georgia Institute of Technology

Date Approved: October 28, 2010

I dedicate this dissertation to my parents Yong Choi and Kum Rhea Lim
who always support my decisions and pray for me to go the right way.

ACKNOWLEDGEMENTS

I would like to express my deep and sincere gratitude to my advisor Dr. Satish Kumar for his support, encouragement, and recommendations throughout this study. His constructive criticism always helps me move forward and gives me insight into academic research. I would also like to thank Dr. Anselm Griffin, Dr. Donggang Yao, Dr. Seung Soon Jang, and Dr. Kyriaki Kalaitzidou for providing their valuable time to serve on the committee and for their precious suggestions.

I would like to acknowledge my fellow group member Dr. Han Gi Chae for his help and instruction in fiber spinning and characterization and for invaluable discussion. I would also like to thank Dr. Marilyn Minus, Dr. Prabhakar Gulgunje, and Dr. Manjeshwar G. Kamath for their critical reading of the thesis. I would also like to thank previous group members Dr. Jong Beom Baek, Dr. Shanju Zhang, Dr. Tong Wang, Dr. Huina Guo, Dr. Jing Liu, Dr. Asif Rasheed, Dr. Sudhakar Jaganathan, Dr. Rahul Jain, Dr. Dhriti Nepal, and current members Dr.Xiangyang Hao, Dr. Kishor Gupta, Dr. Smitha Nair, Mr. Yaodong Liu, Ms. Ericka J. Ford, Mr. An-Ting Chien, Mr. Bradley Newcomb, Mr. Kevin Lyons, and Ms. Laura Lanier for their help and discussion. Special thanks go to Mr.Sarang Deodhar for his assistance in capillary rheometry.

I am grateful to my sister and her family, and my in-laws for their support and encouragement. I am greatly appreciative to my wife Gou Jung Lee and my children Hanseung and Yoonseo for their patience, understanding and love.

And last, but not least, I would like to express my earnest and deepest appreciation to God for his love and for his leadership.

TABLE OF CONTENTS

LIST OF TABLES

LIST OF FIGURES

SUMMARY

This study elucidates the effect of various processing parameters on PAN/carbon nanotube (CNT) composite fiber structure and properties.

In Chapter 1, literature review and the objectives of this thesis are presented. Studies on the structure, processing, and properties of gel-spun PAN/multiwall carbon nanotube (MWNT) composite fibers follow in Chapter 2. Interactions between the PAN and the MWNT enabled the gel-spun PAN/MWNT composite fibers to be drawn longer than the control PAN fibers, resulting in a composite fiber tensile strength of as high as 1.3 GPa. PAN/MWNT composite fibers were stabilized and carbonized, and the resulting fibers have been characterized for their structure and properties. The effect of shelf-time on the mechanical properties of gel-spun PAN/MWNT composite fibers is also reported.

A rheological study of PAN-co-MAA/few wall nanotube (FWNT) composite solution is presented in Chapter 3. At low shear rates, the network of FWNTs contributes to elastic response, resulting in higher viscosity and storage modulus compared to the control solution. On the other hand, at high shear rates, the network of FWNTs can be broken, resulting in lower viscosity for the composite solution, than that for the control solution.

Larger PAN crystal size (~16.2 nm) and enhanced mechanical properties are observed when the fibers were drawn at room temperature (cold-drawing) prior to being drawn at elevated temperature (~ 165 ℃; hot-drawing). Azimuthal scan of wide angle X-ray diffraction (WAXD) and Raman G-band intensities were used for the evaluation of Herman's orientation factor for PAN crystals (f_{PAN}) and FWNT (f_{FWNT}), respectively. Significantly higher nanotube orientation was observed than PAN orientation at an early

stage of fiber processing. Differential scanning calorimetry (DSC) revealed that PAN-co-MAA fiber can be converted into cyclic structure at milder conditions than those for PAN. Continuous in-line stabilization, carbonization, and characterization of the resulting carbon fibers were carried out.

Solution spinning of PAN-co-MAA/VGCNF, characterization of the solution-spun fibers, and rheological studies are presented in Chapter 4. The diameter of PAN-co-MAA/VGCNF composite fiber is smaller than that of the PAN-co-MAA control fiber with same draw ratio due to the suppressed die-swell in the presence of VGCNF. The mechanical properties of PAN-co-MAA control and PAN-co-MAA/VGCNF composite fibers are characterized. Crystalline structure and morphology of the solution-spun PAN-co-MAA/VGCNF fibers are characterized using WAXD and scanning electron microscopy (SEM), respectively. A new method for evaluating the orientation of VGCNF, which has double layer structure, is presented.

Gel spinning of high molecular weight PAN is discussed in Chapter 5. Dynamic rheological test results of high ($4.7\times10^5 \sim 5.2\times10^5$ g/mol), and low (2.4×10^5 g/mol) molecular weight PAN solution are compared to address the issue of molecular weight on PAN spinning. Various types of high molecular weight homo- and co-polymer PAN fibers are prepared and their structure and properties are characterized.

In Chapter 6, the volume fraction of PAN-CNT interphase in PAN matrix is calculated to illustrate the impact of CNTs on structural change in PAN matrix when ordered PAN molecules are developed in the vicinity of CNTs. The effect of PAN-CNT interphase thickness, CNT diameter, and mass density of CNT on volume fraction of PAN-CNT interphase was explored.

Conclusions and recommendations for future work are given in Chapter 8.

CHAPTER 1

INTRODUCTION

1.1 Overview

Carbon fibers consist of at least 92% carbon[1]. Carbon fibers have excellent mechanical strength, yet they are light weight, have good electrical and thermal conductivity, are resistant to chemicals, and have the ability to withstand high temperature in an inert environment. Carbon fibers can be produced by applying high heat-treatment to organic polymer precursor fibers which have high carbon yield. The most used precursor materials for carbon fiber are rayon [2-4], pitch [5-11], and polyacrylonitrile (PAN) [12-35] fibers. Among the three major precursors, rayon fibers are currently not available commercially. Isotropic pitch based carbon fibers are inexpensive but have relatively low mechanical properties. Mesophase pitch based carbon fibers are able to meet specific needs due to their high modulus. PAN based carbon fibers are widely accepted as their compressive strength is greater than that of the pitch based fibers, and the mechanical properties of the final carbon fibers can be tailored by controlling the heat-treatment conditions.

Among the carbon allotropes, CNTs have exceptional mechanical, thermal, electrical, and optical properties [36-37], and they possess the ability to template polymer crystalization [38-44]. Thus, superior physical and mechanical properties have been reported for CNT incorporated polymers [45-78]. Also, enhanced tensile properties of carbon fibers due to incorporation of carbon nanotubes (CNTs) in PAN precursor have been reported [79-80].

1.2 Processes for Making PAN Based Carbon Fiber

1.2.1 Spinning

The acrylic precursor fibers can be produced by various spinning techniques such as solution, melt, and gel spinning. Among these solution spinning is the most common process for acrylic fiber production[81].

1.2.1.1 Solution Preparation

Either an organic or an inorganic solvent can be used for the preparation of polymer solution dope for spinning. Suitable organic solvents are *N*,*N*-dimethylformamide (DMF), *N*,*N*-dimethylacetamide (DMAc), and Dimethylsulfoxide (DMSO). The inorganic solvents are nitric acid, aqueous sodium thiocyanate, and aqueous zinc chloride. To eliminate captured air bubbles, the dope is stored for more than 24 hrs before spinning.

For better processing and fiber properties, the solid contents of the dope should be optimized depending upon the molecular weight of the polymer. A solution of lower molecular weight polymer requires a higher solid content due to the low intrinsic viscosity[82-83]. At low shear rate, viscosity of solution increase with molecular weight of PAN if measure with same solid content[84]. On the other hand, viscosities of different molecular weight PAN solution converge at high shear rate. This implies the difficulty of solution preparation with high molecular weight PAN, since conventional solution preparation is done under low shear rate. Viscosity of PAN solution can also be affected by its temperature[85].

1.2.1.2 Solution Spinning

Solution spinning is a fiber manufacturing process which involves dissolving the polymer into an appropriate solvent, and the injection of the prepared solution through, the nozzle which is also known as spinneret. The solution spinning can be classified by

the arrangement of the spinneret and the coagulation bath: (i) Wet spinning implies that spinneret is immersed in the coagulation bath so that the as-spun fibers pass directly into the coagulation bath. (ii) Dry spinning refers to solution spinning without a coagulation bath. The solvent in the as-spun fibers is evaporated by passing them through the hot chamber. (iii) Dry-jet wet spinning is similar to wet spinning but has an air gap between the spinneret and the coagulation bath. The coagulation bath consists of a nonsolvent and a solvent which is identical to that used for dissolving the polymer. The coagulation rate can be controlled by adjusting the composition of the coagulation bath. The higher the concentration of nonsolvent, the faster the solvent exchange, resulting in rapid coagulation. Temperature of the bath also affects the coagulation rate [86-87]. If the coagulation rate is too fast, then the cross section of fibers becomes irregular and forms a skin-core structure. For these reasons, a slow coagulation rate is favorable to obtain fibers with enhanced structure and properties.

1.2.1.3 Gel Spinning

To achieve high mechanical properties, the number of defects in the high performance polymeric fiber must be minimized. Under deformation, the stress preferentially concentrates on the defect sites such as chain ends, voids, chain entanglement, and foreign particles[88]. Some of those defects can be minimized by utilizing the gel spinning process, which was invented at DSM in the Netherlands[89]. By the use of the gel spinning technique, PAN solution is spun into a quenching bath to form fibers in a gel-like-state. Dilution of polymer solution is considered to minimize the entanglement in the gel spinning process. By assuming that one entanglement between two polymer molecules is enough to ensure the integrity of the PAN molecules and the stability during the drawing process, ideal entanglement status can be achieved at certain concentration level (C*) whose expression is

$$C^* = M_e/M$$

where M_e is entanglement molecular weight and M is the molecular weight of the polymer[89]. So, as molecular weight increases, the desired concentration (C*) decreases. However, the actual concentration of spinning dope is higher than C* to ensure process stability by controlling the number of entanglements.

1.2.2 Stabilization

Prior to the carbonization process, the PAN precursor fibers go through a stabilization process which involves heat-treatment at 180 ~ 300 ℃ under tension in an oxidative atmosphere. The stabilized fibers are thermally stable for the subsequent carbonization process which involves heat-treatment at very high temperature. The stabilization is very crucial to the properties of the final carbon fibers because it determines the structure of the carbon fibers. The structural imperfections which act as defects can be minimized by optimizing the stabilization conditions. To optimize the process, several key factors should be considered and tuned, such as types of comonomer, tension, temperature, heating rate, heating time, and the treatment medium, as discussed below.

1.2.2.1 Types of Comonomers

In general, the copolymer PAN precursors can be converted into better quality carbon fibers than homopolymer fibers because of the different mechanism involved during stabilization. It is well known that the stabilization of homopolymer PAN is governed by a radical mechanism, while copolymerized PAN with acidic comonomer is governed by an ionic mechanism[83]. The radical mechanism of cyclization is shown in Figure 1.1 (a). During the heat-treatment (~180 ^{o}C) of homopolymer PAN, free radicals can be generated. The unpaired electron on the nitrogen atom of the free radical helps to bond adjacent nitrile group (cyclization) and yields a new unpaired electron. Thus, the cyclization reaction continues. On the other hand, the acidic sites in PAN copolymerized

with an acidic comonomer play a key role in the ionic mechanism of cyclization. The debonding between oxygen and hydrogen occurs disproportionately, and an electron pair in the negatively charged oxygen atom forms a bond with the adjacent carbon atom in the nitrile group as shown in Figure 1.1 (b). Subsequently, the nitrogen atom of this adjacent nitrile group forms a new bond to the next carbon atom in the nitrile group. This process continues along the chain until the chain end is terminated by a =NH group.

Due to the exothermic nature of the cyclization reaction, localized heat can lead to abrupt gas evolution, resulting in inhomogeneity in the fiber. In the radical mechanism, the management of heat generation is a problem during homopolymer PAN cyclization. Once the cyclization reaction is initiated, the generated heat supplies more energy to increase the rate of cyclization and the surrounding temperature. The increased surrounding temperature and low thermal conductivity of the fiber make it hard to dissipate the excessive heat. Such excessive heating may cause chain scission that acts as a defect in carbon fibers. To dissipate the heat more effectively, slow propagation is preferred. Based on these explanations, the incorporation of CNTs in the PAN fiber can enhance the quality of the carbon fibers by reducing the rate of cyclization[79] and by helping with the dissipation of heat due to their high thermal conductivity. During cyclization, acidic comonomer lowers the reaction initiation temperature and broadens the exothermic peak of the cyclization reaction. Acrylic acid, methacrylic acid, itaconic acid, methacrylate (ester), acrylamide (amide), and quaternary ammonium salts (ammonium salts of vinyl compounds) are known as possible comonomers[83]. The chemical structures of various comonomeric candidates are listed in Table 1.1.

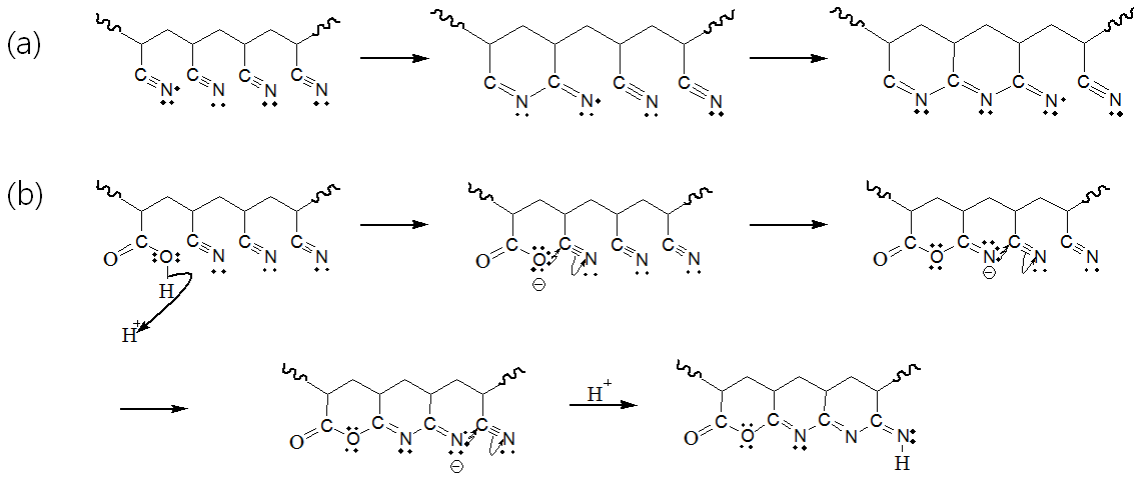

Figure 1.1 (a) Radical mechanism, and (b) ionic mechanism of the cyclization reaction[83].

Table 1.1 Various Comonomers for Acrylic Precursors[90].

Comonomer	Chemical structures
Acrylic acid (AA)	CH_2=CHCOOH
Methacrylic acid (MAA)	CH_2=C(CH_3)COOH
Itaconic acid (IA)	CH_2=C(COOH)CH_2COOH
Methacrylate (MA)	CH_2=CHCOOCH_3
Acrylamide (AM)	CH_2=CHCONH_2

The decrease in initiation temperature in the copolymer with respect to the initiation temperature in the homopolymer PAN is in the following order; itaconic acid > methacrylic acid > acrylic acid > acrylamide [91]. Itaconic acid has two carboxylic groups which involve initiation of the cyclization in ionic mechanism. Thus, itaconic acid showed the largest drop of initiation temperature of the cyclization reaction. Increased comonomer content leads to both reduced cyclization time and reduced carbon yield of the final carbon fibers. For this reason, the optimum content of acidic comonomer is reported to be about 2 mol % [92-94].

1.2.2.2 Effect of Tension

The tension applied during the stabilization process prevents the shrinkage which would otherwise lower the molecular orientation. There are two types of shrinkage during the stabilization process[95]: (i) physical shrinkage is the relaxation of polymer molecules during the heat-treatment due to the entropic recovery, and (ii) chemical shrinkage that comes from changes in the chemical structure since the length of carbon-carbon double bond in the ladder structure is shorter than that of single bond. The regular position of the nitrile group helps to form the ladder structure in the cyclization process. If the polymer molecules are relaxed, cyclization becomes difficult due to the irregular position of the nitrile group. Tension applied during the stabilization process helps to prevent shrinkage so that the polymer molecule alignment can be preserved throughout the process, resulting in better tensile properties.

1.2.2.3 Effect of Temperature and Heating Rate

In general, the heat-treatment temperature for stabilization can be adjusted depending on the types of comonomers, precursor fiber diameter, and morphological structure of the precursor PAN fiber. A heating rate of less than 5 ℃/min was suggested for the stabilization process to obtain better properties carbon fibers[96]. As stated earlier, the localized heat generation can be suppressed by reducing the heating rate since the nature of cyclization reaction is exothermic.

1.2.2.4 Effect of Heat-Treatment Medium

Carbon fibers with superior properties are produced from precursor fibers stabilized under an oxidizing medium rather than under an inert atmosphere. The oxygen containing groups (such as hydroxyl, carbonyl, or carboxyl groups) are introduced into

the backbone of ladder polymer. The fusion of the ladder chains can be promoted in the presence of oxygen containing groups during carbonization step [20].

1.2.3 Carbonization

The carbonization process refers to high temperature (~1500 ℃) heat-treatment after the stabilization process [83]. The heat transfer, chemical reaction, and mass transfer are involved in the carbonization process. Throughout the carbonization process, the non-carbon elements are eliminated in the form of volatile gases such as HCN, NH_3, H_2O, CO_2, N_2, and hydrocarbons. Rapid irruption of gas occurs on the fiber surface with a heating rate higher than 5 ℃ /min and causes irregular fiber surface, which decrease the fiber tensile properties[96]. The carbonization should be done under an inert medium such as nitrogen or argon gas to prevent oxidation at high temperature. Chemical fusion of ladder structure takes place by condensation of water, dehydrogenation, and/or cross-linking (Figure 1.2). Studies on the relationship between final heat-treatment temperature and mechanical properties reveal that the tensile strength reaches a maximum at around 1500 ℃, while the tensile modulus keeps increasing at further higher temperatures of carbonization [97].

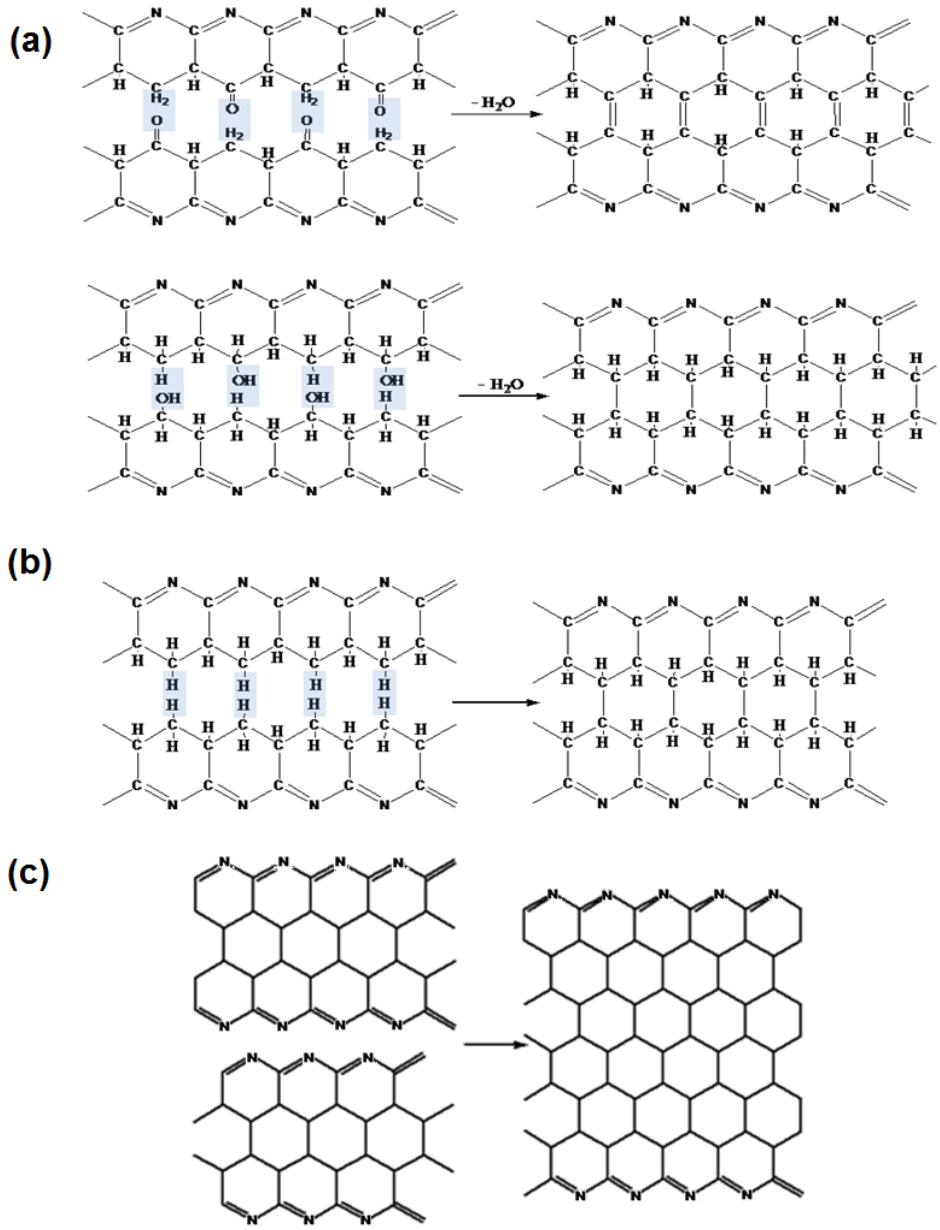

Figure 1.2 Intermolecular crosslinking of stabilized fibers through (a) oxygen containing groups, (b) dehydrogenation, and (c) cyclized sequences[90, 98].

1.3 Effect of Carbon Nanotubes on Evolution of Structure and Properties

1.3.1 CNT Rheology

It is important to understand rheological behavior of CNTs, as it affects processing conditions. Rheological behavior of a polymer/CNT composite has been reported [99-108]. Kim et al.[101] reported that viscosity of epoxy/CNT composite increased when surface modified CNTs (amine, acid, or plasma treated) were used as compared to control epoxy as well as epoxy/CNT without surface treatment. This implies that interfacial bonding between CNT and Epoxy and dispersion of CNT are improved by surface modification of CNT. Ma et al.[102] conducted extensional rheology of epoxy/SWNT (functionalised with Arene Diazonium salts) composite suspension. The epoxy/SWNT suspension showed longer elongation than neat epoxy suspension under extension, suggesting reinforcing effect of SWNT during extension. Xu et al.[108] investigated rheological properties of isotactic polypropylene (iPP)/MWNT nanocomposites. With relatively low aspect ratio (22 to 45), network structure of MWNT is prone to breakage under high shear deformation, resulting in less elastic contribution to rheological response of iPP/MWNT. On the other hand, network of high aspect ratio MWNT can resist more under high shear flow than that of low aspect ratio MWNT. Suppressed die-swell of iPP/MWNT was observed by conducting capillary rheometry.

PAN/CNT solution showed non-newtonian behavior such as shear thinning [109-113] and showed higher storage and loss moduli than PAN solution[112]. Khenoussi et al.[109] observed flow threshold behavior (sudden viscosity drop during shear stress sweep test) of PAN/MWNT dope when MWNT content is higher than 2.0%. Wang et al.[111] studied rheological behavior of PAN/MWNT spinning dope which was prepared by in-situ polymerization. The molecular weight of PAN decreased with increasing MWNT content in the system. The apparent viscosity of PAN/MWNT dope decreased with increasing MWNT content due to the reduced molecular weight of PAN. The

PAN/MWNT solution showed shear thickening behavior if MWNT content is higher than 0.53 wt.%. The reason for shear thickening behavior was not explained.

1.3.2 Structure of PAN Precursor Fiber

The PAN molecule has nitrile side groups that have strong dipole interactions. It is well known that the intra-dipole interactions of nitrile groups are repulsive while inter-dipole interactions are attractive. Because of those strong repulsive dipole interactions, the PAN molecule forms a helical coil structure. The unit cell of the ordered phase in PAN is controversial; (i) hexagonal or pseudo-hexagonal structure with two dimensional order, and (ii) orthorhombic unit cell with three dimensional order [114-119]. Bashir reported that a PAN molecule can co-crystallize with a polar solvent such as propylene carbonate to form an orthorhombic crystal[120]. If the solvent is evaporated, then the orthorhombic crystal structure can revert to a hexagonal crystal structure. Gupta and Singhal et al. proposed a model with PAN molecules of helical conformation as flexible rods of about 6 Å diameter[121]. In the ordered region, these molecular rods are aligned and hexagonally packed together, whereas the amorphous region shows misalignments of rods, such as entanglements, loops, heterogeneity (comonomer), foreign particles, and other defects.

It was reported that structural changes were induced by the incorporation of CNTs [122]. The crystal size of PAN/SWNT composite fiber is comparable or slightly smaller (11.2 or 11.5 nm) than that in the control PAN fiber (11.7 nm). However, the crystallinity increased with the introduction of SWNT (68 ~ 69% for PAN/SWNT composite fiber vs. 65% for PAN control fiber). This is also confirmed by comparing the tensile moduli of fibers. The tensile modulus of PAN/SWNT composite fiber exceeded the predicted value calculated by the rule of mixtures with assumption of ideal orientation of SWNT (which aligned perfectly along the fiber axis), suggesting property changes in the PAN matrix (enhanced crystallinity). The meridional peak position in WAXD pattern shifted to lower

2θ with the incorporation of SWNT, implying an increase in the planar zigzag sequence of PAN chains.

1.3.3 CNT Orientation

Anisotropic mechanical properties have been observed due to the alignment of CNT in composite system [123-135]. To evaluate CNT orientation, various tools are introduced such as, transmission electron microscopy (TEM)[127-128], scanning electron microscopy (SEM)[129], focused ion beam[125], X-ray scattering[124, 136], atomic force microscopy (AFM)[123], and Raman spectroscopy[123-124, 132, 137-138]. Carbon nanotube orientation, and particularly that of the single wall carbon nanotubes can be quantitatively determined using Raman spectroscopy [[137].

1.3.4 Structural Changes during Heat-Treatment

As stated earlier, the PAN molecules can be regarded as flexible rods with a diameter of about 6 Å. Ko et al. showed structural changes in PAN molecular structure during stabilization by using flexible rods model [32-33]. Below 180 ℃, the crystal size and orientation increase slightly as temperature goes up, due to the migration of some acrylonitrile groups from the amorphous phase to the ordered phase. The cyclization is initiated in the amorphous regions when temperature exceeds 180 ℃ because more energy is needed to weaken the attractive dipole interactions of acrylonitrile groups in the ordered phase. Heat generated by the exothermic cyclization reaction in the amorphous phase helps to overcome the molecular interactions in the ordered phase, initiating cyclization reactions in the ordered phase. As the temperature increases further, the cyclization reaction spreads throughout the ordered region, and the reaction rate increases.

Energy-dispersive X-ray spectroscopy (EDS) studies[139] revealed that chemical composition of the stabilized PAN fibers could be 40% of acridone rings, 30% of

naphthyridine rings, 20% of hydronaphthyridine rings, and 10% of other structures, as shown in Figure 1.3.

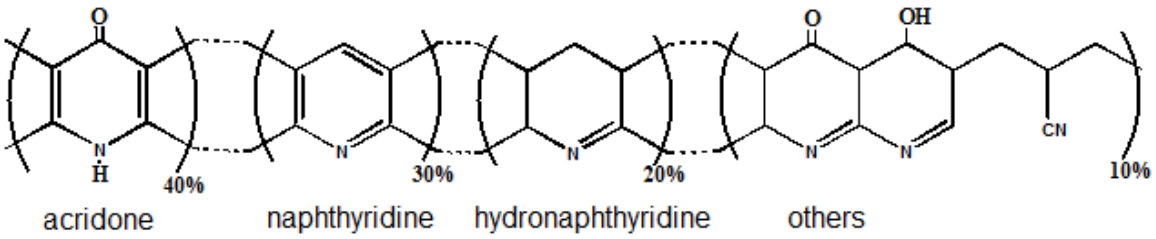

Figure 1.3 Chemical structure of stabilized PAN precursor[139].

During carbonization, the ladder polymer chains fuse together from the elimination of the oxygen containing groups at around 600 ℃, and the remaining nitrile groups are cyclized (Figure 1.2 (a)). At 700 ℃ or higher, the fusion of ladder polymer chains also takes place at the nitrogen atoms (Figure 1.2 (c)). The fusion of ladder chains continues throughout the carbonization process until the majority of non-carbon atoms are removed, and the sp^2 hybridized carbon atoms are hexagonally packed together in basal plane. In the basal plane, the bond length and angles are comparable to the graphite structure, and those graphitic planes are randomly stacked together in parallel fashion and separated by a distance of 3.4 Å .

1.3.5 Structure of CNT Incorporated PAN Based Carbon Fiber

In general, highly ordered graphitic structures are not expected for PAN based carbon fibers without graphitization. When PAN/ single wall nanotubes (SWNT) composite fibers are used as a precursor, well-developed graphitic structure is observed in the vicinity of SWNT. The carbonization temperature of this carbon fiber was 1100 ℃, which is a relatively low temperature for this structure. The graphitic structure affected by SWNT can be confirmed by Raman spectra. Intensity of the G-band (ca. 1590 cm^{-1}) for PAN/SWNT based carbon fiber increased with applied tension during carbonization

as shown in Figure 1.4 B. On the other hand, PAN based carbon fiber didn't exhibit G-band intensity (Figure 1.4 A). Due to structural improvements, the tensile strength of the PAN/SWNT based carbon fiber (3.2 GPa) was 60% higher that of the control PAN based carbon fiber (2.0 GPa). Similarly, the tensile modulus of the PAN/SWNT based carbon fiber (450 GPa) was significantly higher than that of the control PAN based carbon fiber (302 GPa).

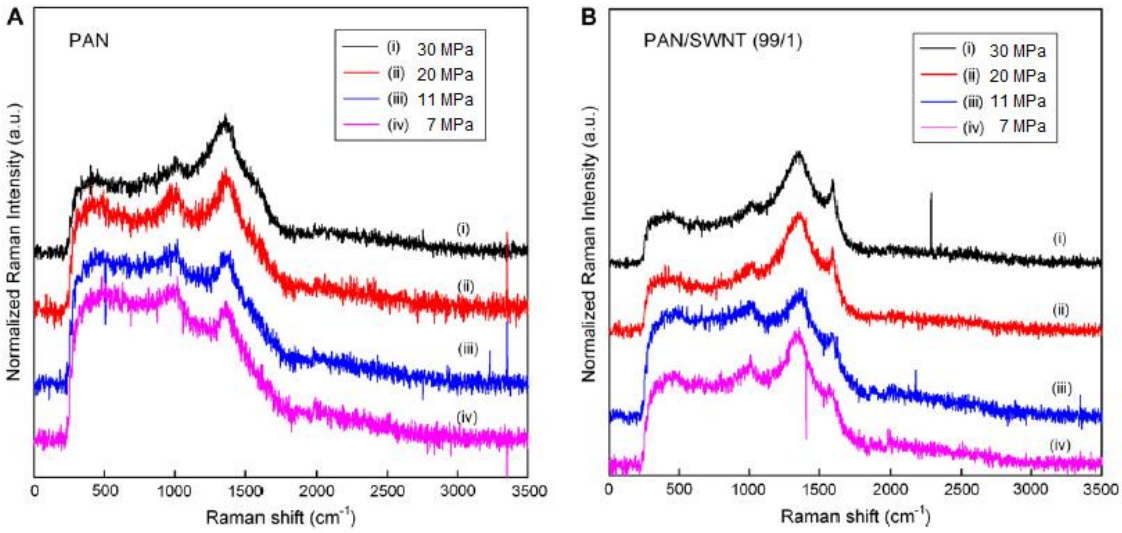

Figure 1.4 Raman spectra for the carbonized (A) PAN and (B) PAN/SWNT (99/1) fibers as a function of applied stress during stabilization and carbonization[79].

1.4 Objectives of Thesis

The overall objectives of this study are:

- To study the effect of Carbon nanotubes (CNTs) on the flow behavior (rheology) of polyacrylonitrile (PAN) solution.
- To study the PAN crystal and CNTs orientation at different stages of fiber processing.

- To study the effect of spin-drawing and hot-drawing on structure, and properties of dry-jet-wet spun polyacrylonitrile-co-methacrylic acid (PAN-co-MAA)/vapor grown carbon nanofiber (VGCNF) composite fiber.
- To study the gel-spinning of high molecular weight PAN (homo-, and co-polymer) and PAN/CNT composite fibers.
- To estimate the volume fraction of the interphase in PAN/CNT system as a function of CNT concentration and interphase thickness.

CHAPTER 2

PAN/MWNT COMPOSITE PRECURSOR FIBERS AND THEIR CARBON FIBERS

2.1 Introduction

Chae et al.[140] compared the reinforcement efficiency of various types of CNTs in solution spun PAN/CNT fibers. They concluded that SWNTs are good for enhancing low strain property (tensile modulus), due to their large surface area, whereas MWNTs show improvement of high strain properties (tensile strength, and work of rupture) due to the longer length of MWNT. The mechanical properties of PAN fibers can be improved through the gel-spinning of PAN[89, 122]. In this study, gel spinning of PAN/MWNT composite fibers was carried out, and characterization of their mechanical properties and structural changes was done. Also, stabilization and carbonization of gel-spun PAN/MWNT composite fibers were performed and the resulting carbon fibers were characterized.

2.2 Experimental

2.2.1 Materials

Polyacrylonitrile [homo-polymer PAN, of molecular weight (M_w) 2.5×10^5 g/mol] was obtained from Japan Exlan, Co. Multi-walled nanotubes (MWNT: with about 5 wt.% metallic impurity) were obtained from Cheaptube Inc. and used as received. WAXD of these MWNT revealed that the average number of walls in this specimen was 18. WAXD scan of these MWNTs is given in Figure 2.1 (a). From this WAXD (002) peak, crystal size was determined using the Scherrer equation and the average number of walls was determined by dividing this value of crystal size by the interlayer graphitic spacing of

0.34 nm. The average diameter of 53 ± 13 nm was obtained from SEM micrographs, as shown in Figure 2.1 (b). *N*, *N*-dimethylformamide (DMF) from BDH, Inc. was used as the solvent.

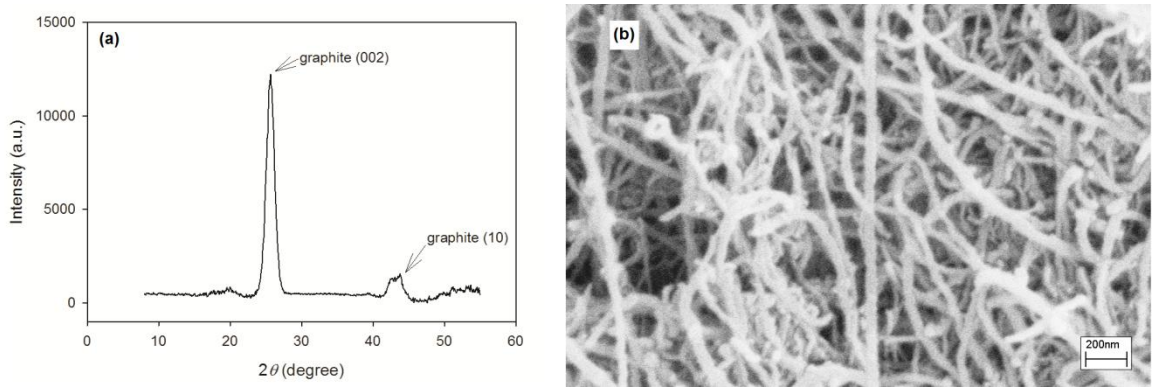

Figure 2.1 (a) WAXD and (b) SEM micrograph of MWNTs.

2.2.2 Solution Preparation

MWNTs (150 mg) were mixed in DMF (400 mL) and homogenized at 22,000 rpm for 30 min prior to ultra-sonication. The as-prepared MWNT/DMF solution was placed in an ultra-sonicator (Branson 3510R-MT, 100 W, 42 kHz) for 24 hours with agitation (1,200 rpm by Cole-Palmer model 4554-10 LAB Mixer). PAN polymer (14.85 g) was dried in a vacuum oven at 100 ℃ and dissolved in DMF (100 mL) at 80 ℃. The dispersed MWNT/DMF solution was added to the PAN/DMF solution; the excess amount of solvent was evaporated by vacuum distillation with mechanical stirring to meet the desired solid content in the solvent (15 g solids (PAN and MWNTs)/100 mL DMF).

2.2.3 Fiber Spinning

The PAN control and PAN /MWNTs composite fibers were spun utilizing the gel spinning technique and using a Bradford University spinning unit equipped with a single-hole spinneret with an orifice diameter of 250 µm. The prepared solution was spun into a cold methanol gelation bath (-50 ℃) with an air gap of 2 cm. The fibers were stretched

five times during the spinning process by increasing the take-up speed with respect to the linear-jet velocity of the spun fibers. The as-spun fibers were immersed in the methanol bath at a temperature of -30 ℃ for 72 hours. The post-drawing process (draw ratio in the range of 5 to 11) was carried out using an in-line heater whose temperature was maintained at 165 ℃. The total draw ratio was expressed as the product of the spin draw ratio and the post draw ratio. Figure 2.2 provides schematics of the spinning and drawing steps.

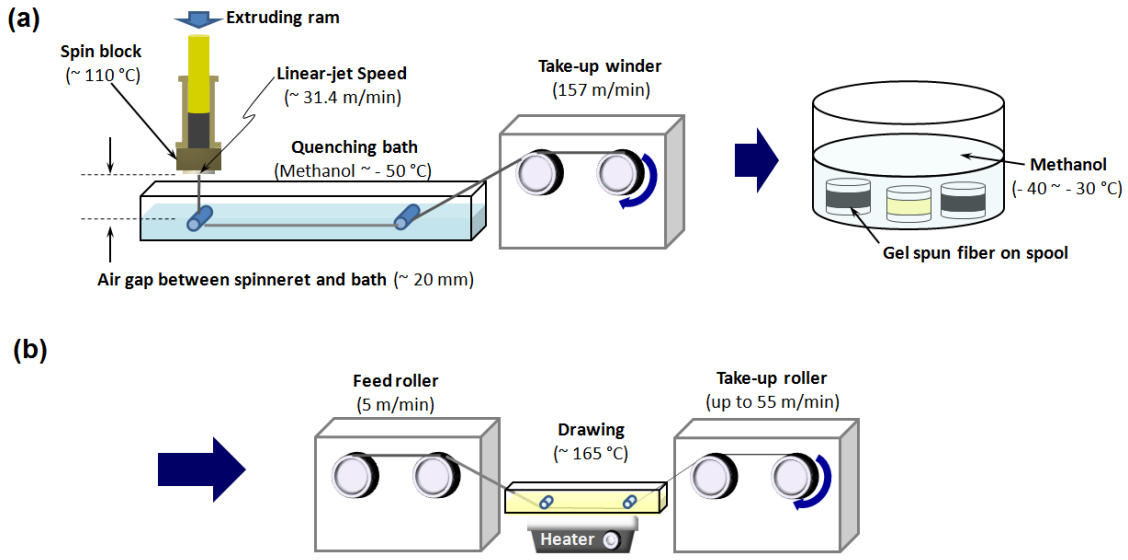

Figure 2.2 Schematics of (a) gel spinning and (b) drawing.

2.2.4 Stabilization and Carbonization

2.2.4.1 Stabilization and Carbonization (Vertical Mount)

Carbon steel blocks were secured as weights at each end of the precursor fiber bundles. Then fiber bundles were vertically hung over a quartz rod (Figure 2.3) at various stress levels (5, 7.5, 10, 20 and 30 MPa) and placed in the box furnace (Lindberg, 51668-HR Box Furnace 1200C, Blue M Electric) for heat-treatment. For stabilization, fibers

were heated from room temperature to 285 ℃ at two different heating rates in the air. Initially, the heating rate was set at 5 ℃/min up to 175 ℃ and subsequently changed to 1 ℃/min. Fibers were heat-treated at 285 ℃ for 4.5 hours, followed by increasing the temperature to 330 ℃ at a heating rate of 1 ℃/min and holding at this temperature for 2 hours. After completing the stabilization process, the fibers were cooled down to room temperature and subsequently carbonized by increasing the temperature to 1100 ℃ at a heating rate of 5 ℃/min under argon and holding at this temperature for 5 min.

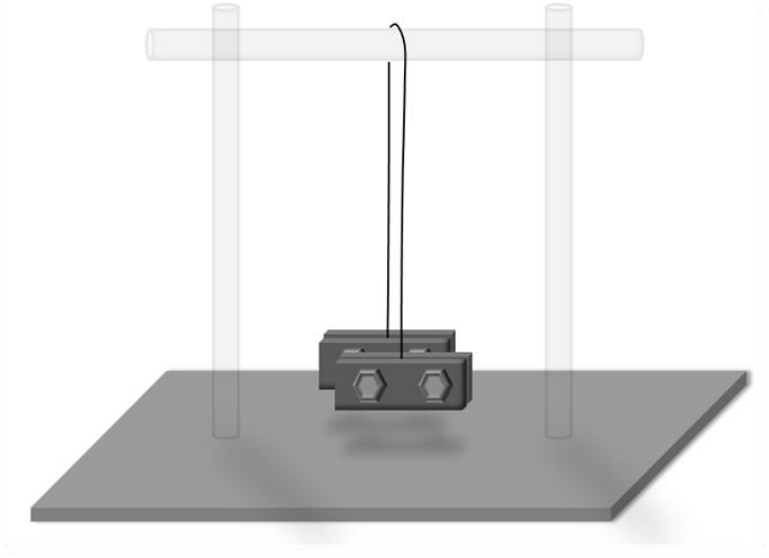

Figure 2.3 Schematic of the set up for vertical heat-treatment.

2.2.4.2 Stabilization and Carbonization (Horizontal Mount)

Graphite blocks were used to clamp both ends of the precursor fiber bundles together, and the fiber bundle was hung horizontally over a graphite rod (Figure 2.4) at a stress level of 22.5 MPa and placed in the tube furnace (MHI H17HT2.5X24 tube type furnace with 100 mm diameter and 1500 mm length alumina tube). The parameters of tension, heat-treatment temperature, heating rate, and isothermal temperature were varied based on the results from the vertical mounting heat-treatment studies. For stabilization,

fibers were heated from room temperature to 250 ℃ at a heating rate of 5 ℃/min in air and held at this temperature for 2 hours, followed by increasing the temperature to 320 ℃ at a heating rate of 5 ℃/min and holding at this temperature for various time intervals (20, 25, 30, 35, 42.5, and 45 min, respectively). After completing the stabilization reaction, the argon was purged through the furnace, and the fibers were subsequently carbonized by increasing the temperature to 1100 ℃ at a heating rate of 5 ℃/min and by holding at this temperature for 5 min.

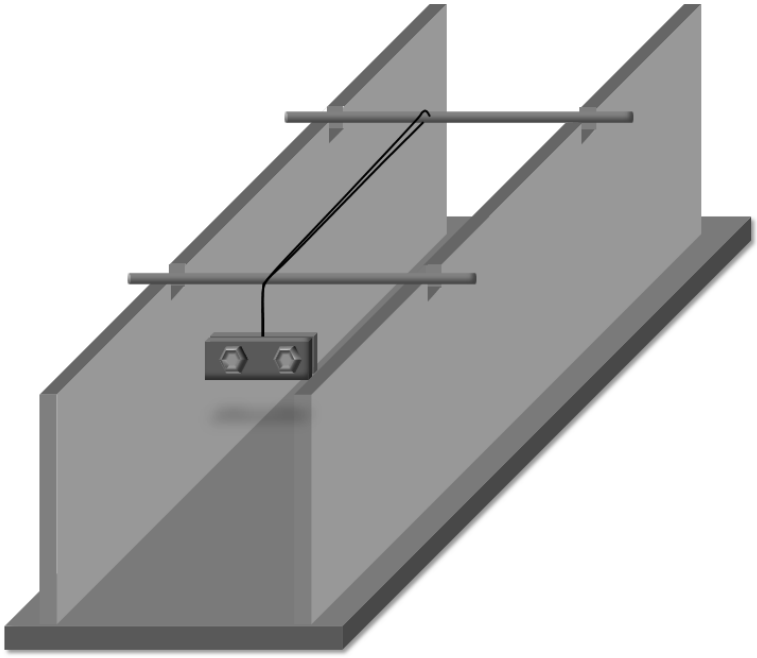

Figure 2.4 Schematic of the set up for horizontal heat-treatment.

2.2.5 Mechanical Properties

The tensile properties were characterized using an RSA III solids analyzer (Rheometric Scientific, Co.) at gauge length of 25.4 mm and crosshead speed of 0.254 mm/s. At least 16 specimens were tested for each sample.

2.2.6 WAXD Analysis of PAN/MWNT Composite Fibers

Wide-angle X-ray diffractions of PAN/MWNT composite fibers were collected using a Rigaku MicroMax 002 X-ray generator with confocal optics to produce Kα radiation (λ = 1.5418 Å) and equipped with a R-axis IV++ detector. The crystallinity was calculated by fitting the integrated scan using MDI Jade 8.5.2 software, and the crystal size was calculated using the Scherrer equation. The Herman's orientation function of the PAN crystal c-axis about fiber axis (f_{PAN}: Herman's orientation factor) was calculated using Wilchinsky's equation.[141-142]. The detailed calculation method is described elsewhere [38, 43, 52, 78, 140].

2.2.7 Thermal Analysis

Differential scanning calorimetry (DSC; TA instruments Q200) on the precursor fibers was conducted. The precursor fiber (1.5-2 mg) was heated from 150 to 400 ℃ at a heating rate of 10 ℃/min (or 1 ℃/min). After 1st heating scan, sample pan was quenched at a cooling rate of 100 ℃/min. The 2nd and 3rd heating scans were conducted at an identical heating rate to the 1st scan.

2.2.8 Dynamic Mechanical and Thermo-Mechanical Properties

Dynamic mechanical tests were conducted using an RSA III solids analyzer (Rheometric Scientific, Co.) at various frequencies (0.1, 1, and 10 Hz) and at a heating rate of 1 ℃/min at 25 mm gauge length. Bundles of 100 filaments were used. Thermal shrinkage of the PAN/MWNT composite fiber was monitored as a function of temperature using a thermo-mechanical analyzer (TMA 2940, TA instruments) at various stress levels. The heating profile was identical to the stabilization condition stated in 2.2.4.2, except holding time was fixed for 60 min at 320 ℃.

2.2.9 Fiber Morphology of PAN/MWNT Composite Fibers

Scanning electron microscopy (SEM; LEO 1530 operated at 10kV, or Hitachi S800 equipped with Hitachi X800 Field Emission Gun operated at 10kV) was used for the observation of gold coated samples. UTHSCSA image tool software was used to compute cross sectional areas and diameters of the fibers.

2.3 Results and Discussion

2.3.1 Tensile Properties

Mechanical properties of PAN and PAN/MWNT fibers are summarized in Table 2.1. At a given draw ratio, the diameter of PAN/MWNT composite fiber is slightly smaller than that of the PAN control fiber at the same draw ratio suggesting suppressed die-swell. In general, polymeric fluids (solution and melt) show non-newtonian behavior which also results in phenomenon such as rod-climbing (fluid rising up a stirring rod during agitation) and die-swell. Suppressed die-swell was observed in polypropylene (PP)/MWNT system as compared to the control polypropylene[108, 143]. In the presence of CNT, the elastic recovery of PP molecules is restricted resulting in lower die-swell. Also, the alignment of CNT[144-145] helps to reduce the diameter of extrudate similar to the contraction of lyotropic liquid crystalline polymer under shear flow[146-147]. Thus, the restricted elastic recovery of PAN molecules, and alignment of MWNT could be the reason for suppressed die-swell and smaller diameter of PAN/MWNT fibers.

Typical stress-strain curves of the PAN control and the PAN/MWNT composite fibers at various draw ratios are shown in Figure 2.5. Mechanical properties of the PAN/MWNT composite fibers increased with increasing draw ratio. The maximum draw ratio of the PAN/MWNT fibers (55) is larger than that of the PAN fibers (35). Ma et al.[102] showed enlarged extensional deformation of epoxy/surface modified CNT suspension as compared to epoxy suspension under the extensional rheometer experiment

Table 2.1 Mechanical properties of PAN/MWNT composite fibers at various draw ratios.

	PAN control		PAN/MWNT (1 wt.%) composite				
Draw ratio (DR)	25	35	25	35	45	50	55
Diameter (μm)	15.8±0.1	13.5±0.1	15.5±0.1	13.2±0.3	11.7±0.1	10.6±0.1	10.4±0.1
Tensile strength (GPa)	0.62±0.08	0.56±0.07	0.77±0.10	1.04±0.17	1.0±0.09	1.15±0.11	1.34±0.13
Tensile modulus (GPa)	17±3	15±2	19±2	24±4	21±3	24±2	26±2
Elongation at break (%)	7.4±0.5	6.5±0.5	9.1±1.2	8.4±1.2	8.3±0.6	7.9±0.6	8.5±0.5
Work of rupture (MPa)	25±5	19±3	39±10	47±13	43±7	46±7	57±8

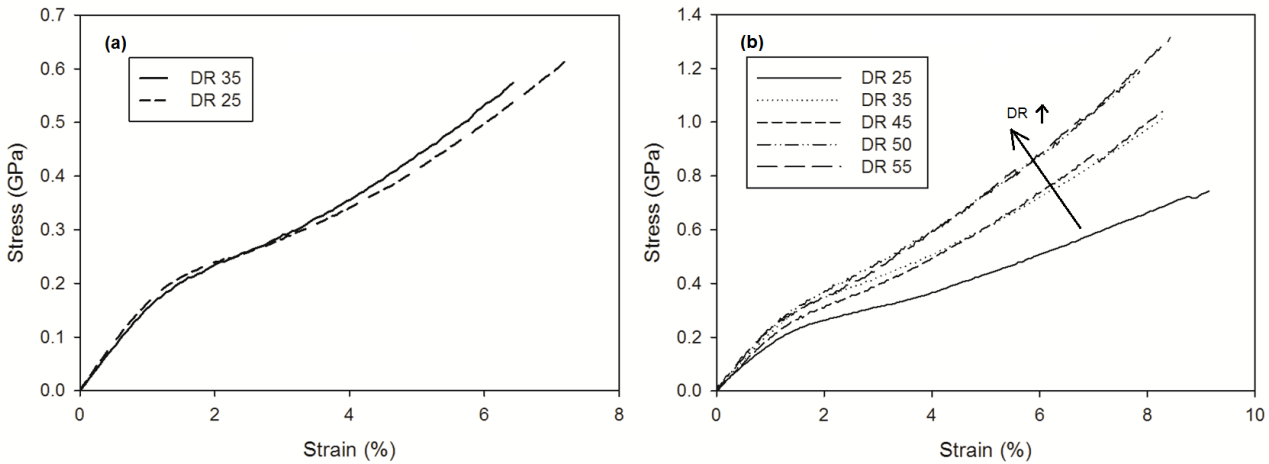

Figure 2.5 Stress-strain curves of (a) PAN control and (b) PAN/MWNT composite fibers at various draw ratios (DR).

due to the reinforcing effect of CNT during deformation (extension). On the other hand, epoxy/untreated CNT showed slightly shorter extension as compared to the control epoxy suspension due to the poor interfacial strength between the epoxy and the CNT. In this study, the larger draw ratio of PAN/MWNT fiber indicates reinforcing effect of CNT during drawing and good interaction between the PAN and the MWNT. The interaction between PAN and MWNT can lead to higher draw ratio of the PAN/MWNT composite fiber as compared to the control PAN fiber. Due to the hindered elastic recovery, PAN molecules remain more aligned along the spin line and the number of entanglements reduces in the as-spun fibers, which leads to better drawability of the PAN/MWNT composite fibers. The enhanced drawability increased the tensile strength of PAN/MWNT composite fiber to a level as high as 1.34 GPa at a draw ratio of 55.

2.3.2 Morphology of PAN/MWNT Composite Fibers

SEM micrographs of PAN/MWNT fibers cross-sections are shown in Figure 2.6. Both, the partially drawn (DR of 25; Figure 2.6 (a) ~ (c)) and the fully drawn fibers (DR of 55; Figure 2.6 (d) ~ (h)) showed good MWNT dispersion. The average diameters of MWNT in partially drawn and fully drawn fibers are 69 ± 5 nm and 62 ± 5 nm, respectively. The average diameter of pristine MWNT is ~ 53 nm prior to the dispersion in PAN, as shown in Figure 2.1 (b), suggesting that PAN molecules maybe wrapped around MWNT. The solubility difference between PAN and PAN/MWNT fiber as shown in Figure 2.7 may supports this hypothesis. After treatment in DMF at 60 ℃ for 24 hours, the control fibers were partially dissolved, while composite fibers showed no distinct change. With treatment in boiling DMF for 30 minutes, the control fibers were completely dissolved, whereas PAN/MWNT fibers were fragmented and partially dissolved, suggesting formation of chemically stable PAN crystal in the vicinity of MWNTs.

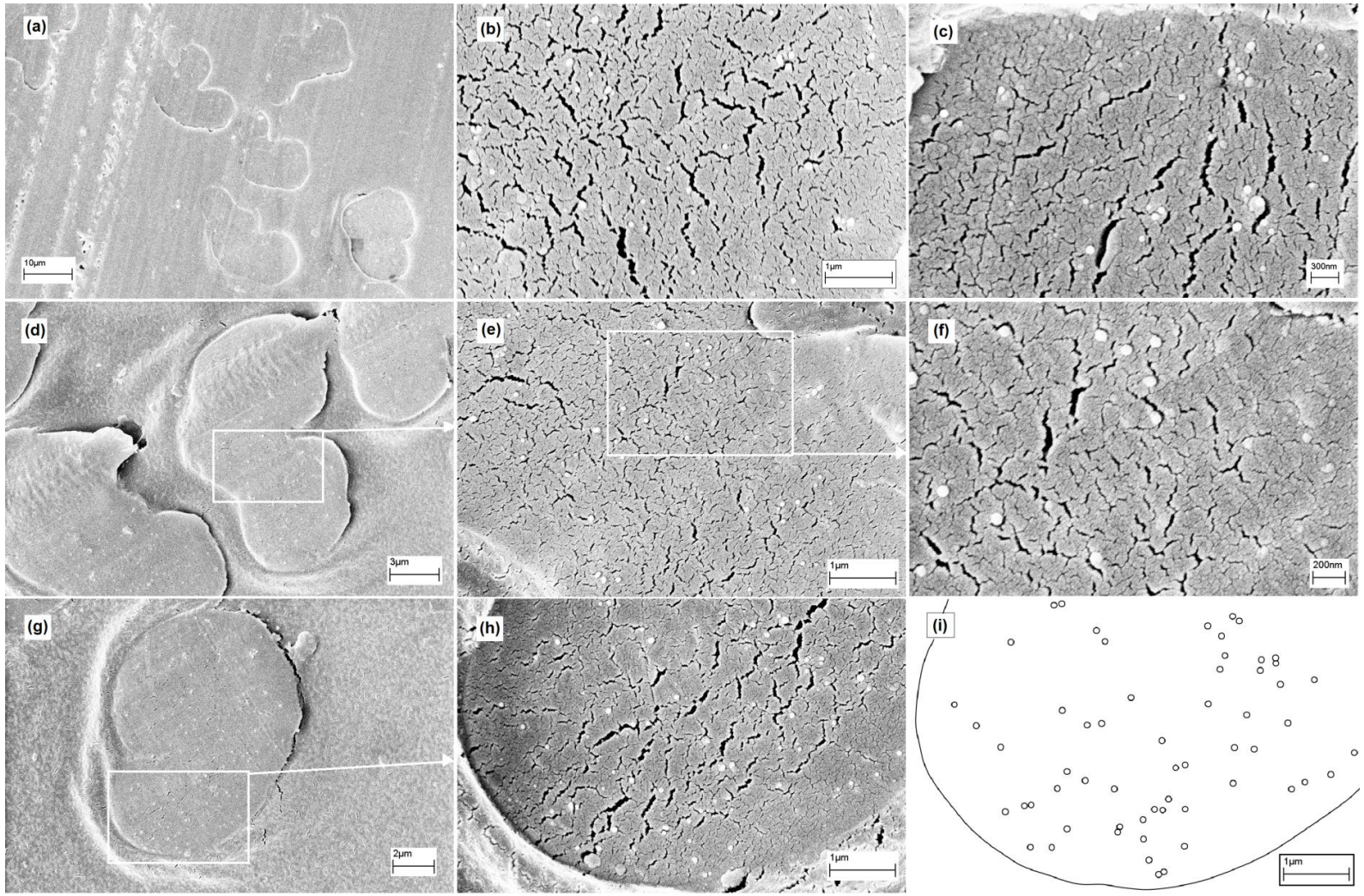

Figure 2.6 SEM micrographs for the cross-section of PAN/MWNT (1 wt.%) composite fibers (a) ~ (c) with a draw ratio of 25 and (d) ~ (h) with a draw ratio of 55. (i) is the schematic representation showing MWNTs in the cross-section in Figure (h).

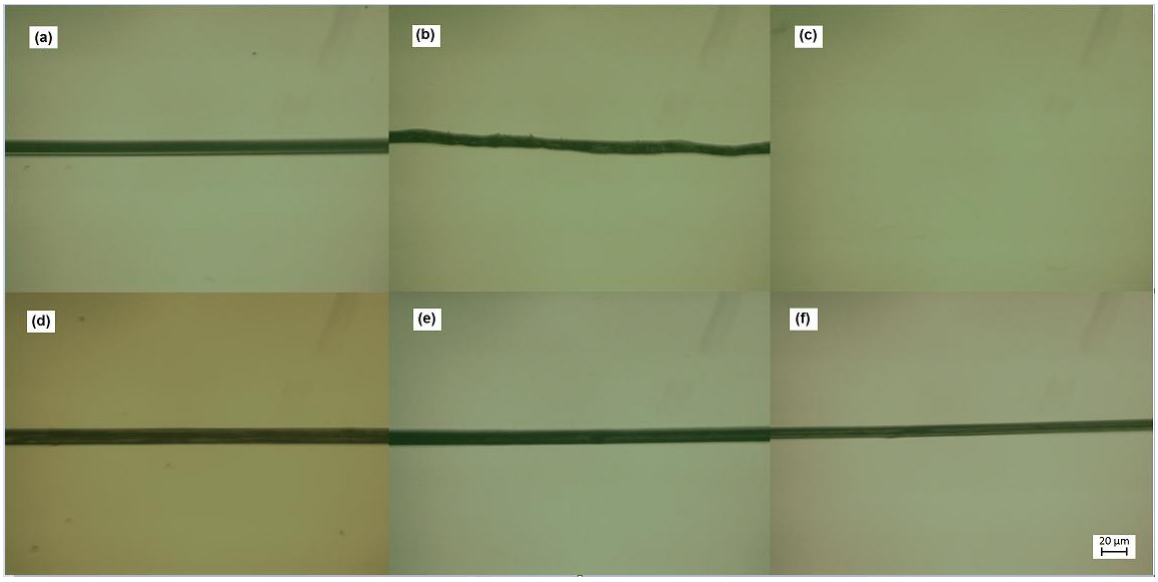

Figure 2.7 Optical micrographs of (a) PAN fiber with a draw ratio of 25 and (d) PAN/MWNT (1 wt.%) with a draw ratio of 25, (b) and (e) are respective fibers after treatment in DMF at 60 ℃ for 24 hrs, (c) and (f) are respective fibers after treatment in boiling DMF for 30 min.

The average distance between individual MWNTs is obtained by tracing the MWNT in the cross-section as shown in Figure 2.6 (i). The average distance between the individual MWNT is 490 ± 270 nm and 430 ± 281 nm for partially drawn fibers and fully drawn fibers, respectively. At the given MWNT diameter (~53 nm), number of walls (~ 18), and weight fraction (1 wt.%), the calculated average distance between individual MWNTs is about 436 nm. This is in good agreement with the observed values. A detailed calculation method for determining the average distance between MWNT will be discussed in Chapter 7.

2.3.3 Structural Analysis of PAN/MWNT Composite Fibers

Integrated intensities and the 2-D wide angle X-ray diffraction patterns of PAN/MWNT composite fibers are shown in Figure 2.8. With regards to PAN crystal structure, two possible crystal structures, orthorhombic and hexagonal have been considered [114-116, 118]. Bashir et al.[120] reported that the PAN molecules can co-

crystallize with a polar solvent to form orthorhombic unit cell and can be transformed to hexagonal crystal by removing the solvent. Based on this observation, the ratio of two *d*-spacings in equatorial reflections ($d_{2\theta\sim17^\circ}$ / $d_{2\theta\sim30^\circ}$) approaches the square root of three (~1.732) when PAN molecules form a hexagonal crystal structure. The ratio of *d*-spacings for PAN/MWNT composite fibers ranged from 1.71 to 1.72 (Table 2.2), which means that the crystal structure of PAN became more perfect hexagonal packing[120]. It can be inferred from the structural analysis results summarized in Table 2.2 that crystallinity and f_{PAN} are responsible for the enhanced mechanical properties of the highly drawn composite fibers.

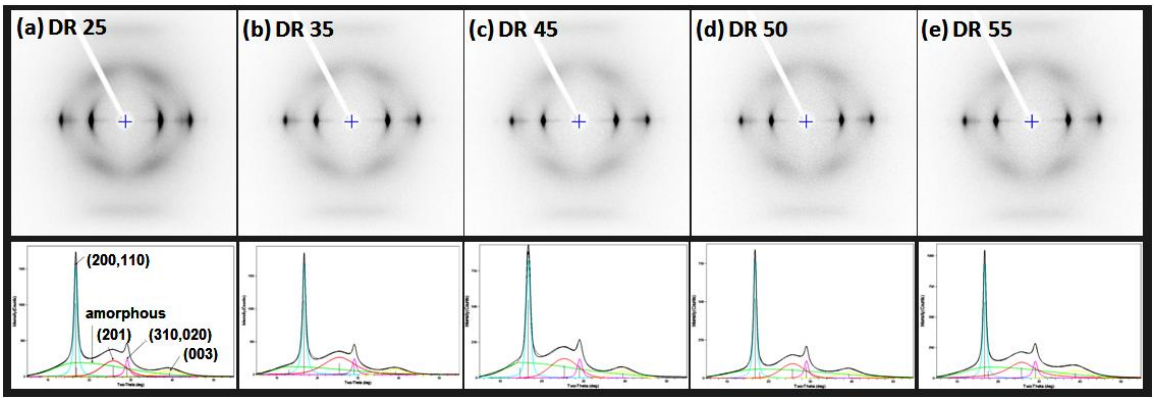

Figure 2.8 2D WAXD patterns of PAN/MWNT composite fibers.

Table 2.2 WAXD results for PAN/MWNT composite fibers.

	Draw ratio				
	25	35	45	50	55
Crystallinity (%)	52.4	53.6	63.6	63.7	67.2
Crystal size (nm)	11.4	11.8	11.8	11.5	11.4
$d_{2\theta\sim17^\circ}$ / $d_{2\theta\sim30^\circ}$	1.718	1.718	1.709	1.719	1.719
f_{PAN}	0.864	0.876	0.890	0.894	0.903

2.3.4 Dynamic Mechanical Analysis

The storage moduli of PAN control fibers and PAN/MWNT composite fibers at the same draw ratios are shown in Figure 2.9. At a given draw ratio, the storage moduli of PAN/MWNT composite fibers are higher than that of the PAN control fibers in the entire temperature range [Figure 2.9 (a) and (b)]. Also, in a given system (control or composite), enhanced storage moduli of fibers were observed with higher draw ratios [Figure 2.9 (c) and (d)].

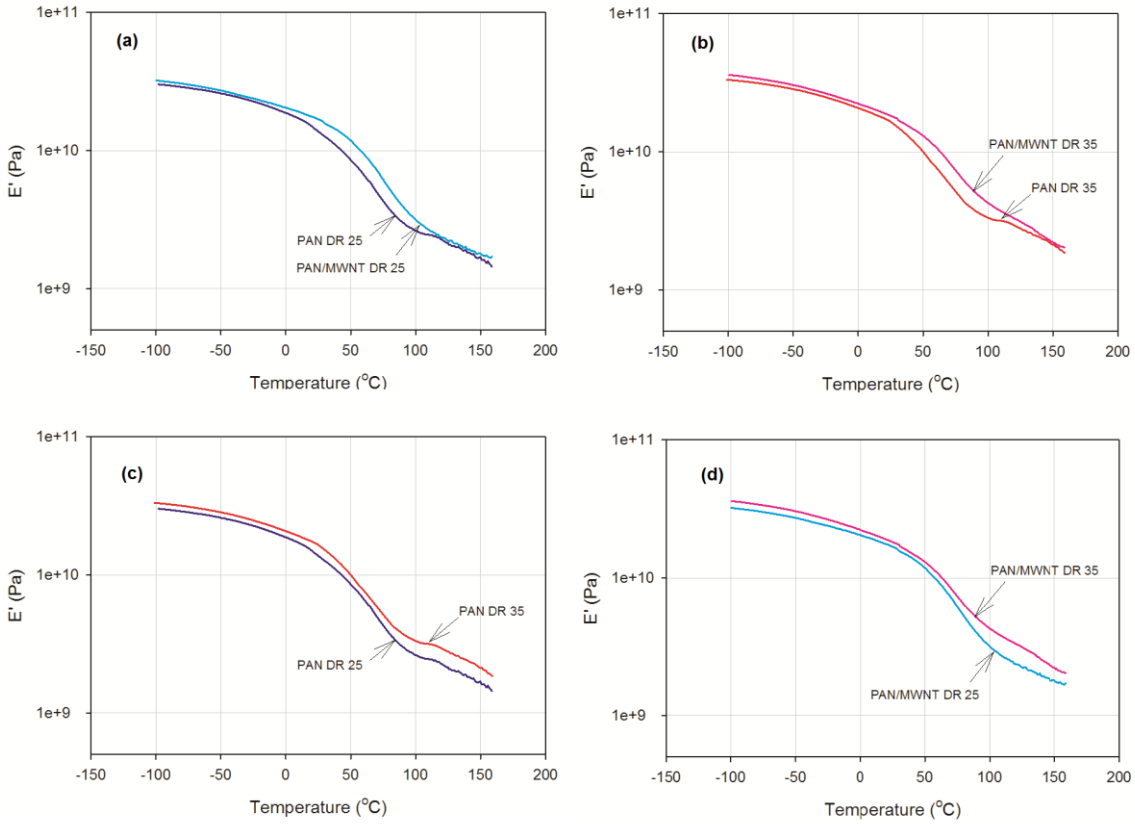

Figure 2.9 Storage moduli of PAN and PAN/MWNT fibers as a function of temperature at a frequency of 0.1 Hz.

Tan δ of PAN control and PAN/MWNT composite fiber showed relaxation at 60 ~ 75 ℃ (Figure 2.10). This relaxation is known as β_c transition and is related to the molecular motion in the helical sequence of atactic- or iso- PAN in the paracrystalline

region[148]. The peak point of the tan δ plot shifted to a higher temperature with the incorporation of MWNT. This implies that the molecular motion of PAN was restricted by MWNT; thus, more energy was required to initiate molecular motion. This was confirmed by calculating the activation energy (E_A) from the Arrhenius equation; the E_A of PAN/MWNT composite fiber is much higher than that of the PAN control fiber as summarized in Table 2.3. At a given draw ratio, tan δ peak position shifted to higher temperature and the magnitude of the tan δ decreased by the incorporation of MWNT. The increased β_c transition temperature and activation energy in the presence of MWNTs support strong interaction between PAN and MWNT (Table 2.3). The higher draw-ratio effect on drop of tan δ magnitude for PAN/MWNT fiber is larger than that for PAN fiber. The β_c transition temperature of PAN and PAN/MWNT increased with increasing frequency as summarized in Table 2.3.

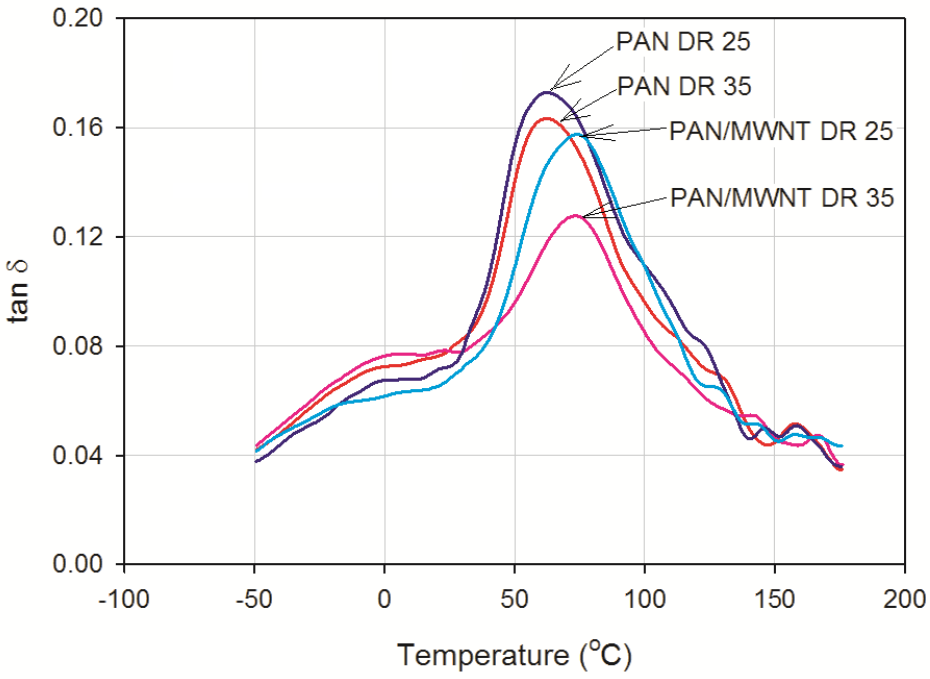

Figure 2.10 Tan δ of PAN and PAN/MWNT fibers as a function of temperature at 0.1 Hz frequency.

Table 2.3 Glass transition temperatures of PAN/MWNT composite fibers.

	Draw ratio	β_c transition temperature (℃) at various frequencies			
		0.1 Hz	1 Hz	10 Hz	E_A^* (kJ/mole)
PAN	25	61.8	70.2	76.1	309
	35	62.6	71.1	77.1	307
PAN/MWNT	25	72.6	75.1	81.1	523
	35	73.6	80.0	82.0	513

*E_A is activation energy calculated using the Arrhenius equation, $f = A\exp\left(-\frac{E_A}{RT}\right)$, where f, A, R, and T are frequency, constant, gas constant, and absolute temperature, respectively.

2.3.5 Thermal Analysis

The first run of DSC thermograms of PAN and PAN/MWNT fibers (Figure 2.11) measured at a heating rate of 10 ℃/min under air show a high exothermal peak around 327 ℃, whereas there was no noticeable peak in the second and third runs in both cases. The exothermic heat flow at the peak position was reduced for PAN/MWNT composite fiber, which implies that the stabilization reaction can be done under milder condition in the presence of MWNT. The heat of stabilization for PAN/MWNT is lower than that for PAN.

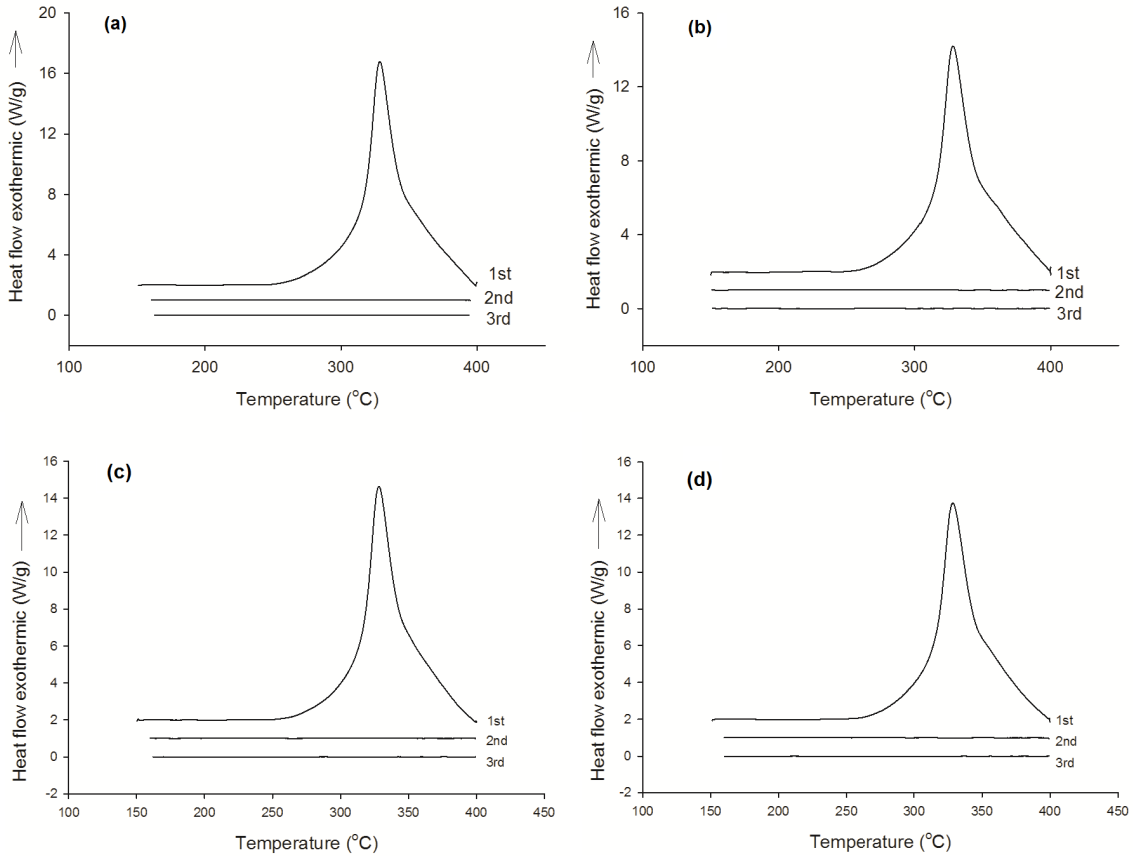

Figure 2.11 DSC thermograms of (a) PAN control (DR=35) fiber, and (b) PAN/MWNT (1 wt.%, DR= 35) composite fiber at a heating rate of 10 ℃ /min. Air was purged at a flow rate of 50 ml/min. The 1st, 2nd, and 3rd heating cycle were plotted together. Note that thermograms of 1st, and 2nd heating cycle were shifted upward for the purpose of clear comparison. Figures (c) and (d) are the results of experiments conducting during second trial and correspond to the first trial experiments of Figures (a) and (b), respectively.

Additional thermal analysis of PAN/MWNT was carried out at a heating rate of 1 ℃/min to see heating rate effects. At a slow heating rate (1 ℃/min), the peak temperature position shifted to lower temperature and heat flow at the peak position is reduced as compared to those of a fast heating rate (10 ℃/min). This implies that the precursor fiber can undergo mild cyclization reaction (stabilization) at a low heating rate; this is favorable for suppressing defective structure generation in carbon fiber.

At slow heating rate, the differences between PAN and PAN/MWNT thermograms are clear as shown in Figure 2.12. DSC thermogram of PAN/MWNT shows

less heat evolved during stabilization and shows residual heat of stabilization in the second and third runs, while that of PAN shows no distinct peaks at second and third runs. The stabilization of PAN/MWNT is hindered in the presence of MWNT. These observations are in good agreement with PAN/SWNT results conducted at 1 ℃/min[79]. The thermal analysis results are summarized in Table 2.4.

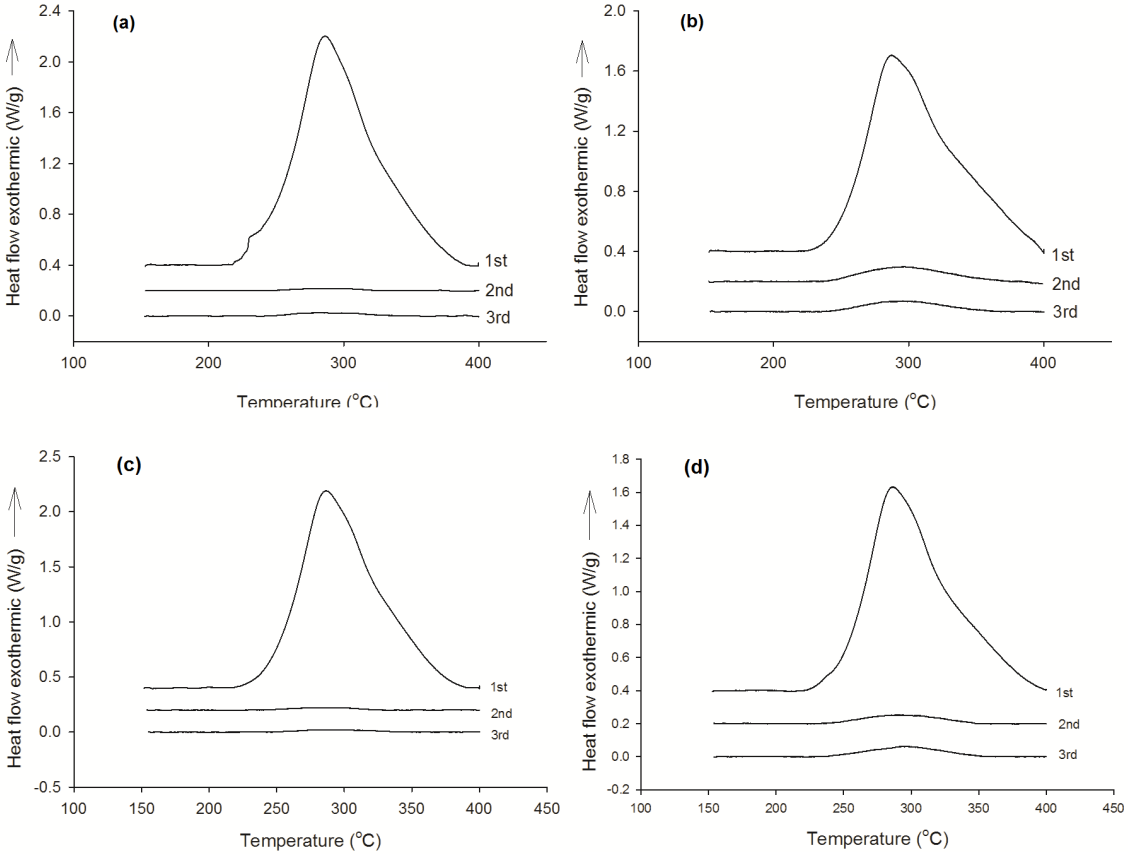

Figure 2.12 DSC thermograms of (a) PAN control (DR=35) fiber and (b) PAN/MWNT (1 wt.%, DR=35) composite fiber at a heating rate of 1 ℃ /min Air was purged at a flow rate of 50 ml/min. The 1st, 2nd, and 3rd heating cycle were plotted together. Note that thermograms of 1st, and 2nd heating cycle were shifted upward for the purpose of clear comparison. Figures (c) and (d) are the results of experiments conducting during second trial and correspond to the first trial experiments of Figures (a) and (b), respectively.

Table 2.4 Thermal analysis results of PAN control and PAN/MWNT composite fibers*.

		Control	MWNT 1wt.%
Fiber diameter (μm)		13.5	13.2
Draw ratio		35	35
heating rate of 10 ℃ /min	ΔH of 1st run (kJ/g)	2.5 (2.3)	2.2 (2.2)
	Peak temperature (℃)	327 (328)	328 (328)
heating rate of 1 ℃ /min	ΔH of 1st run (kJ/g)	7.1 (6.6)	4.8 (4.6)
	Peak temperature (℃)	286 (287)	287 (287)

* ΔH and peak temperature values obtained during the second trial are listed within brackets.

2.3.6 Stabilization and Carbonization (Vertical Mount)

The stress-strain curves of carbon fibers from PAN/MWNT (1 wt.%) precursor fibers are shown in Figure 2.13. Tensile strength and modulus increased with applied stress, except at 30 MPa of tension, as those fibers broke during carbonization. The precursor fibers contracted during heat-treatment due to the physical (entropic) and chemical shrinkage as discussed in Chapter 1. For this reason, maximum tension without fiber breakage should be used to minimize the shrinkage. The mechanical properties of carbon fibers produced under various stress levels are summarized in Table 2.5. The SEM micrographs of carbon fibers are shown in Figure 2.14. The vacant sites are observed in Figure 2.14 (e), and (f). Possible reasons for vacant sites are; (i) gas channels which can be generated by abrupt exothermic reaction, (ii) burn-out of foreign particles. The stabilization conditions need to be optimized further for elimination of gas channels, since vacant sites can act as defects under stress.

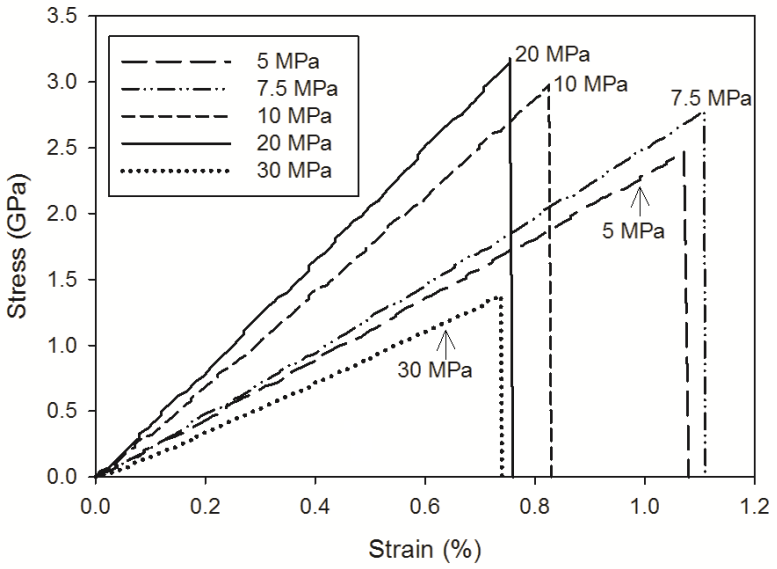

Figure 2.13 Stress-strain curves of PAN/MWNT (DR = 55) based carbon fibers produced under various tensions.

Table 2.5 Mechanical properties of carbon fibers produced under various tension using PAN/MWNT precursor fibers (DR = 55).

	Tension applied (MPa)				
	5	7.5	10	20	30
Tensile strength (GPa)	2.41±0.49	2.77±0.59	3.02±0.47	3.17±0.45	1.39±0.26
Tensile modulus (GPa)	235±26	255±38	362±51	430±72	192±22
Elongation at break (%)	1.0±0.2	1.1±0.2	0.9±0.1	0.8±0.2	0.7±0.1

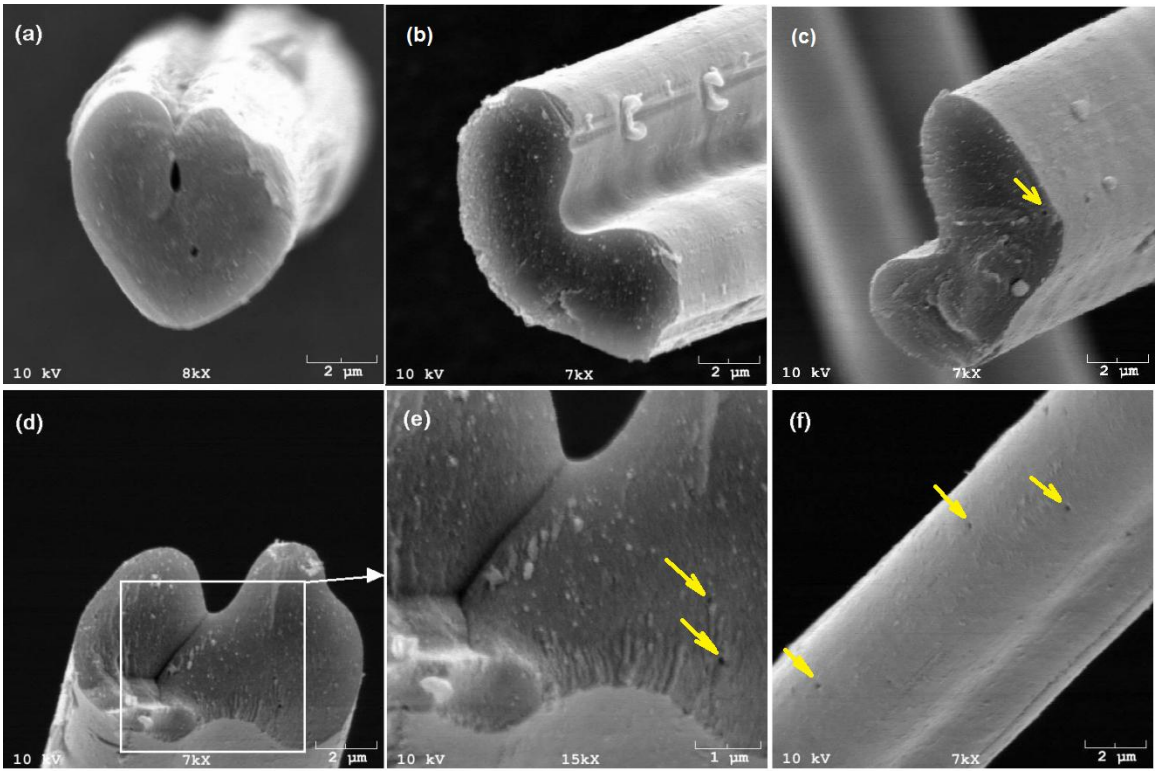

Figure 2.14 SEM micrographs of PAN/MWNT (DR = 55) based carbon fibers (a) and (b) carbonized under 30 MPa tension, (c)~(f) carbonized under 7.5 MPa tension. Arrows indicate vacant sites.

2.3.7 Stabilization and Carbonization (Horizontal Mount)

The vertical mounting carbonization study showed that higher applied stress helps to improve mechanical properties of the resultant carbon fiber. However, vertical mounting heat-treatment might have a temperature gradient problem along the vertical direction that can cause deviation in the mechanical properties and structure of the carbon fiber. Figure 2.15 shows the thermo-mechanical analyzer results for the shrinkage of PAN/MWNT (1 wt.%) fibers under stabilization conditions at various stress levels. The highest stress that can be applied during heat-treatment without breaking the fiber turned out to be 25 MPa, since fibers broke under a tension of 30 MPa. Based on these observations, horizontal mounting heat-treatment was tuned under an applied tension of 22.5 MPa. The mechanical properties were monitored by changing the stabilization time

at 320 ℃, since stabilization time is critical for better properties of the carbon fiber. If the stabilization time is too short, subsequent carbonization leads to abrupt gas formation due to rapid cyclization at high temperature. If the stabilization time is too long, the oxidative stabilization environment leads to the degradation of the fiber, resulting in poor mechanical properties of the carbon fiber. The mechanical properties of carbon fibers are summarized in Table 2.6. Carbon fiber stabilized for 42.5 minutes at 320 ℃ showed the best results with regard to tensile strength. However, the absolute tensile strength and modulus value are lower as compared to the previous vertical mounting results. This may be due to the changes in structure and the mechanical properties of the PAN/MWNT (1 wt.%) composite precursor fiber with shelf time, as summarized in Table 2.7. The PAN/MWNT precursor fibers had been stored three years while fresh precursor fibers were used for vertical mounting carbonization study. Tensile strength, modulus, and elongation at break reduced after three years of shelf time. Crystal size was increased slightly, yet crytallinity and orientation were reduced considerably. Shelf time adversely affects the mechanical properties of the precursor fiber. To prevent mechanical properties from diminishing, additional heat-setting processes might be needed [149-153].

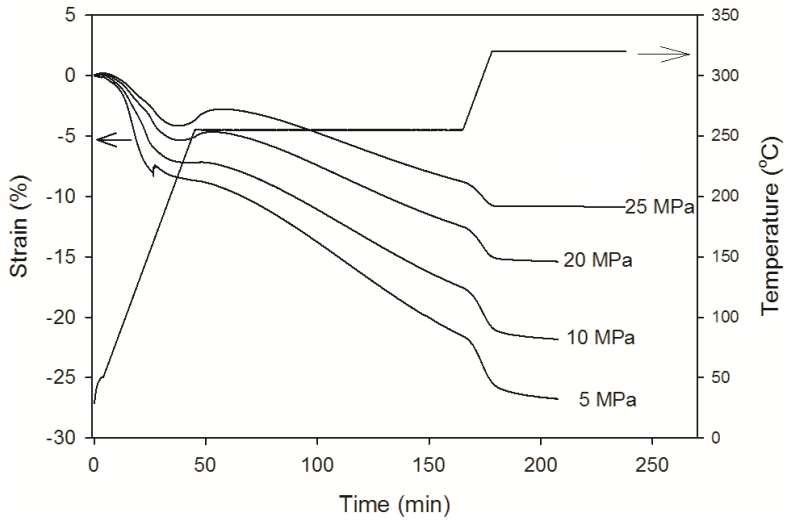

Figure 2.15 Shrinkage behavior of PAN/MWNT (1 wt.%) composite fibers (DR=55) under various tension.

Table 2.6 Mechanical properties of PAN/MWNT (DR = 55) based carbon fibers produced under different stabilization times.

	Stabilization time at 320 ℃ (min)					
	20	25	30	35	42.5	45
TS[a] (GPa)	1.91±0.50	2.10±0.48	2.28±0.47	2.27±0.45	2.31±0.47	1.79±0.45
TM[b] (GPa)	187±20	187±23	175±25	198±24	177±33	172±23
Strain to failure (%)	1.0±0.2	1.1±0.2	1.2±0.2	1.2±0.3	1.3±0.3	1.1±0.3

22.5 MPa of stress was applied during stabilization and carbonization, [a] Tensile strength, [b] Tensile modulus

Table 2.7 Effect of shelf time on mechanical properties and structure of PAN/MWNT (1 wt.%) composite fiber (DR=55).

Shelf time	Fresh	2 years	3 years
Diameter (μm)	10.4	←	←
Tensile strength (GPa)	1.34±0.13	1.11±0.10	1.12±0.08
Tensile modulus (GPa)	26±2	24±3	23±2
Elongation at break (%)	8.5±0.5	6.9±0.6	7.4±0.4
Work of rupture (MPa)	57±8	40±6	42±4
Crystallinity (%)	67.2	-	55.7
Crystal size (nm)	11.4	-	11.8
$d_{2\theta\sim17^\circ}$ / $d_{2\theta\sim30^\circ}$	1.719	-	1.721
	0.903	-	0.845

SEM micrographs of carbon fiber (Figure 2.16) show a smooth surface of the carbon fiber without vacant sites. Pulled out MWNTs on the fracture surface (Figure 2.16 (d) and (f)) imply that different fracture mechanism was involved for PAN/MWNT precursor based carbon fiber as compared to ordinary brittle fracture of PAN based carbon fiber.

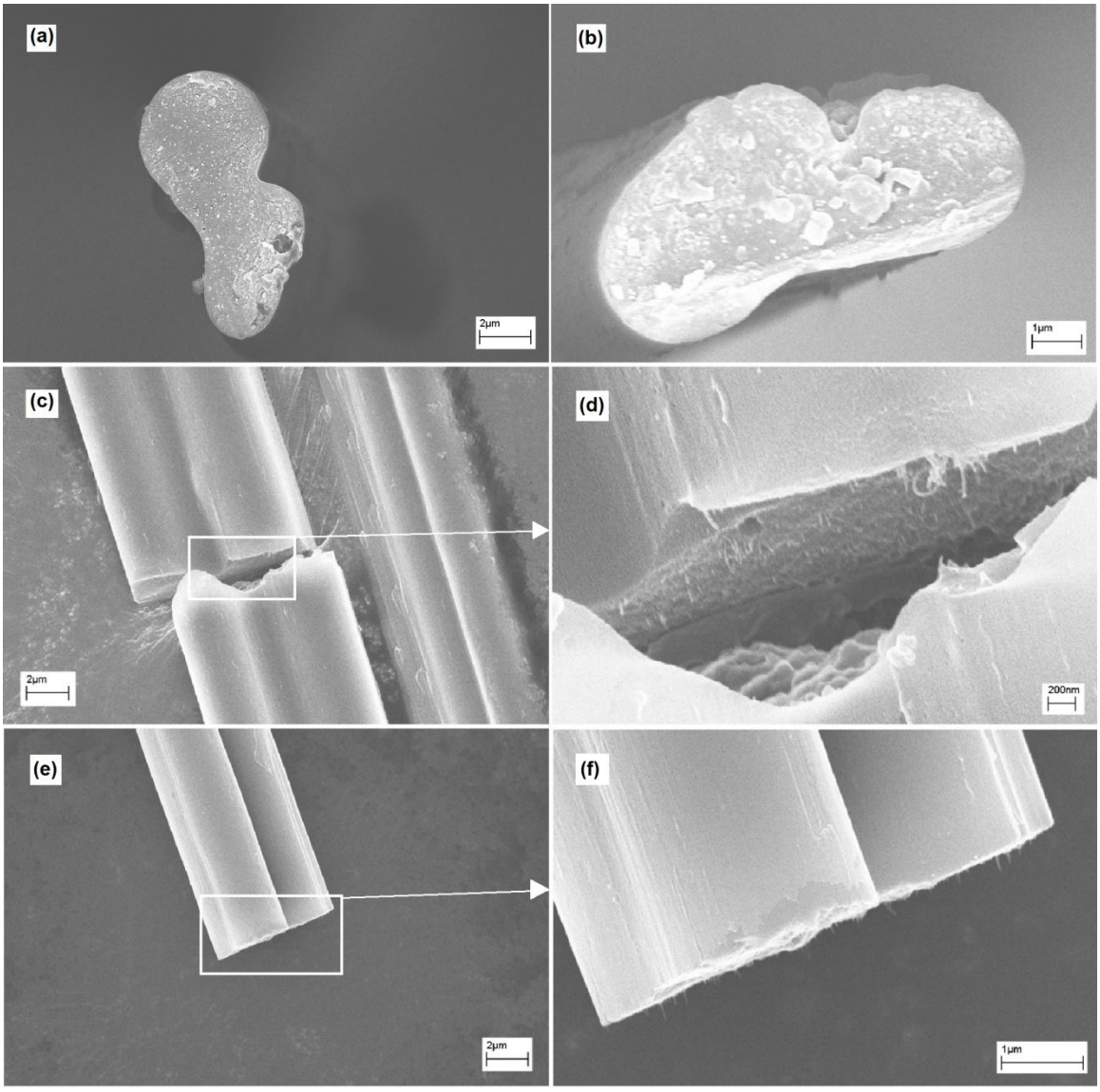

Figure 2.16 SEM images of fractured carbon fibers (a) 45 minutes of stabilization at 320 ℃, (b) 42.5 minutes, and (c) ~ (f) pulled out MWNTs from fractured surfaces of carbon fibers.

2.4 Conclusions

The gel-spun PAN/MWNT fibers showed improved mechanical properties in comparison to the gel-spun control PAN fibers. The maximum draw ratio of the PAN/MWNT composite fiber was significantly higher than that of the control PAN fiber. This was attributed to good interaction between PAN and MWNT. The higher draw ratio of the composite fiber led to superior tensile strength as high as 1.3 GPa. At a given draw ratio, the diameter of PAN/MWNT fiber is smaller than that of the PAN fiber processed under the comparable processing conditions, since the MWNTs restrict PAN molecules' elastic recovery which causes the die-swell (i.e larger diameter) of spun fiber. Shift of tan δ peak point, and enhanced activation energy, support good interaction between the PAN and the MWNT. SEM micrographs show good dispersion of MWNTs in the PAN matrix. Thermal analysis revealed that the heat of stabilization of PAN/MWNT fibers is lower than that of PAN fiber regardless of the heating rate. The mechanical properties of carbon fibers were improved by increasing the tension applied during the heat-treatment. Significant decrease about ~16% in tensile strength of PAN/MWNT composite fiber (1.3 GPa) was observed after 3 years of shelf-time. This is due to the deterioration of the PAN structure which is confirmed by reduced crystallinity (67% of fresh fiber crystallinity reduced to 56% after 3 years) and PAN orientation (f_{PAN} became 0.845 from 0.903 of fresh fiber).

CHAPTER 3

PAN-CO-MAA/FWNT COMPOSITE PRECURSOR FIBERS AND THEIR CARBON FIBERS

3.1 Introduction

PAN as a carbon fiber precursor is typically copolymerized with acidic co-monomer since cyclization of co-polymerized PAN can be completed under milder conditions than the homo-polymer PAN as discussed in Chapter 1 [91, 93-94]. In this study, copolymerized PAN is used to prepare precursor fibers for carbon fiber production. The structure and tensile properties are characterized for both the precursor and the resulting carbon fibers.

3.2 Experimental

3.2.1 Materials

Polyacrylonitrile-co-Methacrylicacid (PAN-co-MAA; 4 wt.% of MAA content, M_w - 2.4×10^5 g/mol) was obtained from Japan Exlan, Co. Few walled nanotubes (FWNT: Lot # XO021UA with 2.4 wt.% metallic impurity) were obtained from Carbon Nanotechnologies, Inc. (Houston, TX) and used as received. Dimethylacetamide (DMAc) from Aldrich co. and N, N-dimethylformamide (DMF) obtained from BDH, Inc. were purified by distillation before use.

3.2.2 Solution Preparation

FWNTs were dispersed in DMAc or DMF by the sonication method (Branson 3510R-MT, 100 W, 42 kHz) at a concentration of 37.5 mg/L for 24 hours. PAN-co-MAA polymer (12.5 g) was dried in a vacuum oven at 100 ℃ and dissolved in DMAc (100

mL) at 80 ℃. The dispersed FWNT/DMAc solution was added to the PAN-co-MAA/DMAc solution and the excess amount of solvent was evaporated by vacuum distillation with mechanical stirring to meet the desired solid content in the solvent (12.5 g solids (PAN-co-MAA and FWNTs)/100 mL DMAc). Similarly, the other composite solutions were prepared at the CNTs concentrations with respect to the polymer of 0, 0.1, 0.5, and 1 wt.%, respectively.

3.2.3 Solution Rheology

Frequency sweep tests were conducted using an ARES rheometer (Rheometric Scientific, Co.) with parallel plate geometry (25 mm plate diameter and 1 mm gap between plates) at room temperature. The angular frequency (ω) range was set from 0.5 to 500 rad/s at a fixed strain of 5%. The capillary rheometer measurements were carried out using a Dynisco LCR7001 Rheometer with an orifice of 29.97 L/D ratio (L=9.14 mm and D=0.305 mm) at 40 ℃ and 110 ℃ (110 ℃ was the spin block temperature used in this study and 40 ℃ is the lowest temperature that the capillary rheometer can stably maintain.). The apparent viscosity was monitored as a function of shear rate ranging from 500~50,000 1/s. Shear rate observed in this study falls in those range (see Appendix B). The solid (PAN-co-MAA and FWNT) concentration of solution used for rheology study is 12.5 g /100 mL of solvent. The FWNT concentration with respect to solid content was varied 0, 0.1, 0.5, and 1 wt.%, respectively.

3.2.4 Fiber Spinning

The PAN-co-MAA control and PAN-co-MAA/FWNTs composite fibers were spun utilizing the gel spinning technique using a Bradford University spinning unit with a one-hole (250 μm diameter) spinneret. The prepared solution was spun into a cold methanol gelation bath (-50 ℃) with an air gap of 2 cm. In some cases, the fibers were stretched during the spinning process by increasing the take-up speed with respect to the

linear-jet velocity of spun fibers. Prior to the drawing process, the as-spun fibers were immersed in a methanol bath at a temperature of -50 ℃ for 72 hours. The two-step-batch-wise drawing process was carried out: (i) the as-spun fibers were stretched at room temperature (namely cold-drawing). The possible maximum cold-draw ratio was varied depending on the composite solution. (ii) the cold drawn fibers were subsequently drawn again by passing them through a glycerol bath whose temperature was maintained at 170 ℃, followed by washing in ethanol and vacuum drying at 50 ℃ for 3 days. The total draw ratio was the product of the spin draw ratio, the cold-draw ratio, and the hot-draw ratio and was expressed respectively in parentheses (e.g. total draw ratio of 15 with spin draw ratio of 2, cold-draw ratio of 1.5, and hot draw ratio of 5 is expressed as 15 $(2\times1.5\times5)$).

3.2.5 Characterization of Fiber

The tensile properties were characterized by using an RSA III solids analyzer (Rheometric Scientific, Co.) with a gauge length of 25.4 mm and crosshead speed of 0.25 mm/s. For each series, 16 specimens were tested. Wide-angle X-ray diffractions of PAN-co-MAA control and composite fibers were collected by Rigaku MicroMax 002 X-ray generator with confocal optics to produce Kα radiation (λ = 1.5418 Å) and equipped with a R-axis IV++ detector. The crystallinity was calculated by fitting the integrated scan using MDI Jade 8.5.2 software, and the crystal size was calculated from the FWHM (Full width at half the maximum intensity) of the crystalline peaks from the equatorial scan. The Herman's orientation function for the PAN crystal c-axis about the fiber axis (f_{PAN}: Herman's orientation factor) was calculated using Wilchinsky's equation [141-142]. The detailed calculation method is given in previous literature [38, 43, 52, 78, 140]. Raman spectra were collected using Holoprobe Research 785 Raman microscopy (Kaiser optical system co, Ltd) equipped with a laser source with an excitation wavelength of 785 nm. To determine orientation, the peak intensity (base line corrected by GRAMS/Al v7.01) of

the tangential band (ca. 1590 cm^{-1}) was read. A specimen was mounted on the angular stage of the Raman spectroscopy. The intensity of laser source was adjusted to 40 mW. For solving simultaneous equations to estimate CNTs orientation, VV and VH mode spectra were collected at 0° (defined direction of polarization of laser source is parallel to the fiber axis) and 90° (defined polarized laser is perpendicular to the fiber axis), respectively. The intensities at $\Phi = 0$ (fiber axis is parallel to axis of the polarization of the analyzer) were obtained by changing the analyzer from VV mode (both laser source and analyzer are vertically polarized) to VH mode (laser source is vertically polarized and analyzer has horizontal polarization direction). For the case of solution specimens, a droplet of each composite solution was carefully placed on a silicon wafer to minimize flow induced orientation and then characterized.

3.2.6 Thermal Analysis

Differential scanning calorimetry (DSC; TA instruments Q200) on the precursor fibers was conducted by heating the fibers from 150 to 400 ℃ at a heating rate of 10 ℃ /min (or 1 ℃/min). After the 1st heating scan, samples were quenched at a cooling rate of 100 ℃/min for the next heating scan. 2nd and 3rd heating scans were conducted under the identical heating rate to the 1st scan. For the isothermal test, the DSC furnace temperature was ramped up to a given temperature (265, 295, and 325 ℃, respectively) and held at that temperature for 6 hours.

3.2.7 Stabilization

The PAN-co-MAA control fibers were stabilized and carbonized using an MHI H17HT2.5X24 tube type furnace with 100 mm diameter and 1500 mm length alumina tube (Figure 3.1). The precursor fibers were carried continuously through the tube furnace by IDC S21 step motor with a Reducing gear box (55:1 gear ratio) and a smart step controller with a keypad. For stabilization, purified air was purged and the

temperature of the furnace was set as given in Table 3.1. The residence time was calculated based on a 12 inch (305 mm) length of heating zone, divided by take-up speed.

Table 3.1 Stabilization conditions.

Stabilization step	Temperature (℃)	Residence time (min)	Stretching (%)	Pretension (gf)
1st	285	7.5	0	1
2nd	290	28.6	6	1
3rd	330	50.8	0	1.6
4th	350	20.3	0	1.6

3.2.8 Carbonization

For carbonization, argon (99.999% purity) gas was purged. To confirm the cyclization reaction, Fourier transform infrared (FT-IR) spectroscopy was conducted on the stabilized fibers using a Perkin Elmer FT-IR microscope and by collecting 256 scans at a resolution of 4 cm^{-1}. Fiber tensile fracture surfaces were observed by scanning electron microscopy (LEO 1530 SEM operated at 10 kV). UTHSCSA image tool software was used to compute the cross-sectional areas and diameters of the fibers.

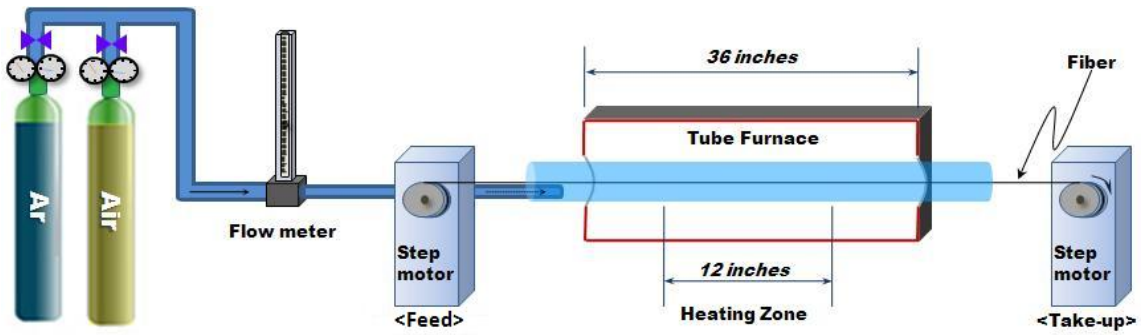

Figure 3.1 Tube furnace setup for the continuous stabilization and carbonization study.

3.3 Results and Discussion

3.3.1 Dynamic Shear Rheology of PAN-co-MAA Control and PAN-co-MAA/FWNT Composite Solution

The changes in the complex viscosity of the PAN-co-MAA/FWNT solution are plotted in Figure 3.2 as a function of angular frequency. The complex viscosities of all of the solutions decreased with increasing angular frequency. It can be interpreted that the PAN/CNTs solution showed shear thinning behavior. The CNTs containing composite solutions showed higher viscosity than the control solution. The viscosity differences between the various solutions are noticeable in the low frequency regime, while not much variation is observed in the high frequency regime. So the effect of CNTs on viscosity is significant at low frequency rather than at high frequency, which is also observed for PP/MWNT melt rheology [154-155].

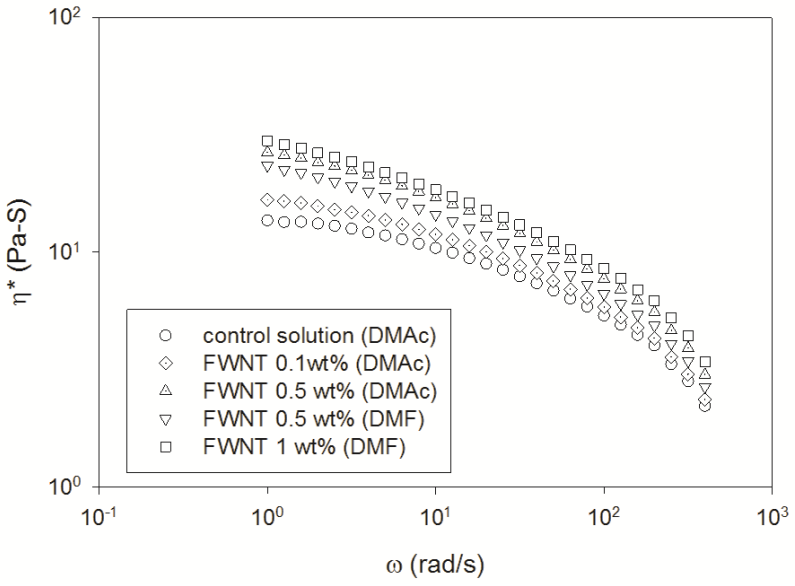

Figure 3.2 Frequency sweep test of the complex viscosity of the PAN-co-MAA/FWNT solutions.

Figure 3.3 shows the storage modulus (G') and the loss modulus (G") response as a function of frequency for PAN-co-MAA solutions. Both moduli increase with frequency; the effect of nanotube content on the storage modulus is higher at a low frequency than at a high frequency. At a low frequency, the storage modulus increased rapidly as nanotube loading increased. However, the contribution of nanotube loading on loss modulus is not as high as that on storage modulus, even in a low frequency regime. Since nanotubes have a rigid rod nature, they can contribute more to the storage modulus than to the loss modulus. So the storage modulus of PAN/CNT solution can be affected by nanotube loading dominantly at low frequency which is in good agreement with the melt rheology of PP/MWNT[108]. At low shear rate, the CNTs remain randomly dispersed, or a network structure in case above the percolation threshold, and dominate the low frequency response since CNTs are stiffer than polymer molecules[108, 143]. On the other hand, the contribution from the polymer molecules becomes dominant at a high frequency, since the network structure of CNTs is broken. The storage (loss) moduli plots for PAN-co-MAA/FWNT (5 wt.% in DMF) and PAN-co-MAA/FWNT (5 wt.% in DMAc) are overlapped, implying that the solvent differences between DMF and DMAc on storage and loss moduli are negligible.

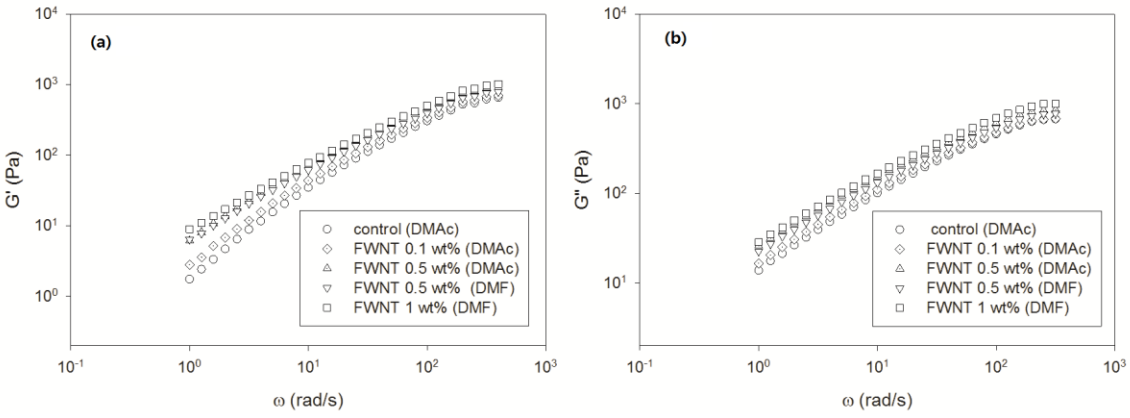

Figure 3.3 Storage modulus G' (a) and loss modulus G" (b) of PAN-co-MAA/CNT solutions as a function of frequency at 25 ℃.

Tan δ results for frequency sweep testing are plotted in Figure 3.4. A smaller tan δ value implies more elastic behavior. In Figure 3.4, the tan δ values of all solutions are decreasing as a function of angular frequency, which implies that PAN-co-MAA/FWNT solutions showed more elastic behavior at a high deformation rate. By incorporating the nanotubes in the PAN-co-MAA solution system, the elastic modulus of the solution goes up, and the tan δ goes down.

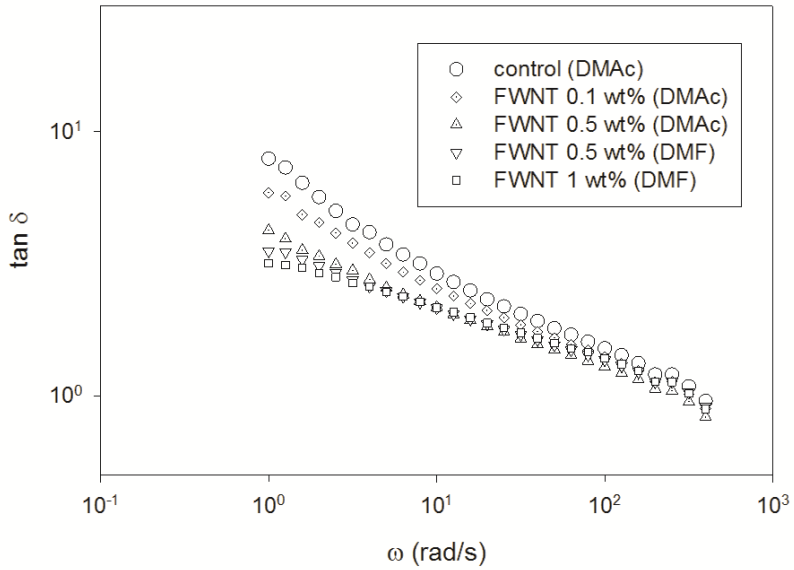

Figure 3.4 Frequency sweep test of tan δ of PAN-co-MAA solutions.

3.3.2. Steady Shear Rheology of PAN-co-MAA Control and PAN-co-MAA/FWNT Composite Solutions

The capillary steady shear tests were conducted to determine the rheological behavior of the PAN-co-MAA control and composite solutions under high steady shear, since the shear rate of fiber spinning in this study is more than 40,000 1/s (see Appendix B for detailed calculation), which is not a feasible condition for dynamic rheological testing. The apparent viscosity values are plotted as a function of shear rate in Figure 3.5. As expected, both the PAN-co-MAA control and composite solutions showed shear thinning behavior. The viscosity of the composite solution is lower than that of the

control solution at a given temperature, which is opposite to the dynamic test results. The fully developed laminar flow can help CNT orientlong the flow direction and cause a viscosity drop. Based on these observations, CNTs can be thought to assist the flow of the spinning solution during the spinning process.

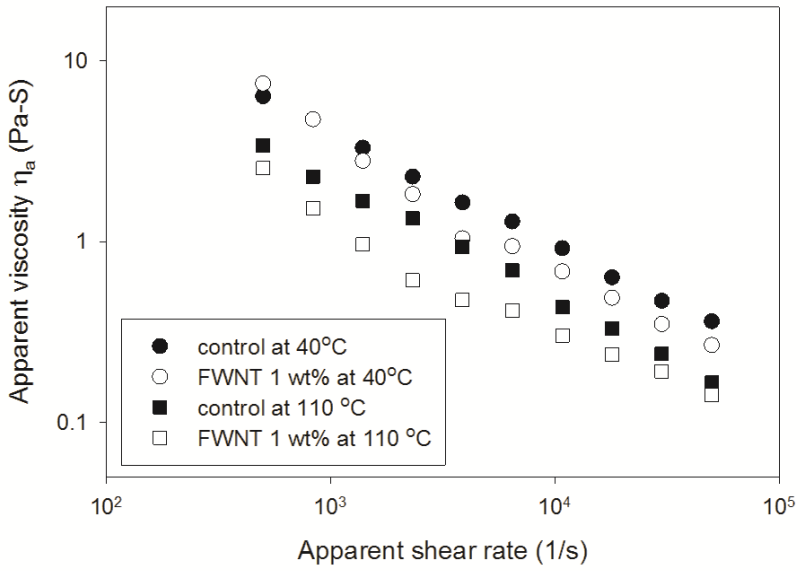

Figure 3.5 Apparent viscosity versus apparent wall shear rate of PAN-co-MAA solutions.

The PAN-co-MAA polymer solution also satisfied the generalized Newtonian model, especially the Power-law model[156] which is given by the equation (3.1).

$$\eta = m\left|\dot{\gamma}\right|^{n-1} \tag{3.1}$$

where *m* is the consistency index and *n* is the power law index (flow behavior index). The m and n values of each solution are listed in Table 3.2. The n values are less than one, which means the solutions showed shear-thinning behavior. All the R^2 values are >0.97, this suggests good agreement of power-law model with the data for these PAN-co-MAA solutions.

Table 3.2 Power law indices and R^2 values for PAN-co-MAA solutions.

Temperature	Solution	Material function ($\eta = m\lvert\dot{\gamma}\rvert^{n-1}$), R^2		
		m	n	R^2
40 ℃	Control	316.98	0.370	0.9987
	FWNT 1 wt.%	508.74	0.289	0.9824
110 ℃	Control	192.16	0.350	0.9977
	FWNT 1 wt.%	75.588	0.410	0.9726

The dynamic and steady rheological behaviors of PAN-co-MAA solution are observed to this point. According to the Cox-Merz rule[157] there is a relationship between complex viscosity and shear viscosity that is expressed by equation (3.2).

$$\eta(\dot{\gamma}) = \left|\eta^*(\omega)\right|_{\omega=\dot{\gamma}} = \eta'(\omega)\left[1+\left(\frac{\eta''}{\eta'}\right)^2\right]^{1/2}_{\omega=\dot{\gamma}} \tag{3.2}$$

In Figure 3.6, the complex viscosity (η^*) and Rabinowitsch [158-159] corrected steady shear viscosity (η) are plotted together for comparison. There is discontinuity observed between the shear rate (angular frequency) of 100 and 1000 (ω or $\dot{\gamma}$). This discontinuity might come from the discrepancy of the Cox-Merz rule or overestimation of viscosity due to the entrance pressure drop in the capillary [159]. At higher shear rate, the PAN-co-MAA/FWNT composite solution showed lower viscosity than the control one. It is believed that the CNTs are aligned along the flow direction at high shear stress resulting in lower viscosity. This can be supported by observing the orientation of FWNT in as-spun fiber, since schematic of capillary rheometer is very similar to that of spinning. The shear rate for spinning conducted in this study was marked with arrow in Figure 3.6. The Herman's orientation factor of FWNT (f_{FWNT}) for as-spun PAN-co-MAA/FWNT (1 wt.%) fiber is ~0.409, implying FWNT are aligned along the fiber axis. Also, f_{FWNT} is

higher than the Herman's orientation factor of PAN (f_{PAN}=0.320). The orientation of PAN and FWNT will be discussed further in section 3.3.4.

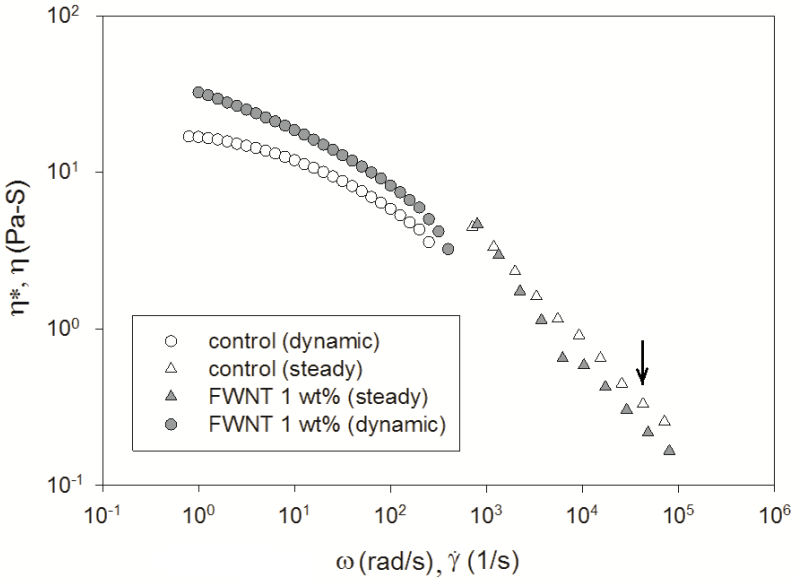

Figure 3.6 Comparison of viscous properties $\eta(\dot{\gamma})$ and $\eta^*(\omega)$.

3.3.3 Tensile Properties

To enhance the tensile properties of fiber, the number of inter- and intra-molecule entanglements should be reduced by lowering the polymer concentration. Those entanglements in the fiber act as defects, and the stress can be concentrated on the defect sites under loading. The aim of gel spinning is also to reduce the number of entanglement so that the polymer molecules can be aligned along the fiber axis [89]. Ideally, a semi-dilute concentration of the polymer solution is desired for highly oriented fiber. For the fibers spun from a highly concentrated solution, the maximum achievable draw ratio can be relatively low due to the excess number of entanglements, while frequent fiber breakage might be observed when dilute solutions are used. This concept is illustrated in Figure 3.7. Practically, the concentration of polymer solution for gel spinning is higher than semi-dilute concentration to ensure drawing stability. The gelate as-spun fiber was

stretched at room temperature prior to hot temperature drawing. This room temperature drawing process (here-after referred as cold-drawing) helps to align the PAN molecules along the fiber axis[160].

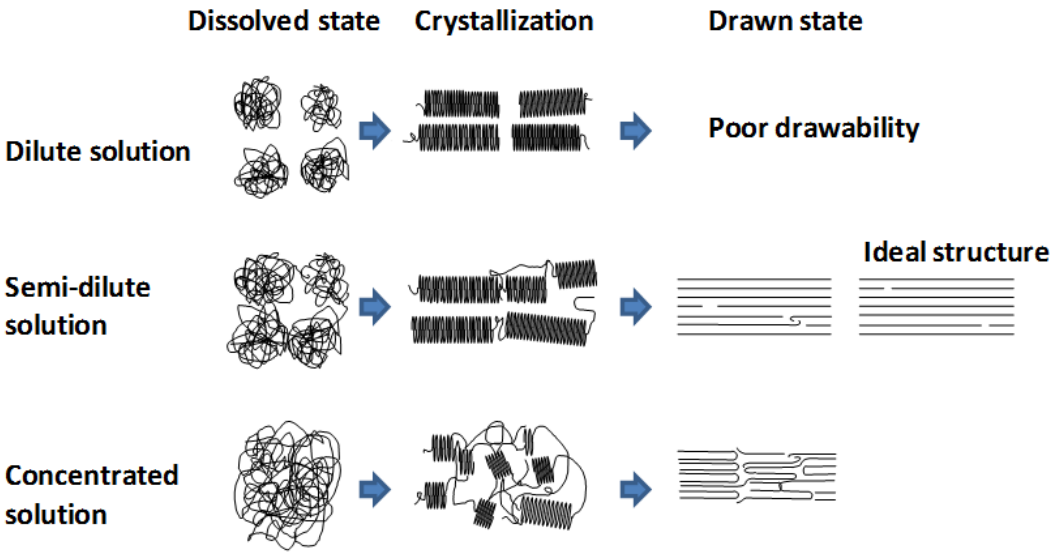

Figure 3.7 Schematic of the entanglement control of drawability [89, 161].

The tensile properties of the PAN-co-MAA control and composite fibers are summarized in Table 3.3. Comparison of control fibers of various draw ratio revealed that the higher hot draw ratio contributes the higher tensile strength and modulus. The number of polymer molecular entanglements which act as defect during tensile test can be reduced by drawing (high draw ratio. Thus, the higher draw ratio generally leads the higher tensile properties of PAN fiber. In this study, PAN-co-MAA control and composite fibers were drawn three times (namely spin-drawing, cold-drawing, and hot-drawing). One can come up with the question "Which drawing process is optimal for enhancing mechanical properties?" Based on previous comparison, it can be inferred that the cold-drawing process contributes effectively to the enhancement of mechanical properties, since the former fiber was stretched 3.6 times prior to hot-drawing (2 times by spin-drawing and 1.8 times by cold-drawing), whereas the latter was stretched 2.7 times

by cold-drawing only. The PAN-co-MAA control fiber ($1\times1\times11$) that didn't go through cold-drawing exhibited poor mechanical properties. The cold-drawing improve the polymer crystal structure similar to the strain hardening of a metal by plastic deformation.

Table 3.3 Tensile properties of PAN-co-MAA control and composite fibers.

		Diameter (μm)	Strength (GPa)	Strain (%)	Modulus (GPa)	Work of rupture[‡] (MPa)
Control	$1\times2.7\times2$	28.0±0.3	0.58±0.04	8.4±0.4	16.2±1.0	29±3
	$1\times2.7\times2.6$	25.3±0.1	0.81±0.12	9.5±0.9	18.5±0.7	41±8
	$1\times2.7\times3.5$	21.5±0.0	1.11±0.07	9.0±0.4	22.5±1.5	50±5
	$1\times2.7\times4.8$[§]	18.7±0.2	1.08±0.10	8.1±0.7	22.5±1.8	45±6
	$1\times2.7\times5.5$[§]	17.6±0.2	1.15±0.13	8.0±0.6	22.3±1.3	46±8
	$2\times1.8\times3.5$	17.9±0.1	0.92±0.08	8.2±0.6	20.1±1.1	40±5
	$1\times1\times11$	20.6±0.1	0.57±0.07	7.1±0.8	15.8±0.6	23±4
0.1 wt.%	$1\times 2.8\times5.6$	16.9±0.2	1.17±0.09	7.9±0.4	24.9±0.8	46±5
	$1\times2.9\times5.4$	16.7±0.3	1.14±0.13	8.0±0.6	23.3±1.4	45±7
0.5 wt.%	$1\times2.3\times5.0$	20.5±0.2	0.95±0.08	7.3±0.5	22.3±2.0	37±5
1 wt.%	$1\times2.0\times6.0$	20.4±0.2	1.03±0.08	7.7±0.3	23.1±1.1	42±4
	$2.0\times1.8\times5$	16.8±0.1	1.11±0.13	7.0±0.6	31.7±1.5	42±7

[§] fibers drawn by a line heater at 165 ℃, [‡] work of rupture was obtained by calculating area under stress-strain curve

For homopolymer PAN (M_w 2.5×10^5 g/mol) [122], the tensile strength achieved was 0.9 GPa and tensile modulus was 22 GPa with total draw ratio of 51. In this study, the highest tensile strength of the control fiber was 1.15 GPa at a relatively low total draw ratio of 14.85. It can be noted that the maximum achievable cold-draw ratio decreased

with increasing the spin-draw ratio. For the case of control fibers, the maximum cold-draw ratio was reduced from 2.7 to 1.8 when the spin draw ratio was increased from 1 to 2. This implies that the orientation of PAN-co-MAA also can be increased by spin-drawing since pre-existing orientation confines additional stretching, resulting in reduced draw ratio[160]. For the case of FWNT 1 wt.% composite fibers, the tensile modulus was improved to 31.7 GPa due to CNT reinforcement.

3.3.4 PAN Crystal and CNT Orientation

The wide-angle X-ray diffraction patterns are shown in Figure 3.8 and the calculated results of the PAN-co-MAA control fibers are summarized in Table 3.4. The diffraction pattern of fully drawn PAN-co-MAA fibers showed distinct peaks on equator. The peak at around 2θ=16.8° corresponds to (200,110) plane of the PAN crystal and the peak at 2θ=29.3° corresponds to the (310,020) plane[120].

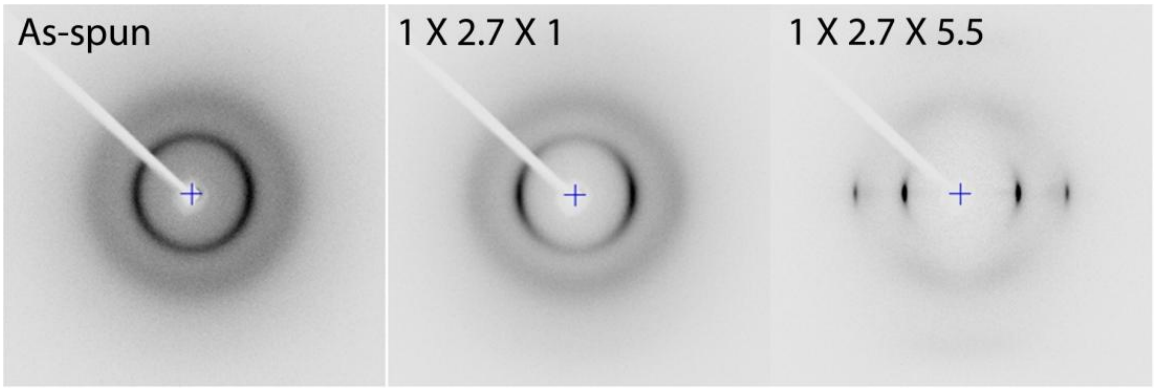

Figure 3.8 WAXD of selected control PAN-co-MAA fibers.

Table 3.4 Structural parameters of PAN-co-MAA control fibers determined by WAXD.

	TDR[a]	Crystallinity (%)	XS[b] (nm)	f_{PAN}	$2\theta_{meridional}$[c]
As spun	1.0	-	2.7	0.385	-
1×2.7×1	2.7	-	3.1	0.558	39.5
1×2.7×2	5.4	62	10.5	0.854	39.6
1×2.7×2.6	7.0	62	13.8	0.854	39.7
1×2.7×3.5	9.5	63	14.8	0.862	39.6
1×2.7×4.8	13.0	63	14.7	0.897	39.4
1×2.7×5.5	14.9	63	16.2	0.902	39.4
2×1.8×1	3.6	-	3.0	0.543	40.3
2×1.8×3.5	12.6	62	15.2	0.884	39.6
2×2×1	4.0	-	3.3	0.564	39.7
1×1×11	11.0	60	12.3	0.892	39.5
1×1.3×1	1.3	-	2.7	0.474	39.5

[a] total draw ratio, [b] crystal size, [c] meridional peak position

The crystal size from the equatorial reflection and Herman's orientation factor (f_{PAN}), calculated using the azimuthal scan are plotted as a function of draw ratio in Figure 3.9 to investigate the effect of drawing. Based on WAXD results, up to total draw ratio ~5.4, the degree of orientation of polymer molecules increased rapidly. The orientation and crystal size increase very slowly above a draw ratio of seven. However, slight improvement in these parameters leads to enhancement in tensile properties. At similar levels of crystallinity (62 ~ 63%), considerable increase in crystal size was observed. In Figure 3.9, the fibers prepared without cold-drawing (black triangle) have a smaller crystal size of 12.3 nm than fibers that experienced cold-drawing (solid triangle) whose crystal size is 14.7 nm, although the former has a higher total draw ratio (DR=11) than the latter (DR=9.5). This suggests that cold-drawing process is effective for the

crystal growth of PAN. This crystal growth is attributed to stress induced crystallization, a phenomenon well known in polymers[162-166].

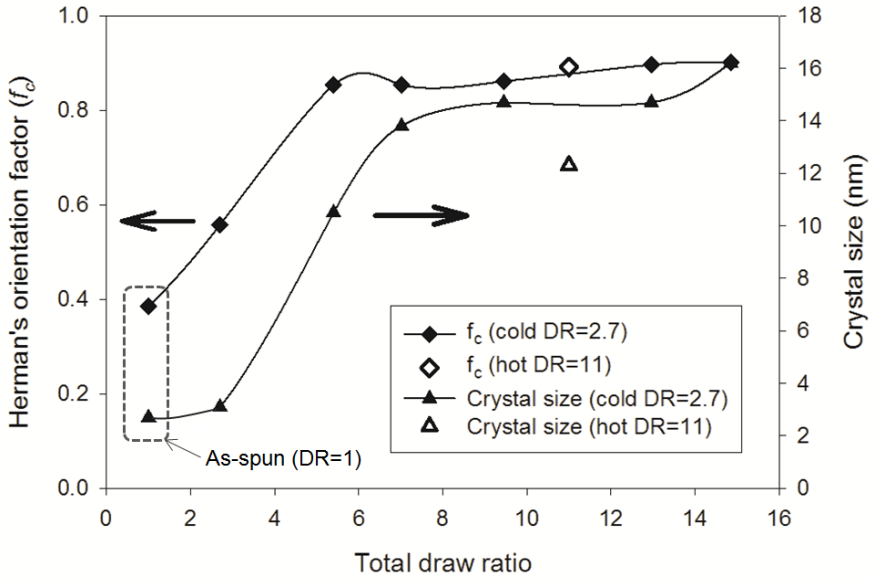

Figure 3.9 Crystal size and orientation of PAN-co-MAA control fibers as a function of draw ratio.

WAXD results of PAN-co-MAA/FWNT composite fibers are summarized in Table 3.5. Herman's orientation factors of PAN-co-MAA crystal (f_{PAN}) increased with advancing processing step. The crystallinity of PAN-co-MAA/FWNT composite fibers (63~68%) increased when compared to that of PAN-co-MAA control fiber (63%), since the FWNTs can act as nucleating agents for crystal growth. On the other hand, the PAN crystal size of FWNT 1 wt.% composite fiber decreased, as the FWNTs occupied room for PAN crystal growth (special hindrance). f_{PAN} as a function of processing step and FWNT concentration are plotted in Figure 3.10.

Table 3.5 Summary of WAXD results of PAN-co-MAA/FWNT fibers.

		Total draw ratio	Crystallinity (%)	Crystal size (nm)	f_{PAN}	$2\theta_{meridional}$
control	As spun	1	-	2.7	0.385	-
	1×2.7×1	2.7	-	3.1	0.558	39.5
	1×2.7×5.5	14.9	63	16.2	0.902	39.4
0.1 wt.%	As spun	1	-	3.0	0.343	-
	1×2.8×1	2.8	-	3.5	0.569	40.2
	1×2.8×5.6	15.68	68	16.1	0.895	39.4
0.5 wt.%	As spun	1	-	2.9	0.302	-
	1×2.3×1	2.3	-	3.4	0.547	40.4
	1×2.3×5.0	11.5	65	16.1	0.877	39.4
1 wt.%	As spun	1	-	3.0	0.320	-
	1×2×1	2	-	3.0	0.449	39.9
	1×2×6	12	63	14.7	0.866	39.1

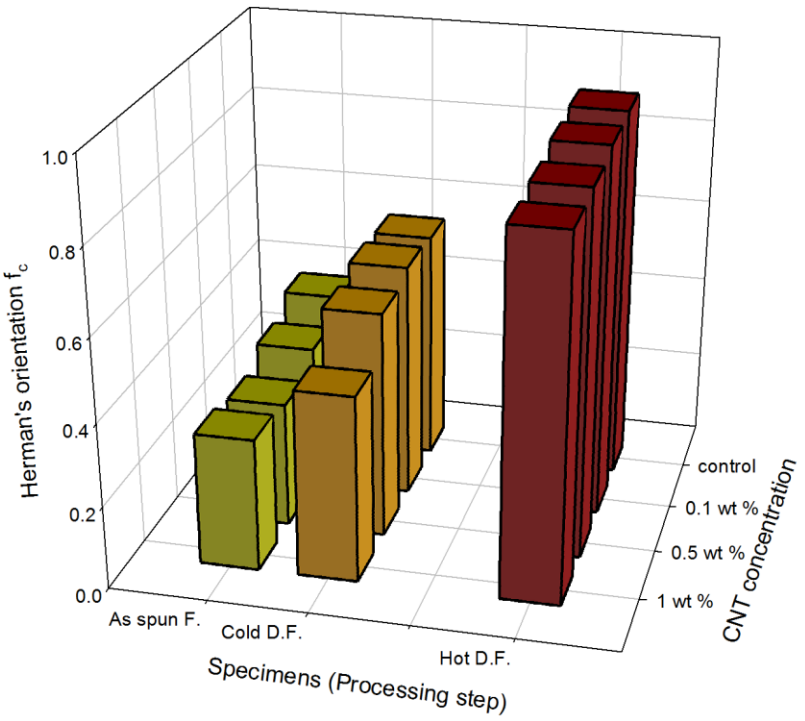

Figure 3.10 Herman's orientation factor (f_{PAN}) of PAN-co-MAA crystal as a function of processing step and CNT concentration.

The PAN crystal information can be obtained from WAXD, and CNT orientation can be monitored using Raman spectroscopy. The evaluation methods of CNT orientation in composite fiber using the simultaneous equations (3.3) and (3.4) are described elsewhere [137, 167-168]:

$$\frac{I^{VV}_{Fiber}(\phi=0)}{I^{VH}_{Fiber}(\phi=0)} = \frac{I^{VV}_{Fiber}(\phi=0)}{I^{VH}_{Fiber}(\phi=90)} = -\frac{24 < P_4(\cos\theta) > +60 < P_2(\cos\theta) > +21}{12 < P_4(\cos\theta) > -5 < P_2(\cos\theta) > -7} \quad (3.3)$$

$$\frac{I^{VV}_{Fiber}(\phi=90)}{I^{VH}_{Fiber}(\phi=0)} = \frac{I^{VV}_{Fiber}(\phi=90)}{I^{VH}_{Fiber}(\phi=90)} = \frac{-9 < P_4(\cos\theta) > +30 < P_2(\cos\theta) > -21}{12 < P_4(\cos\theta) > -5 < P_2(\cos\theta) > -7} \quad (3.4)$$

where ϕ is the angle between the polarization direction of excitation laser and the fiber axis, θ is the angle between the fiber axis and the CNT (FWNT) axis, I^{VV}_{Fiber} is Raman G-

band intensity measured under VV mode (excitation laser with polarizer and analyzer parallel), I_{Fiber}^{VH} is Raman G-band intensity measured under VH mode (excitation laser with polarizer and analyzer perpendicular), $< P_2(\cos\theta) >$ is a 2nd order Legendere polynomial, and $< P_4(\cos\theta) >$ is a 4th order Legendere polynomial. Calculated 2nd order parameter values (Herman's orientation factor; f_{FWNT}) are listed in Table 3.6.

Table 3.6 CNT orientation results from solving simultaneous equations.

CNT (wt. %)	Draw Ratio	$<P_2(\cos\theta)>$		
		Result 1	Result 2	Average
0.1	Solution	0.0722	0.0730	0.0726
	As-spun	0.7889	0.8286	0.8087
	$1\times2.8\times1$	0.8460	0.8774	0.8617
	$1\times2.8\times5.6$	0.8404	0.8769	0.8586
0.5	Solution	0.1916	0.1899	0.1907
	As-spun	0.6243	0.6265	0.6254
	$1\times2.3\times1$	0.8359	0.8835	0.8597
	$1\times2.3\times5.0$	0.7993	0.8859	0.8426
1	Solution	0.0161	0.0214	0.0187
	As-spun	0.4032	0.4089	0.4061
	$1\times2.0\times1$	0.7841	0.8271	0.8056
	$1\times2.0\times6.0$	0.8270	0.9008	0.8639

The "result 1" was obtained by substituting $I_{Fiber}^{VV}(\phi=0)$, $I_{Fiber}^{VH}(\phi=0)$, and $I_{Fiber}^{VV}(\phi=90)$ into equation (3.3) and (3.4). Likewise, "result 2" was calculated by substituting $I_{Fiber}^{VV}(\phi=0)$, $I_{Fiber}^{VH}(\phi=90)$, and $I_{Fiber}^{VV}(\phi=90)$ into equation (3.3) and (3.4).

The calculated results are averaged to minimize experimental error and are plotted in Figure 3.11. In composite solution, the nanotubes are randomly oriented (isotropic state). The CNT orientation in as-spun fibers was adversely affected by the concentration. The f_{FWNT} (0.8087) in the PAN-co-MAA/FWNT (0.1 wt.%) as-spun fiber represents good alignment of FWNT along the fiber axis, while f_{FWNT} decreased with increasing FWNT concentration. It is believed that the orientation motion of the nanotubes is hindered by neighboring nanotubes as nanotube concentration increases, thereby decreasing CNT orientation.

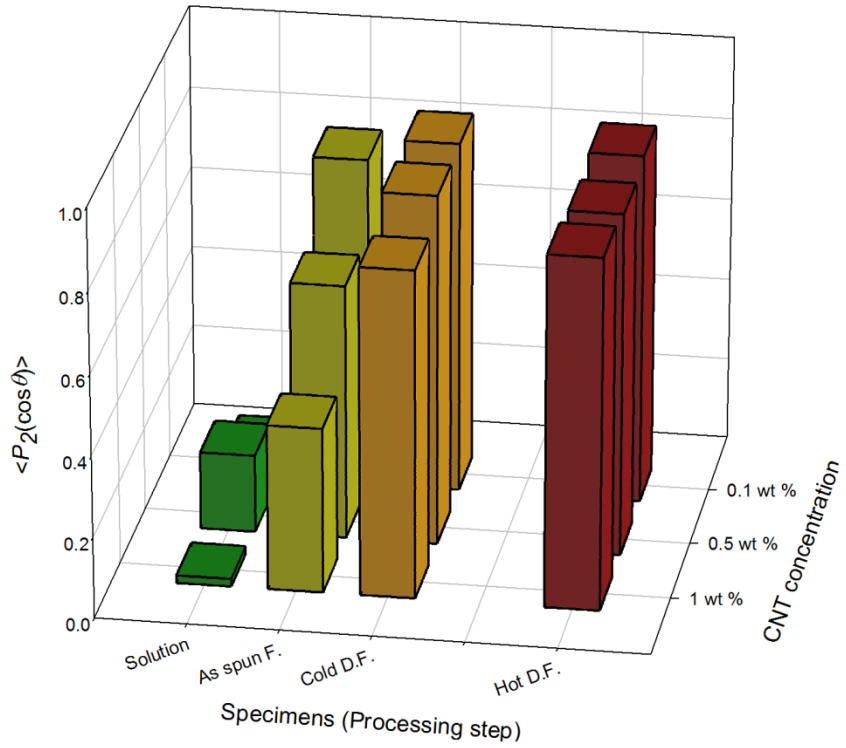

Figure 3.11 CNT orientation as a function of processing step and CNT concentration.

For cold drawn fibers, FWNT concentration also showed adverse effect on f_{FWNT}; however, it can be due to different cold-draw ratios. The orientation of CNTs in cold drawn fiber is almost the same as in fully drawn fibers, indicating that the degree of CNT orientation is almost saturated by the cold-drawing process. Fully drawn fibers showed

no noticeable relationship between CNT concentration and their orientation, since differences in f_{FWNT} fall within the error. Also, it should be noted that the PAN crystal orientation is affected adversely as nanotube loading increases (f_{PAN} of fully drawn fibers with 0, 0.1, 0.5, and 1 wt.% of FWNTs are 0.902, 0.895, 0.877, and 0.866, respectively (Table 3.4 and 3.5)). PAN polymers are easily aligned along CNTs. For this reason, PAN molecules in the vicinity of CNTs might reduce the average f_{PAN}, since the best orientation of CNTs (f_{FWNT} =0.8639) is lower than that of PAN (f_{PAN}=0.902).

Based on WAXD and Raman results, the orientation of CNT and polymer molecules can be illustrated as shown in Figure 3.12. In the as-spun composite fiber, the nanotubes start to align along the fiber axis, while PAN crystals have much lower orientation. At the as-spun stage, the PAN crystal structure is not a perfectly hexagonal one, as can be judged from the *d*-spacing ratio of 1.63 of equatiorial reflections at 2θ of 17° and 30° (Figure 3.13). After composite fibers experience cold-drawing, the nanotubes are well aligned along the fiber axis, yet PAN crystals are not well aligned along the fiber axis. The fully drawn fibers show good CNT and PAN crystal orientation. In the fully drawn fiber, PAN crystal exhibits hexagonal packing, as the *d*-spacing ratio between 17° and 30° of equatorial scan is close to $\sqrt{3}$ (1.72). Generally, reflection in the meridional scan of highly drawn PAN fibers can be deconvoluted into two peaks at 2θ~36° (zigzag sequence of PAN) and 2θ~40° (helical sequence of PAN) [169-170]. Although reflection in the meridional scan of PAN-co-MAA/FWNT composite fibers shows a single peak, lower peak position of the fully drawn fibers (Table 3.5) suggests more planar zigzag sequence of the PAN molecules. The meridional peak position of fully drawn PAN-co-MAA/FWNT composite fibers decreased with increasing FWNT concentration (Table 3.5). This implies that more planar zigzag sequence of PAN is feasible in the presence of FWNTs, which is in good agreement with PAN/SWNT composite fiber studies[122].

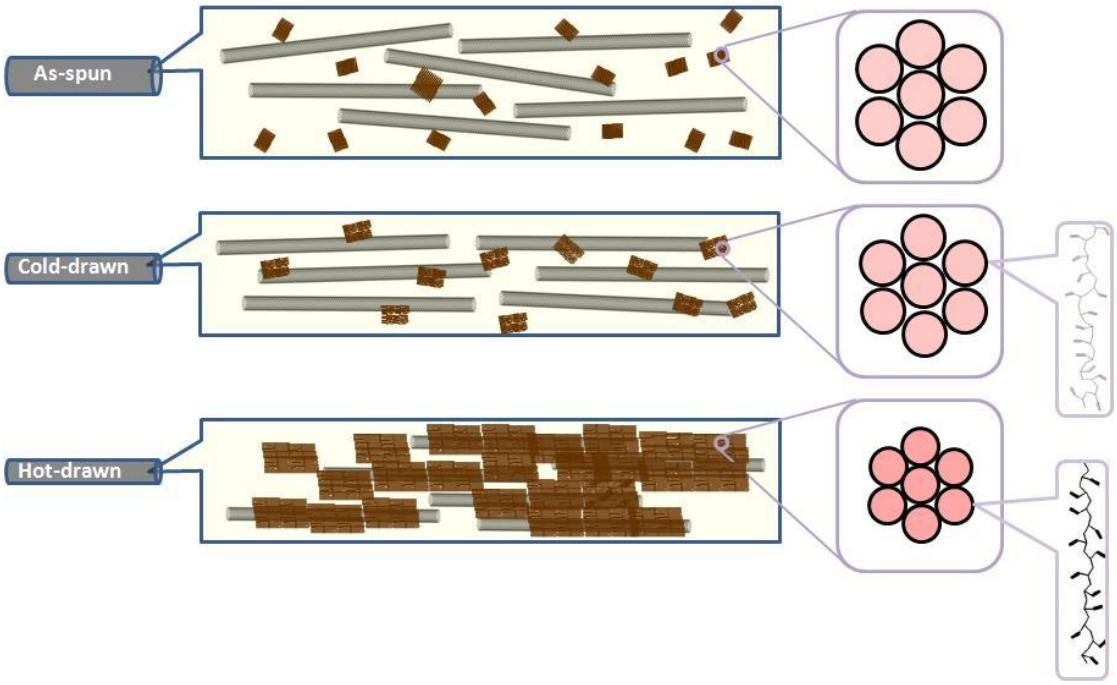

Figure 3.12 Schematics of structural changes of PAN-co-MAA/FWNT fibers at various processing steps.

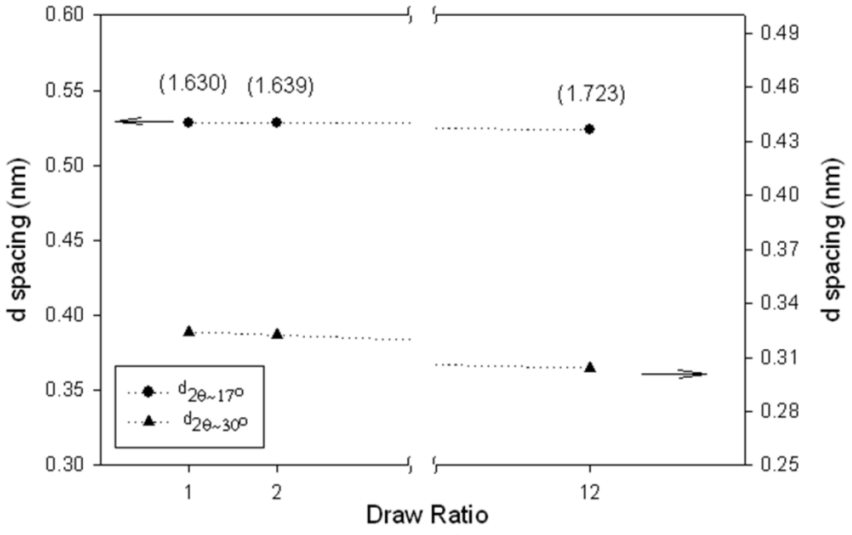

Figure 3.13 Effect of drawing on equatorial PAN-co-MAA *d*-spacings (for 2θ~17° and ~ 30° diffraction peaks). The values in parenthesis are the ratios of the two *d*-spacing.

3.3.5 Thermal Analysis of PAN-co-MAA Precursor Fibers

The DSC thermograms of the PAN-co-MAA control fibers and PAN-co-MAA/FWNT composites fibers are plotted in Figure 3.14. The ramping rate was 10 ℃/min, and 3 heating cycles were carried out under air for each sample. In both cases, the peaks appear at 273, 295, and 335 ℃, and no heat evolution is observed in the 2^{nd} and 3^{rd} cycles. The heats of stabilization are 1.4 kJ/g and 1.6 kJ/g for the control and the PAN-co-MAA/FWNT composite fibers, respectively. The heat of stabilization is increased in the presence of CNTs. To evaluate the effect of heating rate, the same tests were performed at a ramping rate of 1 ℃ /min and the results are plotted in Figure 3.15. For DSC thermograms for control and composite show two peaks at around 230 and 280 ℃, respectively and unexpected heat evolution was observed at around 375 ℃. The heats of stabilization are 2.1 kJ/g for the control and 2.4 kJ/g for composite fibers. For the control fiber, no noticeable heat evolution was observed during the second run conversely, the composite fiber exhibited heat evolution at 350 ℃. In the stabilization process, cyclization and introduction of oxygen (oxidation) are involved, as discussed in Chapter 1. The oxidation process is affected by the diffusion of oxygen, which can be slowed down in the presence of CNTs due to the path length. Also, mild stabilization conditions are originated by slow heating rate: (i) the peak value is reduced as compared to the 10 ℃/min, (ii) the exothermic peak broadens.

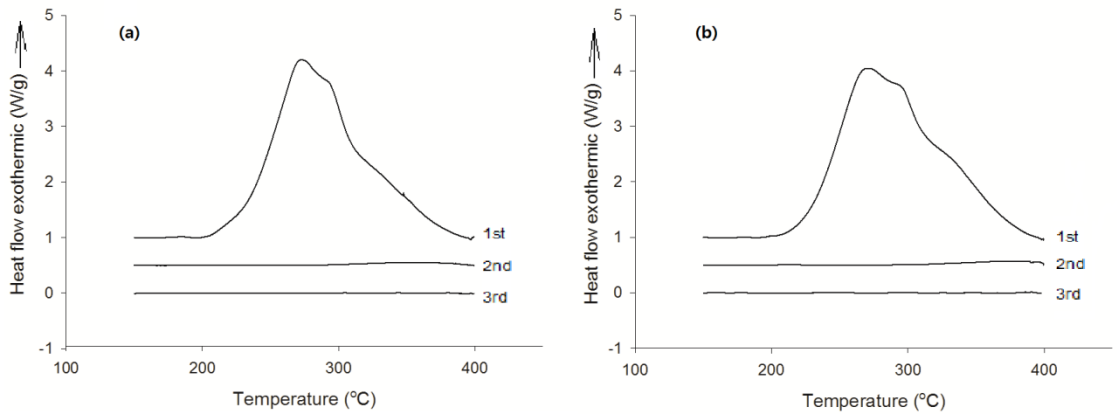

Figure 3.14 DSC thermograms of (a) PAN-co-MAA (DR=1×2.7×3.5) fiber and (b) PAN-co-MAA/FWNT (1 wt.%, DR=1×2.0×6.0) fiber at the heating rate of 10 °C/min. Air was purged at a flow rate of 50 ml/min. The 1st, 2nd, and 3rd heating cycle were plotted together. Note that thermograms of 1st, and 2nd heating cycle were shifted upward for the purpose of clear comparison.

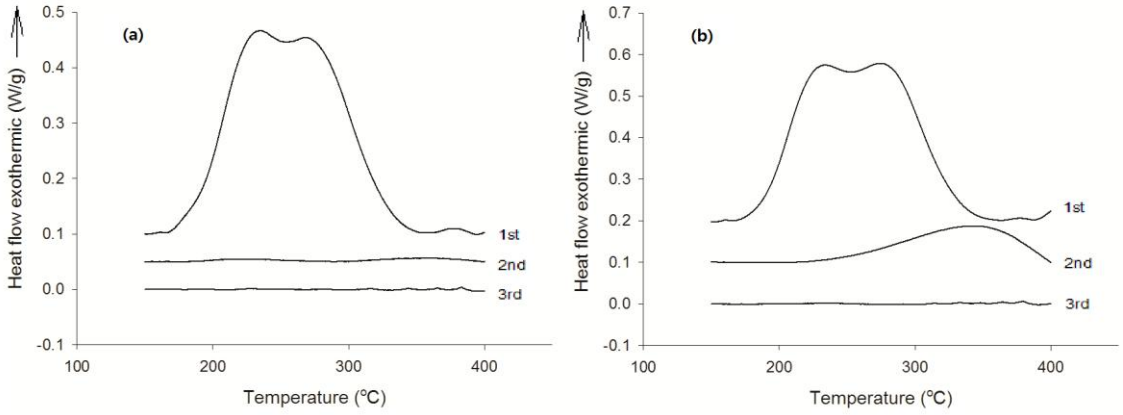

Figure 3.15 DSC thermograms of (a) PAN-co-MAA (DR=1×2.7×3.5) fiber and (b) PAN-co-MAA/FWNT (1 wt.%, DR=1×2.0×6.0) fiber at the heating rate of 1 °C/min. Air was purged at a flow rate of 50 ml/min. The 1st, 2nd, and 3rd heating cycle were plotted together. Note that thermograms of 1st, and 2nd heating cycle were shifted upward for the purpose of clear comparison.

It is well known that the cyclization reaction mechanism of PAN homo-polymer is a radical mechanism while that in acid containing copolymer PAN is governed by ionic mechanism[83]. The heat of stabilization of the PAN-co-MAA copolymer (M_w of 2.4×10^5 g/mol), PAN-co-MAA/FWNT composite, homopolymer PAN (M_w of 2.5×10^5 g/mol), and PAN/multi wall nanotube (MWNT) composite are summarized in Table 3.7 for comparison. In all cases, the heat of stabilization was reduced by increasing the heating rate. The excessive localized heat can lead to inhomogeneity in the fiber by abrupt gas evolution. The heat of stabilization of the PAN-co-MAA control is lower than that of the PAN homopolymer control. This implies that the ionic mechanism generates less exothermic heat during the stabilization than does the radical mechanism. The cyclization reaction initiated around 170 ℃ in the case of the ionic mechanism (PAN-co-MAA), while it initiated around 220 ℃ for the radical case (PAN homopolymer). Based on these observations, PAN-co-MAA precursor is favorable to avoid excessive heat during stabilization.

Table 3.7 Summary of ΔH of stabilization (kJ/g).

	PAN-co-MAA (co-polymer)		PAN (homo-polymer)	
	Control	FWNT 1wt.%	Control	MWNT 1wt.%
Fiber diameter (μm)	21.5	20.4	13.5	13.2
Drawing condition	$1\times2.7\times3.5$	$1\times2\times6$	$5\times1\times7$	$5\times1\times7$
ΔH (kJ/g) at heating rate of 10 ℃ /min (1^{st} run)	1.4	1.6	2.4	2.2
ΔH (kJ/g) at heating rate of 1 ℃ /min (1^{st} run)	2.1	2.4	7.1	4.8

To judge the effect of stabilization time, 6 hours of isothermal tests were conducted at 265, 295, and 325 ℃, which were selected from the peak position of the ramp test at a ramping rate of 10 ℃/min (Figure 3.16). In all cases, the exothermic heat flow decayed after the temperature reached setting temperature. The stabilization seems to be complete after six hours. The heat of stabilization results of this study are summarized in Table 3.8. The heat of stabilization values for control fibers increased with increasing isothermal temperature (5.5, 7.2, and 8.8 kJ/g for 265, 295, and 325 ℃, respectively).

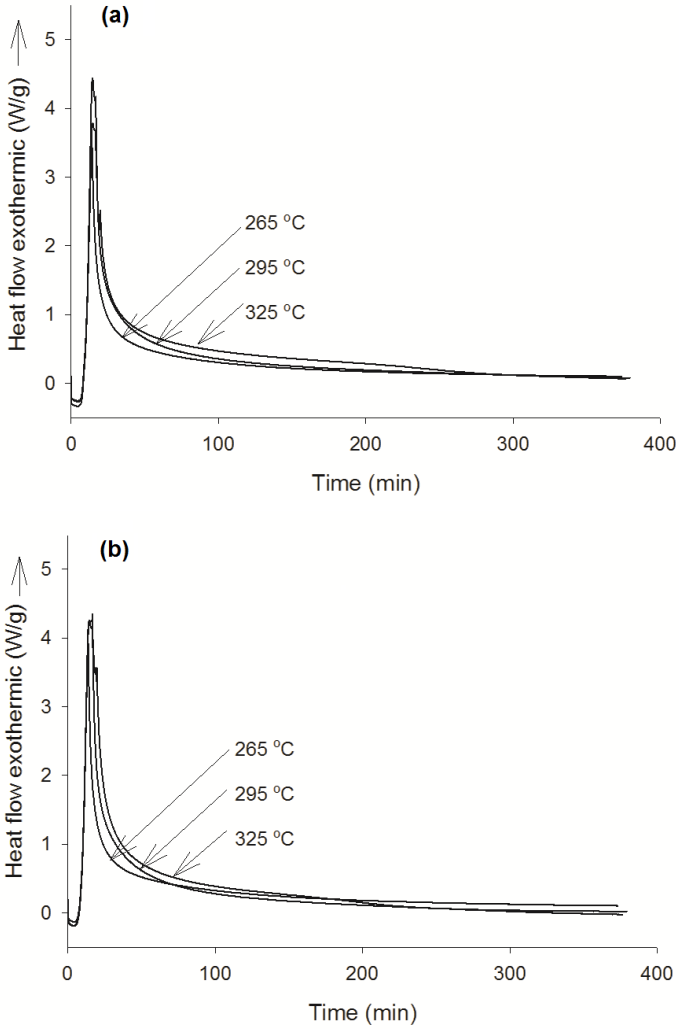

Figure 3.16 DSC thermograms of isothermal test of PAN-co-MAA control (a) and PAN-co-MAA/XO021UA 1 wt.% composite (b) fibers.

Table 3.8 Heats of stabilization of various fibers at different isothermal conditions.

		PAN-co-MAA (co-polymer)	
		control	FWNT 1 wt.%
Fiber diameter (μm)		21.5	20.4
ΔH (kJ/g)	265 ℃, holding 6 hrs	5.5	5.3
	295 ℃, holding 6 hrs	7.2	6.8
	325 ℃, holding 6 hrs	8.8	8.3
	265 ℃, holding 6 hrs → 325 ℃, holding 4 hrs	4.2/0.9	3.9/0.8

To check the chances of further stabilization reaction after finishing the isothermal test at 265 ℃, an additional isothermal temperature was imposed at 325 ℃ for four hours after the isothermal temperature test of 265 ℃ for six hours (Figure 3.17). Additional heat flow evolution was observed at the second isothermal cycle, indicating incompletion of stabilization after 6 hours of stabilization at 265 ℃. This implies that more than one holding temperature is favorable to ensure the completion of stabilization. FT-IR spectra for the isothermal-tested DSC specimens of the control fiber (Figure 3.18) confirm that the unreacted nitrile band (ca. 2240 cm^{-1}) still exists due to the large diameter of the specimen (~20 μm).

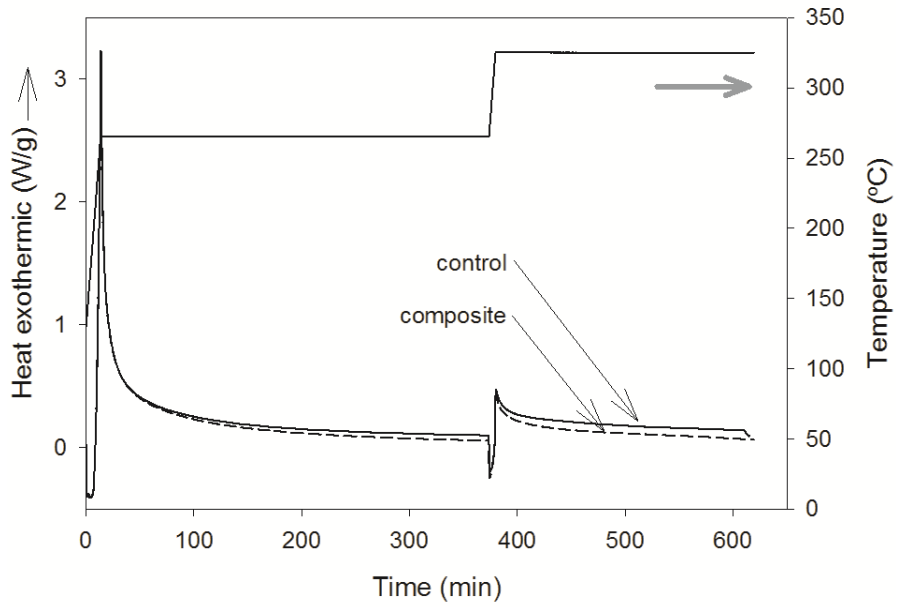

Figure 3.17 DSC thermograms of isothermal test of PAN-co-MAA control and PAN-co-MAA/FWNT (1 wt.%) composite fibers.

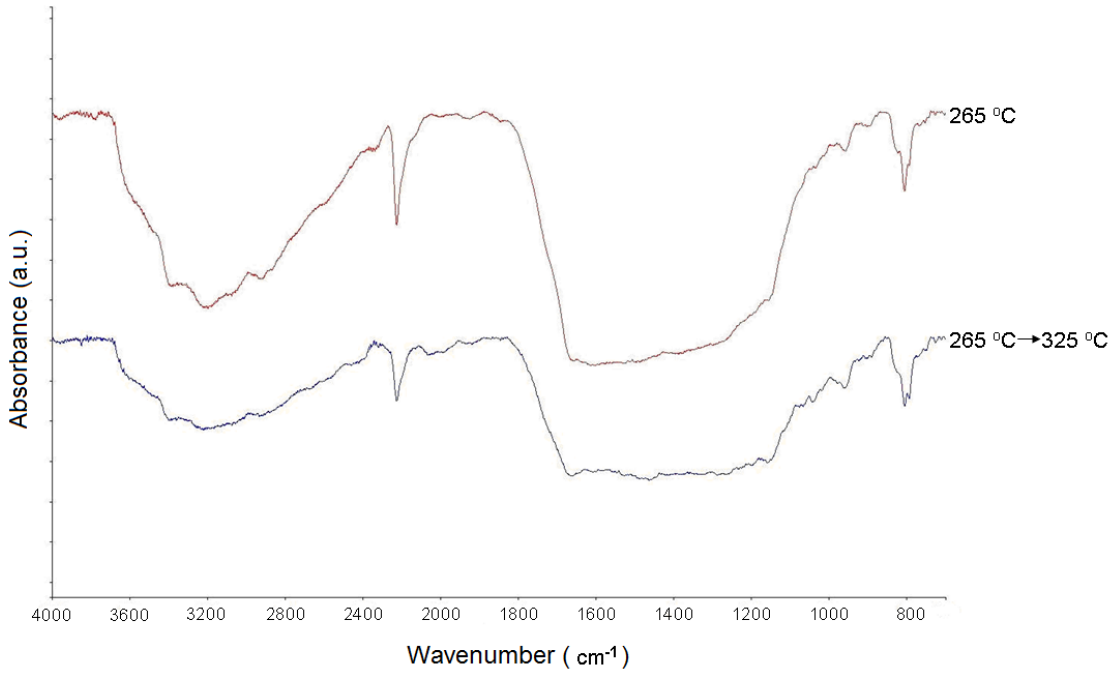

Figure 3.18 FTIR spectra of DSC run (isothermal) PAN-co-MAA/FWNT composite (1 wt.%) fibers.

3.3.6 Stabilization and Carbonization of PAN-co-MAA Control Fibers

The stabilization conditions and associated tensile properties of the stabilized fibers are summarized in Table 3.9. As the cyclization reaction proceeds further, entropic and chemical shrinkages occur[95], so the diameter of the stabilized fiber should be reduced, as no contraction was allowed along the continuous furnace line. Since the precursor fiber diameter was used for the calculation of stresses of the stabilized fibers, the tensile strength and modulus are underestimated here. The elongation at break decreases with advancing the stabilization step, as shown in Figure 3.19.

Table 3.9 Tensile properties of stabilized (stab.) control fibers.

	Precursor	1st stab.	2nd stab.	3rd stab.	4th stab.
Temperature (℃)	-	285	290	330	350
Residence time (min)	-	7.5	28.6	50	20
Stretching (%)	-	0	6	0	0
Pre tension (gf)	-	1	1	1.6	1.6
Measured tension (gf)	-	1	2.7~3.4	1.3~1.4	0.9
Elongation at break (%)	9.0±0.4	9.4±2.4	8.9±0.9	4.7±0.7	4.6±0.7
Tensile Modulus* (GPa)	22.5±1.5	16.2±10	13.00±1.9	11.3±1.9	12.2±1.7
Tensile Strength* (GPa)	1.11±0.07	0.67±0.1	0.60±0.05	0.34±0.03	0.31±0.02

* precursor fiber diameter (21.5μm) was used for calculating tensile properties of all stabilized fibers

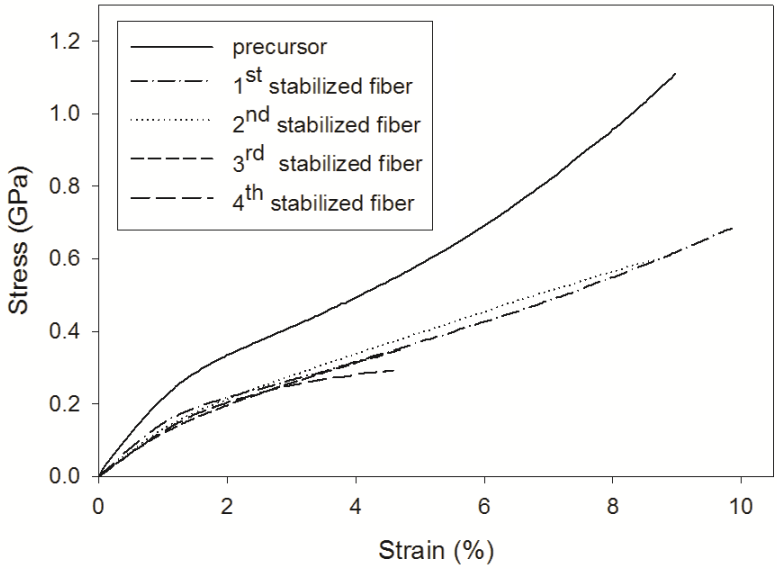

Figure 3.19 Stress-Strain curves of precursor control and stabilized fibers.

The WAXD results of the stabilized fibers are summarized in Table 3.10. As the stabilization step proceeds further, the diffraction patterns diffuse and the crystal size of PAN reduces as the PAN crystals are converted to the cyclic structure. The peak at 26° indicates that the graphitic crystal structure starts to form. Upon stabilization the conversion from PAN crystal to cyclic structure can be visualized by plotting the equatorial scan intensity as a function of 2θ angle as shown in Figure 3.20. The PAN crystal peaks at around 17° and 30° decreased as stabilization progresses, while the graphitic crystal peak at 26° starts to increase. The equatorial scan after the 4th stabilization step exhibits weak intensity at 17°, which implies the existence of PAN structure and is in good agreement with FT-IR results shown in Figure 3.21.

Table 3.10 WAXD pattern and crystal size information of PAN-co-MAA control (DR=1×2.7×3.5) and stabilized fibers.

	precursor	1st stab.	2nd stab.	3rd stab.	4th stab.
Diffraction Pattern	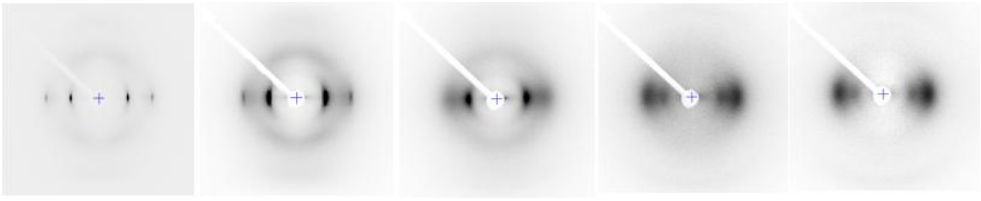				
Crystal size at 2θ~16° (nm)	14.7	9.0	3.7	1.3	1.3
Crystal size at 2θ~26° (nm)	-	-	1.1	1.1	1.1

Judging from the intensity of the nitrile group and hydro-carbon peaks in the FT-IR spectra, the stabilization was almost complete after 3rd step. To verify the completion of stabilization, the 3rd step and 4th step stabilized fibers were carbonized and compared. The WAXD and tensile properties of the carbon fibers are summarized in Table 3.11.

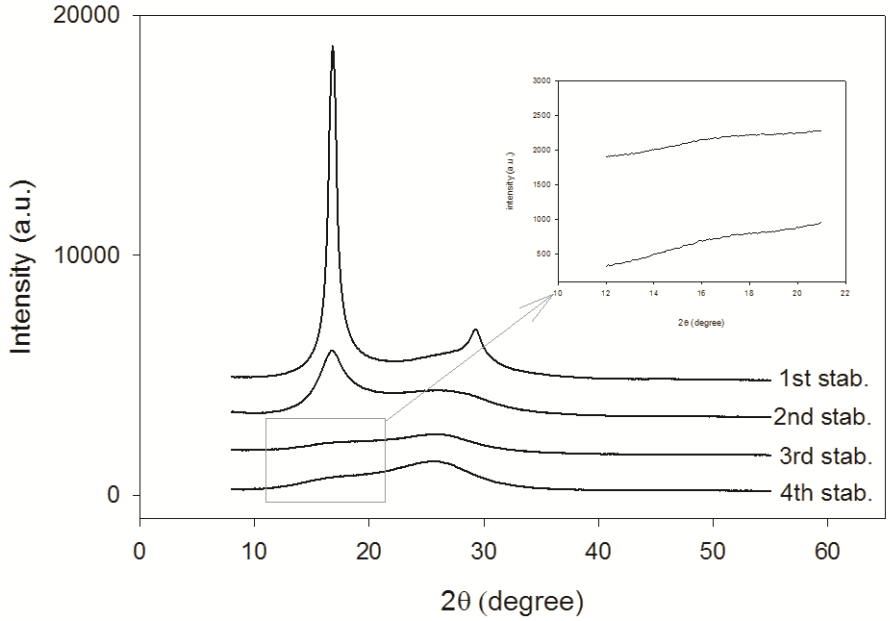

Figure 3.20 WAXD spectra of equatorial scans of stabilized fibers from PAN-co-MAA control (DR=1×2.7×3.5) precursor.

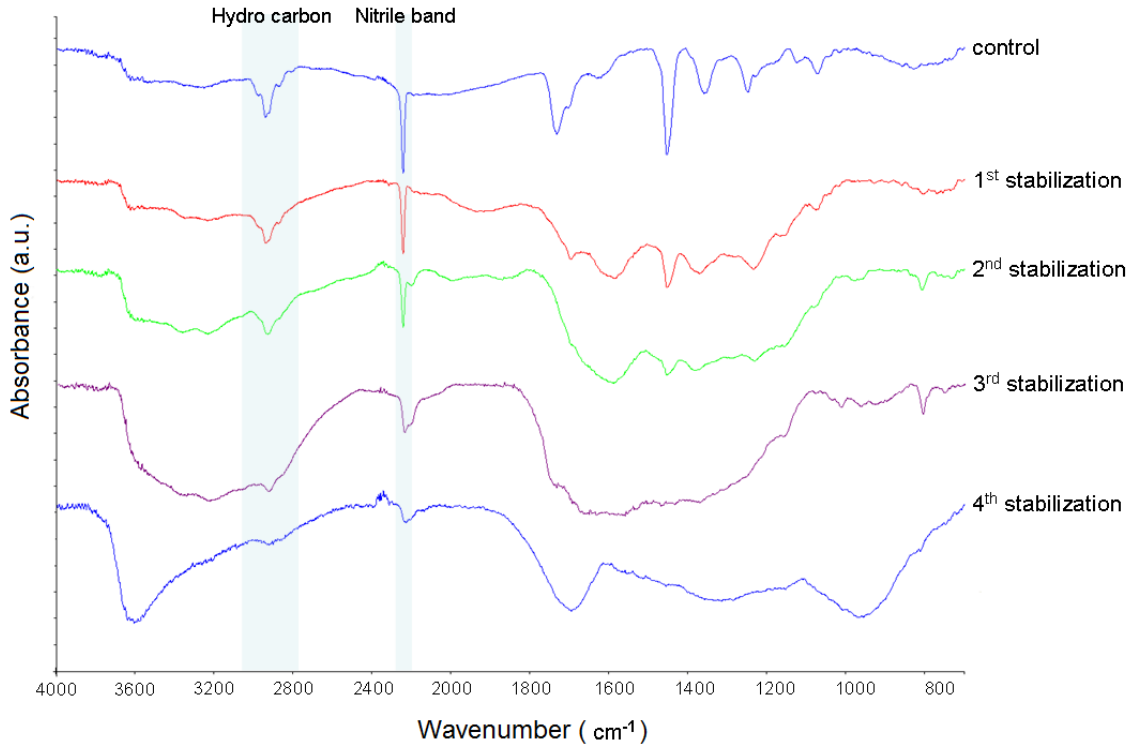

Figure 3.21 FTIR spectra of the precursor and stabilized fibers. Spectra were shifted to facilitate comparison.

Table 3.11 WAXD results of carbon fibers from PAN-co-MAA precursor fibers.

	1st carb. A (after 4th stab.)	1st carb. B (after 3rd stab.)	2nd carb. (after 1st carb. A)	3rd carb.
Temperature (℃)	600	600	800	1100
Residence time (min)	20.3	20.3	20.3	10.2
Pre-tension (gf)	1.6	1.6	1.6	1.3
Diffraction Pattern	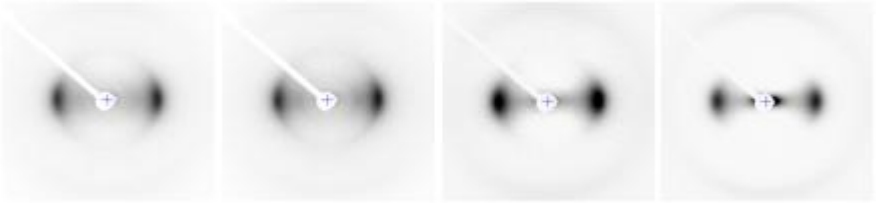			
Diameter (μm)	16.6	16.6	16	15.2
Crystal size (nm) at 26°	1.5	1.5	1.6	1.5
Modulus (GPa)	36±3	33±4	89±9	127±24
Tensile Strength (GPa)	0.84±0.15	0.73±0.16	0.85±0.13	1.0±0.2
Elongation at break (%)	2.31±0.47	2.26±0.53	0.92±0.14	0.75±0.13

The tensile properties of the carbon fibers from the stabilized fibers after the 4th stabilization are superior to that from the stabilized fibers after the 3rd stabilization. Since the un-cyclized structures cannot withstand the carbonization temperature, they turn into defects during carbonization. More perfection of structure in the 4th stabilized fibers is responsible for the high measured tension under which they withstand without breaking during carbonization; these factors explain the resulting tensile properties. However, the fibers carbonized at 1100 ℃ only reached 1 GPa in tensile strength and 127 GPa in tensile modulus. The poor tensile properties might be due to the larger fiber diameter,

which requires longer reaction time for oxygen diffusion and is not favorable to minimize defective structure formation. Also, the stabilization and carbonization conditions should be optimized to enhance the tensile properties. The tensile strength and tensile modulus increase as carbonization temperature increases, while the diameter and elongation at break decrease (Figure 3.22).

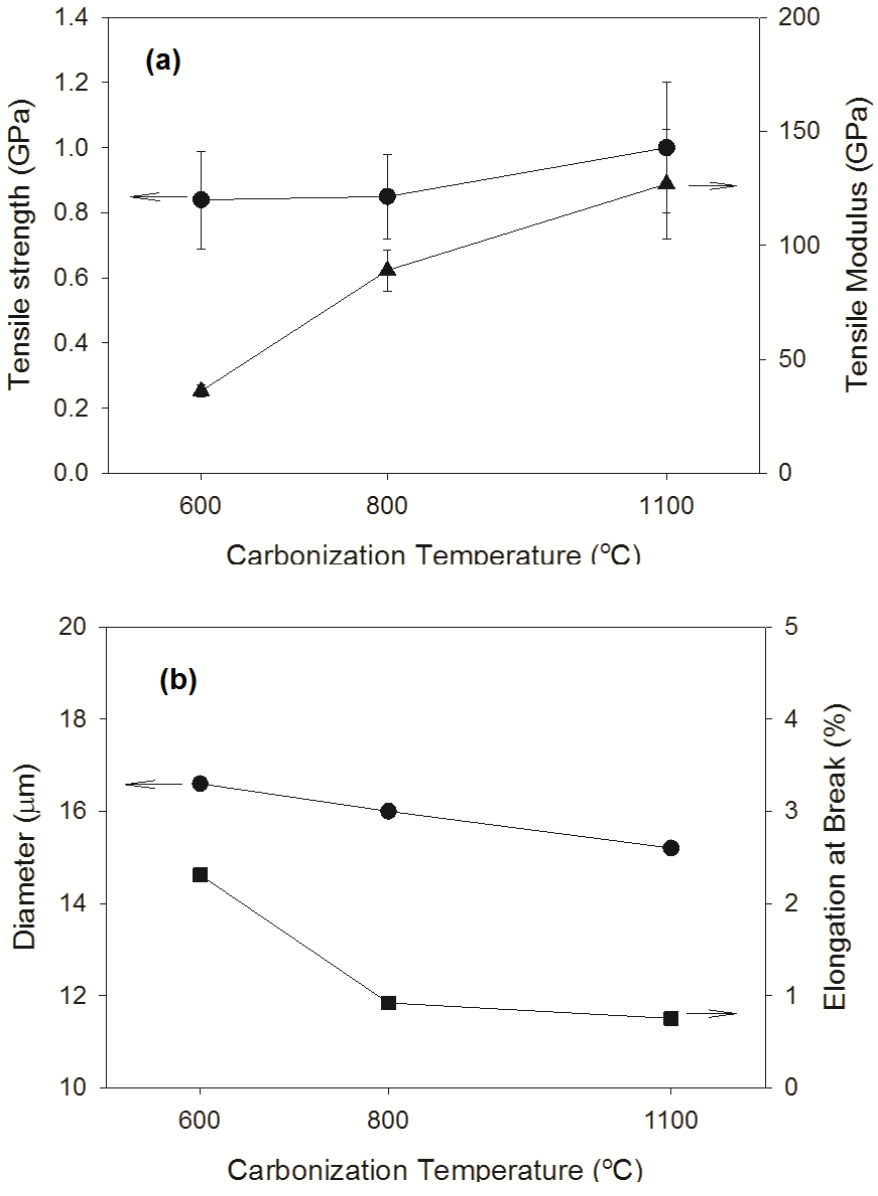

Figure 3.22 Effect of carbonization temperature on tensile properties (a), and diameter, and elongation at break (b).

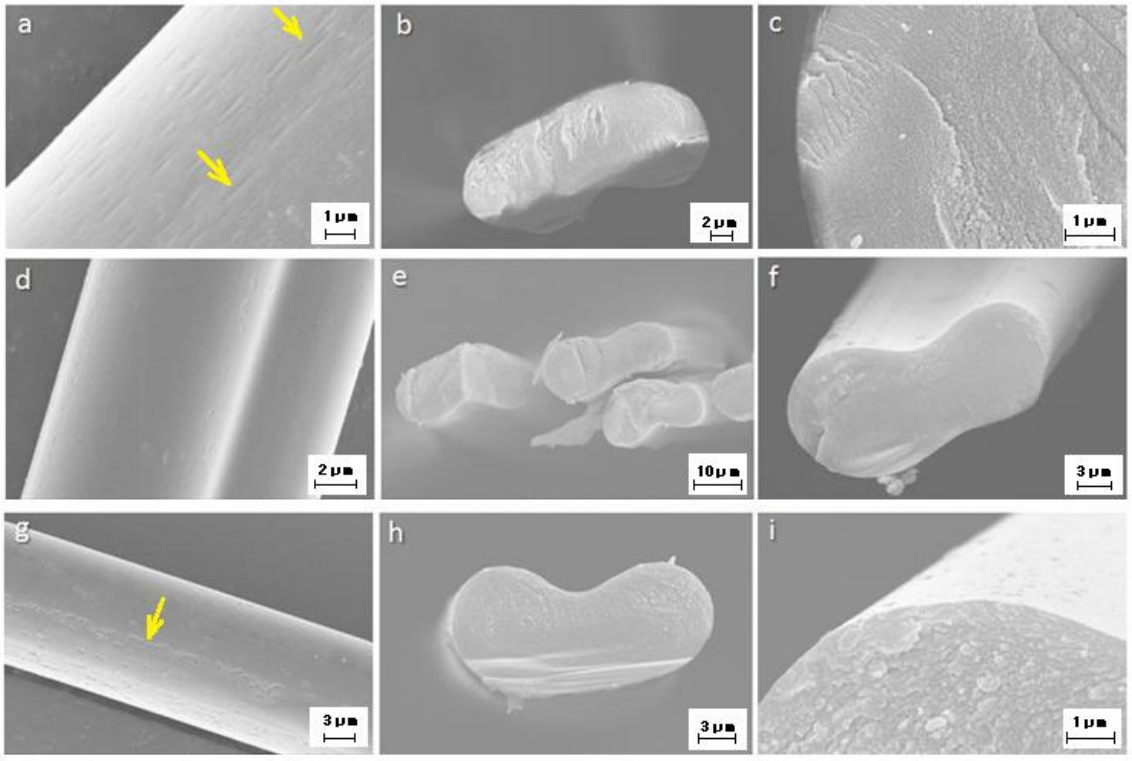

Figure 3.23 SEM images of carbon fibers (a, b, and c: carbonized at 600 ℃; d, e, and f: carbonized at 800 ℃; g, h, and i : carbonized at 1100 ℃, respectively).

To observe the cross section and surface of the carbon fibers, scanning electron microscopy (SEM) was used (Figure 3.23). SEM image a and g showed grooves (pointed by arrows) on the fiber surface which might be due to the friction between the fiber and fiber guide during the whole procedure or the original came from gel spinning condition. In summary, the tensile strength and modulus increased with carbonization temperature, while elongation at break and diameter decreased. However, the final carbon fiber tensile strength is lower than the previous results presented in Chapter 2. The tensile properties can be enhanced by optimizing stabilization conditions such as residence time, temperature, and tension.

3.4 Conclusions

In the low shear rate regime, viscosity of the PAN-co-MAA/FWNT (1 wt.%) composite solution is higher than that of the control solution without nanotubes. The opposite behavior was observed in the high shear rate regime. By adopting a cold-drawing process, tensile strength of 1.15 GPa and tensile modulus of 26.1 GPa was achieved for the control PAN-co-MAA fibers which are higher than literature values (tensile strength of 0.90 GPa and tensile modulus of 22.1 GPa from gel-spun control PAN homopolymer fibers[122]). For PAN-co-MAA/FWNT (1 wt.%) composite fibers, cold-drawing process facilitated the development of a fiber with a tensile modulus of 31.7 GPa at relatively low total draw ratio of 18. WAXD studies reveal that the highest crystal size of fully-drawn PAN-co-MAA fiber that went through the cold-drawing process is 16.2 nm, whereas typical crystal size of homo-polymer gel-spun PAN fiber is about 11-12 nm. For comparison, for a solution-spun PAN fiber, the typical crystal size is only about 5-6 nm. The Herman's orientation factor of the FWNTs (f_{FWNT}) in the PAN-co-MAA/FWNT (1 wt.%) fiber is higher than that of PAN (f_{PAN}), if measured after spinning and cold-drawing process.

The heat of stabilization of the PAN-co-MAA control fibers is lower than that of the PAN homo-polymer control fiber. For PAN-co-MAA, the heat of stabilization increased with incorporation of the FWNT in the fiber. The PAN-co-MAA control fibers are stabilized and carbonized by a continuous heat-treatment process.

CHAPTER 4

PAN-CO-MAA/VAPOR GROWN CARBON NANO FIBER (VGCNF) COMPOSITE FIBERS

4.1 Introduction

Oxidized PAN has the Limiting Oxygen Index (LOI) of 40 which is good for fire barrier application, while the neat PAN has LOI of 21 which is equivalent to PET as listed in Table 4.1. Literature [171-172] reported that the fire barrier property of polymer can be enhanced with reduced heat release rate by incorporation of vapor grown carbon nanofibers (VGCNFs) due to the high thermal conductivity of VGCNFs. In this study, the PAN-co-MAA (methacrylic acid)/VGCNFs composite fibers were spun using dry-jet wet-spinning technique with VGCNFs concentration of 0, 5, and 10 wt.%, respectively and characterized for their mechanical properties and structural changes.

Table 4.1 Limiting Oxygen Index (LOI) of various polymers[173].

Polymer type	LOI*	Polymer type	LOI*
Acrylic (PMMA)	17	PPO/HIPS	24
Polyolefin (PE,PP)	17	Polycarbonate (PC)	25
Polystyrene (PS)	18	Polyphenylene sulphide (PPS)[174]	34
Polyethylene terephthalate (PET)	21	Preoxidized PAN[175]	40
Polyacrylonitrile (PAN)[176]	21	Polyvinylchloride (PVC)	45
Polyamide (Nylon)	24	Polytetrafluoroethylene (PTFE)	>95

* LOI: The minimum concentration of oxygen in oxygen – nitrogen mixture, required to just support downward burning of a vertically mounted test specimen. Therefore, higher LOI values represent better flame retardancy.

4.2 Experimental

4.2.1 Materials

PAN-co-MAA (4 wt.% MAA content, M_w - 1.08×10^5 g/mol) was obtained from Japan Exlan, Co. Vapor grown carbon nanofibers (VGCNFs: PR-24-HHT, heat-treated at 3000 ℃) were obtained from Applied Sciences, Inc. (Cedarville, OH). *N*,*N*-dimethylformamide (DMF) was obtained from BDH, Inc. and was used as received.

4.2.2 Solution Preparation

VGCNFs were dispersed in DMF by sonication method (Branson 3510R-MT, 100 W, 42 kHz) at a concentration of 0.5g/300mL for 24 hours. PAN-co-MAA polymer (28.5 g) was dried in vacuum at 100 ℃ and dissolved in DMF (100 mL) at 80 ℃. VGCNFs/DMF dispersion was added to the PAN-co-MAA/DMF solution and the excess amount of solvent was evaporated by vacuum distillation with mechanical stirring to meet desired solid content in solvent [30 g solids (PAN-co-MAA and VGCNFs)/100 mL DMF]. Similarly, the other composite solutions with 30g solids were prepared at the VGCNF concentration with respect to the polymer of 0, 5, and 10 wt.%, respectively.

4.2.3 Solution Rheology

Solution rheology was conducted according to the same procedure and conditions described in 3.2.3 except for capillary steady shear test which was conducted only at 40 ℃.

4.2.4 Fiber Spinning

The PAN-co-MAA control and the PAN-co-MAA/VGCNFs composite fibers were spun at 40 ℃ by dry-jet wet-spinning using the laboratory scale spinning system manufactured by Bradford University Research Ltd. with single-hole spinneret (250 μm diameter). The prepared solution was spun into the coagulation media (maintained at

room temperature) with air gap of about 2 – 3 cm. The schematic of the spinning set up is shown in Figure 4.1.

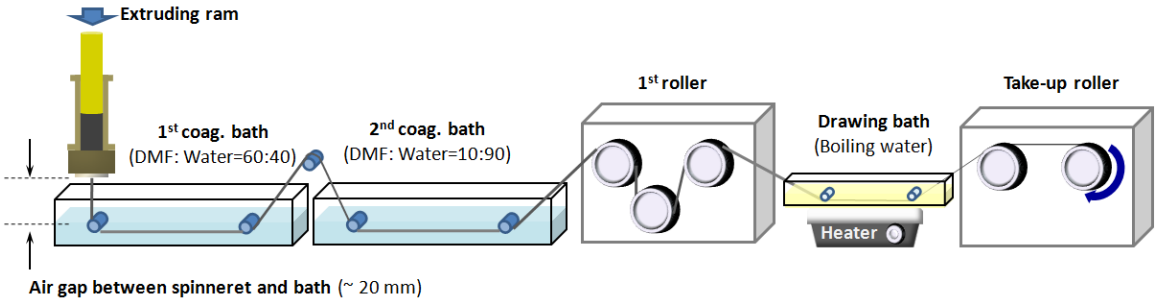

Figure 4.1 The schematic of spinning setup for dry-jet wet-spinning of the PAN-co-MAA/VGCNFs composite fibers.

A 635 mesh (20 μm) stainless steel filter pack (Purolator EFP, Inc) was used in the spinning line. DMF/Water volumetric ratios in the coagulation baths (bath 1 and 2) and drawing bath (bath 3) were 60/40, 10/90, and 0/100, respectively. Bath 1 and 2 were maintained at room temperature, while the drawing bath (bath 3) was maintained at 95 - 98 ℃. Fibers were drawn by passing through drawing bath at various draw ratios followed by vacuum drying at 50 ℃ for 3 days. Figure 4.2 shows PAN control, and PAN/VGCNFs composite fibers on spools.

Figure 4.2 Photograph of the PAN-co-MAA and PAN-co-MAA/VGCNFs composite fibers wound on plastic spools.

4.2.5 Characterization of Fibers

The PAN-co-MAA and PAN-co-MAA/VGCNF fibers are characterized as described in the previous Chapter 2 and 3.

4.3. Results and Discussion

4.3.1 Dynamic and Steady Shear Rheology of PAN-co-MAA Control and PAN-co-MAA/VGCNF Composite Solutions

The changes in complex viscosity of PAN-co-MAA and PAN-co-MAA/VGCNF solutions as a function of angular frequency are expressed in Figure 4.3. The complex viscosity of composite solution is lower than that of the control solution. This is because the weight content of the PAN-co-MAA polymer in the composite solution is lower than that of the control (28.5 g, and 27 g for VGCNF 5 wt.% and 10 wt.%, respectively vs. 30 g for control solution) to meet total solid contents of 30 g. Likewise, the $\tan \delta$ of the PAN-co-MAA/VGCNF composite solution is higher than that of the PAN-co-MAA control solution (Figure 4.4), implying that composite solution is less elastic due to the reduced number of entanglements between polymer molecules.

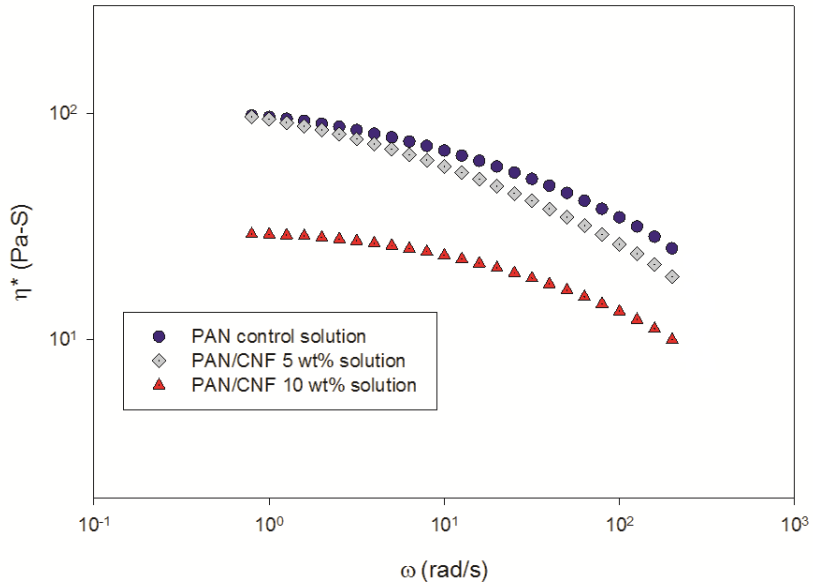

Figure 4.3 Frequency sweep test of complex viscosity of PAN-co-MAA/VGCNF solutions. PAN-co-MAA 30 g for control solution, PAN-co-MAA 28.5 g/VGCNF 1.5 g (5 wt.%), and PAN-co-MAA 27 g/VGCNF 3 g (10 wt.%) for composite solution, are dissolved, respectively in 100 mL DMF.

Figure 4.5 shows static rheology results of the PAN-co-MAA control and the PAN-co-MAA/VGCNF composite solutions. Though the molecular weight of PAN-co-MAA used in this chapter is lower than that in Chapter 3, apparent viscosity of the former control solution is higher than that of the latter due to higher concentration. All capillary results showed good agreement with Power law model whose parameters are summarized in Table 4.2.

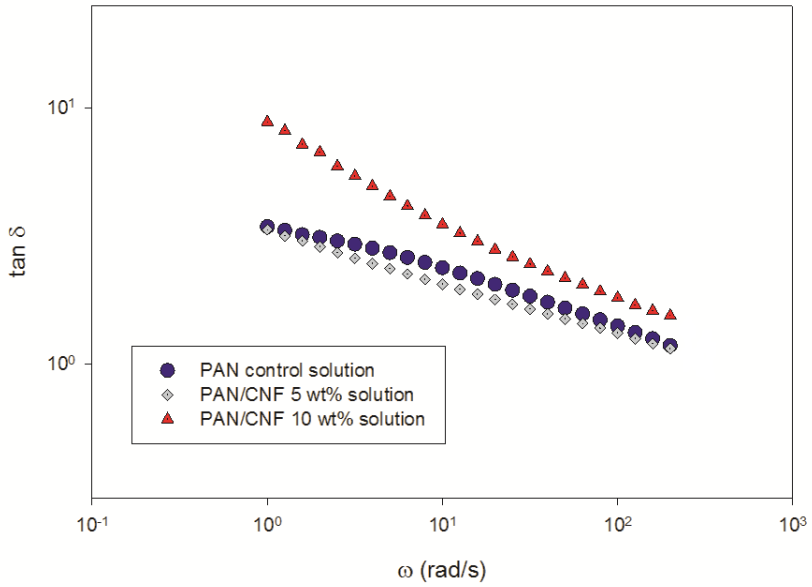

Figure 4.4 Loss factor (tan δ) of the PAN-co-MAA, and the PAN-co-MAA/VGCNF solutions as a function of angular frequency. PAN-co-MAA 30 g for control solution, PAN-co-MAA 28.5 g/VGCNF 1.5 g (5 wt.%), and PAN-co-MAA 27 g/VGCNF 3 g (10 wt.%) for composite solution, are dissolved, respectively in 100 mL DMF.

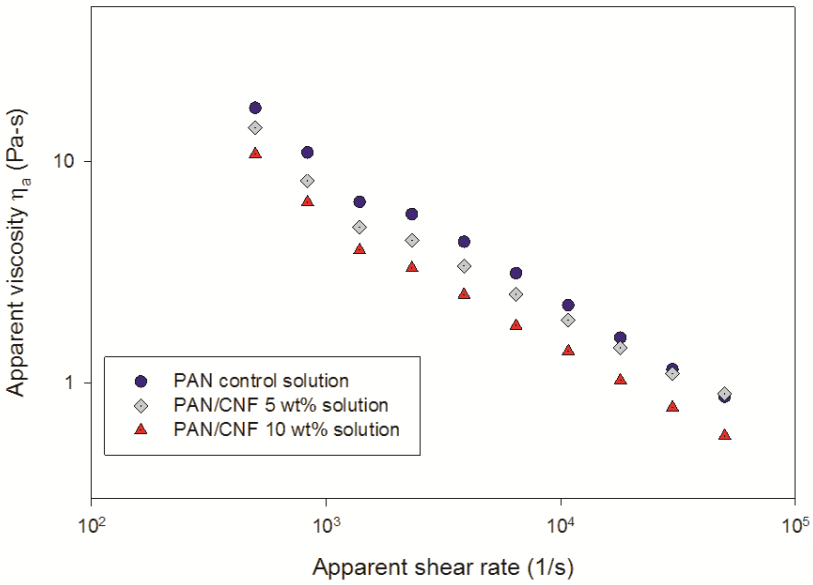

Figure 4.5 Apparent viscosity versus apparent wall shear rate by capillaries of the PAN-co-MAA/VGCNF solutions. PAN-co-MAA 30 g for control solution, PAN-co-MAA 28.5 g/VGCNF 1.5 g (5 wt.%), and PAN-co-MAA 27 g/VGCNF 3 g (10 wt.%) for composite solution, are dissolved, respectively in 100 mL DMF.

Based on the dynamic and static rheological results, the viscosities of the PAN-co-MAA control and the PAN-co-MAA/VGCNF (10 wt.%) composite solution are plotted in Figure 4.6 using Cox-Merz rule. The viscosity of composite solution is lower than that of control throughout the whole shear rate range, since the PAN-co-MAA concentration (27 g in 100 mL DMF) of composite solution is lower than that (30 g in 100 mL DMF).

Table 4.2 Power law indices and R^2 values for the PAN-co-MAA/VGCNF solutions.

	Material function, R^2		
	m	n	R^2
Control	756	0.372	0.993
5 wt.%	380	0.432	0.984
10 wt.%	400	0.388	0.987

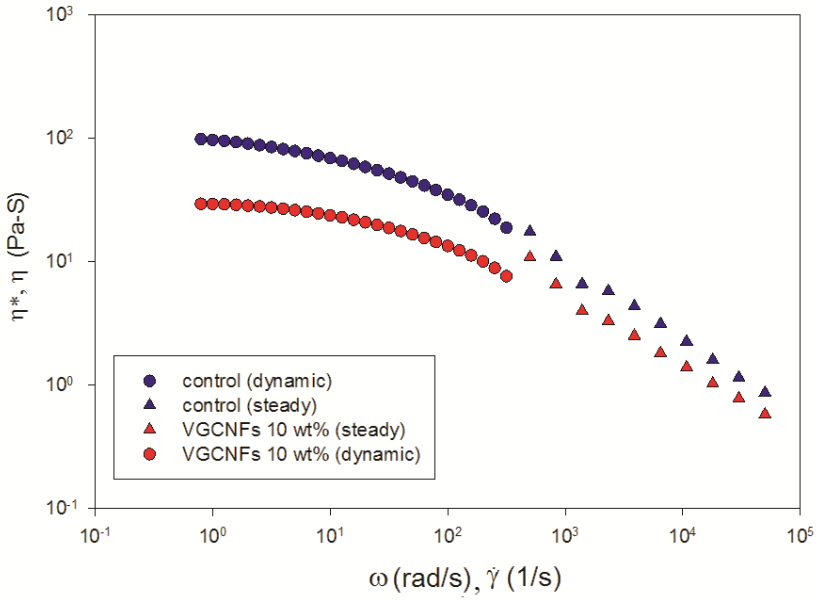

Figure 4.6 Comparison of viscous properties $\eta(\dot{\gamma})$ and $\eta^*(\omega)$. PAN-co-MAA 30 g for control solution, PAN-co-MAA 28.5 g/VGCNF 1.5 g (5 wt.%), and PAN-co-MAA 27 g/VGCNF 3 g (10 wt.%) for composite solution, are dissolved, respectively in 100 mL DMF.

4.3.2 Tensile Properties

The diameter of the solution-spun PAN-co-MAA/VGCNF fiber became smaller than that of the PAN-co-MAA control one produced under similar drawing conditions as VGCNF loading increased (Figure 4.7). This implies that the die swell of polymer solution extrudate was suppressed by the presence of VGCNF and is consistent with gel spun fiber results discussed in Chapter 2 and melt rheology results of PP/MWNT in literature[108]. The VGCNFs can be aligned along the flow in the spinneret and help to reduce the die swell during the spinning. The spin pack pressure during the spinning of composite solution (10 kgf) was lower than that of control one (20 kgf) implying that lower viscosity of composite solution than control solution at spinning condition. The PAN-co-MAA/VGCNF composite solution spun more stably without fiber breakage than

the PAN-co-MAA control solution, even though the viscosity of former was lower than the latter. Higher the viscosity (η)/surface tension (α) ratio of a material, the higher is the spinning stability according to Ziabicki's correlation between η and α [177]. Though not measured in this study, the surface tension of the PAN-co-MAA/VGCNF composite solution should be lower than that of the PAN-co-MAA control solution to make the η/α ratio large. The diameters of the PAN-co-MAA control and the PAN-co-MAA/VGCNF composite fibers at various drawing conditions are summarized in Table 4.3 and 5.4.

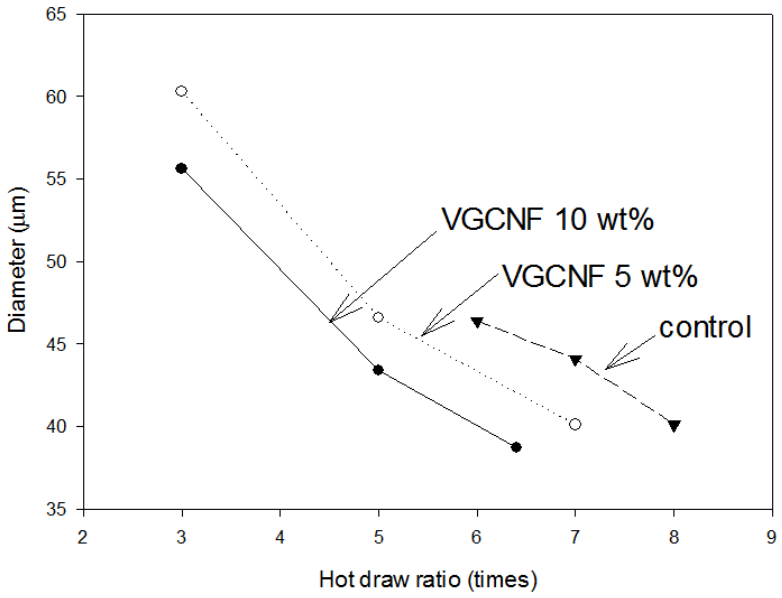

Figure 4.7 Diameter changes of the PAN-co-MAA control and the PAN-co-MAA/VGCNF composite fibers as a function of hot draw ratio (spin draw ratio was fixed as one).

Table 4.3 Mechanical properties of the solution-spun PAN-co-MAA control fibers.

	Drawing conditions[§]	Diameter (μm)	Tensile Strength (MPa)	Tensile Modulus (GPa)	Elongation at break (%)	Work of rupture (MPa)
Control	0.6 × 6.7	54.8	340±15	9.4±0.2	7.3±0.4	15±1
	0.6 × 8	49.4	500±43	12.1±0.4	8.5±0.8	25±4
	0.6 × 9.5	45.9	530±56	12.9±0.5	7.2±0.6	22±4
	1 × 6	46.2	430±37	11.1±0.4	9.3±0.9	25±4
	1 × 7	44.1	470±49	11.7±0.3	8.5±0.9	24±4
	1 × 8	40.1	500±67	12.5±0.5	7.9±1.0	23±6
	3 × 3	37.1	360±24	9.6±0.2	10.8±1.0	25±4
	3 × 4	32.0	440±33	12.2±0.3	8.0±0.9	22±4
	3 × 5	28.6	480±38	13.3±0.3	6.8±0.7	20±3
	5 × 3	28.9	420±27	11.5±0.3	7.4±0.6	19±3

[§] SDR × HDR

Table 4.4 Mechanical properties of the solution-spun PAN-co-MAA/VGCNF composite fibers.

VGCNF content	Drawing conditions[§]	Diameter (μm)	Strength (MPa)	Modulus (GPa)	Elongation at break (%)	Work of rupture (MPa)
5 wt.% (VGCNF 1.5 g , PAN-co-MAA 28.5 g)	0.3 × 8	66.4	480±29	12.4±0.5	7.9±0.4	23±3
	1 × 3	60.3	230±5	7.5±0.3	8.6±0.3	14±1
	1 × 5	46.6	430±18	11.8±0.5	9.4±0.6	26±2
	1 × 7	40.1	510±20	13.1±0.4	8.1±0.4	25±2
	3 × 3	35.6	320±15	9.6±0.2	11.3±1.0	26±3
	3 × 4	30.2	410±55	11.8±0.5	11.8±0.5	26±2
	3 × 5	27.1	450±21	13.0±0.4	7.9±0.5	23±3
	3 × 5.5	26.6	460±15	13.3±0.3	6.6±0.4	19±2
	5 × 2	33.4	250±6	8.3±0.4	12.7±0.9	24±2
	5 × 3	27.8	350±22	11.0±0.4	9.3±1.4	23±4
	5 × 4.1	23.7	370±19	11.6±0.3	6.1±1.4	14±2
10 wt.% (VGCNF 3 g , PAN-co-MAA 27 g)	0.6 × 6.5	48.9	360±18	12.1±0.5	6.0±0.5	14±2
	1 × 3	55.6	180±4	7.3±0.2	5.8±0.3	7±0.4
	1 × 5	43.4	310±4	10.6±0.3	6.9±0.6	15±1
	1 × 6.4	38.7	390±7	12.4±0.3	6.4±0.5	16±1
	2 × 3.5	36.5	260±39	9.9±0.9	6.4±0.3	11±1
	2 × 4.5	32.9	310±11	10.6±0.4	6.8±0.5	14±1
	2 × 5.6	29.3	410±12	12.8±0.5	6.7±1.0	18±3
	3 × 3.5	31.9	210±46	7.6±3.0	8.1±0.8	12±3
	3 × 4.2	27.3	350±10	11.9±0.4	7.3±0.4	17±1
	3 × 5	24.9	410±18	12.8±0.5	6.6±0.4	17±2
	4 × 4.4	23.2	400±18	12.8±1.0	7.3±0.8	20±3

[§] SDR × HDR

The stress-strain curves of the fully drawn (DR=15) PAN-co-MAA control and PAN-co-MAA/VGCNF composite fibers show that they have similar tensile modulus (about 13 GPa) but have different tensile strength (Figure 4.8). Micro-voids are observed in cross-section of PAN-co-MAA/VGCNF fibers (VGCNF 5 wt.% :Figure 4.9 (a), and (b) and VGCNF 10 wt.%: Figure 4.9 (e), and (f), respectively). These voids could be the reason for lower tensile strength of PAN-co-MAA/VGCNF composite fibers when compared with that of control fibers, thought dispersion of VGCNF is good in both 5 wt.% (Figure 4.9 (b)), and 10 wt.% (Figure 4.9 (f). Figure 4.9 (c), (d), (g), and (h) exhibited fractured surface of PAN-co-MAA/VGCNF composite fibers. Fibrillated fiber cross-sections are observed in Figure 4.9 (c) and (g), implying good adhesion between PAN-co-MAA and VGCNF.

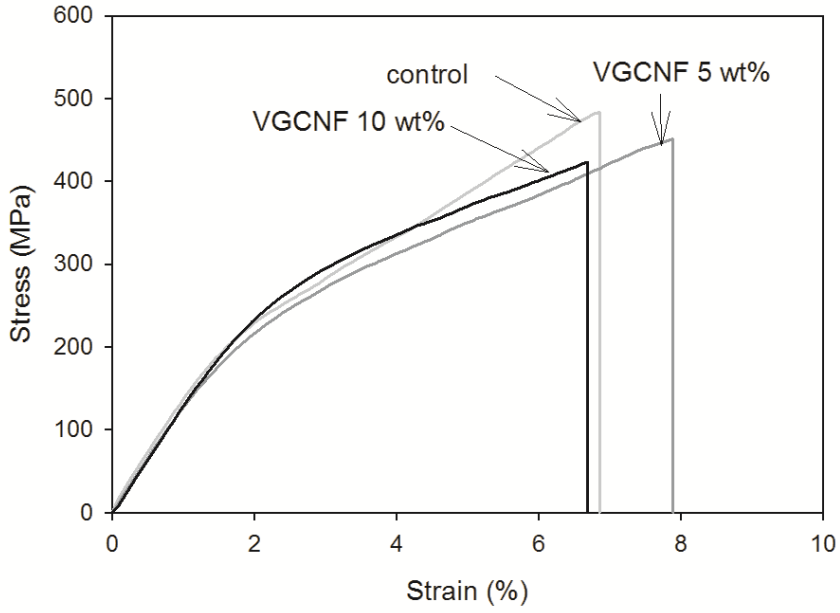

Figure 4.8 Stress-strain relationship of the PAN-co-MAA control and the PAN-co-MAA/VGCNF composite fibers. All the fibers have total draw ratio 15.

To investigate the effect of spin-drawing on mechanical properties, the PAN-co-MAA control and the PAN-co-MAA/VGCNF composite fibers were prepared at various drawing conditions and their mechanical properties are summarized in Table 4.3 (PAN-

co-MAA control fibers), and Table 4.4 (PAN-co-MAA/VGCNF composite fibers). Maximum hot draw ratio was pursued for each as-spun fiber with different spin-draw-ratio to achieve the highest mechanical properties. For control fibers, as the spin-draw-ratio increased from 0.6, 1, 3, and to 5, the maximum hot draw ratio decreased as 9.5, 8, 5, and 3, respectively. Resulting total-draw-ratios were 5.7, 8, 15, and 15 respectively. Also, the tensile strength of the drawn fibers decreased from 530, to 500, 480, and finally to 420 MPa with increasing spin draw ratio (Figure 4.10), whereas the tensile modulus reaches 13 GPa in most cases except for SDR 5 (Figure 4.11) sample. James et al. [160] derived mathematical relation between pre-existing orientation and natural draw ratio (the amount of strain when stable neck form during deformation[177]) and concluded that the natural draw ratio of polymeric materials decreases with increasing existing orientation. In this sense, the maximum hot draw ratio decreased with increasing spin draw ratio as summarized in Table 4.3 and 5.4. Higher hot draw ratio fiber with lower spin draw ratio showed better mechanical properties (Table 4.3 and 5.4).

Composite fibers containing 5 wt.% VGCNF showed similar trend of tensile strength to that of the control fibers. The PAN-co-MAA/VGCNF (5 wt.%) composite fibers with the higher spin draw ratio showed the lower tensile strength except spin draw ratio of 0.3 as shown in Figure 4.10 (a). The diameter of fully drawn fiber with spin draw ratio of 0.3 is the largest among the fully drawn fibers and this could be the reason for slightly lower tensile strength than the overall trend. 10 wt.% VGCNF incorporated composite fibers showed different tensile strength trends as compared to the previous cases as shown in Figure 4.10 (b). Failure to follow the trend in this case comes from low hot draw ratio. Jain et al. [112] observed voids at the ends of VGCNF in his solution-spun PAN/VGCNF study. These voids can act as defect during deformation.

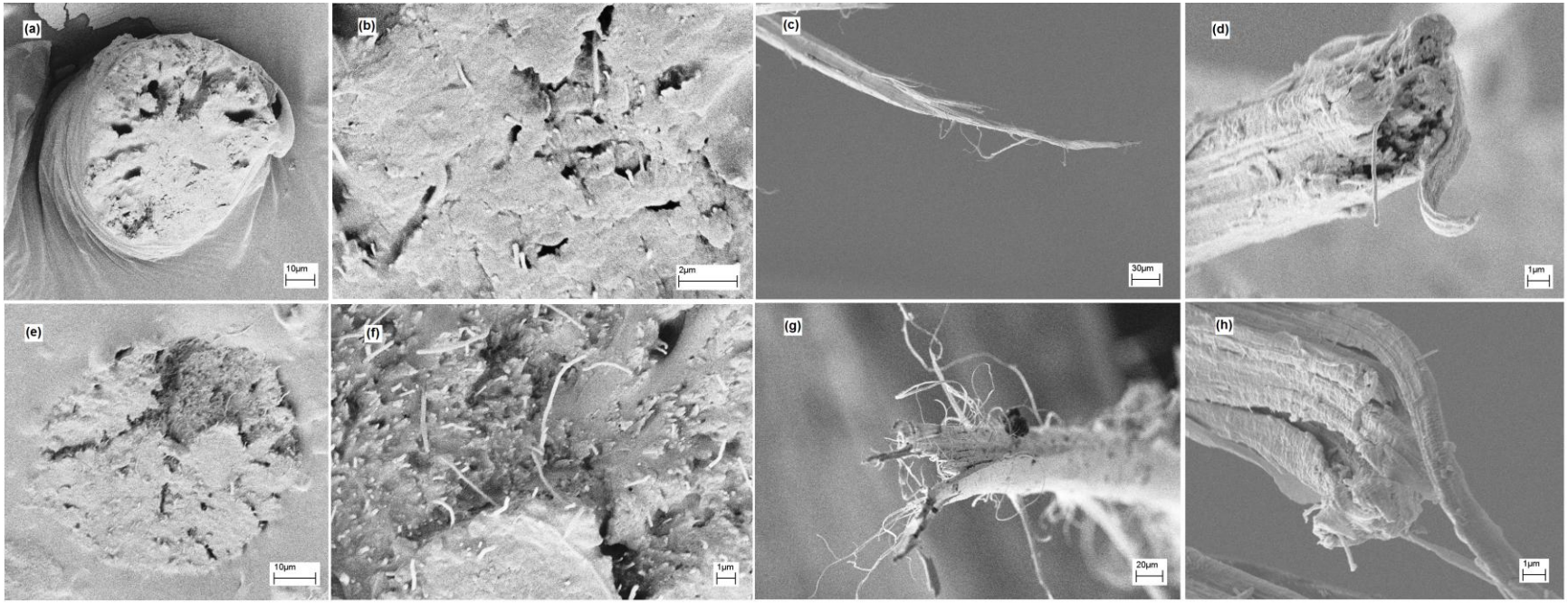

Figure 4.9 SEM micrographs of PAN-co-MAA/VGCNF (5 wt.%) composite fibers: (a)~(d) and PAN-co-MAA/VGCNF (10 wt.%) composite fibers: (e)~(h).

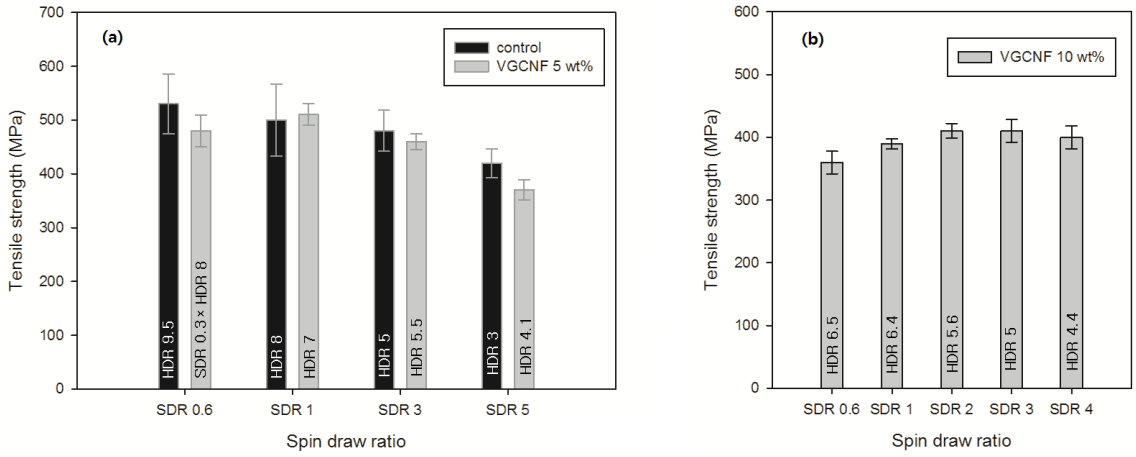

Figure 4.10 Tensile strength at various spin draw ratios (a) PAN-co-MAA control and PAN-co-MAA/VGCNF (5 wt.%) composite fibers, (b) PAN-co-MAA/VGCNF (10 wt.%) composite fibers.

Based on this assumption, large population of voids at both ends of VGCNF could be the reason for lower draw ratio. Also tensile moduli of 10 wt.% VGCNF composite fibers are slightly lower than that of control fibers as shown in Figure 4.11.

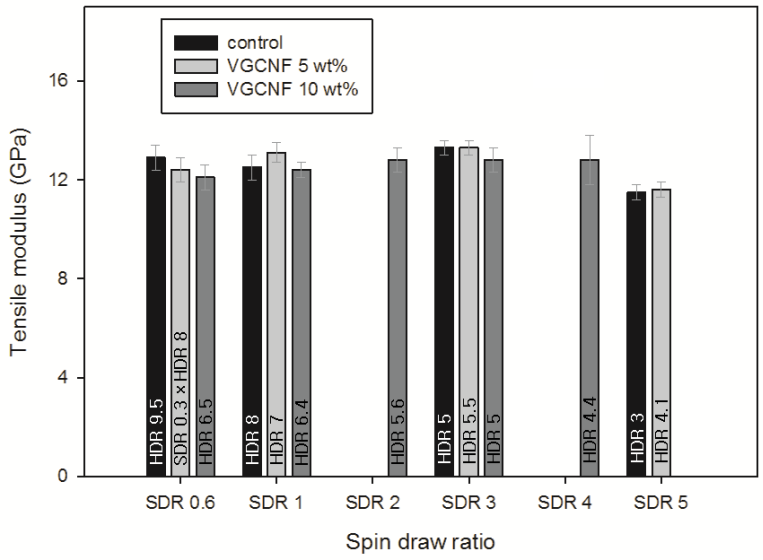

Figure 4.11 Maximum achievable tensile modulus at various spin draw ratios.

4.3.3 Structural Changes by Processing

WAXD 2D patterns and integrated scans of the PAN-co-MAA control, and the PAN-co-MAA/VGCNF composite fibers are shown in Figure 4.12. Graphite peak at 2θ~26° appears as sharp arc, of which intensity increases as VGCNF loading increases. The average graphite crystal size is 15.8 ± 1.3 nm (L_{002} column in Table 4.6) by using full width at half maximum of graphite peak at 2θ~26° which is in good agreement with reported value of ~17 nm in literature [136]

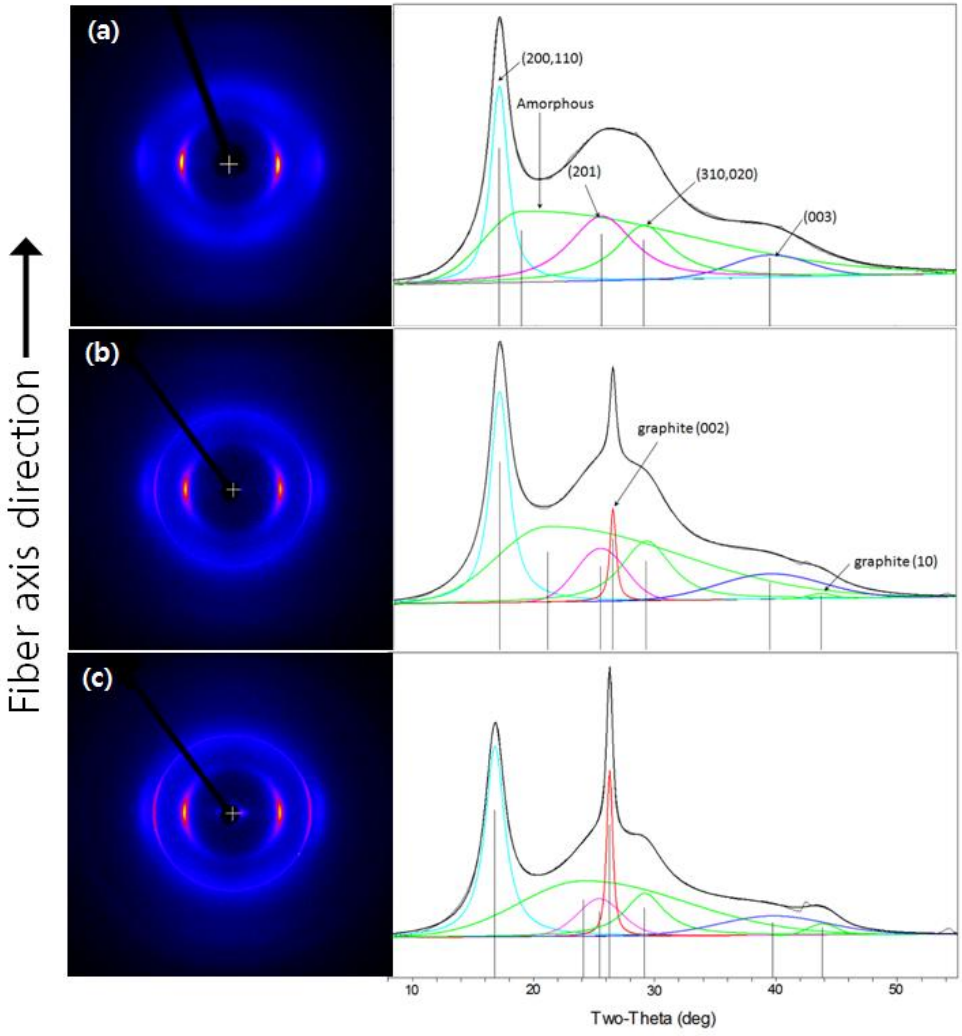

Figure 4.12 WAXD photograph and integrated scan for fully drawn (a) PAN-co-MAA control (HDR=8), (b) PAN-co-MAA/5 wt.% VGCNF (HDR=7), and (c) PAN-co-MAA/10 wt.% VGCNF (HDR=6.4) composite fiber, respectively. SDR=1 for the all fibers.

The ratio between two *d*-spacings at 2θ~17° and at 2θ~30° of the solution-spun PAN-co-MAA fibers are plotted in Figure 4.13 with gel-spun control fiber results for comparison. The *d*-spacing ratio (2θ~17°/2θ~30°) of gel-spun fiber increases with increasing total draw ratio and approaches square root of three (~1.732) as shown in Figure 4.13 in solid circles, while that of solution-spun fiber remains similar (1.692 ~1.725) regardless of total draw ratio. Differences in the amount of residual solvent in the as spun fiber could be the reason: residual solvent in the solution as-spun fiber could be smaller than that in the as-spun fiber by using gel spinning technique. The detailed *d*-spacing at 2θ~17°, at 2θ~30°, and their ratio are summarized in Table 4.5, and 5.6.

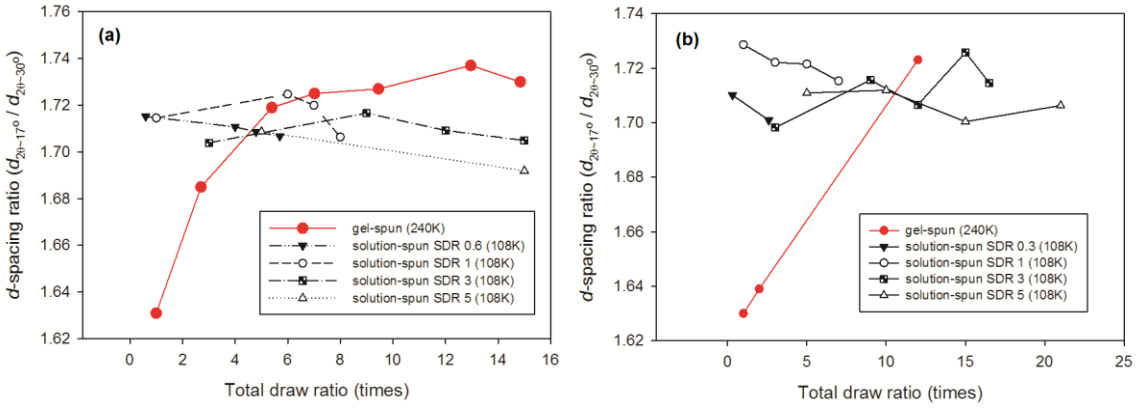

Figure 4.13 Comparison of d-spacing ratio as a function of total draw ratio between gel-spun and solution spun fibers (a) PAN-co-MAA (2.4×10^5 g/mol) control gel spun fiber and PAN-co-MAA (1.08×10^5 g/mol) control solution spun fiber (b) PAN-co-MAA (2.4×10^5 g/mol)/FWNT (1 wt.%) gel spun fiber and PAN-co-MAA (1.08×10^5 g/mol)/VGCNF (5 wt.%) solution spun fiber.

The average meridional peak position of the fully drawn PAN-co-MAA/VGCNF composite fibers decreased with increasing VGCNF concentration (39.8° ± 0.10, 39.6° ± 0.13, and 39.5° ± 0.17 for the solution-spun PAN-co-MAA control, the PAN-co-MAA/VGCNF (5wt.%), and the 10 wt.% composite fibers, respectively Table 4.5 and 5.6). This implies that more planar zigzag sequence of PAN is feasible in the presence of VGCNF.

Table 4.5 PAN crystal information of the solution spun PAN-co-MAA control fibers.

		Total Draw ratio	Crystallinity (%)	PAN Crystal size (nm)	f_{PAN} †	$2\theta_{meridional}$ ‡	$d_{2\theta\sim17^\circ}$ (nm)	$d_{2\theta\sim30^\circ}$ (nm)	$d_{2\theta\sim17^\circ}$ / $d_{2\theta\sim30^\circ}$
Control	As spun	0.6	45.4	4.3	0.008	40.54	0.51977	0.30303	1.7152
	As spun	1	43.6	4.3	0.022	40.35	0.52155	0.30419	1.7145
	As spun	3	42.8	4.0	0.040	40.80	0.51673	0.30325	1.7039
	As spun	5	43.7	3.9	0.069	40.66	0.51960	0.30408	1.7087
	0.6×6.7	4	52.1	6.0	0.602	39.80	0.52377	0.30628	1.7101
	0.6×8	4.8	50.5	5.8	0.591	39.80	0.52667	0.30823	1.7086
	0.6×9.5	5.7	52.0	6.0	0.604	39.80	0.52598	0.30818	1.7067
	1×6	6	47.7	4.9	0.552	39.82	0.52782	0.30603	1.7247
	1×7	7	49.8	5.3	0.588	39.82	0.52528	0.30540	1.7199
	1×8	8	51.6	5.9	0.609	39.77	0.52548	0.30793	1.7064
	3×3	9	50.9	4.7	0.470	39.95	0.52500	0.30582	1.7166
	3×4	12	51.5	5.6	0.545	39.84	0.52514	0.30724	1.7092
	3×5	15	52.7	5.8	0.596	39.76	0.52619	0.30863	1.7049
	5×3	15	51.0	5.2	0.545	39.97	0.52702	0.31154	1.6916

† Herman's orientation factor of PAN, ‡ meridional peak position, $d_{2\theta\sim17^\circ}$ *d*-spacing at 2θ~17°, $d_{2\theta\sim30^\circ}$ *d*-spacing at 2θ~30°

Table 4.6 PAN and VGCNF crystal information of solution spun PAN-co-MAA/VGCNF composite fibers (continued on next page).

		Total Draw ratio	Crystallinity† (%)	Crystal† size (nm)	L_{002}[a] (nm)	L_{10}[b] (nm)	f_{PAN}	f_{VGCNF}§	$2\theta_{meridional}$	$d_{2\theta\sim17°}$† (nm)	$d_{2\theta\sim30°}$† (nm)	$d_{2\theta\sim17°}$ †/$d_{2\theta\sim30°}$
	As spun	0.3	46.2	4.1	15.3		0.012	0.484		0.52145	0.30491	1.7101
	As spun	1	47.8	3.9	14.2		0.027	0.517		0.52268	0.30236	1.7286
	As spun	3	48.4	3.4	15.7		0.058	0.554		0.52463	0.30892	1.6982
	As spun	5	48.5	3.6	16.5		0.053	0.556		0.52148	0.30479	1.7109
	0.32×8	2.6	51.6	5.4	18	3.4	0.569	0.697	39.71	0.52457	0.30840	1.7009
	1×3	3	47.7	4.9	17.6	3.9	0.340	0.643	39.63	0.52628	0.30560	1.7221
	1×5	5	49.2	5.0	17.6	3.0	0.459	0.691	39.75	0.52563	0.30533	1.7215
5 wt.%	1×7	7	50.4	5.4	13.7	3.2	0.570	0.705	39.53	0.52638	0.30687	1.7153
	3×3	9	51.9	4.7	16.1	3.7	0.422	0.651	39.46	0.52514	0.30609	1.7156
	3×4	12	53.6	4.9	16.4	3.4	0.478	0.690	39.45	0.52473	0.30747	1.7066
	3×5	15	53.4	5.0	16.8	3.9	0.559	0.711	39.60	0.52451	0.30796	1.7258
	3×5.5	16.5	53.9	5.2	15.2	3.3	0.549	0.719	39.67	0.52547	0.30646	1.7146
	5×2	10	49.9	4.8	15.1	3.2	0.378	0.657	39.42	0.52469	0.30649	1.7119
	5×3	15	52.7	4.9	14.0	4.5	0.461	0.679	39.39	0.52456	0.30848	1.7004
	5×4.13	21	54.2	5.2	15.0	3.8	0.534	0.697	39.44	0.52464	0.30747	1.7063

† PAN, [a] VGCNF crystal size from equatorial scan, [b] VGCNF crystal size from meridional scan, § Herman's orientation factor of VGCNF

Table 4.6 PAN and VGCNF crystal information of solution spun PAN-co-MAA/VGCNF composite fibers (continued).

		Total Draw ratio	Crystallinity† (%)	Crystal† size (nm)	L_{002}[a] (nm)	L_{10}[b] (nm)	f_{PAN}	f_{VGCNF}§	$2\theta_{meridional}$	$d_{2\theta\sim17°}$† (nm)	$d_{2\theta\sim30°}$† (nm)	$d_{2\theta\sim17°}$ †/$d_{2\theta\sim30°}$
10 wt.%	As spun	0.6	44.3	3.9	15.3		0.024	0.460		0.52492	0.30486	1.7218
	As spun	1	41.1	3.2	16.2		0.022	0.441		0.52284	0.30399	1.7199
	As spun	2	45.8	3.3	15.5		0.028	0.500		0.52549	0.30710	1.7111
	As spun	3	44.5	3.2	15.7		0.044	0.514		0.52092	0.30698	1.6969
	As spun	4	45.1	3.6	15.6		0.052	0.510		0.52416	0.30307	1.7295
	0.57×6.5	3.7	51.1	5.3	16.7	3.4	0.510	0.643	39.41	0.52648	0.30640	1.7182
	1×3	3	47.9	5.4	15.9	3.5	0.346	0.617	39.62	0.52587	0.30490	1.7247
	1×5	5	51.4	5.1	17.1	3.3	0.471	0.637	39.45	0.52688	0.30597	1.7219
	1×6.4	6.4	52.4	5.3	17.1	3.3	0.528	0.632	39.40	0.52731	0.30633	1.7213
	2×3.5	7	49.8	5.3	15.5	3.5	0.433	0.626	39.59	0.52664	0.30594	1.7213
	2×4.5	9	50.3	5.1	15.0	3.4	0.497	0.646	39.44	0.52591	0.30574	1.7201
	2×5.6	11.2	51.1	5.2	18.1	2.6	0.543	0.643	39.67	0.52623	0.30569	1.7214
	3×3.5	10.5	49.6	4.8	15.9	3.0	0.438	0.630	39.32	0.52764	0.30604	1.7240
	3×4.2	12.6	50.3	5.1	16.7	3.3	0.554	0.585	39.68	0.52805	0.30999	1.7034
	3×5	15	51.6	5.1	16.7	2.8	0.555	0.583	39.78	0.52563	0.30879	1.7022
	4×4.4	17.6	50.4	4.9	18.2	3.1	0.535	0.688	39.47	0.52650	0.30740	1.7127

† PAN, [a] VGCNF crystal size from equatorial scan, [b] VGCNF crystal size from meridional scan, § Herman's orientation factor of VGCNF

Comparison of crystal size of fully drawn fiber revealed that higher the spin draw ratio of as-spun fiber, the smaller is the crystal size achieved after hot-drawing (Figure 4.14). Also the crystal size of fully drawn fibers with same SDR decreased with increasing VGCNF content. These observations confirmed strong relation between hot draw ratio and crystal size because the maximum achievable hot draw ratio decreases with SDR[160], and VGCNF content. Crystallinity and crystal size of solution-spun fibers (control and composite) at given spin draw ratio increased as hot draw ratio increased (Figure 4.15).

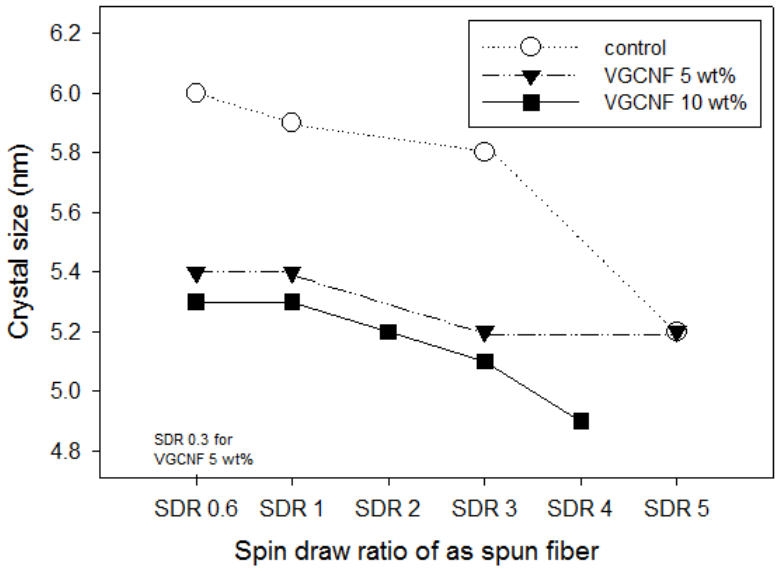

Figure 4.14 Comparison of crystal size of the fully drawn PAN-co-MAA control and the PAN-co-MAA/VGCNF composite fibers with various spin draw ratio. Hot draw ratio of each fiber is same with that listed in Figure 4.11.

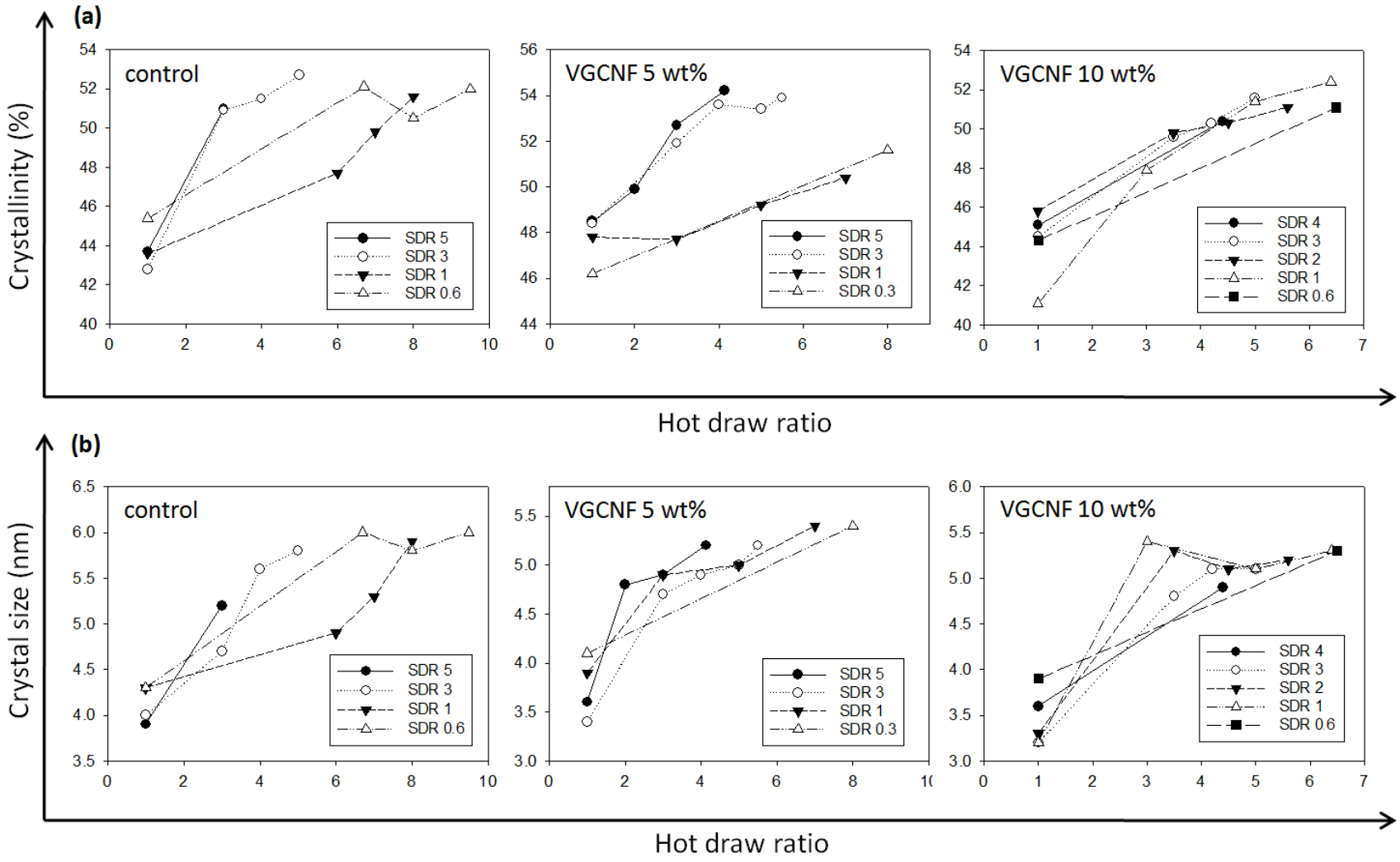

Figure 4.15 (a) Crystallinity, and (b) Crystal size of PAN-co-MAA and PAN-co-MAA/VGCNF fibers at various draw ratios.

4.3.4 Orientation of PAN Crystal and VGCNF

The orientation of PAN is determined by the azimuthal scan at 2θ~17° and that of VGCNF can be obtained from the azimuthal scan at 2θ~26°. However, the azimuthal scan at 2θ~26° also contains intensities coming from PAN (201) and (310,020) crystals. This can be observed in Figure 4.16 (a) and overlap of de-convoluted integrated scans at 2θ~26° as shown in Figure 4.12. Thus, intensities from PAN (201) and (310,020) crystals at 2θ~26° should be subtracted from original azimuthal scan. Figure 4.16 shows (i) original azimuthal scan at 2θ~26°, (ii) intensities from PAN (201) and (310,020) crystals at 2θ~26°, and (iii) corrected Azimuthal scan at 2θ~26° after subtraction azimuthal scan of (ii).

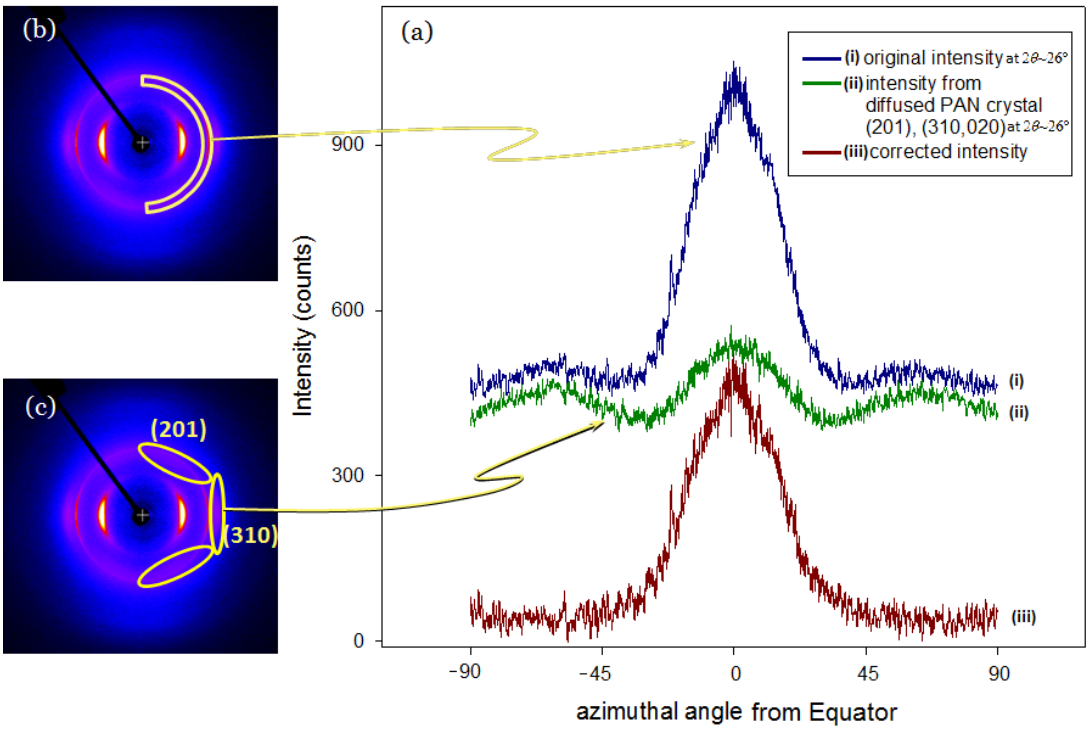

Figure 4.16 (a) Original, and corrected intensity of azimuthal scan for the PAN-co-MAA/VGCNF (1 wt.%) composite fiber (DR=3×5), (b) azimuthal 2D pattern of graphite (002) at 2θ~26º, (c) intensity contribution from diffused PAN crystal (201), (310,020).

The VGCNFs used in this study have double-layer structure as shown in Figure 4.17[136]. The outer graphite layer lies parallel to the VGCNF axis while inner graphite layer forms stacked cup geometry and has angle of between VGCNF axis[136]. As a result, the intensities coming from inner and outer graphite layer are combined in azimuthal scan. The corrected azimuthal scan in Figure 4.16 was de-convoluted into three peaks (Figure 4.18); de-convoluted blue line for outer graphite wall of double layer VGCNF and two green intensities come from inner graphite wall of which direction has angle of 14 degrees between VGCNF axis, which is in good agreement with literature value (11~17°) [136]. The de-convoluted blue line was used for evaluation of Herman's orientation factor of VGCNF (f_{VGCNF}).

Calculated Herman's orientation factor of PAN (f_{PAN}) and f_{VGCNF} are summarized in Table 4.5 and 5.6. The f_{PAN} of as-spun fiber is poor (~0.07), whereas f_{VGCNF} for as-spun fiber is ~0.56 implying that orientation of VGCNF occurs before PAN crystal orientation. The highest f_{PAN} for solution-spun fiber is as high as 0.61 (Table 4.5), whereas that for gel-spun fiber is 0.90 (Table 3.5 in Chapter 3). For solution spun fiber, hot-drawing was performed at lower temperature (100 ℃) as compared to the draw temperature used for gel-spun fiber (170 ℃). Higher drawing temperature above T_g gives enough mobility to the entangled PAN molecules so that they can be drawn to higher draw ratio. Thus, molecular orientation increases along the drawing direction.

Spin draw also contributes to f_{PAN} as shown in Figure 4.19 (a). At the same hot draw ratio, f_{PAN} increased with spin draw ratio (SDR). The Herman's orientation factor of VGCNF (f_{VGCNF}) also increased with SDR and hot draw ratio (HDR) as shown in Figure 4.19 (b). The f_{VGCNF} decreases with increasing the amount of VGCNF loading at given draw ratio as shown in Figure 4.19 (b). This suggests that orientation of VGCNFs is also affected by their concentration, since VGCNF in high concentration has more chance to be restricted in its movement by neighboring VGCNFs.

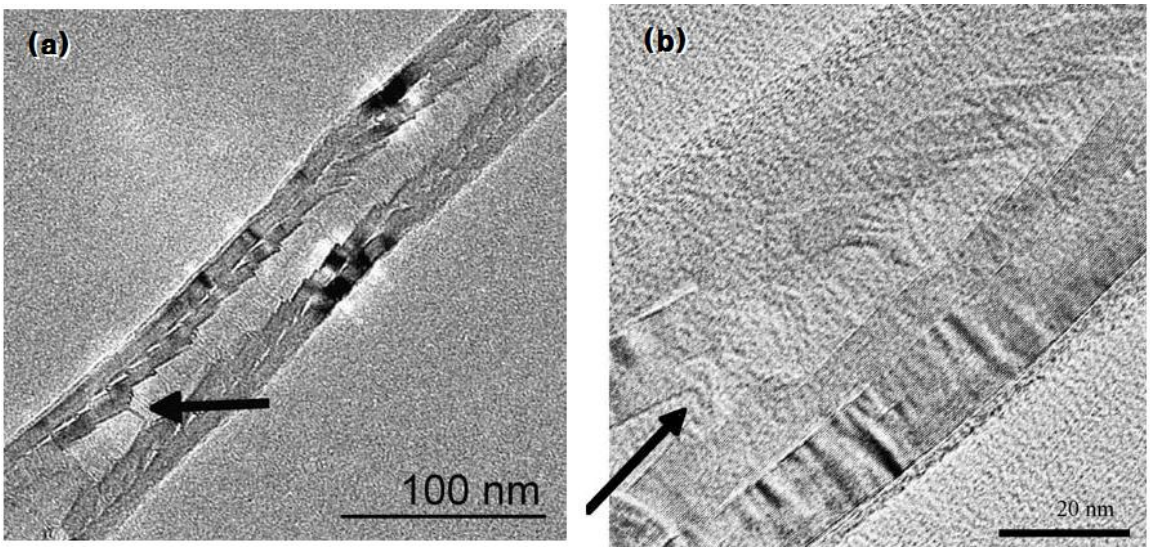

Figure 4.17 (a) Transmission electron micrograph, and (b) high resolution transmission electron micrograph of the double-layer VGCNF [136].

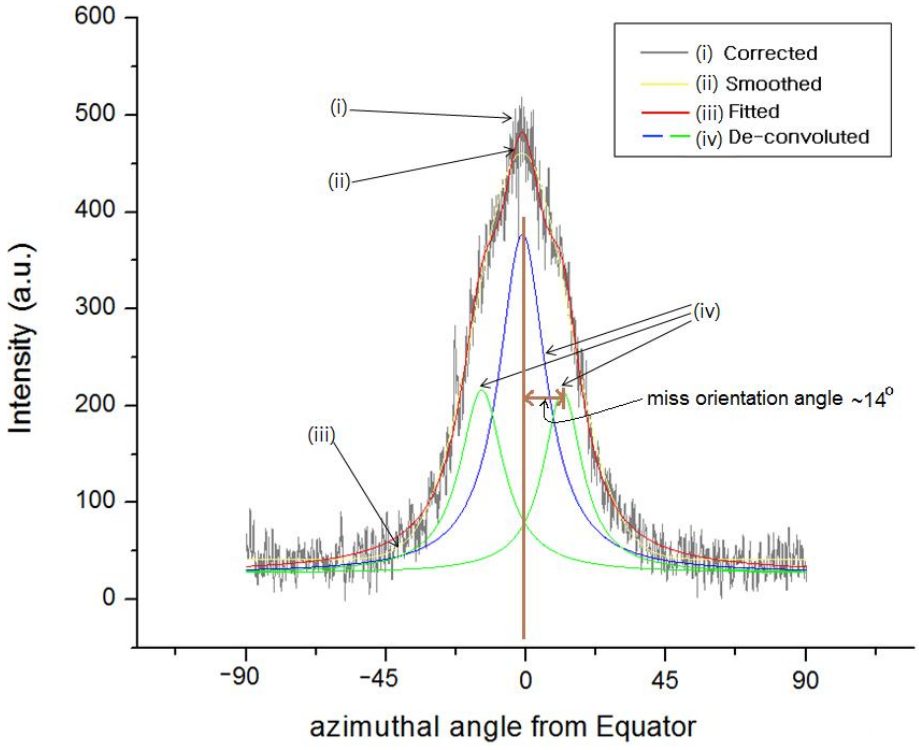

Figure 4.18 Peak fitted corrected azimuthal scan at 2θ~26° (after Figure 4.16).

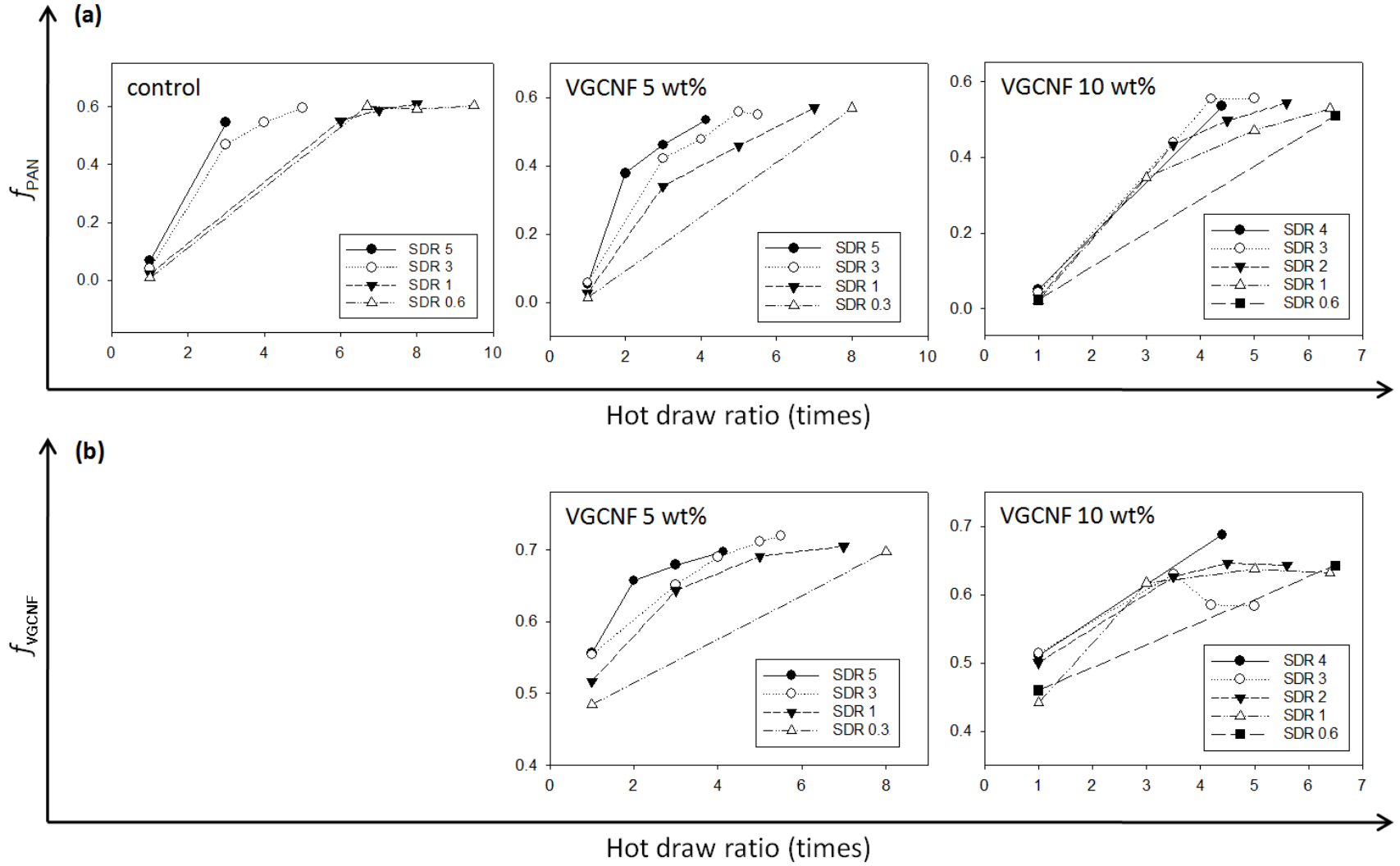

Figure 4.19 Changes in Herman's orientation factor of (a) PAN (f_{PAN}), and (b) VGCNF (f_{VGCNF}) under various drawing conditions.

4.4 Conclusions

The PAN-co-MAA/VGCNF composite fibers exhibit smaller diameter than that of the control fibers, at comparable processing conditions. This is a result of reduced die-swell in the presence of VGCNF. This also implies that good interaction between the PAN-co-MAA molecules and the VGCNF. The mechanical properties of the PAN-co-MAA composite fibers are comparable (at 5 wt.% VGCNF) or slightly lower (at 10 wt.% VGCNF) than the control fibers. Micro-voids observed in the cross-section of composite fiber could be the reason for low mechanical properties of the solution-spun PAN-co-MAA/VGCNF fibers. Mechanical properties of the PAN-co-MAA control, and the PAN-co-MAA/VGCNF (5 wt.%) composite fibers increased with decreasing spin-draw ratio, whereas that of the composite fibers with 10 wt.% VGCNF loading showed opposite trend due to poor fiber drawability. The crystal size of PAN-co-MAA decreased with increasing VGCNF concentration. The *d*-spacing ratio ($d_{2\theta\sim17^\circ}$ / $d_{2\theta\sim30^\circ}$) of the solution-spun PAN-co-MAA fiber was around square root of three (~1.732) regardless of the total draw ratio, whereas that of the gel-spun PAN-co-MAA fiber increased from ~ 1.63 (as-spun fiber) to square root of three (drawn fiber). The new method for evaluation of double-layer VGCNF orientation in composite fibers was developed. In the case of as-spun fiber, the Herman's orientation factors of VGCNF (f_{VGCNF}) is much higher than that of PAN crystal (f_{PAN}) implying that orientation of VGCNF occurs before PAN crystal orientation. For as-spun PAN-co-MAA/VGCNF fiber, PAN orientation (f_{PAN}) increases with increasing spin draw ratio (SDR). At a given hot-draw ratio, f_{PAN} increases with spin draw ratio (SDR) implying that spin-drawing helps PAN molecules align to the fiber axis.

CHAPTER 5

GEL SPINNING OF HIGH MOLECULAR WEIGHT PAN/CNT

5.1 Introduction

To increase the tensile strength of PAN fiber, number of defects across the cross section of fiber should be decreased. Possible defects are foreign particles, voids, chain ends, and entanglement[88]. Number of chain end defects can be reduced by using high molecular weight PAN for spinning[89]. In this study, gel spinning of high molecular weight PAN was attempted to enhance the mechanical properties of precursor fiber.

5.2 Experimental

5.2.1 Materials

Three different polymers were obtained from Japan Exlan, Co.; (i) Polyacrylonitrile (PAN homopolymer, M_w - 7.0×10^5 g/mol), (ii) Polyacrylonitrile-co-Methacrylicacid (PAN-co-MAA; 4 wt.% of MAA content, M_w - 4.7×10^5 g/mol), and (iii) Polyacrylonitrile-co-Itaconicacid (PAN-co-IA; 2 wt.% of IA content, M_w - 5.2×10^5 g/mol). For bi-component spinning, Polymethylmethacrylate (PMMA, M_w – 3.5×10^5 g/mol, Sigma-Aldrich Co. Ltd.) was used as sacrificial shell component which can be removed after spinning. Few walled nanotubes (FWNT: Lot # XO122UA with 2.4 wt.% metallic impurity) were obtained from Carbon Nanotechnologies, Inc. (Houston, TX) and used as received. Dimethylacetamide (DMAc) received from Aldrich co. was purified by distillation before use.

5.2.2 Solution Preparation

Control and composite solution preparation followed the procedure described in Chapter 3. For homopolymer PAN spinning, control solution was prepared at

concentration of 9 g/ 100 mL of DMAc. PAN-co-MAA of 8.5, 9, or 11 g was dissolved in 100 mL DMAc for each trial of spinning with molecular weight of 4.7×10^5 g/mol. Likewise, solid contents of 10, 10.5, and 12 g in 100 mL DMAc solution were prepared for spinning of PAN-co-IA. For bi-component spinning, 30 g of PMMA was dissolved in 100 mL DMAc as sacrificial component solution.

5.2.3 Solution Rheology

Dynamic frequency sweep tests were conducted as described in Chapter 3. Three different solutions are prepared for dynamic rheology study; (i) PAN-co-MAA (2.4×10^5 g/mol, 12.5 g)/DMAc (100 mL), (ii) PAN-co-MAA (4.7×10^5 g/mol, 11 g)/DMAc (100 mL), and (iii) PAN-co-IA (5.2×10^5 g/mol, 11g)/DMAc (100 mL).

5.2.4 Fiber Spinning

Various spinning techniques were combined with gel-spinning to obtain small diameter precursor fibers. The spun fibers were drawn at room temperature, and were subsequently re-drawn at 170 ℃ in glycerol bath.

5.2.4.1 Multi-Filament Spinning

The PAN-co-IA control and the PAN-co-IA/FWNTs composite fibers were spun by utilizing gel spinning using Bradford University spinning unit with seven-hole spinneret. For gel spinning of the PAN-co-IA control fiber, seven-hole spinneret with 250 μm diameter orifice was used. The PAN-co-IA/FWNT composite solution was gel spun by utilizing seven-hole spinneret whose orifice diameter is100 μm.

5.2.4.2 Bi-Component Fiber Spinning

To make small diameter fibers, bi-component spinning with core (PAN-co-IA)-shell (PMMA) geometry was tried using the laboratory scale bi-component spinning equipment manufactured by Hills, Inc. The schematic setup for bi-component spinning is

shown in Figure 5.1. The orifice diameter of spinneret was 250 µm, and temperature of spin block and spinneret was maintained at 110 ℃. The volumetric flow rates of core and shell component were set equally at 1.0 cm^3/min, which is equivalent to the linear jet speed of 40 m/min. The as-spun fiber was immersed into gelation medium (methanol) of which temperature was maintained at - 50 ℃. The air gap between spinneret and gelation bath was maintained at 2 cm. The as-spun fibers were collected on plastic spools at two different speeds, 40, and 120 m/min to achieve spin draw ratio of 1, and 3, respectively. Then the as-spun fibers were preserved in methanol at temperature of - 50 ℃ for 24 hours to ensure gelation. The shell component (PMMA) was removed during the cold-drawing by partially immersing take-up spools in nitromethane.

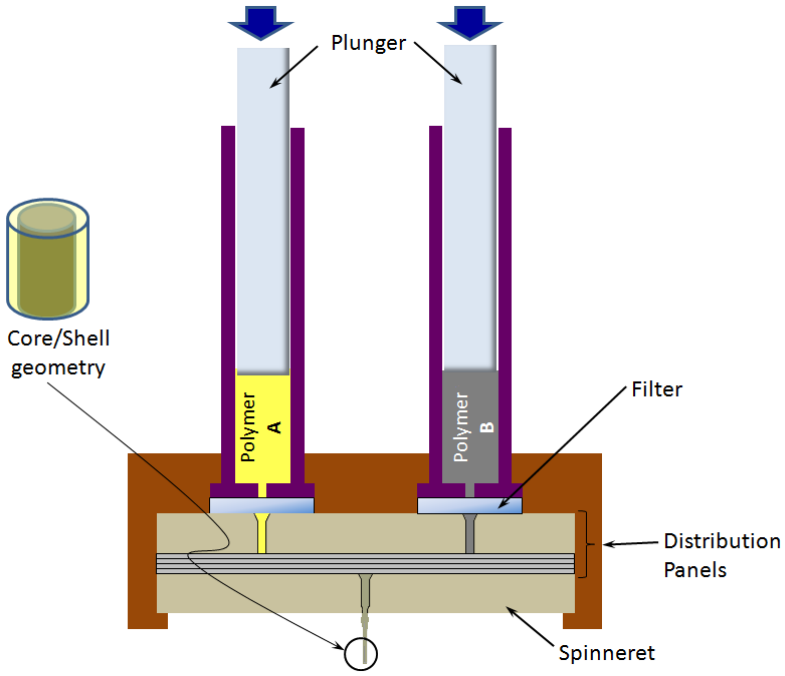

Figure 5.1 Schematics of bi-component spinning.

5.2.4.3 Gel Spinning

Gel spinning of all three high molecular weight PAN was conducted using smaller diameter spinneret (diameter of 120 μm). Other spinning conditions and process parameters are same with what described in Chapter 3.

5.2.5 Characterization of Fibers

The fibers prepared in this study are characterized as described in the previous Chapters 2 and 3.

5.3 Results and Discussion

5.3.1 Dynamic Shear Rheology of High Molecular Weight PAN Solutions

The changes in complex viscosity of various PAN solutions from dynamic frequency sweep test are shown in Figure 5.2. The high molecular weight PAN-co-MAA and PAN-co-IA solutions (4.7×10^5 g/mol, and 5.2×10^5 g/mol, respectively) showed considerable shear thinning behavior as compared to the solution of low molecular weight PAN-co-MAA (2.4×10^5 g/mol). The viscosities of high molecular weight PAN-co-MAA and PAN-co-IA solutions are much higher than that of low molecular weight PAN-co-MAA solutions at lower frequency, and decrease very fast and start to converge with plot of low molecular weight PAN-co-MAA solution. This is in good agreement with high molecular weight solution behavior during solution preparation and spinning; (i) while preparing solution, the viscosity of high molecular weight solution (11 g /100 ml DMAc) was higher than that of low molecular weight (12.5 g/100 mL DMAc). The former needed more time to flow and to drop the same amount of solution from glass rod dipped and taken out of solution. (ii) during spinning, the viscosity of higher molecular weight solution was observed to be lower [pressure value (~8 kgf) on extruding ram at a

given extruding-ram speed was lower than that (~15 kgf) in low molecular weight solution spinning case).

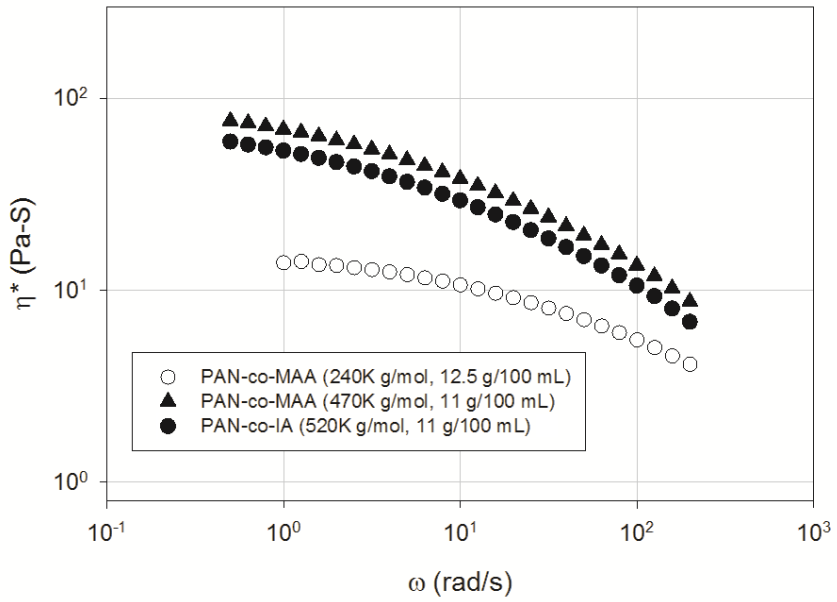

Figure 5.2 Dynamic complex viscosity of various PAN solutions.

5.3.2 Tensile Properties

One of the important issues on gel-spinning of high molecular weight PAN is to determine suitable solution concentration. If the concentration is too low, poor spinning and drawing stability is expected although solution preparation becomes relatively easy due to the lower viscosity. On the contrary, too high concentration of high molecular weight PAN solution makes solution preparation difficult due to its high viscosity and increased number of entanglement will adversely affect mechanical properties of resulting fibers. To find proper concentration of the PAN-co-MAA (4.7×10^5 g/mol) solution, solutions with various concentration levels (8.5, 9, and 11 g/ 100 mL DMAc) were prepared and gel-spun into fibers. The solution with solid content of 8.5 g/100 mL DMAc showed high viscosity during solution preparation (dissolving the polymer and agitating solution). However, during the spinning the pressure on extruding ram was low

(under 10 kgf at 0.5 mm/min of ram speed while 20 kgf was usual for homo-polymer PAN (2.5×10^5 g/mol, 15 g/ 100 mL) under same processing parameters). The maximum draw ratio was pursued for each case. The mechanical properties of these gel-spun fibers are summarized in Table 5.1.

Table 5.1 Mechanical properties of the PAN-co-MAA (4.7×10^5 g/mol) control fibers.

Concentration (g/100 mL)	Drawing conditions†	Diameter (μm)	Strength (GPa)	Strain (%)	Modulus (GPa)	Toughness (MPa)
8.5	1×1.25×4.5	13.5	0.68±0.17	6.9±0.7	16.3±4.1	26±9
9	0.74×1.1×5	13.7	0.60±0.11	7.7±0.5	23.0±5.1	23±5
	0.74×1.1×6	11.9	0.83±0.14	7.3±0.5	17.8±3.1	31±6
11	1×2.1×3.75	11.7	1.06±0.15	7.3±0.4	22.3±3.5	41±8
	3×1.15×4.5	8.4	1.1±0.25	7.6±0.6	22.5±5.5	42±13

120 μm of spinneret orifice diameter, †SDR×CDR×HDR

For the case of 8.5 g/100 mL solution, the fiber couldn't be drawn at higher draw ratio due to frequent fiber breakages during drawing. In general, number of entanglements in as-spun fiber can be reduced by utilizing gel spinning technique, and number of chain ends decreases with increasing molecular weight of polymer[89]. Based on this concept, gel spinning of ultra high molecular weight polyethylene (UHMWPE) was successful to make high strength fiber [178-181]. If number of entanglements is too small, the as-spun fiber cannot withstand drawing condition, due to the slippage of molecules resulting in fiber breakage. The maximum achievable draw ratio and mechanical properties increased with solid content. However, the variation in strength of PAN-co-MAA (4.7×10^5 g/mol) with the highest tensile strength (1.1 GPa) is more than 20% which might be due to micro level inhomogeneity of solution due to the high viscosity.

The mechanical properties of homo polymer PAN (7.0×10^5 g/mol) are summarized in Table 5.2. The throughput ram speed was increased from 0.5 to 1.0 mm/min to maintain the pressure on the thrust ram (plunger) at ~20 kgf, since the extrudate was unstable at 0.5 mm/min ram speed due to low pressure. Considering spinneret size and draw ratio, the diameter of fully drawn fibers is relatively large due to the high throughput rate. Also, tensile strength of these fibers is lower than the predicted value reported in literature [182] as shown in Figure 5.3. Based on these observations, further process optimizations are necessary for fiber spun using high molecular weight PAN.

Table 5.2 Mechanical properties of PAN (7.0×10^5 g/mol) control fibers.

Concentration (g/100 mL)	Drawing conditions[†]	Diameter (μm)	Strength (GPa)	Strain (%)	Modulus (GPa)	Toughness (MPa)
9	3×1.1×5.2	14.7	0.92±0.06	6.8±0.4	21.8±2.2	34±4
	4×1×5.2	8.6	0.95±0.06	6.3±0.4	22.2±1.8	32±4

120 μm of spinneret orifice diameter, [†]SDR×CDR×HDR

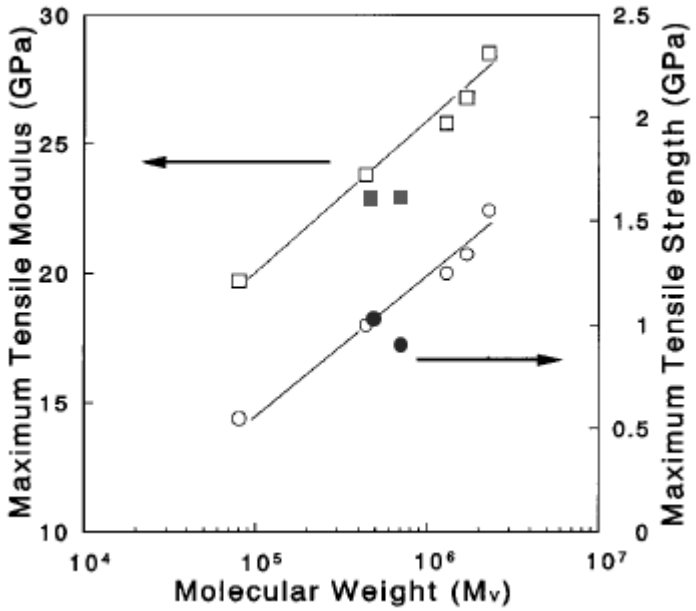

Figure 5.3 Tensile strength and modulus of PAN film drawn from gel state as a function of molecular weight [182]. Mechanical properties of gel-spun PAN fibers are plotted together in solid circle (maximum tensile strength) and solid square (maximum tensile modulus).

Gel-spinning of PAN-co-IA control and PAN-co-IA/FWNT (1 wt.%) composite fibers were conducted with various concentrations and spinning setup. Mechanical properties of gel-spun fibers are summarized in Table 5.3 (control fibers) and 6.4 (composite fibers). Firstly, multi filament (7- hole) spinneret was used. The pressure on extruding ram was higher than 20 kgf and maintained stably due to the high ram speed for delivering solution to each hole. However, the differences in diameter between individual filaments were observed and resulted in large deviation in tensile strength. Secondly, single-hole spinneret with small diameter orifice (120, and 150 μm) was used for spinning. Large diameter (~15.8 μm) fibers were made from the lowest solid content solution, since high throughput rate (ram speed of 1.0 mm/min) was set to maintain the fiber formation due to the low viscosity of solution. The maximum draw ratio of composite fibers was from 12 to 21, whereas the draw ratio for the control fibers ranged

between 6 and 9.7. Lastly, bi-component gel-spinning was performed to produce small diameter fiber. The diameter of the PAN-co-IA/FWNT core component composite fiber was 6.3 ~ 6.7 μm after removing shell component. The improvement of mechanical properties of the high molecular weight PAN-co-IA fibers are expected by process optimization (optimum solid content, dimension of spinneret, draw ratio etc.).

5.3.3 Structural Changes by Processing

To understand the effect of processing parameter on structural changes, the PAN-co-IA/FWNT (1 wt.%) composite fibers with various draw ratio was sampled and characterized using WAXD. As-spun fibers with different spin-draw ratio (SDR) demonstrate positive relation between SDR and *d*-spacing ratio ($d_{2\theta\sim17^\circ}$/ $d_{2\theta\sim30^\circ}$) as shown in Figure 5.4 and tabulated in Table 5.5. The *d*-spacing ratio of fully drawn fibers approached value of $\sqrt{3}$ regardless of SDR implying hexagonal crystal structure. However, *d*-spacing ratio of intermediate (as-spun, or cold drawn) fiber is less than 1.65.

Crystallinity versus total draw ratio plot is shown in Figure 5.5. Crystal size of the fully drawn PAN-co-IA/FWNT (5.2×10^5 g/mol) composite fiber is ca. 11 nm which is smaller than that of PAN-co-MAA (2.4×10^5 g/mol) reported in Chapter 3. At a given draw ratio, crystallinity of PAN in fully drawn fiber may not affected by molecular weight of PAN, since PAN crystal structure in fully drawn fiber is thought to be hexagonal crystal with 2-dimensional order. The Herman's orientation factor (f_{PAN}) of the fully drawn PAN-co-IA fiber is low (~0.81).

The WAXD results of the PAN-co-IA/FWNT (1 wt.%) composite fibers are summarized in Table 5.5.

Table 5.3 Mechanical properties of the PAN-co-IA (5.2×10^5 g/mol) control fibers.

	Concentration (g/100 mL)	Drawing conditions	Diameter (μm)	Strength (GPa)	Strain (%)	Modulus (GPa)	Toughness (MPa)
7 hole (250 μm)	12	2×2.6×6.6	16	1.08±0.27	7.6±1.0	23.1±4.5	42±15
120 μm spinneret	10.5	1×1×6	13.8	0.73±0.20	9.4±2.0	16.3±5.4	43±23
		1.5× 1.4×4.6	10.5	0.78±0.12	6.3±0.4	27.6±3.0	26±6
		1.5× 1×5.4	11.7	0.72±0.12	7.4±0.8	16.0±2.6	30±8
		2×1×4.3	11.1	0.76±0.13	7.4±0.8	16.6±3.5	32±10
		2×1×4.5	10.8	0.82±0.11	7.2±0.7	18.0±2.7	33±8
Bi-component (core/shell)	10	1× 2.1×5.7	13.4	0.73±0.05	6.1±0.4	17.0±1.4	24±3

Diameter of fibers was obtained by measuring weight of fiber of a given length, assuming PAN-co-IA density as ~1.18[183]

Table 5.4 Mechanical properties of the PAN-co-IA (5.2×10^5 g/mol)/FWNT (1 wt.%) composite fibers.

	Concentration (g/100 mL)	Drawing conditions	Diameter (μm)	Strength (GPa)	Strain (%)	Modulus (GPa)	Toughness (MPa)
7 hole (100μm)	12	1×2×4.5	9.3	0.93±0.14	7.2±0.5	22.4±3.7	34±7
Bi-component (core/shell)	12	3×1.15×7.5	6.7	0.86±0.08	7.2±0.6	20.0±1.7	32±4
		3×1.15×8	6.3	0.99±0.16	7.0±1.1	24.6±3.3	38±11
120 μm spinneret	12	2×1.42×5.45	10.7	0.93±0.08	6.7±0.6	23.0±2.1	33±5
		2×1.42×5.66	10.6	0.88±0.05	6.4±0.6	21.0±1.4	30±3
	10	2×1.5×4	15.8	0.94±0.09	7.9±0.6	22.3±2.3	40±6
		2×1.5×7	14.9	0.79±0.10	6.1±0.7	21.7±2.2	25±5
		2×2.5×3	15.5	1.02±0.09	7.5±0.7	23±1.5	41±6
150 μm spinneret	10	0.35×1.2×10	18.6	0.87±0.09	6.5±0.5	21.6±1.1	30±4
		1×1.1×6.7	15.2	0.71±0.11	6.1±0.7	20.1±1.8	25±6
		2×1.3×5	10.1	0.87±0.08	6.2±0.4	20.9±1.3	29±5
		2×1.6×4.4	9.6	0.89±0.08	6.6±0.3	21.0±1.3	30±4

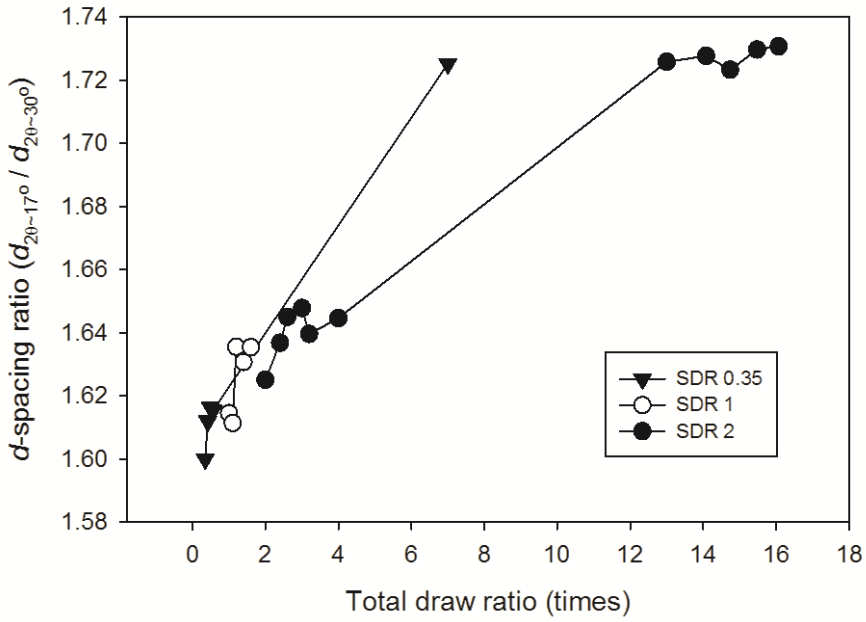

Figure 5.4 Changes in *d*-spacing ratio ($d_{2\theta\sim17^\circ}$/ $d_{2\theta\sim30^\circ}$) of the PAN-co-IA (5.2×10^5 g/mol)/FWNT (1 wt.%) composite fibers as a function of total draw ratio.

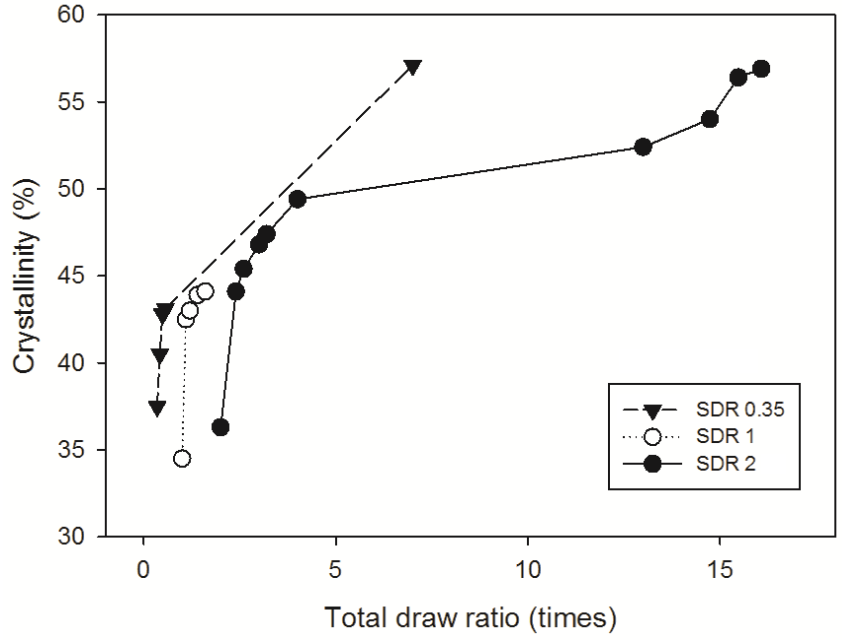

Figure 5.5 Relationship between crystallinity and draw ratio for the PAN-co-IA (5.2×10^5 g/mol)/FWNT (1 wt.%) composite fibers.

Table 5.5 WAXD results of various PAN-co-IA (5.2×10^5 g/mol)/FWNT (1 wt.%) composite fibers.

Drawing conditions	Crystallinity (%)	Crystal size (nm)	f_{PAN} †	$2\theta_{meridional}$ ‡	$d_{2\theta\sim17^\circ}/d_{2\theta\sim30^\circ}$
0.35×1×1	37.5	2.9	0.051	40.08	1.6000
0.35×1.2×1	40.5	3.3	0.141	39.99	1.6120
0.35×1.4×1	42.8	3.3	0.184	39.81	1.6164
0.35×1.6×1	43.1	3.3	0.215	39.81	1.6153
0.35×2×10	57.1	8.8	0.784	39.04	1.7252
1×1×1	34.5	3.2	0.162	40.19	1.6145
1×1.1×1	42.5	3.2	0.152	40.02	1.6114
1×1.2×1	43.0	3.4	0.239	39.99	1.6355
1×1.4×1	43.9	3.3	0.261	39.86	1.6307
1×1.6×1	44.1	3.6	0.291	39.61	1.6354
2×1×1	36.3	3.3	0.105	40.12	1.6251
2×1.2×1	44.1	3.4	0.277	39.72	1.6368
2×1.3×1	45.4	3.4	0.297	39.74	1.6450
2×1.5×1	46.8	3.5	0.302	39.50	1.6478
2×1.6×1	47.4	3.4	0.304	39.69	1.6396
2×2×1	49.4	3.6	0.354	39.63	1.6446
2×1.1×6.7	54.0	9.2	0.764	39.17	1.7233
2×1.3×5	52.4	10.6	0.782	39.27	1.7258
2×1.42×5.45	56.4	10.5	0.791	39.16	1.7297
2×1.42×5.66	56.9	10.9	0.810	39.36	1.7307
2×1.6×4.4	49.1	11.1	0.792	39.23	1.7277

† Herman's orientation factor of PAN, ‡ meridional peak position, $d_{2\theta\sim17^\circ}$ *d*-spacing at 2θ~17°, $d_{2\theta\sim30^\circ}$ *d*-spacing at 2θ~30°

5.3.4 Effect of Heat-Setting

Some of the fully drawn PAN-co-IA/FWNT (1 wt.%) composite fibers were heat-treated and characterized for their mechanical properties to prevent change of structural and mechanical properties after prolonged shelf time as discussed in Chapter 2. No noticeable changes of mechanical properties are observed prior to and after heat-setting (Table 5.6). However, increased crystallinity and reduced crystal size and orientation were observed as listed in Table 5.7.

Table 5.6 Comparison of mechanical properties of the PAN-co-IA (5.2×10^5 g/mol)/FWNT (1 wt.%) composite fibers before and after heat-treatment.

Drawing conditions	Diameter (μm)	Strength (GPa)	Strain (%)	Modulus (GPa)	Toughness (MPa)
2×1.42×5.45	10.7	0.93±0.08	6.7±0.6	23.0±2.1	33±5
Heat setting *	10.7	0.83±0.07	6.8±0.4	21.1±1.5	31±4
2×1.42×5.66	10.6	0.88±0.05	6.4±0.6	21.0±1.4	30±3
Heat setting*	10.4	0.88±0.09	6.7±0.5	21.9±2.4	32±5

* at 100 ℃ for 48 hours

Table 5.7 WAXD results of the PAN-co-IA (5.2×10^5 g/mol)/FWNT (1 wt.%) composite fiber before and after heat-treatment.

Drawing conditions	Crystallinity (%)	Crystal size (nm)	f_{PAN}	$2\theta_{meridional}$	$d_{2\theta\sim17^\circ}$ / $d_{2\theta\sim30^\circ}$
2×1.42×5.66	56.9	10.9	0.810	39.36	1.7307
Heat setting*	62.6	10.3	0.801	38.98	1.7290

* at 100 ℃ for 48 hours

5.4 Conclusions

Dynamic rheological test of the high molecular weight PAN solution showed stronger shear thinning behavior than low molecular weight PAN, suggesting the feasibility of extrusion and spinning, regardless of their high viscosity at low shear rate region. PAN-co-IA (M_w 5.2×10^5 g/mol)/FWNT (1 wt.%) composite fibers with ~1 GPa tensile strength and ~22-23 GPa tensile modulus were obtained. Using bi-component fiber spinning technique with core-shell geometry, small diameter (about 6 μm) PAN-co-IA (M_w 5.2×10^5 g/mol)/FWNT (1 wt.%) composite fibers were obtained and exhibited ~1 GPa tensile strength and ~25 GPa tensile modulus.

CHAPTER 6

INTERPHASE VOLUME FRACTION IN THE COMPOSITE

6.1 Introduction

Efforts have been made to improve the interaction between CNT and matrix by surface modification [101, 184-194]. Also, enhanced mechanical properties which exceed the rule of mixtures were reported due to the development of well order polymer phase in the vicinity of CNTs [122]. This implies expanded interphase due to the templating capability of CNT. Several studies have been reported importance of interphase in the nanocomposite systems [99, 195-204]. The schematic illustrations for interface and interphase are shown in Figure 6.1. In this study, volume fraction of interphase in polymer (PAN) matrix was calculated as a function of interphase thickness, CNT concentration, and diameter. It is expected that this study will give an idea about the quantity of CNT loading required for obtaining the desired structure.

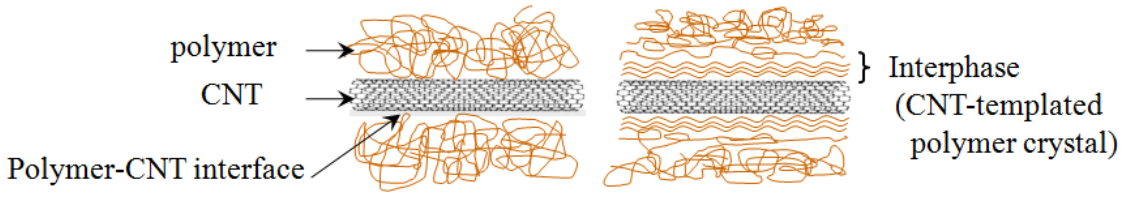

Figure 6.1 Schematic illustration for interface and interphase.

6.2 Experimental

6.2.1 Calculation of Interphase Volume Fraction

Consider interphase thickness (i) between polymer matrix and CNT as shown in Figure 6.1, and then volume of interphase ($V_{interphase}$) is:

$$V_{interphase} = \pi\left\{\frac{\left(\overline{D}_{CNT}+2i\right)^2}{4}-\frac{\overline{D}_{CNT}^2}{4}\right\}\cdot l_{CNT} = \pi\left(i^2+i\overline{D}_{CNT}\right)\cdot l_{CNT} \quad (6.1)$$

where, $\overline{D}_{CNT}$ is average diameter of CNT, l_{CNT} is total sum of all CNT length $\left(l_{CNT}=\sum\left(individual\ \ length\ \ of\ \ CNT\right)\right)$. It is assumed that all CNTs are individually dispersed.

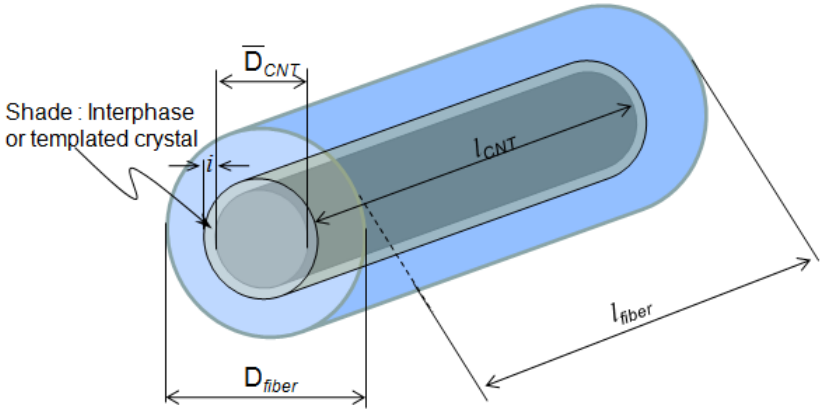

Figure 6.2 Schematic diagram of interphase between polymeric fiber matrix and CNT.

Suppose f_m as mass percent of CNT in polymer matrix, then relation between mass of PAN (M_{PAN}) and that of CNT (M_{CNT}) is:

$$M_{PAN} = \frac{100-f_m}{f_m}M_{CNT} \quad (6.2)$$

The masses of PAN and CNT are:

$$M_{CNT} = \rho_{CNT} \cdot V_{CNT} = \rho_{CNT} \cdot \frac{\pi}{4} \overline{D}_{CNT}^{2} l_{CNT} \tag{6.3}$$

$$M_{PAN} = \rho_{PAN} \cdot V_{PAN} = \rho_{PAN} \cdot \left(\frac{\pi}{4} D_{fiber}^{2} l_{fiber} - \frac{\pi}{4} \overline{D}_{CNT}^{2} l_{CNT} \right) \tag{6.4}$$

where, ρ_{CNT} is density of CNT and V_{CNT} is total volume occupied by CNTs, ρ_{PAN} is density of PAN, V_{PAN} is volume of PAN D_{fiber} is the diameter of PAN/CNT composite fiber, and l_{fiber} is the length of composite fiber, respectively.

Using Eq.(6.3) and Eq.(6.4), Eq. (6.2) can be rewritten as follows:

$$\rho_{PAN} \left(\frac{\pi}{4} D_{fiber}^{2} l_{fiber} - \frac{\pi}{4} \overline{D}_{CNT}^{2} l_{CNT} \right) = \frac{100 - f_m}{f_m} \rho_{CNT} \frac{\pi}{4} \overline{D}_{CNT}^{2} l_{CNT} \tag{6.5}$$

From the Eq.(6.5) total length of CNT can be expressed as given by Eq.(6.6):

$$l_{CNT} = \frac{f_m \rho_{PAN} D_{fiber}^{2}}{\overline{D}_{CNT}^{2} \left[(100 - f_m) \rho_{CNT} + f_m \rho_{PAN} \right]} \times l_{fiber} \tag{6.6}$$

As stated earlier, CNTs have the ability to template crystal structure. For this reason, interphase region between polymer matrix and CNT might affect properties of composite considerbly due to the perfection of the structure. Chae et al.[122] reported enhanced mechanical properties of PAN/CNT composite system due to the crystal structure in the vicinity of CNTs. Crystallinity contribution from PAN crystal templated from CNT can be calculated by volume fraction of interphase in matrix:

$$\frac{V_{interphase}}{V_{PAN}} = \frac{\pi \left(i^{2} + i \overline{D}_{CNT} \right) l_{CNT}}{\frac{\pi}{4} \left(D_{fiber}^{2} l_{fiber} - \overline{D}_{CNT}^{2} l_{CNT} \right)}$$

$$\frac{V_{interphase}}{V_{PAN}} = \frac{4 f_m \rho_{PAN} \left(i^2 + i\overline{D}_{CNT}\right)}{\left(100 - f_m\right)\overline{D}_{CNT}^2 \rho_{CNT}} \text{ by substituting Eq.(6.6)} \quad (6.7)$$

6.2.2 Calculation of CNT-CNT Distance

Average distance between individual CNTs gives the information of room for interphase. To calculate CNT center to center distance, ideal dispersion of CNTs was assumed as shown in Figure 6.3. Also, ideal alignment of CNTs along the fiber direction throughout composite fiber was assumed. Assuming hexagonal arrangement of CNTs of which side length is *a*, and the number of CNTs are *x*, then total number of CNTs are $3x^2+3x+1$. Total area occupied by all CNTs in the fiber cross section is:

$$A_{tot\_CNT} = \frac{\pi \cdot \overline{D}_{CNT}^2}{4} \times (3x^2 + 3x + 1) \quad (6.8)$$

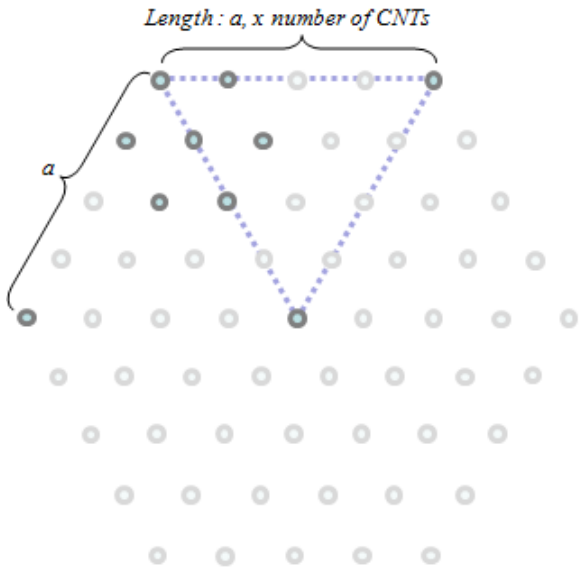

Figure 6.3 Schematic diagram of CNT arrangement in ideal dispersion.

Volume fraction of CNTs in the composite could be preserved as area fraction of CNT in composite for the case of ideal dispersion as stated earlier. So cross-sectional area of composite fiber is:

$$A_{Comp.} = \left(\frac{100}{f_v}\right) \times \frac{\pi \cdot \overline{D}_{CNT}^2}{4} \times (3x^2 + 3x + 1) \tag{6.9}$$

where, f_v is volume % of CNTs in composite.

Consider a hexagonal array shown in Figure 6.3 of which area ($A_{eqv.}$) is equal to cross sectional area of composite fiber, then the side length (a) of hexagon can be expressed as follows:

$$A_{eqv.} = \frac{3\sqrt{3}}{2} \times a^2 = \left(\frac{100}{f_v}\right) \times \frac{\pi \cdot \overline{D}_{CNT}^2}{4} \times (3x^2 + 3x + 1) = A_{Comp.}$$

$$a = \overline{D}_{CNT} \sqrt{\left(\frac{\pi}{6\sqrt{3}} \cdot \frac{100}{f_v}\right)} \times \sqrt{(3x^2 + 3x + 1)} \tag{6.10}$$

Since side of hexagon of length a consists of x number of CNTs, the CNT-CNT distance can be calculated as follows:

$$a/x - 1 = \overline{D}_{CNT} \sqrt{\left(\frac{\pi}{6\sqrt{3}} \cdot \frac{100}{f_v}\right)} \times \sqrt{\frac{3x^2 + 3x + 1}{x^2 - 2x + 1}} \tag{6.11}$$

The number of CNTs (x) is fairly large, so the CNT-CNT distance is given by following expression:

$$\overline{D}_{CNT} \sqrt{\left(\frac{\pi}{6\sqrt{3}} \cdot \frac{100}{f_v}\right)} \times \sqrt{3} \tag{6.12}$$

The relation between the volume percent (f_v) and mass percent (f_m) can be obtained as follows:

$$f_v = \frac{V_{CNT}}{V_{PAN} + V_{CNT}} \times 100 = \frac{\dfrac{M_{CNT}}{\rho_{CNT}}}{\dfrac{100 - f_m}{f_m} \cdot \dfrac{M_{CNT}}{\rho_{PAN}} + \dfrac{M_{CNT}}{\rho_{CNT}}} \times 100$$

$$= \frac{f_m \cdot \rho_{PAN}}{(100 - f_m) \cdot \rho_{CNT} + f_m \cdot \rho_{PAN}} \times 100 \qquad (6.13)$$

By using Eq.(6.13), CNT-CNT distance can be expressed in terms of mass percent as given by Eq.(6.14):

$$\overline{D}_{CNT} \sqrt{\frac{\pi\left[(100 - f_m) \cdot \rho_{CNT} + f_m \cdot \rho_{PAN}\right]}{2\sqrt{3} \cdot f_m \cdot \rho_{PAN}}} \qquad (6.14)$$

6.2.3 Mass Density of CNTs

Mass densities of CNTs are listed in Table 6.1 Density values for MWNTs are obtained by averaging possible values from Table D.1 in Appendix D. The possible values were calculated based on various numbers of walls that may exist for a given outer diameter MWNT. For example, a MWNT with an outer diameter of 4 nm, may possibly contain 2 to 6 possible walls. Density values for such 4 nm MWNTs will vary from 1.09 to 2.06 g/cm^3. The average number density for all possible 4 nm diameter MWNTs is 1.67 nm (see appendix D).

Table 6.1 Average mass density of CNTs.

	SWNT				MWNT						
ϕ_{CNT}* (nm)	1	2	3	4	4	5	6	7	8	9	10
$\overline{\rho_{CNT}}$ (g/cm^3)	1.55	1.01	0.75	0.59	1.67	1.71	1.88	1.88	1.91	1.95	1.97

* diameter of CNT.

6.3 Results and Discussion

6.3.1 Interphase in the Composite System

In the Eq.(6.7), volume fraction of interphase appear to be inversely proportion to diameter of CNT and density at given interphase thickness. However, density of SWNT increases with decreasing its diameter. These two different contributions make it difficult to predict the changes in volume fraction of interphase as a function of SWNT diameter. Figure 6.4 shows various volume fractions of PAN-CNT interphase in matrix as a function of interphase thickness for the case of 0.1 wt.% CNT loading. At a given interphase thickness, the volume fraction of interphase increases with decreasing diameter of SWNT as shown in Figure 6.4 implying that contribution of diameter of SWNT is stronger than that of density for volume fraction increase. For the case of MWNTs, slope of the volume fraction of interphase curves decreases fast with increasing diameter of MWNT, since their density differences between MWNTs of different size are small. Density contribution on volume fraction can be observed by comparing volume fraction curve for SWNT of 4 nm (ρ=0.59) and that for MWNT of identical diameter (ρ=1.97). Volume fraction curve of the former increases more rapidly than the latter due to the low density.

Previously reported high resolution transmission electron microscopy (HR-TEM) of the PAN/SWNT showed well ordered PAN structure (~ 10 nm in thickness) in the vicinity of SWNT. In PAN/CNT composite, the ordered PAN structures surrounding CNT can be regarded as the interphase region between CNT and PAN matrix. Based on the calculations in this study, volume fraction of ordered PAN (interphase) can be 33% (marked in Figure 6.4) by using only 0.1 wt% of SWNT (1 nm diameter) loading when interphase thickness is 10 nm. This implies that significant structural change can be achieved even with low level of CNT loading if fully exfoliated small-diameter SWNTs are used.

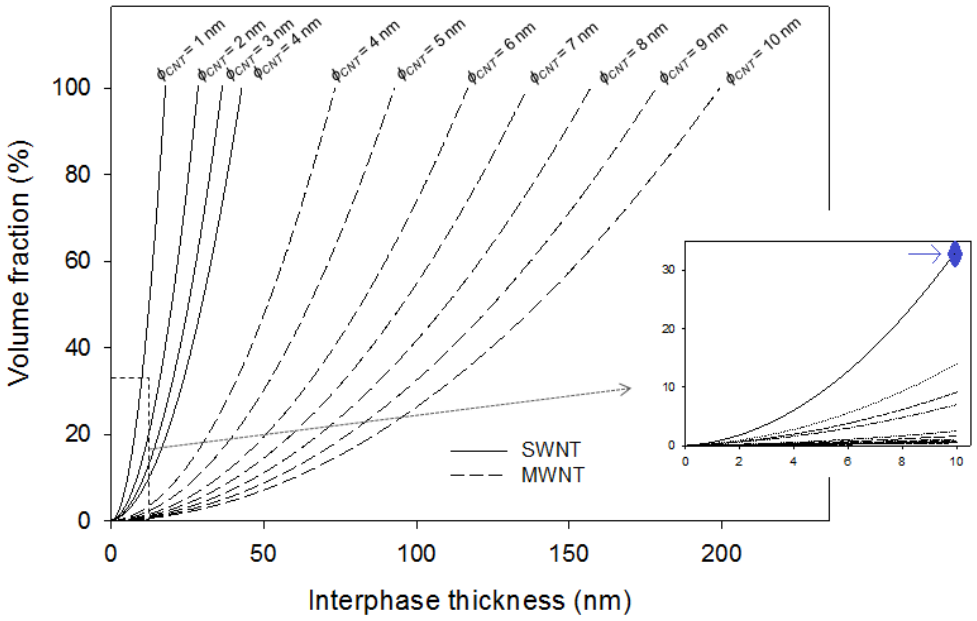

Figure 6.4 Volume fraction of interphase as a function of interphase thickness at 0.1 wt.% of CNT loading.

In previous Chapter 3, ~ 4 nm diameter FWNTs were used as shown in HR-TEM image[80] of Figure 6.5 (a). If all FWNTs are individually dispersed and coated by 10 nm of ordered PAN-co-MAA molecules, about 17% (expressed with diamond mark in Figure 6.5 (b)) of ordered PAN in the vicinity of FWNTs are expected. However, MWNT of 10 nm diameter could contribute less than 5% change of PAN-CNT interphase (express with square mark in Figure 6.5 (b)) when 10 nm thick ordered PAN molecules wrap around MWNTs. This implies that diameter of CNT is the dominant factor for structural evolution of PAN/CNT composite at given CNT concentration. Based on this observation, it is difficult to expect increased crystallinity by templated crystal from large diameter MWNT such as used in Chapter 2 (~53 nm) at 1 wt.% of MWNT loading. Volume fraction curves in boxed area of Figure 6.5 (b) are magnified in Figure 6.6 to clearly compare the curves.

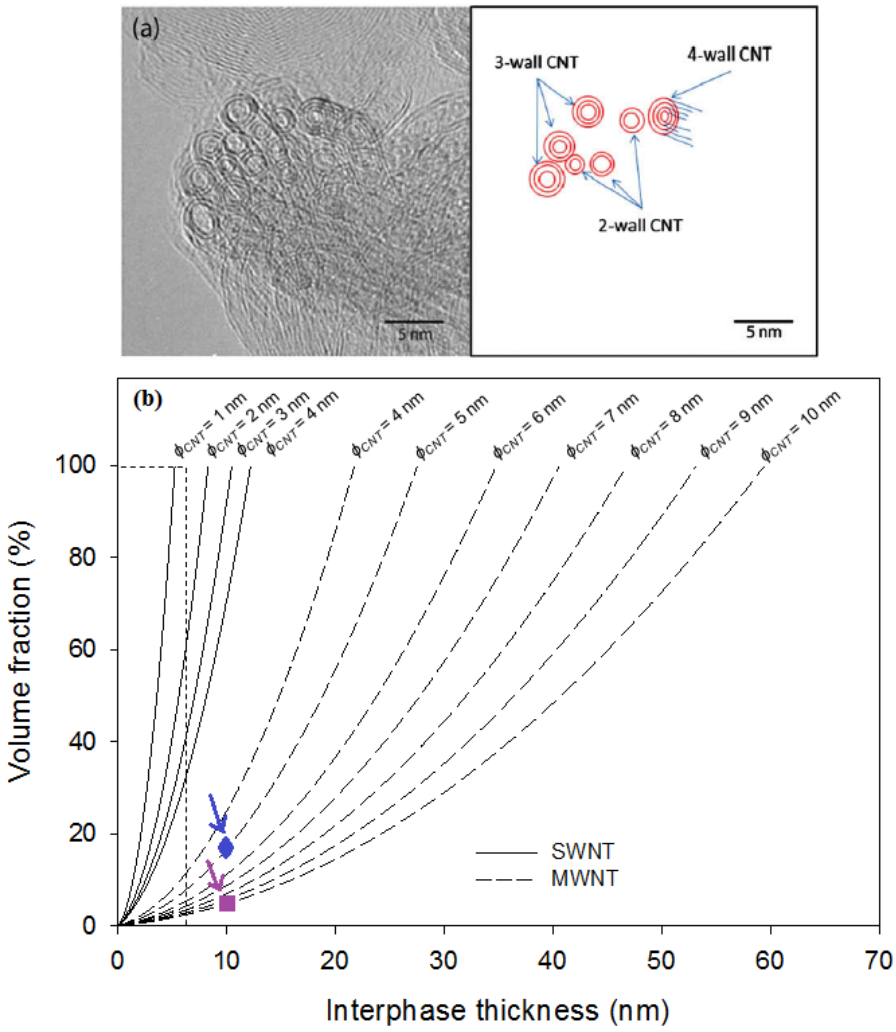

Figure 6.5 (a) HR-TEM micrograph of pristine FWNT with schematic[80] (b) volume fraction of interphase as a function of interphase thickness at 1 wt.% of CNT loading.

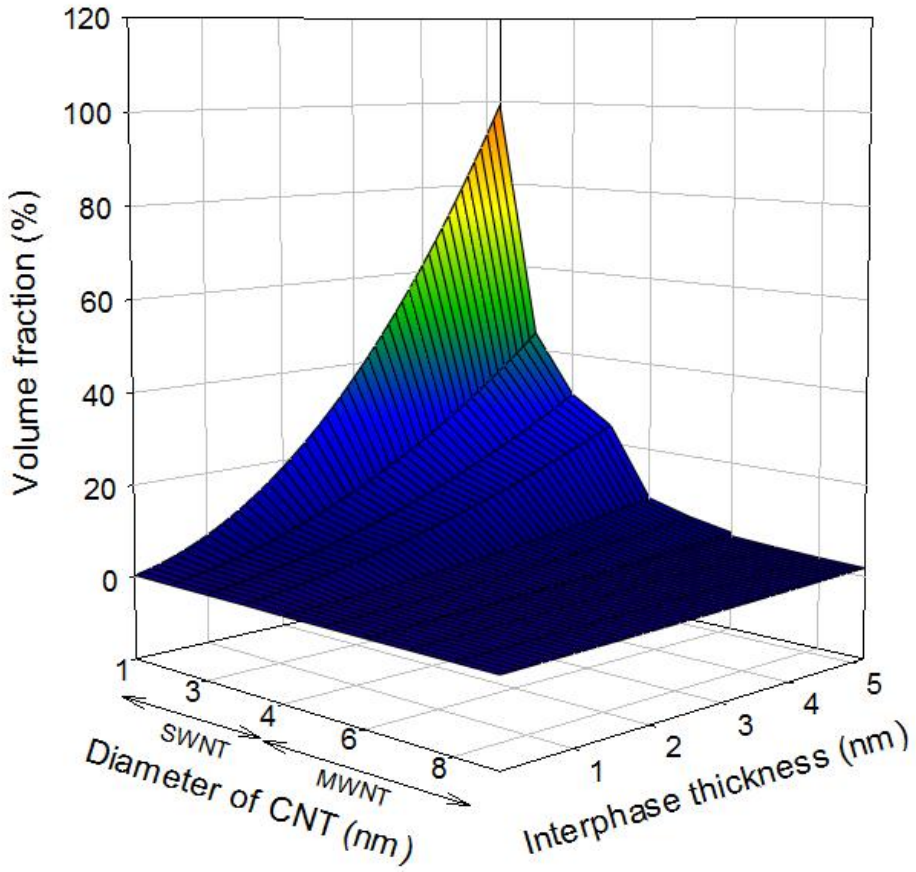

Figure 6.6 Volume fraction of interphase as a function of thickness at 1 wt.% of CNT loading.

The change in crystallinity by templated crystal can be significantly enhanced when 10 wt.% of CNT loading is used, as shown in Figure 6.7. Even with large diameter CNT (~ 10 nm), considerable crystallinity change (> 20%) can be expected when ordered PAN molecules are developed outside of CNT at thickness of 6 nm as expressed in Figure 6.7 with oval mark.

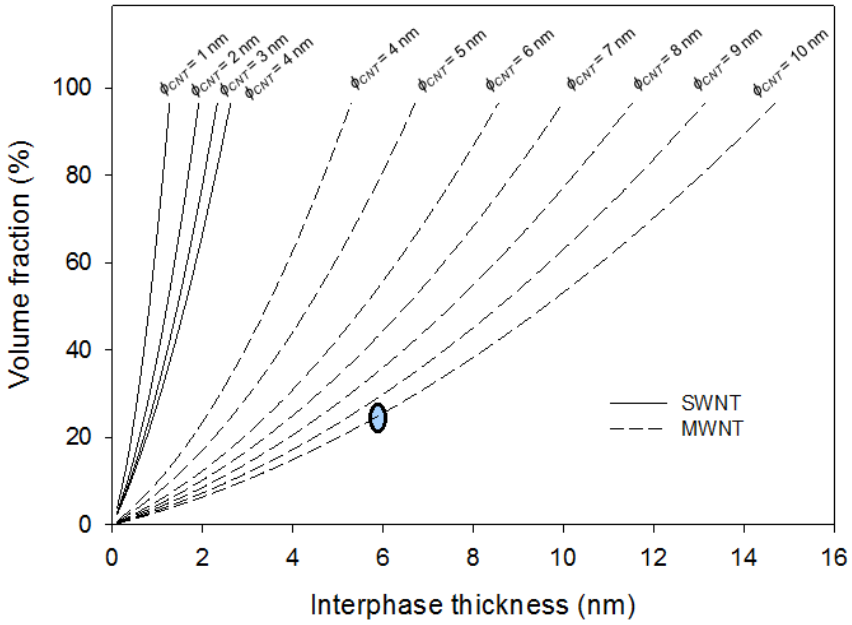

Figure 6.7 Volume fraction of interphase as a function of interphase thickness at 10 wt.% of CNT loading.

6.3.2 CNT-CNT Distance

The average distance between individual CNTs in the ideally dispersed PAN/CNT composite is proportional to the room where PAN molecules can exist. If PAN matrix consists of 100% crystal templated by CNT, then CNT-CNT distance is equal to:

$$\overline{D}_{CNT} + 2i \tag{6.15}$$

Average distance between individual CNTs is calculated by Eq.(6.14) and Eq.(6.15), and is compared in Table 6.2 at various CNT diameters and amount of CNT loading. Each corresponding distances are almost equal in all cases. Calculated distance from Eq.(6.14) is slightly shorter than that from Eq.(6.15) because the former can under-estimate the distance by assuming large number *x* in Eq.(6.11). Well matched results mutually prove both equation (6.14) and (6.15). At given CNT loading, average distance between individual CNTs increases with increasing diameter of CNTs. By adding more CNTs, average CNT-CNT distance decreases as shown in Figure 6.8.

Table 6.2 Comparison of calculated distance between individual CNTs.

		CNT-CNT distance (nm)													
		from interphase calculation (equation (6.15))							from equation (6.14)						
ϕ_{CNT}* (nm) \ wt.%		0.1	0.5	1	2	5	10	20	0.1	0.5	1	2	5	10	20
SWNT	1	36.3	16.2	11.5	8.1	5.1	3.6	2.5	34.5	15.4	10.9	7.7	4.9	3.4	2.4
	2	58.6	26.2	18.6	13.1	8.3	5.9	4.2	55.8	25.0	17.7	12.5	7.9	5.6	4.0
	3	75.4	33.8	23.9	17.0	10.8	7.8	5.6	71.8	32.2	22.8	16.2	10.3	7.4	5.4
	4	89.4	40.0	28.4	20.2	12.9	9.4	6.9	85.1	38.1	27.0	19.2	12.3	8.9	6.6
MWNT	4	150.5	67.3	47.5	33.5	21.1	14.8	10.3	143.3	64.0	45.3	31.9	20.1	14.1	9.8
	5	190.3	85.1	60.1	42.4	26.7	18.7	13.0	181.2	81.0	57.2	40.4	25.4	17.8	12.4
	6	239.4	107.0	75.6	53.4	33.6	23.5	16.3	228.0	101.9	72.0	50.8	32.0	22.4	15.5
	7	279.4	124.8	88.2	62.2	39.1	27.4	19.0	266.0	118.9	84.0	59.3	37.3	26.1	18.1
	8	321.8	143.8	101.6	71.7	45.1	31.6	21.9	306.5	136.9	96.7	68.3	42.9	30.1	20.8
	9	365.8	163.5	115.5	81.5	51.2	35.9	24.8	348.3	155.7	110.0	77.6	48.8	34.1	23.6
	10	408.5	182.5	128.9	91.0	57.2	40.0	27.7	389.0	173.8	122.8	86.7	54.5	38.1	26.4

* diameter of CNT

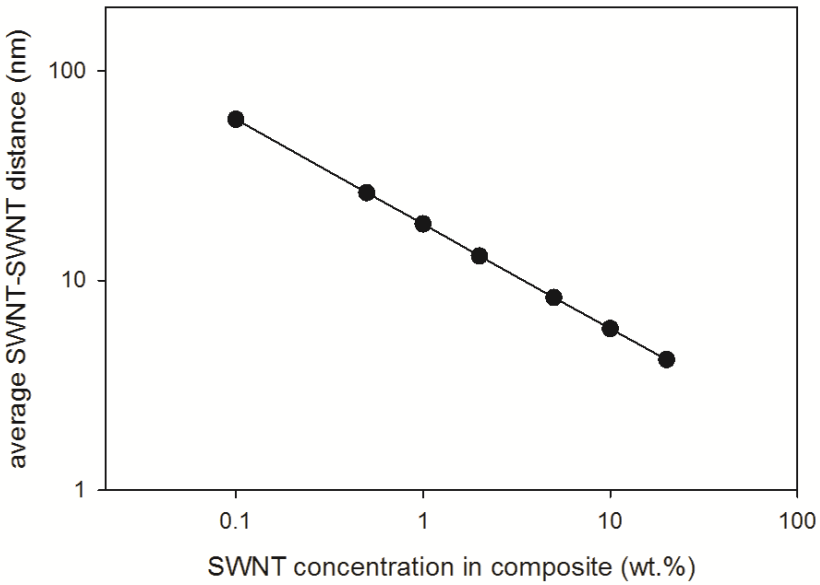

Figure 6.8 Average SWNT-SWNT distance as a function of SWNT (2nm diameter) loading.

6.4 Conclusions

Volume fraction of the PAN-CNT interphase in the composite system was calculated. Calculations show that 6 nm thickness of ordered PAN molecules in the vicinity of 1 nm diameter SWNT can enhance the crystallinity by ~ 13% when only 0.1 wt.% of SWNTs are incorporated in the system. The PAN-co-MAA/~4 nm diameter FWNT (1 wt.%) fibers prepared in Chapter 3 can expect about 10% volume fraction of ordered structure in the vicinity of FWNTs when 6 nm of interphase thickness is assumed. On the other hand, PAN/~53 nm diameter MWNT (1 wt.%) fibers used in Chapter 2 can expect little crystallinity change by MWNT templated PAN crystal structure in the interphase region at thickness of 6 nm due to the large diameter of MWNT.

CHAPTER 7

CONCLUSOINS AND RECOMMENDATIONS

7.1 Conclusions

Interaction between PAN and MWNT enabled the gel-spun PAN/MWNT composite fiber to be drawn to a higher draw ratio (DR=55), than the control PAN fiber (DR=35), resulting in the composite fiber tensile strength value as high as 1.3 GPa. At a given draw ratio, the diameter of PAN/MWNT fiber is smaller than that of PAN fiber, since the elastic recovery (which causes die-swell) of PAN molecule can be reduced in the presence of MWNTs during spinning. After 3 years of shelf-time, significant decrease in tensile strength (about ~16%) of PAN/MWNT composite fiber was observed with deterioration of the PAN structure such as reduced crystallinity (67% of fresh fiber reduced to 56%) and PAN orientation (f_{PAN} became 0.845 from 0.903 of fresh fiber).

Dynamic and steady shear rheological response of gel-spinning solution showed that viscosity and storage modulus of the PAN-co-MAA/FWNT (1 wt.%) composite solution is higher than that of the control solution at low shear rate regime due to the network of FWNTs which contributes to elastic response. On the other hand, at high shear rates, the network of FWNTs can be broken resulting in low viscosity for the composite solution than for the control solution. By introducing cold-drawing process, tensile strength as high as 1.15 GPa was achieved for the gel-spun PAN-co-MAA (M_w: 2.4×10^5 g/mol) control fiber and tensile modulus (31.7 GPa) of the PAN-co-MAA/FWNT composite fibers were improved when compared with fibers prepared without cold-drawing. Cold-drawing process is also responsible for larger crystal size (16.2 nm) and higher degree of FWNT orientation (f_{FWNT}). FWNT orientation (f_{FWNT}) is significantly higher than PAN crystal orientation (f_{PAN}) at early stage processes implying

that the alignment of FWNT along fiber axis occurs prior to the orientation of PAN crystal. Continuous stabilization and carbonization of single filament of PAN-co-MAA was demonstrated.

The solution-spun PAN-co-MAA/VGCNF composite fibers exhibited smaller diameter compared to control fibers produced under the comparable processing conditions. This is consistent with diameter observation of gel-spun fibers. The *d*-spacing ratio ($d_{2\theta\sim17^\circ} / d_{2\theta\sim30^\circ}$) of the solution-spun PAN-co-MAA fiber is around square root of three (~1.732) regardless of total draw ratio, whereas that of the gel-spun PAN-co-MAA fiber increases from ~ 1.63 to square root of three with increasing total draw ratio. The new method for evaluation of double-layer VGCNF orientation was developed. For as-spun fibers, f_{VGCNF} is higher than f_{PAN} , implying that orientation of VGCNF lead that of PAN crystal. PAN orientation (f_{PAN}) for as-spun PAN-co-MAA/VGCNF fiber increases with increasing spin draw ratio (SDR). At a given hot-draw ratio, f_{PAN} also increases with increasing SDR implying that spin-drawing helps PAN molecules align to the fiber axis. On the other hand, hot-draw ratio decreases with increasing SDR. For fully drawn fibers, the mechanical properties increased with decreasing spin-draw ratio, due to the higher hot-draw ratio.

Dynamic rheological test of the high molecular weight PAN solution showed stronger shear thinning behavior than low molecular weight PAN solution. Small diameter (~6 μm) PAN-co-IA (M_w 5.2×10^5 g/mol)/FWNT (1 wt.%) fibers with tensile strength of ~1 GPa and tensile modulus of ~25 GPa were prepared by utilizing bi-component spinning technique.

Volume fraction of PAN-CNT interphase in PAN matrix was calculated. Calculations predict that incorporation of only 0.1 wt.% of 1 nm diameter SWNT can increase crystallinity by ~13% when ordered PAN phase of 6 nm thickness are developed in the vicinity of SWNTs.

7.2 Recommendations

1. Changes in structure and properties of the gel-spun PAN fiber as a function of shelf-time were observed (Chapter 2). To avoid these changes, heat-setting methods of the fully drawn PAN fiber should be developed and optimized. The optimization of heat setting conditions will include heat treatment temperature, time, and applied tension.

2. Gelation condition is important to improve perfection of crystal structure of PAN and to minimize defects. Limited studies of evaluation for the gelation temperature of PAN solution were presented in Appendix A. Further systematic study is required under the consideration of various parameters such as polymer molecular weight, polymer concentration (solid content), temperature, cooling rate, and types of gelation medium.

3. Preparation of homogeneous high molecular weight PAN solution is challenging, due to the high viscosity of the solution under a low shear rate process such as stirring, and agitating. High shear mixing method should be developed for high molecular weight solution preparation.

4. The reliability of carbon fiber in mechanical properties is an important issue for composite application. The degree of scatter in tensile strength of carbon fiber prepared in this study was evaluated using Weibull model (Appendix C). Correlating the Weibull modulus of carbon fiber and its structure will support validity of this model. For structure characterization, HR-TEM and small angle X-ray scattering (SAXS) studies are needed to evaluated defect in carbon fiber.

5. Continuous stabilization and carbonization of single filament was demonstrated in Chapter 3, yet needs further process optimization. In this respect, further investigation should be carried out on time (residence time in heating zone), temperature, and tension during stabilization and carbonization and resulting carbon fiber structure and properties.

APPENDIX A

OBSERVATION OF GELATION BY MONITORING RHEOLOGICAL RESPONSE OF POLYMER SOLUTION

A.1 Introduction

During the gel spinning, PAN polymer solution immersed into quenching bath turns gel-like state which is thermo-reversible network structure formed by three dimensional physical bonds. These physical bonds can be broken by increasing temperature [205] due to the low energy level as compared to chemical bonds. Possible reasons for reversible gelation are: (i) rapid crystallization, (ii) changes of polymer solution such as increasing concentration, growing the molecular weight, or cooling, and (iii) change of solubility in polymer solution by adding non-solvent or quenching. In this study, dynamic rheology was used to determine gelation temperature whether gel-like state during gel-spinning is ascribed to rapid cooling, since dynamic rheology is suitable and powerful tool to monitor the change of cross-linking and microstructure [206-212].

A.2 Experimental

Polymer solutions used in this study were prepared as described in Chapter 2. Solid content of the PAN-co-MAA (5.0×10^5 g/mol)/DMAc solution was set as 10 g/100 ml in DMAc. Temperature sweep tests were conducted using ARES rheometer (Rheometric Scientific, Co.) with parallel plate geometry (25 mm of plate diameter and 1 mm of gap between plates). Temperature was decreased from room temperature to -50 ℃ at a cooling rate of -5 ℃/min. The angular frequency (ω) was fixed as 100 rad/s with strain of 5% after temperature-frequency sweep test.

A.3 Results and Discussion

Temperature sweep of complex viscosity results with various spinning solution used in Chapter 2 and 4 are shown in Figure A.1. If gel-like state of solution at the stage of spinning exclusively caused by quenching(low temperature) then abrupt changes in rheological response should be observed by temperature sweep test[207].

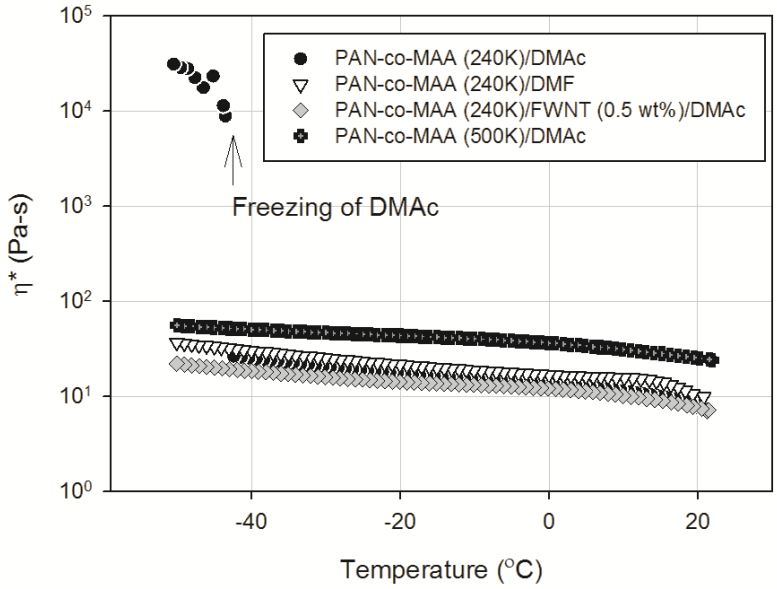

Figure A.1 Complex viscosity of the PAN-co-MAA solutions as a function of temperature.

PAN-co-MAA (2.4×10^5 g/mol) /DMAc solution showed rapid shooting of complex viscosity at the temperature below -43 ℃. However, this sudden increase was not caused by gelation of solution but caused by frozen DMAc whose freezing temperature is -4 ℃. This was confirmed by changing the solvent from DMAc to DMF whose freezing temperature is -61 ℃. Complex viscosity of the PAN-co-MAA (2.4×10^5 g/mol) /DMF solution increases gradually as temperature goes down (blank triangle in Figure A.1). Freezing of DMAc was not observed when small amount (0.5 wt.%) of carbon nanotubes was added in polymer solution even at -50 ℃ (grey diamond in Figure A.1). PAN-co-

MAA (5.0×10^5 g/mol) /DMAc solution didn't show swift viscosity change caused by gelation even though the more entanglements are expected by the higher molecular weight. Nonetheless, PAN-co-MAA (5.0×10^5 g/mol) /DMAc solution didn't show freezing of DMAc.

Loss factor (tan δ) of various solution, plotted in Figure A.2, shows that tan δ decreased monotonously as decreasing temperature except for the PAN-co-MAA (2.4×10^5 g/mol) /DMAc due to frozen of DMAc.

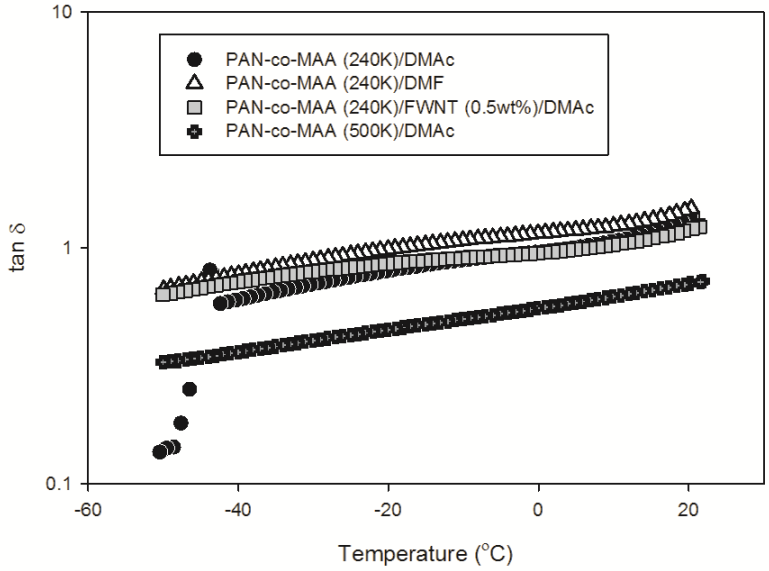

Figure A.2 Loss factor (tan δ) of PAN-co-MAA solutions as a function of temperature.

Figure A.3 shows storage and loss moduli of various solutions. The PAN-co-MAA (2.4×10^5 g/mol) polymer dissolved in DMAc also showed same crossover temperature of 8 ℃ regardless of carbon nanotubes, whereas crossover temperature of -19 ℃ was observed for same polymer dissolved in DMF. For the case of PAN-co-MAA (5.0×10^5 g/mol) /DMAc solution showed higher storage modulus compared to lower molecular weight polymer (2.4×10^5 g/mol).

Based on these observations, it is concluded that quenching of PAN polymer (M_w ~ 5.0×10^5 g/mol) to -50 ℃ in the rheometer does not result in instantaneous gel-

formation. However, what role methanol plays in the gel formation is not clear from this study.

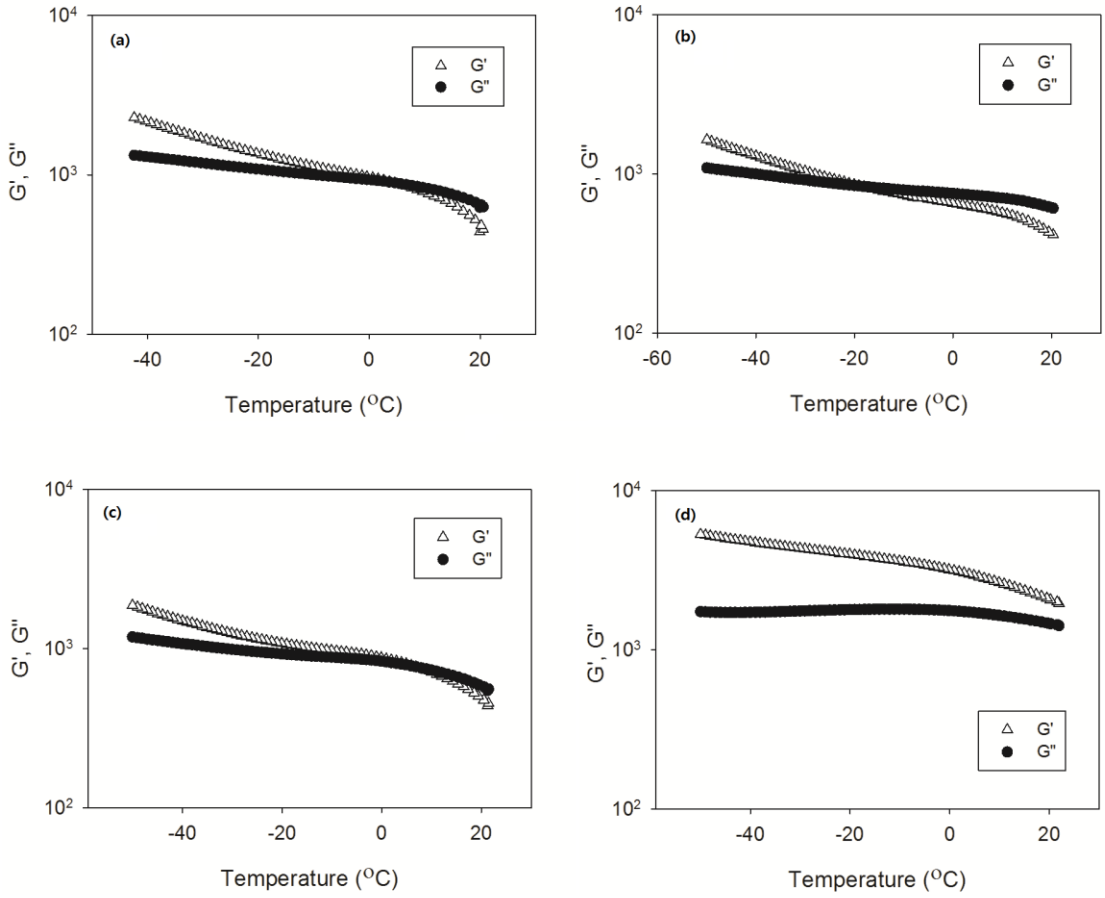

Figure A.3 Storage and loss moduli of (a) PAN-co-MAA (2.4×10^5 g/mol) /DMAc, (b) PAN-co-MAA (2.4×10^5 g/mol) /DMF, (c) PAN-co-MAA (2.4×10^5 g/mol) /FWNT (0.5 wt.%)/DMAc, and (d) PAN-co-MAA (5.0×10^5 g/mol) /DMAc solution as a function of temperature.

APPENDIX B

CALCULATION OF APPARENT SHEAR RATE OF SPINNING

Apparent shear rates at various spinning conditions used in this study are calculated. In general, Hagen-Poiseuille equation is widely used for shear rate calculation of cylindrical geometry such as spinning and capillary rheometer[156].

$$\dot{\gamma}_w = \frac{4Q}{\pi R^3}$$

where $\dot{\gamma}_w$ is wall shear rate of spinneret, Q is flux across the spinneret, R is radius of spinneret orifice. Q is proportion to extruding ram speed and diameter of reservoir. Diameter of reservoir used in this study was 28 mm. Two different orifice size used for calculation are 120, and 250 μm, respectively. Calculated shear rates are summarized in Table B.1 and actual spinning conditions are expressed in bold letter and underlined.

Table B.1 Shear rates at various spinning speed.

Extruding ram speed (mm/min)	250 μm spinneret		120 μm spinneret	
	Linear jet speed (m/min)	Shear rate (1/s)	Linear jet speed (m/min)	Shear rate (1/s)
0.5	**6.3**	**3345**	**25.1**	**26761**
1	12.5	6690	50.2	53521
1.5	18.8	10035	75.3	80282
2	25.1	13380	100.4	107042
2.5	31.4	16725	125.4	133803
3	37.6	20070	150.5	160563
3.5	43.9	23415	175.6	187324
4	50.2	26761	200.7	214084
4.5	56.4	30106	225.8	240845
5	62.7	33451	250.9	267605
5.5	69.0	36796	276.0	294366
6	**75.3**	**40141**	301.1	321126
6.5	81.5	43486	326.1	347887
7	87.8	46831	351.2	374647
7.5	94.1	50176	376.3	401408
8	100.4	53521	401.4	428169
8.5	106.6	56866	426.5	454929
9	112.9	60211	451.6	481690
9.5	119.2	63556	476.7	508450
10	125.4	66901	501.8	535211

APPENDIX C

STATISTICAL ANALYSIS OF DEVIATION IN TENSILE STRENGTH OF CARBON FIBERS: WEIBULL MODEL

C.1 Introduction

Carbon fibers have been extensively used as reinforcing materials [213-220]. The evaluation of scatter in mechanical strength of carbon fibers is important to estimate the reliability of them [221-225]. The Weibull model is widely used for evaluation of the reliability for brittle materials [226-229]. In this study, variations in mechanical properties, especially tensile strength, were evaluated and factors that affect distributions in tensile strength were investigated using the Weibull model. The carbon fibers used for the evaluation of reliability are listed in Table C.1.

C.2 Results and Discussion

C.2.1 Weibull Modulus

The tensile strength data of brittle materials has shown a wider degree of scatter in comparison to ductile materials. This scatter in tensile strength has turned out to have a well-known empirical relationship proposed by Weibull [226].

$$P = 1 - \exp\left\{ - \int_X \left(\frac{\sigma - \sigma_u}{\sigma_o} \right)^m dX \right\} \tag{C.1}$$

where P is the probability of failure at a stress of σ, m is known as Weibull modulus (Weibull shape parameter), σ_u is the threshold stress below which probability of failure is zero, σ_o is the Weibull scale parameter (characteristic stress at which 1/e, i.e. 37% of the

Table C.1 Heat-treatment conditions of carbon fibers and properties of the corresponding precursor fibers.

	Section covering the fiber	C.2.2	C.2.3	C.2.4	C.2.5 set 1	C.2.5 set 2	C.2.5 opt[c]
Precursor Fiber	Polymer M_w ($\times 10^3$ g/mol)	240	250	250	250	250	250
	co-monomer used	MAA[a]	None	None	None	None	None
	CNT	None	MWNT	MWNT	SWNT[d]	SWNT[d]	FWNT
	Draw ratio	9.5	55	55	15	15	29
	Diameter (μm)	21.5	10.4	10.4	9.0	9.0	7.4
	Tensile strength (GPa)	1.11	1.12	1.34	0.94	0.94	1.1
	Tensile modulus (GPa)	23	23	26	25	25	26
	Elongation at break (%)	9.0	7.4	8.5	8.3	8.3	8.0
Stabilization conditions	1st temperature (℃)	Specified in Table 3.1. and C.3	285	285	285	285	285
	1st duration time (min)		120	270	300	300	45
	1st heating rate (℃/min)		5	5, 1	1	1	5
	2nd temperature (℃)		320	330	330	330	330
	2nd duration time (min)		20 ~ 45	120	60	60	60
	2nd heating rate (℃/min)		5	1	1	1	5
	Tension (MPa)		22	5 ~ 30	25	20	35
Carbonization conditions	Temperature (℃)	1100	1100	1100	1100	1100	1300
	Duration time (min)	10	5	5	5	5	5
	Heating rate (℃/min)	N/A	5	5	5	5	5
	Tension (MPa)	1.3 gf[b]	22	5 ~ 30	25	20	9

[a] Methacrylic acid, [b] gram force, [c] optimized condition, [d] obtained from Carbon Nanotechnologies, Inc. (Houston, TX)

samples survive), and *X* is the strength-confining dimension (e.g. length of the fiber specimen). Normally, the value of σ_u is taken to be zero. For the case of fibers, Eq.(C.1) can be rewritten in the form of a two parameter model as [223, 230]:

$$P = 1 - \exp\left\{-\left(\frac{\sigma}{\sigma_o}\right)^m\right\} \tag{C.2}$$

The greater the material's value of *m*, steeper is the transition from survival to failure indicating higer reliability, as shown in Figure C.1.

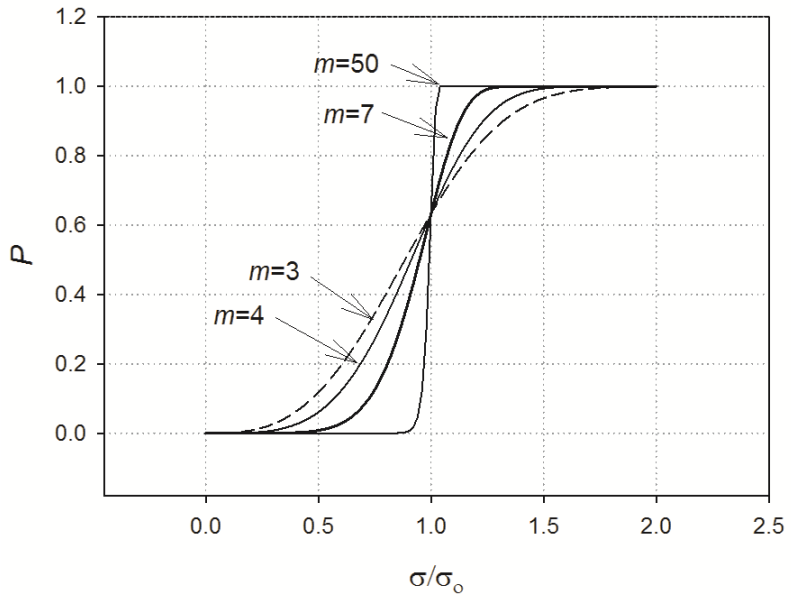

Figure C.1 Weibull distribution for the probability of failure with various Weibull moduli.

If a material shows large scatter in strength between samples, it is expected to have a low *m* value and poor reliability against stress failure due to unevenly existing flaws. On the other hand, high value of *m* reflects low deviation in measured strength, resulting in high reliability of the material in strength. Practically, the probability of failure, *P*, can be

obtained by the mean rank method (ranking data from smallest to largest value and assigning *P* values) as described elsewhere [224, 228]:

$$P = \frac{i}{N+1} \tag{C.3}$$

where *i* is the rank and *N* is the total number of specimens.

Finally, the linear form of Weibull statistical distribution can be obtained by applying natural logarithms to Eq.(C.2):

$$\ln\left[\ln\left(\frac{1}{1-P}\right)\right] = m\ln\sigma - m\ln\sigma_o \tag{C.4}$$

Weibull modulus (*m*) and Weibull scale parameter (σ_o) can be obtained by linear regression from the Weibull plot of Eq.(C.4).

C.2.2 Effect of Stabilization and Carbonization Processes on Weibull Modulus

Weibull moduli of the stabilized and carbonized PAN-co-MAA control fibers are summarized in Table C.2. The mechanical properties can be found in Tables 3.9 and 3.11.

Table C.2 Weibull moduli of PAN-co-MMA fibers (DR=$1\times2.7\times3.5$) after various heat-treatments.

	Stabilization[a] step						Carbonization[a] temp. (℃)			
	1st	2nd	3rd A	3rd B	3rd C	4th	600[b]	600[c]	800	1100
m	5.4	12.0	7.8	10.7	12.3	15.6	3.7	5.4	5.9	7.6
R^2	0.970	0.970	0.967	0.979	0.884	0.946	0.879	0.969	0.883	0.958

[a] processing conditions are listed in Table 3.1, 3.9, 3.11, and C.3, [b] carbonization subsequently done after 3rd C step, [c] carbonization subsequently done after 4th step

Table C.3 Stabilization conditions for 3rd step optimization.

Stabilization step	Temperature (℃)	Residence time (min)	Stretching (%)	Pretension (gf)
3rd A	300	30	0	1.6
3rd B	330	43	0	1.6
3rd C	330	50	0	1.6

Pan et al.[230] showed that polymeric fibers can also be specified by the Weibull model. In his work, the Weibull moduli of polymeric fibers ranged from 12.7 to 17.5 depending upon types of polymer. The Weibull modulus of the PAN-co-MAA precursor fiber was 15.2, which is in good agreement with literature[230]. After the 1st stabilization process, the Weibull modulus became 5.4, implying structural deterioration in the fiber due to cyclization. Structure of the stabilized fibers after 1st step of stabilization is thought to be a mixture of PAN and cyclic molecules, as seen from FT-IR (Figure 3.21) and WAXD (Figure 3.20) studies. Distribution of this mixed structure causes wider scatter in tensile strength. Cyclization of PAN could not be completed at the given temperature (285 ℃) and residence time (7.5 min); the data shows that the incomplete cyclization process leads to a lower Weibull modulus in comparison with the precursor fibers. As the stabilization step progresses, PAN molecules are almost completely converted to ladder structure and the Weibull modulus increases, as shown in Figure C.2 (a). On the other hand, under-stabilized fibers (3rd A, and 3rd B) showed relatively lower *m* value, as shown in Figure C.2 (b). The *m* value of the 2nd step finished fiber (12.0) decreased with the subsequent heat-treatment 3rd A (7.8) or B (10.7). Various conditions used for optimization of the 3rd step stabilization are listed in Table C.3. Based on FT-IR spectra (Figure 3.21) and WAXD (Figure 3.20) results, 3rd C conditions were chosen for

3rd step stabilization; these fibers showed a high Weibull modulus (12.3), implying more uniform structure.

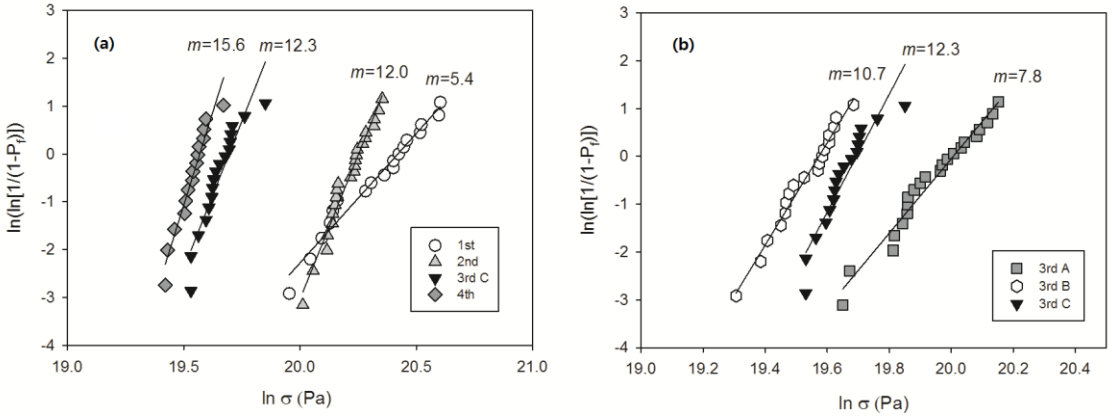

Figure C.2 Weibull plot for (a) various stabilized fibers (b) stabilized fibers after 3rd step optimization.

For carbon fiber cases, the *m* values increase with heat-treatment temperature, as shown in Figure C.3 and Table C.2. Considerable changes in the Weibull modulus were observed upon carbonizing the stabilized fibers: (i) *m* of stabilized fibers from step 3rd C decreased from 12.3 to 3.7 after carbonization at 600 ℃ and (ii) heat-treatment at 600 ℃ leads to a drop in Weibull modulus from 15.6 to 5.4 for stabilized fibers that experienced 4th step stabilization. The highly reduced *m* value implies structural deterioration in the fibers. It can be noted that the lower *m* valued stabilized fibers resulted in lower Weibull modulus of carbon fiber after heat-treatment. This can be supported by comparing the changes of *m* in (i) and (ii). It can be thought that flaws generated in prior processes, such as micro pores, damage on surface, and imperfection of structure, are preserved after heat-treatment and cause this lower value of *m*. The Weibull modulus of carbon fiber (CF) treated at 1100 ℃ (7.6) is somewhat larger when compared to that of the commercial grade CF (5.9 : Toray T-1000GB[224]). In this study, mono filament was used for heat-treatment. This excludes the deviation of tensile strength between filaments and could be the reason for the good *m* value in present study.

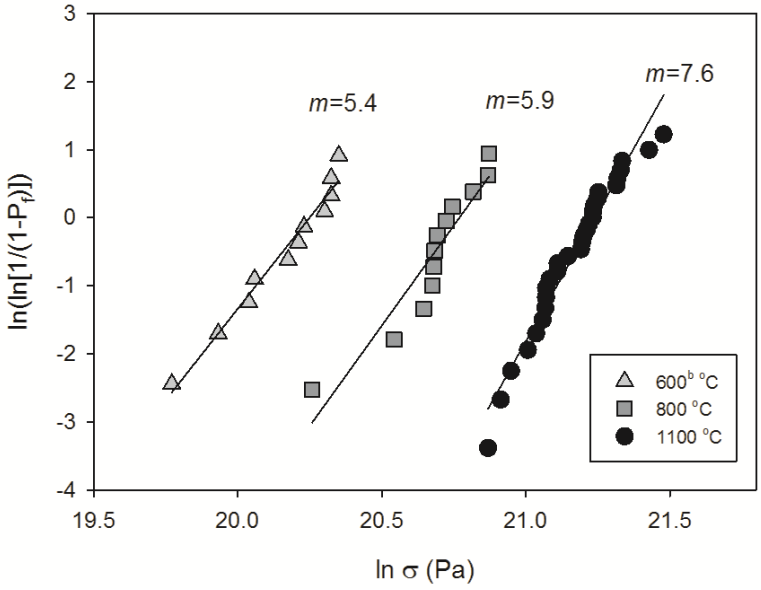

Figure C.3 Weibull plot for Carbon fibers heat-treated at different temperatures.

C.2.3 Effect of Stabilization Time

The effect of stabilization time on the statistical distribution of tensile strength (TS) was observed with the tensile results from Chapter 2 and summarized in Table C.4. The Weibull modulus reflects trend similar to that of the tensile strength of the corresponding carbon fibers as shown in Figure C.4.

Table C.4 Weibull moduli of PAN/MWNT (1 wt.%) based carbon fibers[a].

	Stabilization time at 320 ℃ (min)					
	20	25	30	35	42.5	45
TS[b] (GPa)	1.91±0.50	2.10±0.48	2.28±0.47	2.27±0.45	2.31±0.47	1.79±0.45
m	3.5	4.8	5.1	5.1	4.8	4.1
σ_o (GPa)	2.13	2.29	2.47	2.47	2.52	1.97
R^2	0.952	0.956	0.940	0.958	0.949	0.977

[a] stabilized and carbonized using vertical mount, [b] tensile strength

Improvement in tensile strength along with higher *m* value suggests that up to optimum stabilization time or ~ 40 min, structural defects reduce and enhance the reliability.

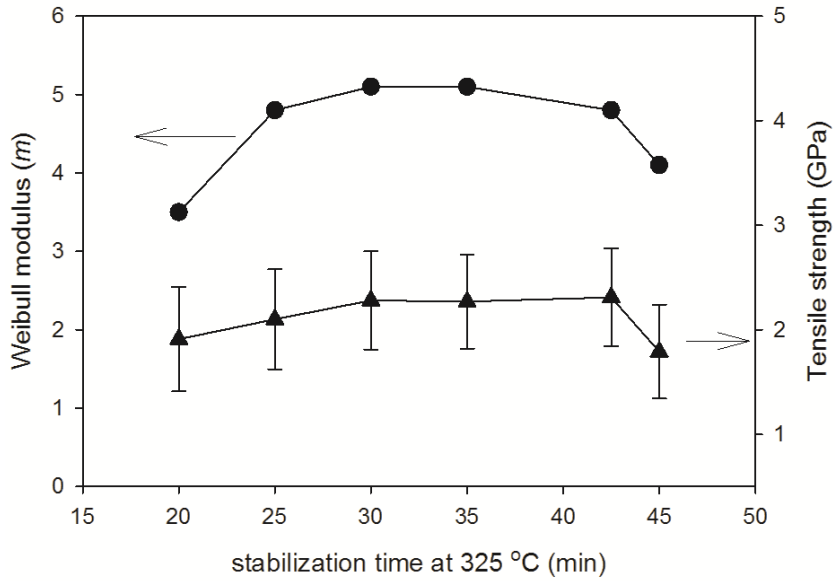

Figure C.4 Weibull modulus and tensile strength as a function of stabilization time.

C.2.4 Effect of Tension

Tensile strength of carbon fiber is expected to enhance with increasing tension during stabilization process, since tension prevents shrinkage, and thereby aligning the graphitic basal plane along the fiber direction. Changes in the tensile strength shown in Figure C.5 follow the expected trend, except at 30 MPa tension due to fiber breakage during heat-treatment. However, the distribution in strength didn't show dependence on applied tension. It might be due to the nature of the batch process. In batch-wise heat-treatment, individual fibers may experience slightly different temperature and tension due to their stationary position.

Table C.5 Weibull moduli of PAN/MWNT (1 wt.%) carbon fibers processed under various tension during stabilization and carbonization.

	Tension applied (MPa)				
	5	7.5	10	20	30
TS (GPa)	2.41±0.49	2.77±0.59	3.02±0.47	3.17±0.45	1.39±0.26
m	5.0	4.3	6.7	5.5	5.3
σ_o(GPa)	2.62	3.03	3.23	3.30	1.51
R^2	0.899	0.907	0.978	0.908	0.965

TS : tensile strength

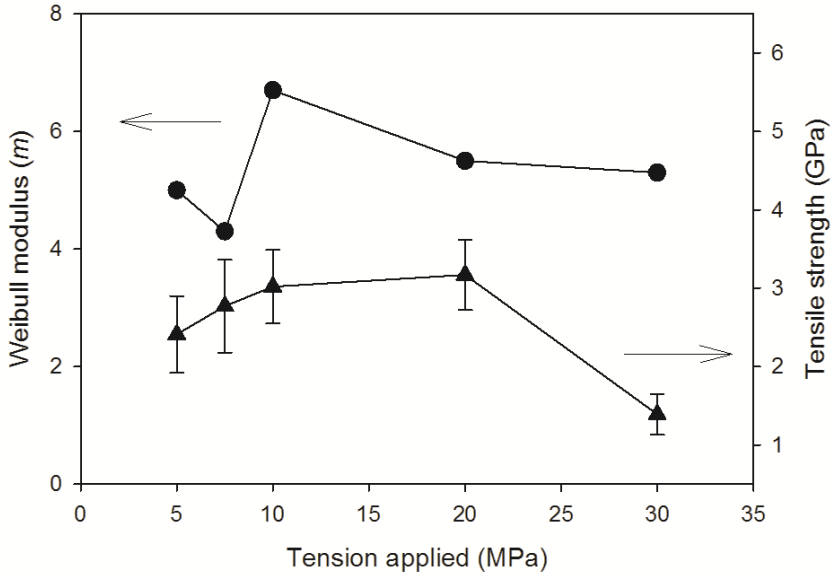

Figure C.5 Weibull modulus and tensile strength as a function of applied tension.

C.2.5 Effect of Gauge Length

Mechanical properties especially, tensile strength of carbon fibers can be affected by the weakest flaw in them[223, 231]. Stress is concentrated on the weakest flaw and leads breakage of fiber. Assuming L_c is the critical length at which the tensile strength is uniform, then probability of survival of fiber under given stress level is proportional to $\exp\{-(L/L_c)\}$, where L is testing gauge length. Thus, the longer tensile testing gauge length used, the lower tensile strength is expected due to the lower probability of survival. Figure C.6 and C.7 show the gauge length effect on mechanical properties of carbon fibers produced without process optimization. In both cases, tensile strength decreased with increasing gauge length. Each test series showed considerable large scatter in strength (average Weibull modulus for Figure C.6, and C.7 are 3.1, and 4.1, respectively). Tensile modulus plotted in Figure C.7 (b) showed positive relation with gauge length, whereas no noticeable relation was observed in Figure C.6 (b). SEM micrographs of PAN/SWNT composite fiber based carbon fibers are shown in Figure C.8.

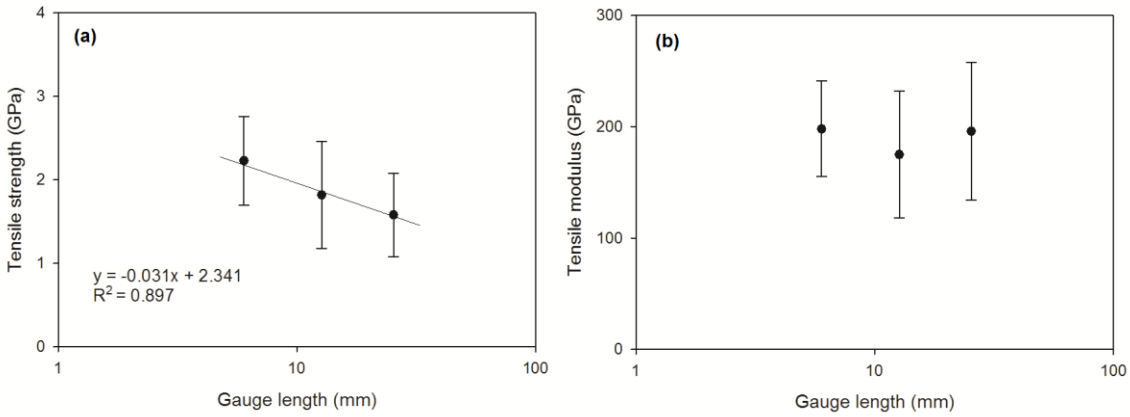

Figure C.6 Gauge length dependence on (a) tensile strength and (b) tensile modulus of carbon fibers (specified in 6th column in Table C.1 and test set 1 in Table C.5).

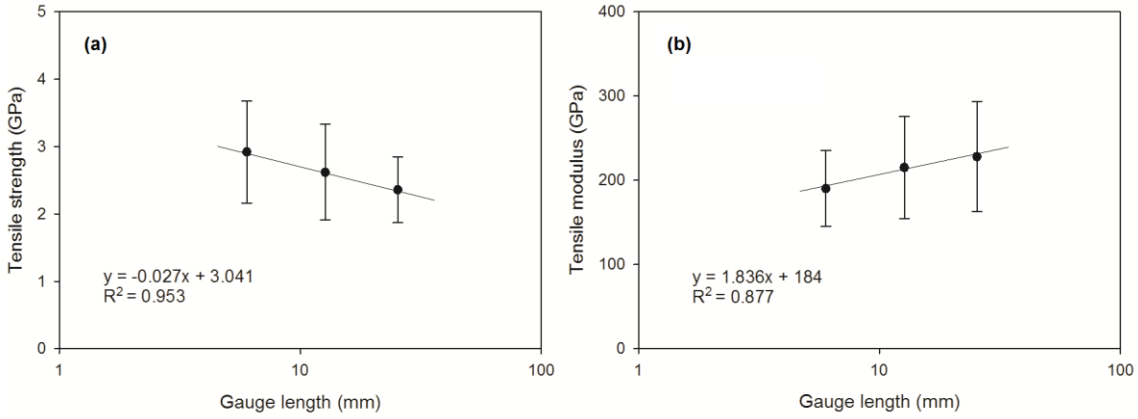

Figure C.7 Gauge length dependence on (a) tensile strength and (b) tensile modulus of carbon fibers (specified in 7th column in Table C.1 and test set 2 in Table C.5).

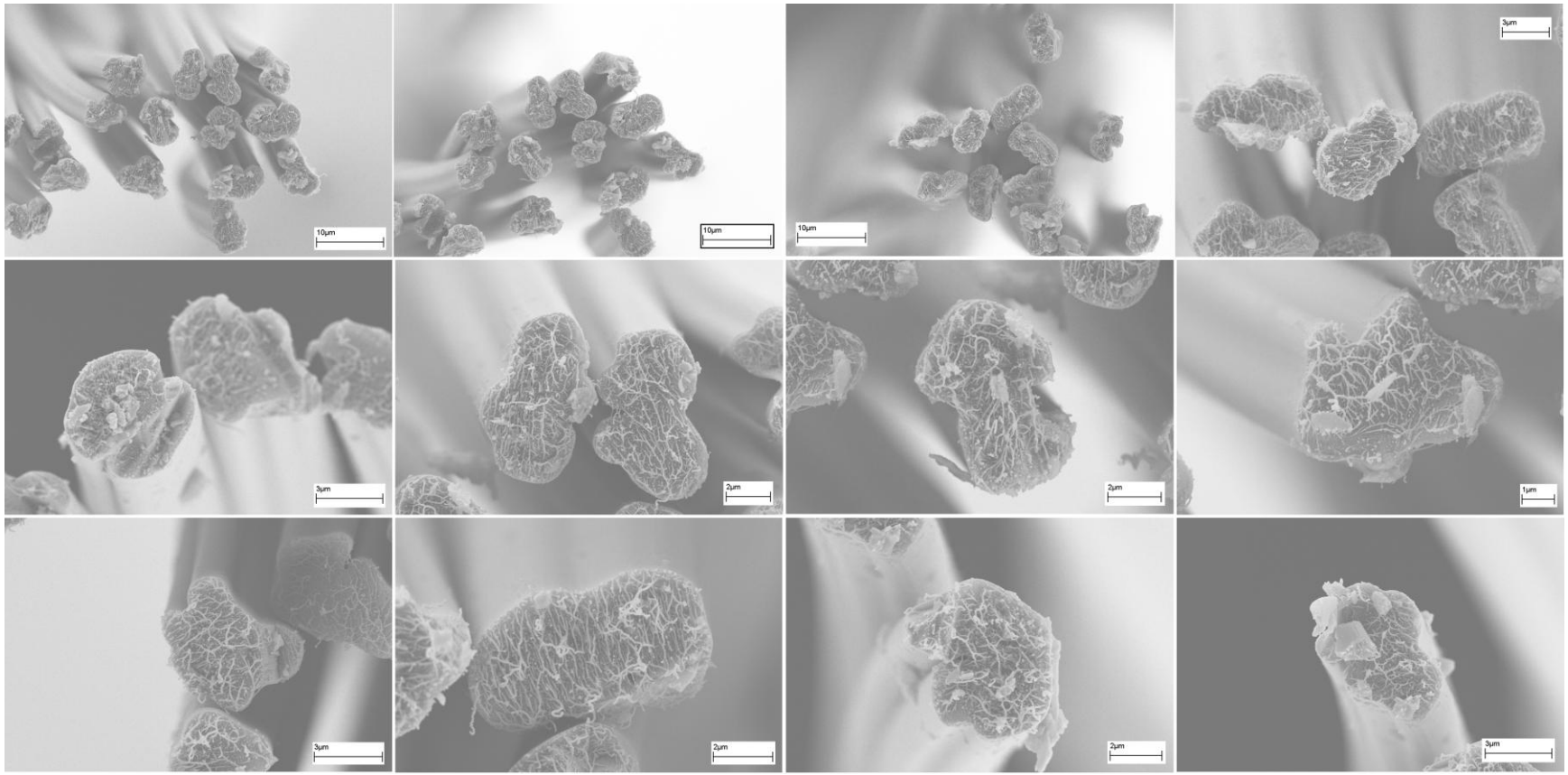

Figure C.8 SEM micrographs of carbon fibers from PAN (homopolymer, M_w of 2.4×10^5 g/mol) /SWNT (1 wt.%) precursor fiber (specified in 7th column in Table C.1 and test set 2 in Table C.5).

With process optimization, the reliability in strength was improved (average Weibull modulus 9.3) for the case of Figure C.9. By process optimization, frequency of flaws in carbon fiber was decreased and this caused increase in reliability and decrease in gauge length dependence. Commercial grade carbon fiber (Toaryca T-300) showed small scatter in strength and modulus as shown in Figure C.10. Also T-300 showed less dependence on the tested gauge length than the other carbon fibers.

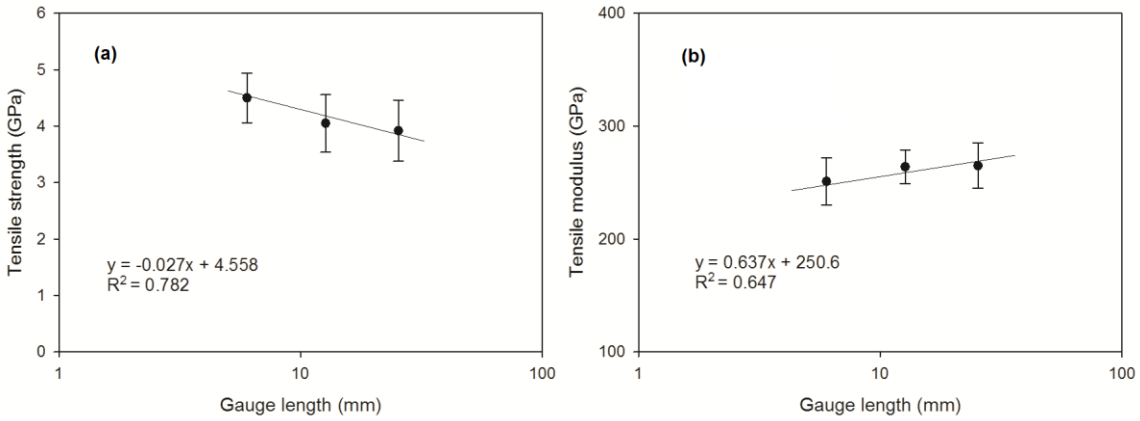

Figure C.9 Gauge length dependence on (a) tensile strength and (b) tensile modulus of carbon fibers produce under optimized conditions (specified in 8th column in Table C.1 and optimized CF in Table C.5).

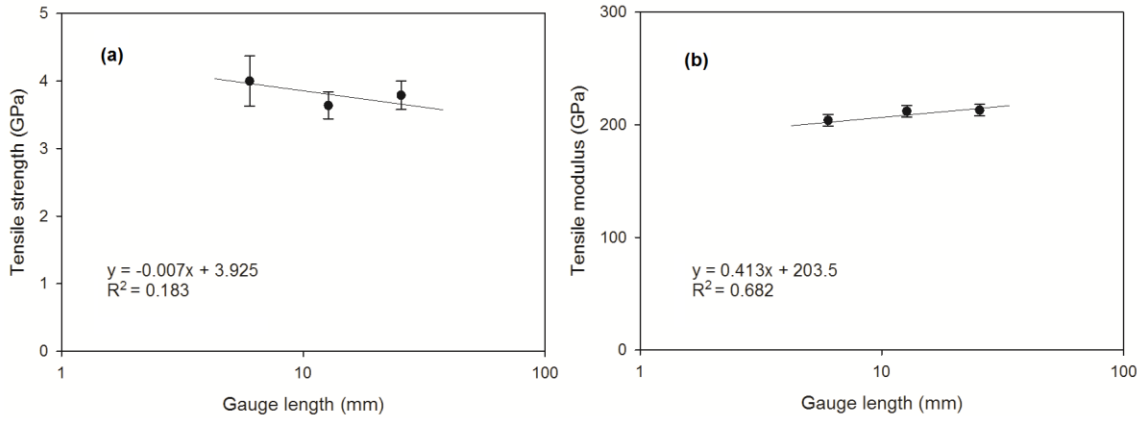

Figure C.10 Gauge length dependence on (a) tensile strength and (b) tensile modulus of T-300 carbon fibers (summarized in Table C.5).

The effect of gauge length on average tensile strength of carbon fiber has been reported [231]. However, the effect of gauge length on the distribution of tensile strength has not been extensively studied. In this study, the gauge length effect was observed using carbon fibers produced with and without process optimization and commercial grade carbon fiber T-300. The results of tensile tests and Weibull model parameters are summarized in Table C.6. Weibull plots for each series are shown in Figure C.11. The Weibull modulus (m) of carbon fibers produced without process optimization (test set 1 and 2) showed no distinct relation to gauge length and ranged between 2.3 and 4.9. Lower m values (low reliability in strength) are due to flaws of structure imperfection, since resultant carbon fibers are produced without optimization. On the other hand, carbon fibers produced under optimum conditions showed that the m value decreased with increasing gauge length. This implies that tensile strength of carbon fibers is more reliable when the test gauge length becomes shorter. Also, carbon fibers produced under optimum process condition exhibited high m values (7.7 ~11.9). The Weibull moduli of commercial grade carbon fibers T-300 are high (11.0 ~ 18.8). However, scatter in strength tested with 6 mm gauge length is wider than that with the 12.7 and 25.4 mm cases, although the tensile strength of T-300 with 6 mm gauge length showed the highest value. Judging from these results, commercial grade carbon fiber T-300 has narrow scatter in tensile strength and has less gauge length dependence on tensile strength reliability, which is good as a reinforcing material.

Table C.6 Tensile strength and distribution of various carbon fibers measured with different gauge length.

	Test set 1[a]			Test set 2[a]			Optimized CF[a]			T-300		
Gauge length (mm)	6	12.7	25.4	6	12.7	25.4	6	12.7	25.4	6	12.7	25.4
TS (GPa)	2.23	1.82	1.58	2.92	2.62	2.36	4.50	4.05	3.92	4.00	3.64	3.79
Std.dev	0.53	0.64	0.50	0.76	0.71	0.49	0.44	0.51	0.54	0.37	0.20	0.21
m	3.9	2.3	3.0	3.8	3.7	4.9	11.9	8.4	7.7	11.0	18.8	18.0
σ_o (GPa)	2.46	2.11	1.77	3.24	2.91	2.57	4.69	4.28	4.16	4.17	3.74	3.89
R^2	0.952	0.922	0.971	0.909	0.991	0.961	0.969	0.948	0.927	0.962	0.992	0.960

[a] precursor specification and stabilization and carbonization conditions are listed in Table C.1, [b] tensile strength

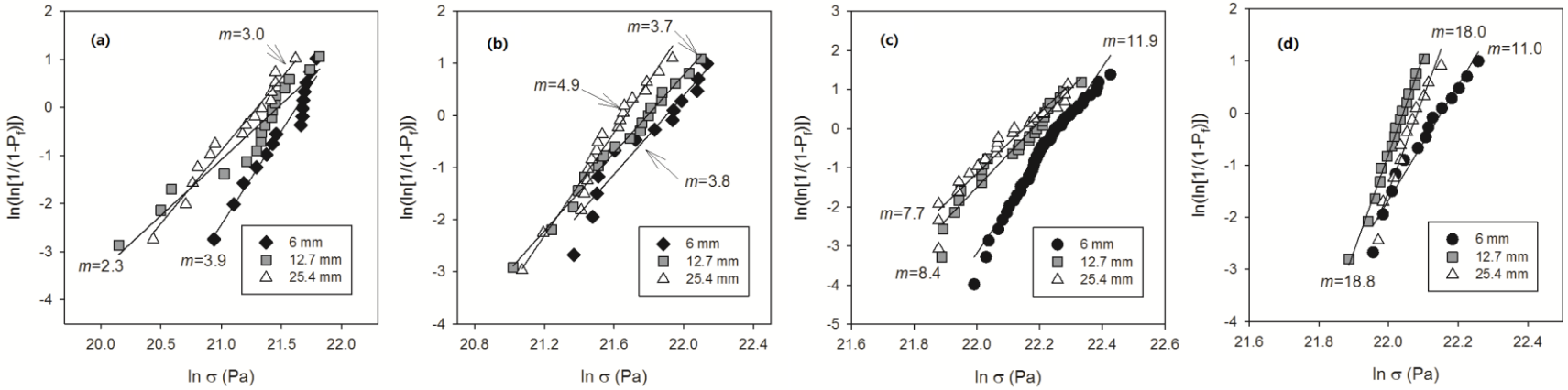

Figure C.11 Weibull plot for (a) test set 1, (b) test set 2, (c) optimized carbon fibers and (d) T-300 (precursor specification and stabilization and carbonization conditions for (a), (b), and (c) are listed in Table C.1).

C.3 Conclusions

The distribution of tensile strength of carbon fibers was investigated using the Weibull model which can evaluate scatter in tensile strength. Based on statistical analysis of stabilized fibers and carbon fibers produced under the continuous heat-treatment environment, progress of stabilization or carbonization could be monitored the using Weibull modulus (*m*) of the fibers. With process optimization, the *m* value increases. The Weibull moduli of commercial carbon fibers (T-300) are high, yet are less dependent on gauge length.

APPENDIX D

MASS DENSITY CALCULATION OF CARBON NANOTUBES

D.1 Introduction

Mass density of CNT (ρ_{CNT}) is critical when volume fraction of CNT as reinforcement is considered in composite system, since interfacial area (surface area where CNTs contact with polymer matrix) is significantly affected by density of CNT in a given CNT concentration. ρ_{CNT} can be obtained by experiment [232] or by rigorous simulation [233]. In this study, ρ_{CNT} was calculated as a function of CNT diameter based on CNT packed crystal assumption.

D.2 Calculation

D.2.1 Density of SWNT

To calculate SWNT density, the number of carbon atoms in a given dimension (diameter, and length) should be counted first. Jain et al.[112] calculated density of SWNT in his thesis. However, arbitrary chosen area for counting carbon atoms needs further justification. Hexagonal lattice was considered for counting number of carbon atoms in SWNT as shown in Figure D.1.

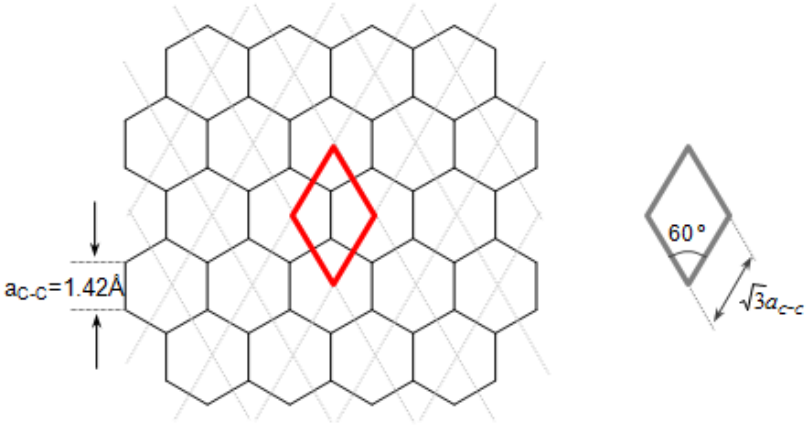

Figure D.1 Hexagonal lattice and lattice parameters for CNTs.

The lattice parameter of hexagonal unit cell is $\sqrt{3}\,a_{c\text{-}c}$, and 60°, where $a_{c\text{-}c}$ is the shortest carbon-carbon distance in hexagonal arrangement (1.42 angstrom). Two carbon atoms are allocated in one hexagonal unit cell of which area is expressed as follows:

$$\frac{\sqrt{3}}{2}\times\left(\sqrt{3}\times 1.42\right)^2 \text{Å}^{\,2} = 5.2387\times 10^{-2}\ nm^2 \tag{D.1}$$

Number of carbon atoms in SWNT (N_{SWNT}) are expressed in Eq.(D.2):

$$\pi dh\times N_{unit} \tag{D.2}$$

where d is diameter of SWNT, h is length of SWNT, and N_{unit} is number of carbon atoms in unit area ($2/(5.2387\times 10^{-2}\ nm^2) \approx 38.1769$ nm^{-2}).

Density of SWNT (ρ_{SWNT}) is proportional to:

$$\frac{M_{w\_SWNT}}{N_A\cdot V_{SWNT}} = \frac{\pi dh\times N_{unit}\times 12.011}{N_A\cdot V_{SWNT}} \tag{D.3}$$

where, M_{w_SWNT} is molecular weight of SWNT, N_A is Avogadro's number, and V_{SWNT} is volume of SWNT.

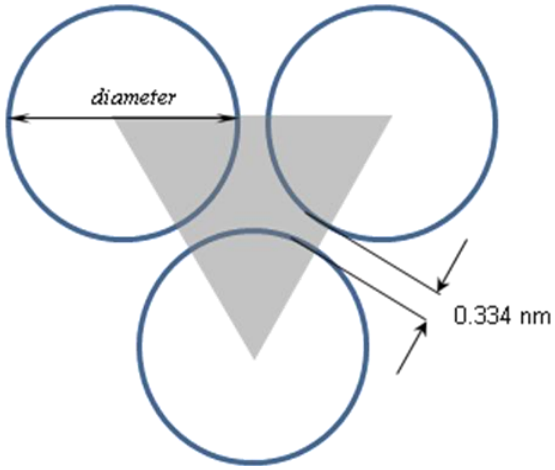

Figure D.2 Schematic diagram for SWNT bundles.

Suppose, triangular arrangement of SWNTs of which bundle forms hexagonal array maintaining Van der Waals distance of 0.334 nm, then triangle area (shaded region in Figure D.2) formed by three SWNTs can be considered for density calculation. SWNTs with open ends and no contribution of gas molecule inside the SWNT in density calculation were assumed. In the triangle, contribution of SWNT in molecular weight is half, so the density of SWNT can be computed as follows:

$$\rho_{SWNT} = \frac{\frac{\pi dh}{2} \times N_{unit} \times 12.011}{N_A \times \frac{\sqrt{3}}{4}(d+0.334)^2 h} = 2.76216 \times \frac{d}{(d+0.334)^2}\, g.cm^{-3} \tag{D.4}$$

Changes in density of SWNT as a function of diameter are exhibited in Figure D.3 using Eq.(D.4).

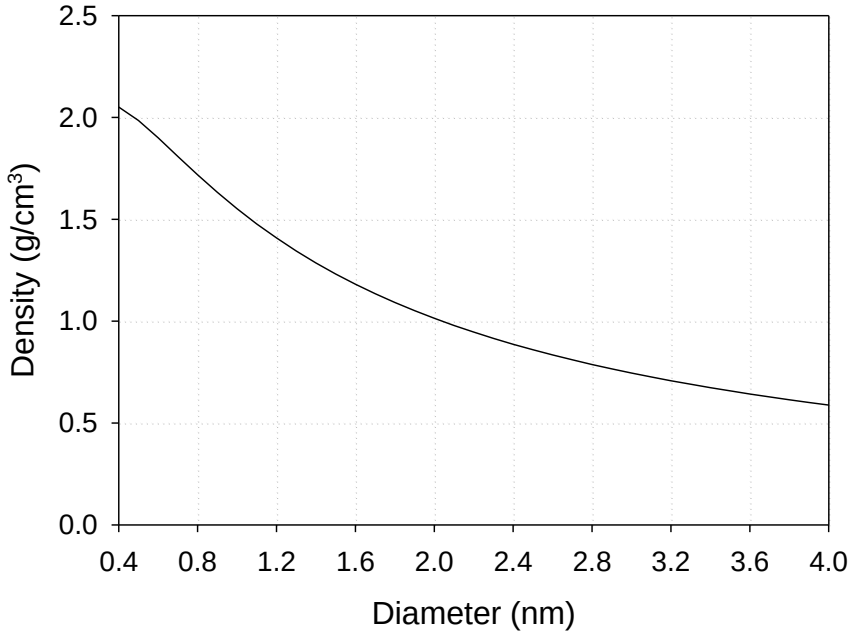

Figure D.3 Density of SWNT as a function of diameter.

The density of SWNT decreases with increasing diameter and becomes less than one when diameter of SWNT is larger than 2 nm. This implies that SWNTs with diameter larger than 2 nm are able to float on the water and are applicable to reinforcing material for light weight composite. However, it should be noted that SWNTs with large diameter (~ 4 nm) could be collapsed rather than they maintain cylindrical (tube) shape. In such cases, density of SWNT could be higher than calculated results.

D.2.2 Density of MWNT

In case of MWNT, each wall assumed to be separated equally at a distance of 0.34 nm. In the sense that the simplest example of MWNT is double walled nanotubes (DWNT), it is easy to start with DWNT for density calculation of MWNT. Considering two walls in DWNT as illustrated in Figure D.4, the total number of carbon atoms in DWNT are given by Eq.(D.5):

$$\left(\frac{\pi dh}{2}+\frac{\pi(d-0.68)h}{2}\right)\times N_{unit} \tag{D.5}$$

where, d is outer diameter of DWNT, d-0.68 is diameter of inner wall, h is length of DWNT, and N_{unit} is number of carbon atoms as used in equation (D.2).

Density of DWNT is obtained as follows:

$$\rho_{DWNT}=\frac{\left(\frac{\pi dh}{2}+\frac{\pi(d-0.68)h}{2}\right)\times N_{unit}\times 12.011}{N_A\times\frac{\sqrt{3}}{4}(d+0.334)^2 h}$$

$$=\frac{2\pi(2d-0.68)\times N_{unit}\times 12.011}{N_A\times\sqrt{3}(d+0.334)^2}\,g.cm^{-3} \tag{D.6}$$

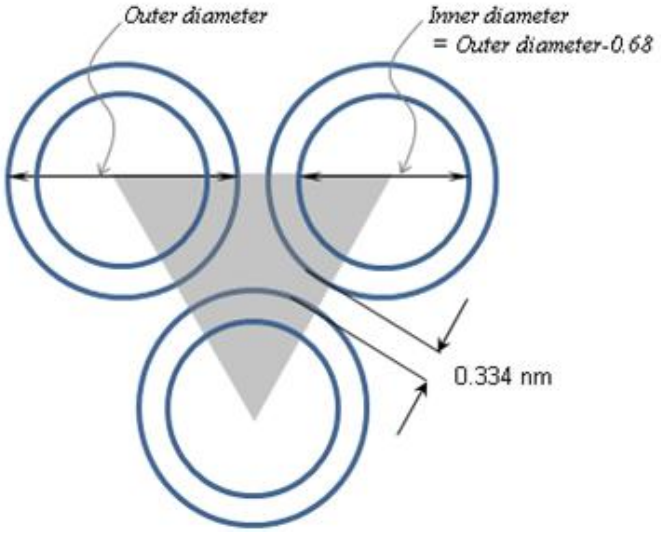

Figure D.4 Schematic diagram for DWNT density calculation.

Next, density of triple walled nanotubes (TWNT) can be calculated. In this case, if the out most wall has diameter of d, then second and third wall have diameter of d-0.68, d-1.336 nm, respectively. Based on this information, the density of TWNT is expressed as follows:

$$\rho_{TWNT} = \frac{\left(\frac{\pi dh}{2} + \frac{\pi(d-0.68)h}{2} + \frac{\pi(d-2\times 0.68)h}{2}\right)\times N_{unit}\times 12.011}{N_A \times \frac{\sqrt{3}}{4}(d+0.334)^2 h}$$

$$= \frac{2\pi(3d-3\times 0.68)\times N_{unit}\times 12.011}{N_A \times \sqrt{3}(d+0.334)^2}\, g.cm^{-3} \qquad \text{(D.7)}$$

Likewise, density of MWNT with *n* number of walls is given by Eq.(D.8):

$$\rho_{MWNT} = \frac{\left(\frac{\pi dh}{2} + \frac{\pi(d-0.68)h}{2} + \cdots + \frac{\pi(d-(n-1)\cdot 0.68)h}{2}\right)\times N_{SWNT}\times 12.011}{N_A \times \frac{\sqrt{3}}{4}(d+0.334)^2 h}$$

$$= \frac{\pi(2nd - n(n-1)\cdot 0.68)\times N_{SWNT}\times 12.011}{N_A \times \sqrt{3}(d+0.334)^2}\, g.cm^{-3} \qquad \text{(D.8)}$$

Calculated results are summarized in Table D.1.

Table D.1 Mass density of Carbon nanotubes (Continues on next pages).

Φ (nm)	SWNT	DWNT	TWNT	MWNT(4)	MWNT(5)	MWNT(6)	MWNT(7)	MWNT(8)	MWNT(9)	MWNT(10)	MWNT(11)	MWNT(12)	MWNT(13)	MWNT(14)	MWNT(15)
0.4	2.051														
0.5	1.986														
0.6	1.900														
0.7	1.808														
0.8	1.718														
0.9	1.633														
1	1.552														
1.1	1.478	2.058													
1.2	1.409	2.033													
1.3	1.345	1.999													
1.4	1.286	1.959													
1.5	1.232	1.915													
1.6	1.182	1.870													
1.7	1.135	1.824													
1.8	1.092	1.778	2.060												
1.9	1.052	1.733	2.046												
2	1.014	1.689	2.026												
2.1	0.979	1.647	2.003												
2.2	0.946	1.605	1.977												
2.3	0.916	1.565	1.949												
2.4	0.887	1.527	1.920												
2.5	0.860	1.490	1.890	2.061											
2.6	0.834	1.454	1.860	2.051											
2.7	0.810	1.420	1.829	2.038											
2.8	0.787	1.387	1.799	2.023											
2.9	0.766	1.355	1.768	2.005											
3	0.745	1.325	1.738	1.986											
3.1	0.726	1.296	1.709	1.966	2.066										
3.2	0.708	1.268	1.680	1.944	2.061										
3.3	0.690	1.241	1.652	1.923	2.054										
3.4	0.674	1.215	1.624	1.900	2.044										
3.5	0.658	1.190	1.596	1.878	2.033										
3.6	0.643	1.166	1.570	1.855	2.020										
3.7	0.628	1.143	1.544	1.832	2.006										
3.8	0.614	1.120	1.519	1.809	1.991	2.066									
3.9	0.601	1.099	1.494	1.786	1.975	2.062									
4	0.588	1.078	1.470	1.763	1.959	2.056									
4.1		1.058	1.447	1.741	1.942	2.048									
4.2		1.039	1.424	1.719	1.924	2.040									
4.3		1.020	1.402	1.697	1.906	2.030									
4.4		1.002	1.380	1.675	1.888	2.019									
4.5		0.985	1.359	1.654	1.870	2.007	2.065								
4.6		0.968	1.338	1.633	1.852	1.995	2.062								
4.7			1.318	1.612	1.833	1.982	2.057								

Table D.1 Mass density of Carbon nanotubes (Continued).

Φ (nm)	SWNT	DWNT	TWNT	MWNT(4)	MWNT(5)	MWNT(6)	MWNT(7)	MWNT(8)	MWNT(9)	MWNT(10)	MWNT(11)	MWNT(12)	MWNT(13)	MWNT(14)	MWNT(15)
4.8			1.299	1.592	1.815	1.968	2.051								
4.9			1.280	1.572	1.797	1.954	2.044								
5			1.262	1.553	1.779	1.940	2.036								
5.1			1.244	1.533	1.760	1.925	2.027	2.067							
5.2			1.226	1.515	1.743	1.910	2.018	2.065							
5.3			1.209	1.496	1.725	1.895	2.008	2.062							
5.4				1.478	1.707	1.880	1.997	2.058							
5.5				1.460	1.690	1.865	1.986	2.053							
5.6				1.443	1.672	1.850	1.975	2.047							
5.7				1.426	1.655	1.834	1.963	2.040							
5.8				1.409	1.639	1.819	1.951	2.033	2.067						
5.9				1.392	1.622	1.804	1.938	2.025	2.065						
6					1.606	1.789	1.926	2.017	2.062						
6.1					1.589	1.774	1.913	2.008	2.059						
6.2					1.573	1.758	1.900	1.999	2.054						
6.3					1.558	1.744	1.887	1.989	2.049						
6.4					1.542	1.729	1.874	1.979	2.044						
6.5					1.527	1.714	1.861	1.969	2.038	2.066					
6.6					1.512	1.699	1.848	1.959	2.031	2.065					
6.7						1.685	1.835	1.948	2.024	2.062					
6.8						1.671	1.822	1.937	2.016	2.059					
6.9						1.656	1.809	1.926	2.008	2.055					
7						1.642	1.796	1.915	2.000	2.051					
7.1						1.628	1.783	1.904	1.992	2.046					
7.2						1.615	1.770	1.893	1.983	2.041	2.066				
7.3						1.601	1.757	1.881	1.974	2.035	2.065				
7.4							1.744	1.870	1.965	2.029	2.062				
7.5							1.732	1.859	1.956	2.023	2.060				
7.6							1.719	1.847	1.946	2.016	2.056				
7.7							1.706	1.836	1.937	2.009	2.052				
7.8							1.694	1.824	1.927	2.001	2.048	2.067			
7.9							1.681	1.813	1.917	1.994	2.044	2.066			
8							1.669	1.801	1.907	1.986	2.039	2.064			
8.1								1.790	1.897	1.978	2.033	2.062			
8.2								1.779	1.887	1.970	2.028	2.060			
8.3								1.767	1.877	1.962	2.022	2.057			
8.4								1.756	1.867	1.953	2.015	2.054			
8.5								1.745	1.857	1.945	2.009	2.050	2.067		
8.6								1.734	1.846	1.936	2.002	2.046	2.066		
8.7									1.836	1.927	1.995	2.041	2.064		
8.8									1.826	1.918	1.988	2.037	2.062		
8.9									1.816	1.909	1.981	2.032	2.060		
9									1.806	1.900	1.974	2.026	2.057		
9.1									1.795	1.891	1.966	2.021	2.054	2.067	

Table D.1 Mass density of Carbon nanotubes (Continued).

Φ (nm)	SWNT	DWNT	TWNT	MWNT(4)	MWNT(5)	MWNT(6)	MWNT(7)	MWNT(8)	MWNT(9)	MWNT(10)	MWNT(11)	MWNT(12)	MWNT(13)	MWNT(14)	MWNT(15)
9.2									1.785	1.882	1.959	2.015	2.051	2.067	
9.3									1.775	1.873	1.951	2.009	2.047	2.066	
9.4										1.864	1.943	2.003	2.043	2.064	
9.5										1.855	1.935	1.997	2.039	2.063	
9.6										1.846	1.927	1.990	2.035	2.060	
9.7										1.836	1.919	1.984	2.030	2.058	
9.8										1.827	1.911	1.977	2.025	2.055	2.067
9.9										1.818	1.903	1.970	2.020	2.052	2.067
10										1.809	1.895	1.963	2.015	2.049	2.066

*figures in parentheses represent number of walls in CNT

APPENDIX E

VOLUME FRACTION OF INTERPHASE

E.1 Volume Fraction of Interphase in Matrix

Additional plots for CNT loading of 0.5, 2, 5, and 20 wt.% are shown below.

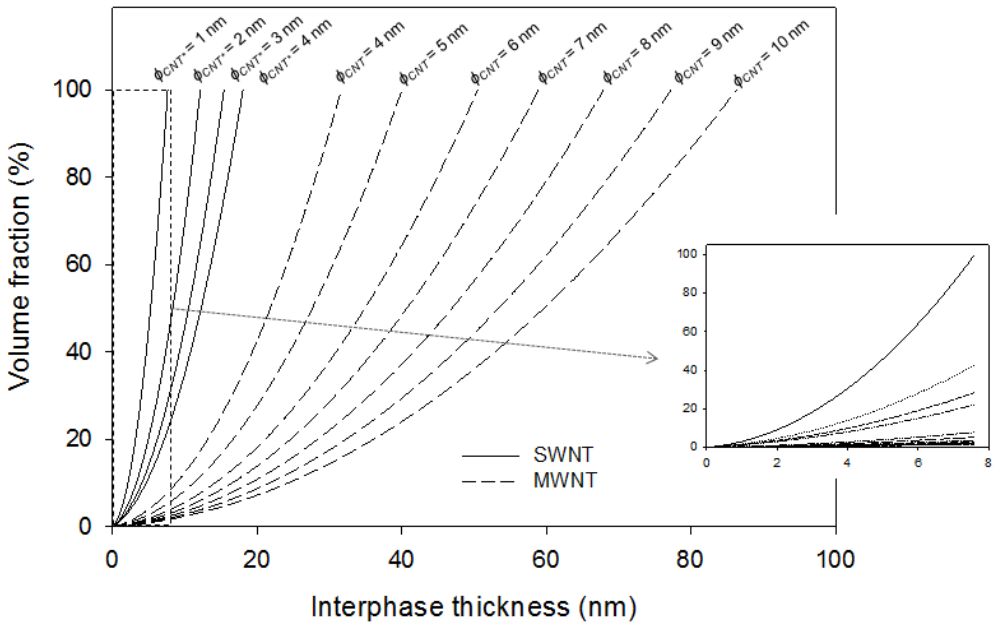

Figure E.1 Volume fraction of interphase as a function of interphase thickness at 0.5 wt.% of CNT loading.

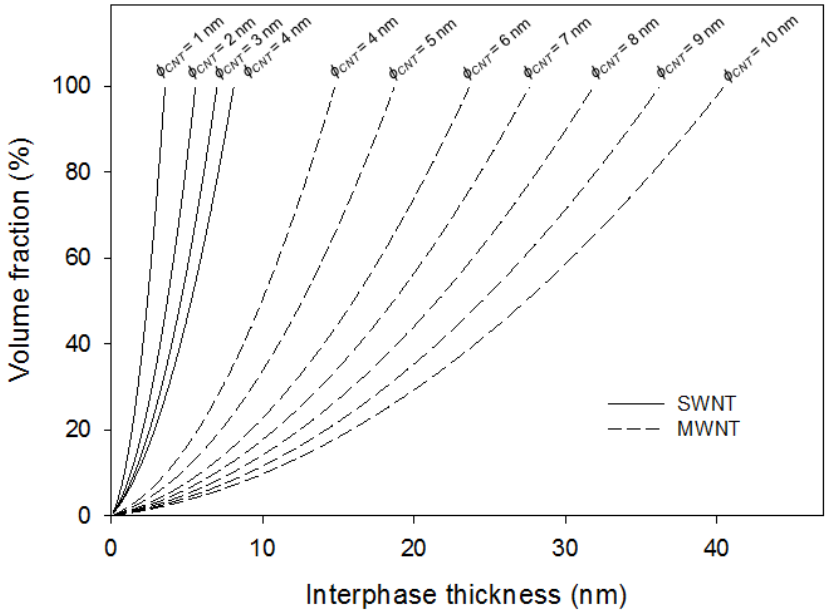

Figure E.2 Volume fraction of interphase as a function of interphase thickness at 2 wt.% of CNT loading.

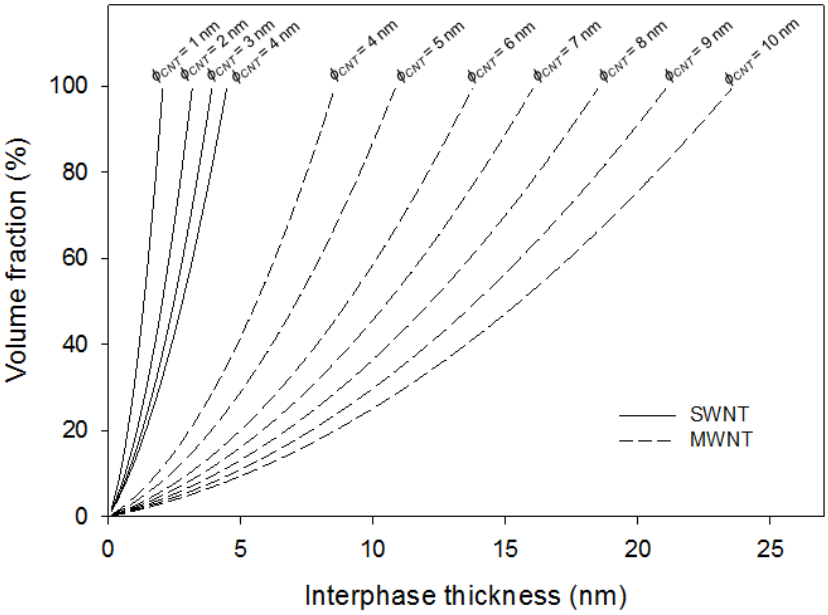

Figure E.3 Volume fraction of interphase as a function of interphase thickness at 5 wt.% of CNT loading.

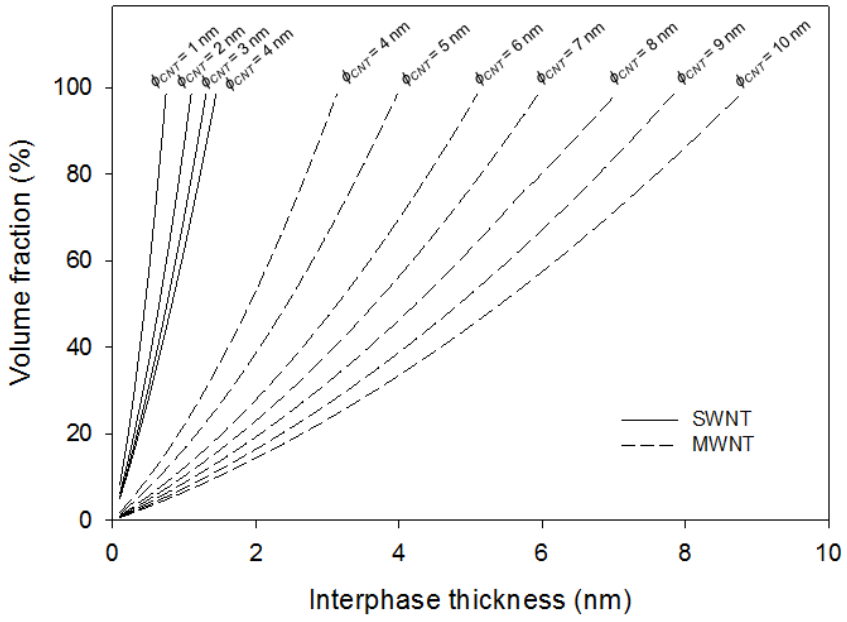

Figure E.4 Volume fraction of interphase as a function of interphase thickness at 20 wt.% of CNT loading.

E.2 Volume Fraction of Interphase in Composite

The volume fraction of interphase in composite system also can be considered. Using Eq.(6.1) and (6.6), the volume fraction of interphase in composite system is given by Eq.(E1) :

$$\frac{V_{interphase}}{V_{composite}} = \frac{\pi\left(i^2 + iD_{CNT}\right)}{\frac{\pi}{4} D_{fiber}^2 l_{fiber}} \cdot l_{CNT}$$

$$= \frac{4 f_w \rho_{PAN} \left(i^2 + iD_{CNT}\right)}{D_{CNT}^2 \left((100 - f_w)\rho_{CNT} + f_w \rho_{PAN}\right)} \qquad \text{(E.1)}$$

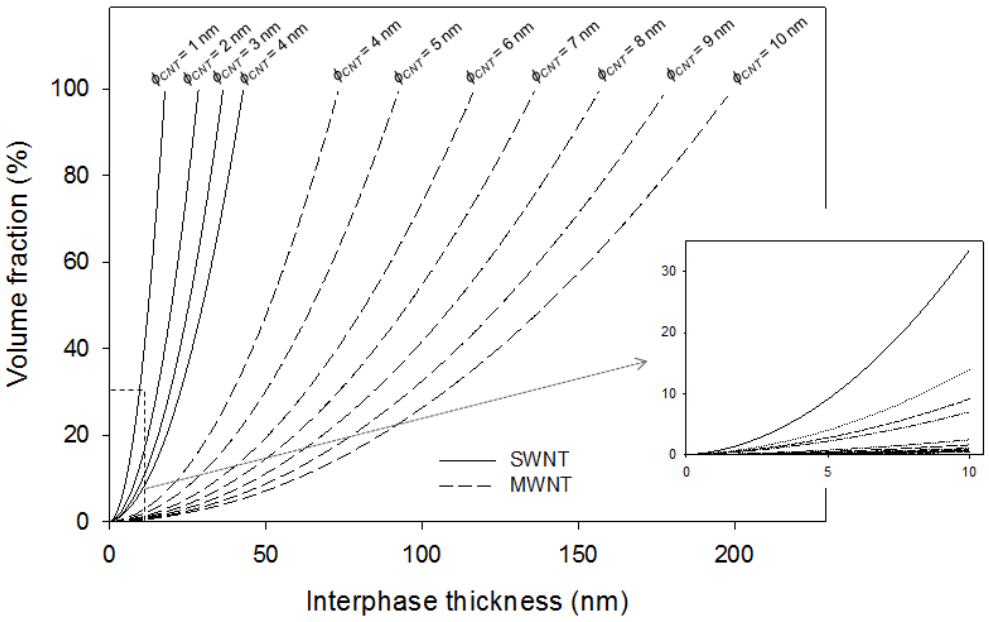

Figure E.5 Changes of volume fraction of interphase in composite at 0.1 wt.% of CNT loading.

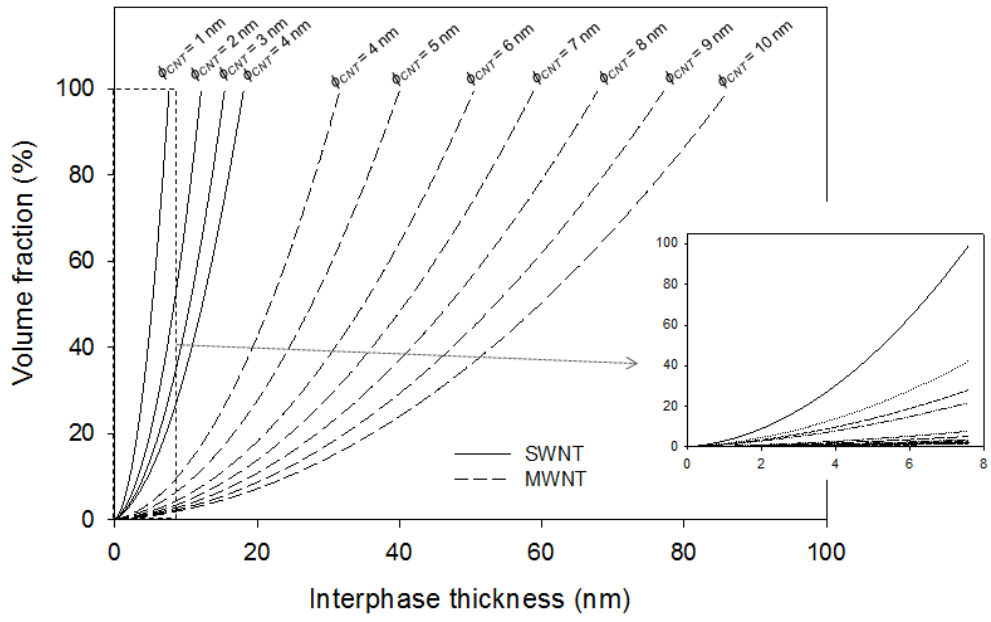

Figure E.6 Changes of volume fraction of interphase in composite at 0.5 wt.% of CNT loading.

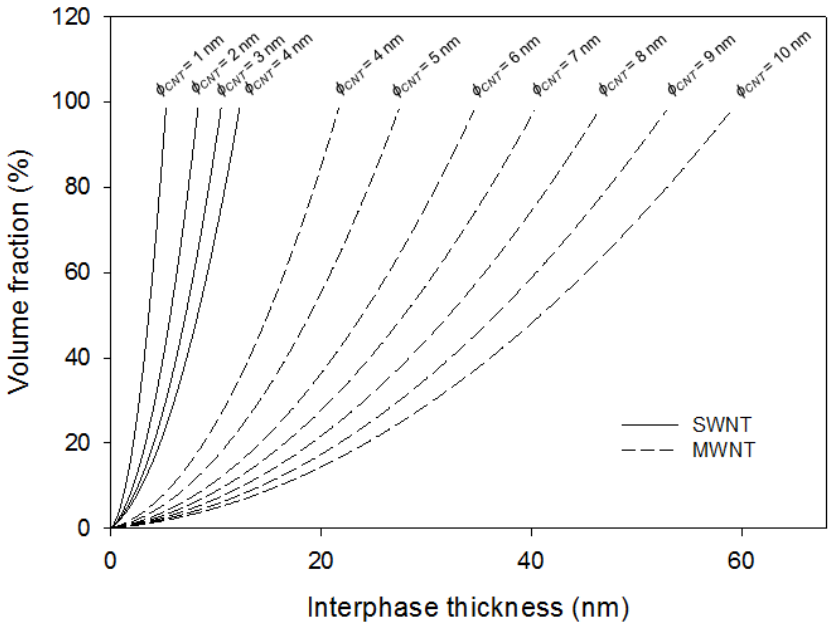

Figure E.7 Changes of volume fraction of interphase in composite at 1 wt.% of CNT loading.

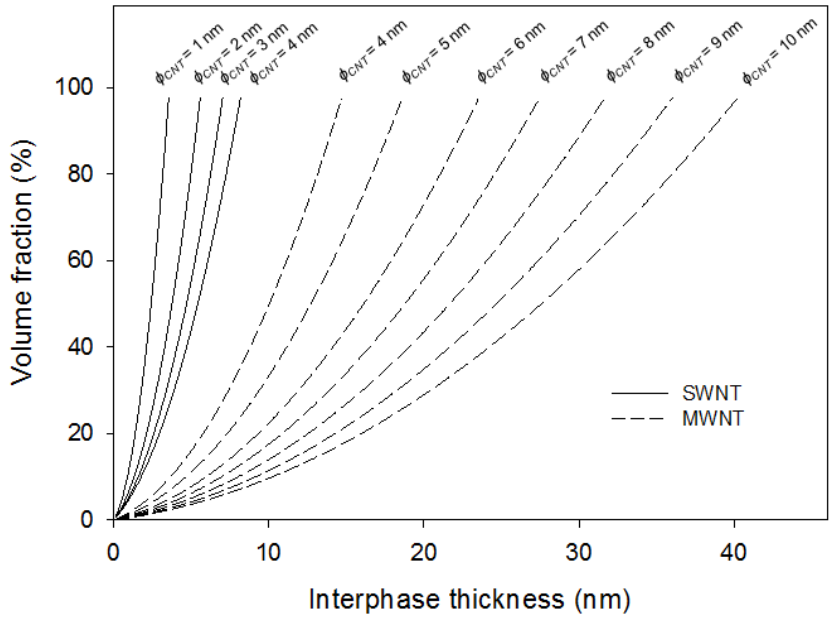

Figure E.8 Changes of volume fraction of interphase in composite at 2 wt.% of CNT loading.

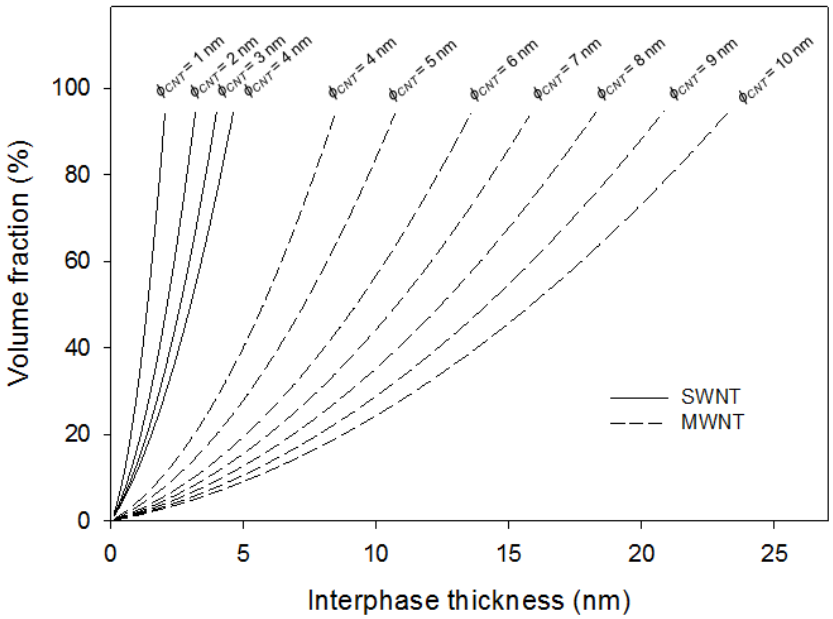

Figure E.9 Changes of volume fraction of interphase in composite at 5 wt.% of CNT loading.

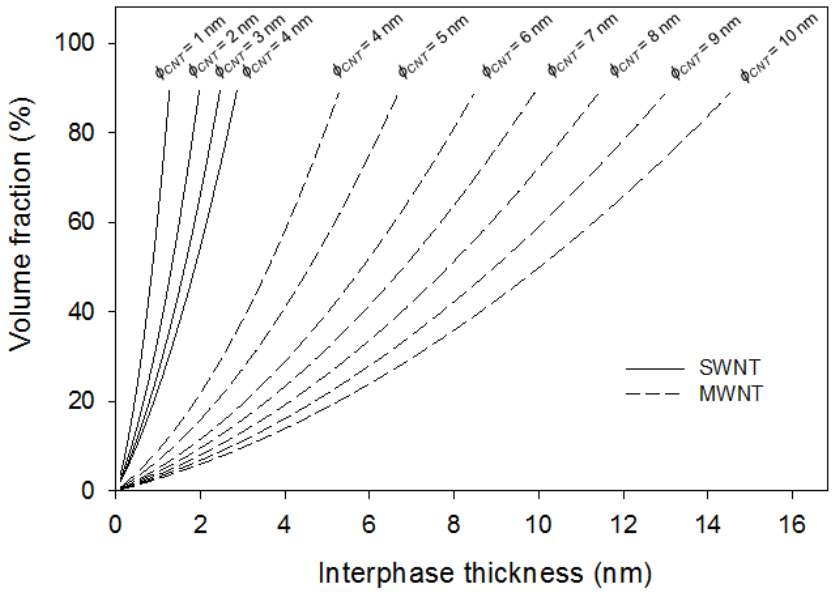

Figure E.10 Changes of volume fraction of interphase in composite at 10 wt.% of CNT loading.

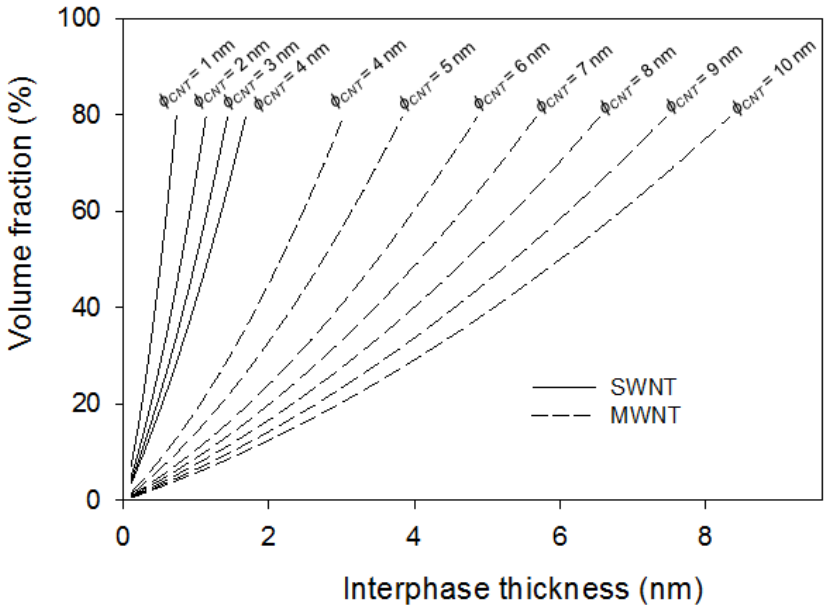

Figure E.11 Changes of volume fraction of interphase in composite at 20 wt.% of CNT loading.

REFERENCES

1. Chung, D.D.L., *Carbon fiber composites*. 1994, Boston Butterworth-Heinemann.

2. Duffy, J.V., *Pyrolysis of treated rayon fiber.* Journal of Applied Polymer Science, 1971. **15**(3): p. 715-729.

3. Li, H., Y. Yang, Y. Wen, and L. Liu, *A mechanism study on preparation of rayon based carbon fibers with (NH4)2SO4/NH4Cl/organosilicon composite catalyst system.* Composites Science & Technology, 2007. **67**(13): p. 2675-2682.

4. Wu, Q.-L., S.-Y. Gu, J.-H. Gong, and D. Pan, *SEM/STM studies on the surface structure of a novel carbon fiber from lyocell.* Synthetic Metals, 2006. **156**(11-13): p. 792-795.

5. Dickakian, G., *AROMATIC PITCH*. 1983, E. I. Du Pont de Nemours and Company: US4715945.

6. Gerard Lavin, J., *Chemical reactions in the stabilization of mesophase pitch-based carbon fiber.* Carbon, 1992. **30**(3): p. 351-357.

7. Singer, L.S., *The mesophase and high modulus carbon fibers from pitch.* Carbon, 1978. **16**(6): p. 409-415.

8. Sawran, W.R., F.H. Turrill, J.W. Newman, and N.W. Hall, *PROCESS FOR THE MANUFACTURE OF CARBON FIBERS*. 1982, Ashland Oil, Inc.: US4497789.

9. Brooks, J.D. and G.H. Taylor, *The formation of graphitizing carbons from the liquid phase.* Carbon, 1965. **3**(2): p. 185-186, IN9-IN18, 187-193.

10. Edie, D.D., *The effect of processing on the structure and properties of carbon fibers.* Carbon, 1998. **36**(4): p. 345-362.

11. Ogale, A.A., C. Lin, D.P. Anderson, and K.M. Kearns, *Orientation and dimensional changes in mesophase pitch-based carbon fibers.* Carbon, 2002. **40**(8): p. 1309-1319.

12. Bahl, O.P., R.B. Mathur, and K.D. Kundra, *STRUCTURE OF PAN FIBERS AND ITS RELATIONSHIP TO RESULTING CARBON-FIBER PROPERTIES.* Fibre Science & Technology, 1981. **15**(2): p. 147-151.

13. Bang, Y.H., S. Lee, and H.H. Cho, *Effect of methyl acrylate composition on the microstructure changes of high molecular weight polyacrylonitrile for heat treatment.* Journal of Applied Polymer Science, 1998. **68**(13): p. 2205-2213.

14. Brown, N.M.D. and H.-X. You, *A scanning tunnelling microscopy study of PAN-based carbon fibre in air.* Surface Science, 1990. **237**(1-3): p. 273-279.

15. Deurbergue, A. and A. Oberlin, *Stabilization and carbonization of pan-based carbon fibers as related to mechanical properties.* Carbon, 1991. **29**(4-5): p. 621-628.

16. Deurbergue, A. and A. Oberlin, *TEM study of some recent high modulus pan-based carbon fibers.* Carbon, 1992. **30**(7): p. 981-987.

17. Donnet, J.-B. and R.-Y. Qin, *Study of carbon fiber surfaces by scanning tunneling microscopy, part II--Pan-based high strength carbon fibers.* Carbon, 1993. **31**(1): p. 7-12.

18. Dunham, M.G. and D.D. Edie, *Model of stabilization for pan-based carbon fiber precursor bundles.* Carbon, 1992. **30**(3): p. 435-450.

19. Fitzer, E., *PAN-BASED CARBON-FIBERS PRESENT STATE AND TREND OF THE TECHNOLOGY FROM THE VIEWPOINT OF POSSIBILITIES AND LIMITS TO INFLUENCE AND TO CONTROL THE FIBER PROPERTIES BY THE PROCESS PARAMETERS.* Carbon, 1989. **27**(5): p. 621-645.

20. Fitzer, E. and D.J. Muller, *The influence of oxygen on the chemical reactions during stabilization of pan as carbon fiber precursor.* Carbon, 1975. **13**(1): p. 63-69.

21. Gupta, A. and I.R. Harrison, *New aspects in the oxidative stabilization of pan-based carbon fibers.* Carbon, 1996. **34**(11): p. 1427-1445.

22. Katzman, H.A., P.M. Adams, T.D. Le, and C.S. Hemminger, *Characterization of low thermal conductivity pan-based carbon fibers.* Carbon, 1994. **32**(3): p. 379-391.

23. Ko, T.H., *Influence of continuous stabilization on the physical properties and microstructure of PAN-based carbon fibers.* Journal of Applied Polymer Science, 1991. **42**(7): p. 1949-1957.

24. Ko, T.H., *Raman spectrum of modified PAN-based carbon fibers during graphitization.* Journal of Applied Polymer Science, 1996. **59**(4): p. 577-580.

25. Liu, J., P.H. Wang, and R.Y. Li, *CONTINUOUS CARBONIZATION OF POLYACRYLONITRILE-BASED OXIDIZED FIBERS - ASPECTS ON MECHANICAL-PROPERTIES AND MORPHOLOGICAL STRUCTURE.* Journal of Applied Polymer Science, 1994. **52**(7): p. 945-950.

26. Rahaman, M.S.A., A.F. Ismail, and A. Mustafa, *A review of heat treatment on polyacrylonitrile fiber.* Polymer Degradation and Stability, 2007. **92**(8): p. 1421-1432.

27. Rand, B. and R. Robinson, *A preliminary investigation of PAN based carbon fibre surfaces by flow microcalorimetry.* Carbon, 1977. **15**(5): p. 311-315.

28. Tsai, J.S. and C.H. Lin, *THE EFFECT OF MOLECULAR-WEIGHT ON THE CROSS-SECTION AND PROPERTIES OF POLYACRYLONITRILE PRECURSOR AND RESULTING CARBON-FIBER.* Journal of Applied Polymer Science, 1991. **42**(11): p. 3045-3050.

29. Tsai, J.S. and C.H. Lin, *Effect of comonomer composition on the properties of polyacrylonitrile precursor and resulting carbon fiber.* Journal of Applied Polymer Science, 1991. **43**(4): p. 679-685.

30. Tsai, J.S. and C.H. Lin, *The effect of the side chain of acrylate comonomers on the orientation, pore-size distribution, and properties of polyacrylonitrile precursor and resulting carbon fiber.* Journal of Applied Polymer Science, 1991. **42**(11): p. 3039-3044.

31. Tse-Hao, K., D. Tzy-Chin, P. Jeng-An, and L. Ming-Fong, *The characterization of PAN-based carbon fibers developed by two-stage continuous carbonization.* Carbon, 1993. **31**(5): p. 765-771.

32. Tse-Hao Ko, C.-H.L., Hsing-Yie Ting,, *Structural changes and molecular motion of polyacrylonitrile fibers during pyrolysis.* Journal of Applied Polymer Science, 1989. **37**(2): p. 553-566.

33. Tse-Hao Ko, H.-Y.T., Chung-Hua Lin,, *Thermal stabilization of polyacrylonitrile fibers.* Journal of Applied Polymer Science, 1988. **35**(3): p. 631-640.

34. Wang, P., J. Liu, Z. Yue, and R. Li, *Thermal oxidative stabilization of polyacrylonitrile precursor fiber--progression of morphological structure and mechanical properties.* Carbon, 1992. **30**(1): p. 113-120.

35. James T. Paul, J., *HIGH MODULUS PAN-BASED CARBON FIBER.* 1989, Hercules Incorporated: US5268158.

36. Baughman, R.H., A.A. Zakhidov, and W.A. de Heer, *Carbon Nanotubes--the Route Toward Applications.* Science, 2002. **297**(5582): p. 787-792.

37. Thess, A., R. Lee, P. Nikolaev, H. Dai, P. Petit, J. Robert, C. Xu, Y.H. Lee, S.G. Kim, A.G. Rinzler, D.T. Colbert, G.E. Scuseria, D. Tomanek, J.E. Fischer, and R.E. Smalley, *Crystalline Ropes of Metallic Carbon Nanotubes.* Science, 1996. **273**(5274): p. 483-487.

38. Minus, M.L., H.G. Chae, and S. Kumar, *Single wall carbon nanotube templated oriented crystallization of poly(vinyl alcohol).* Polymer, 2006. **47**(11): p. 3705-3710.

39. Li, C., L. Li, W. Cai, S. Kodjie, and K. Tenneti, *Nanohybrid Shish-Kebabs: Periodically Functionalized Carbon Nanotubes.* Advanced Materials, 2005. **17**(9): p. 1198-1202.

40. Li, L., C.Y. Li, and C. Ni, *Polymer Crystallization-Driven, Periodic Patterning on Carbon Nanotubes.* Journal of the American Chemical Society, 2006. **128**(5): p. 1692-1699.

41. Li, L., C.Y. Li, C. Ni, L. Rong, and B. Hsiao, *Structure and crystallization behavior of Nylon 66/multi-walled carbon nanotube nanocomposites at low carbon nanotube contents.* Polymer, 2007. **48**(12): p. 3452-3460.

42. Uehara, H., K. Kato, M. Kakiage, T. Yamanobe, and T. Komoto, *Single-Walled Carbon Nanotube Nucleated Solution-Crystallization of Polyethylene.* The Journal of Physical Chemistry C, 2007. **111**(51): p. 18950-18957.

43. Bhattacharyya, A.R., T.V. Sreekumar, T. Liu, S. Kumar, L.M. Ericson, R.H. Hauge, and R.E. Smalley, *Crystallization and orientation studies in polypropylene/single wall carbon nanotube composite.* Polymer, 2003. **44**(8): p. 2373-2377.

44. Zhang, S., M.L. Minus, L. Zhu, C.-P. Wong, and S. Kumar, *Polymer transcrystallinity induced by carbon nanotubes.* Polymer, 2008. **49**(5): p. 1356-1364.

45. Schadler, L.S., S.C. Giannaris, and P.M. Ajayan, *Load transfer in carbon nanotube epoxy composites.* Applied Physics Letters, 1998. **73**(26): p. 3842-3844.

46. Jin, Z., K.P. Pramoda, G. Xu, and S.H. Goh, *Dynamic mechanical behavior of melt-processed multi-walled carbon nanotube/poly(methyl methacrylate) composites.* Chemical Physics Letters, 2001. **337**(1-3): p. 43-47.

47. Biercuk, M.J., M.C. Llaguno, M. Radosavljevic, J.K. Hyun, A.T. Johnson, and J.E. Fischer, *Carbon nanotube composites for thermal management.* Applied Physics Letters, 2002. **80**(15): p. 2767-2769.

48. Erik, T.T. and C. Tsu-Wei, *Aligned multi-walled carbon nanotube-reinforced composites: processing and mechanical characterization.* Journal of Physics D: Applied Physics, 2002. **35**(16): p. L77.

49. Kumar, S., T.D. Dang, F.E. Arnold, A.R. Bhattacharyya, B.G. Min, X. Zhang, R.A. Vaia, C. Park, W.W. Adams, R.H. Hauge, R.E. Smalley, S. Ramesh, and P.A. Willis, *Synthesis, Structure, and Properties of PBO/SWNT Composites&.* Macromolecules, 2002. **35**(24): p. 9039-9043.

50. Pötschke, P., T.D. Fornes, and D.R. Paul, *Rheological behavior of multiwalled carbon nanotube/polycarbonate composites.* Polymer, 2002. **43**(11): p. 3247-3255.

51. Sandler, J.K.W., J.E. Kirk, I.A. Kinloch, M.S.P. Shaffer, and A.H. Windle, *Ultra-low electrical percolation threshold in carbon-nanotube-epoxy composites.* Polymer, 2003. **44**(19): p. 5893-5899.

52. Zhang, X., T. Liu, T.V. Sreekumar, S. Kumar, V.C. Moore, R.H. Hauge, and R.E. Smalley, *Poly(vinyl alcohol)/SWNT Composite Film.* Nano Letters, 2003. **3**(9): p. 1285-1288.

53. Baek, J.-B., C.B. Lyons, and L.-S. Tan, *Grafting of Vapor-Grown Carbon Nanofibers via in-Situ Polycondensation of 3-Phenoxybenzoic Acid in Poly(phosphoric acid).* Macromolecules, 2004. **37**(22): p. 8278-8285.

54. Coleman, J., M. Cadek, R. Blake, V. Nicolosi, K. Ryan, C. Belton, A. Fonseca, J. Nagy, Y. Gun'ko, and W. Blau, *High Performance Nanotube-Reinforced Plastics: Understanding the Mechanism of Strength Increase.* Advanced Functional Materials, 2004. **14**(8): p. 791-798.

55. Gojny, F.H., M.H.G. Wichmann, U. Köpke, B. Fiedler, and K. Schulte, *Carbon nanotube-reinforced epoxy-composites: enhanced stiffness and fracture toughness at low nanotube content.* Composites Science and Technology, 2004. **64**(15): p. 2363-2371.

56. Jose, K.A. and et al., *A compact wireless gas sensor using a carbon nanotube/PMMA thin film chemiresistor.* Smart Materials and Structures, 2004. **13**(5): p. 1045.

57. Ren, Y., Y.Q. Fu, K. Liao, F. Li, and H.M. Cheng, *Fatigue failure mechanisms of single-walled carbon nanotube ropes embedded in epoxy.* Applied Physics Letters, 2004. **84**(15): p. 2811-2813.

58. Zhang, X., T. Liu, T.V. Sreekumar, S. Kumar, X. Hu, and K. Smith, *Gel spinning of PVA/SWNT composite fiber.* Polymer, 2004. **45**(26): p. 8801-8807.

59. Guo, H., T.V. Sreekumar, T. Liu, M. Minus, and S. Kumar, *Structure and properties of polyacrylonitrile/single wall carbon nanotube composite films.* Polymer, 2005. **46**(9): p. 3001-3005.

60. Wang, Q.H., A.A. Setlur, J.M. Lauerhaas, J.Y. Dai, E.W. Seelig, and R.P.H. Chang, *A nanotube-based field-emission flat panel display.* Applied Physics Letters, 1998. **72**(22): p. 2912-2913.

61. Gong, X., J. Liu, S. Baskaran, R.D. Voise, and J.S. Young, *Surfactant-Assisted Processing of Carbon Nanotube/Polymer Composites.* Chemistry of Materials, 2000. **12**(4): p. 1049-1052.

62. Zhao, Q., M.D. Frogley, and H.D. Wagner, *The use of carbon nanotubes to sense matrix stresses around a single glass fiber.* Composites Science and Technology, 2001. **61**(14): p. 2139-2143.

63. Cadek, M., J.N. Coleman, V. Barron, K. Hedicke, and W.J. Blau, *Morphological and mechanical properties of carbon-nanotube-reinforced semicrystalline and amorphous polymer composites.* Applied Physics Letters, 2002. **81**(27): p. 5123-5125.

64. Mamedov, A.A., N.A. Kotov, M. Prato, D.M. Guldi, J.P. Wicksted, and A. Hirsch, *Molecular design of strong single-wall carbon nanotube/polyelectrolyte multilayer composites.* Nat Mater, 2002. **1**(3): p. 190-194.

65. Kim, J.-Y., M. Kim, and J.-H. Choi, *Characterization of light emitting devices based on a single-walled carbon nanotube-polymer composite.* Synthetic Metals, 2003. **139**(3): p. 565-568.

66. Ma, H., J. Zeng, M.L. Realff, S. Kumar, and D.A. Schiraldi, *Processing, structure, and properties of fibers from polyester/carbon nanofiber composites.* Composites Science and Technology, 2003. **63**(11): p. 1617-1628.

67. Pham, J.Q., C.A. Mitchell, J.L. Bahr, J.M. Tour, R. Krishanamoorti, and P.F. Green, *Glass transition of polymer/single-walled carbon nanotube composite films.* Journal of Polymer Science Part B: Polymer Physics, 2003. **41**(24): p. 3339-3345.

68. Velasco-Santos, C., A.L. Martínez-Hernández, F.T. Fisher, R. Ruoff, and V.M. Castaño, *Improvement of Thermal and Mechanical Properties of Carbon Nanotube Composites through Chemical Functionalization.* Chemistry of Materials, 2003. **15**(23): p. 4470-4475.

69. Xiao, Q. and X. Zhou, *The study of multiwalled carbon nanotube deposited with conducting polymer for supercapacitor.* Electrochimica Acta, 2003. **48**(5): p. 575-580.

70. Grunlan, J., A. Mehrabi, M. Bannon, and J. Bahr, *Water-Based Single-Walled-Nanotube-Filled Polymer Composite with an Exceptionally Low Percolation Threshold.* Advanced Materials, 2004. **16**(2): p. 150-153.

71. Zeng, J., B. Saltysiak, W.S. Johnson, D.A. Schiraldi, and S. Kumar, *Processing and properties of poly(methyl methacrylate)/carbon nanofiber composites.* Composites Part B: Engineering, 2004. **35**(3): p. 245-249.

72. Park, J.H., J.H. Choi, J.-S. Moon, D.G. Kushinov, J.-B. Yoo, C.Y. Park, J.-W. Nam, C.K. Lee, J.H. Park, and D.H. Choe, *Simple approach for the fabrication of carbon nanotube field emitter using conducting paste.* Carbon, 2005. **43**(4): p. 698-703.

73. Sayago, I., E. Terrado, E. Lafuente, M.C. Horrillo, W.K. Maser, A.M. Benito, R. Navarro, E.P. Urriolabeitia, M.T. Martinez, and J. Gutierrez, *Hydrogen sensors based on carbon nanotubes thin films.* Synthetic Metals, 2005. **148**(1): p. 15-19.

74. Kumar, S., H. Doshi, M. Srinivasarao, J.O. Park, and D.A. Schiraldi, *Fibers from polypropylene/nano carbon fiber composites.* Polymer, 2002. **43**(5): p. 1701-1703.

75. Kymakis, E., I. Alexandrou, and G.A.J. Amaratunga, *High open-circuit voltage photovoltaic devices from carbon-nanotube-polymer composites.* Journal of Applied Physics, 2003. **93**(3): p. 1764-1768.

76. Shenogin, S., L. Xue, R. Ozisik, P. Keblinski, and D.G. Cahill, *Role of thermal boundary resistance on the heat flow in carbon-nanotube composites.* Journal of Applied Physics, 2004. **95**(12): p. 8136-8144.

77. Liu, T., T.V. Sreekumar, S. Kumar, R.H. Hauge, and R.E. Smalley, *SWNT/PAN composite film-based supercapacitors.* Carbon, 2003. **41**(12): p. 2440-2442.

78. Sreekumar, T.V., T. Liu, B.G. Min, H. Go, S. Kumar, R.H. Hauge, and R.E. Smalley, *Polyacrylonitrile single-walled carbon nanotube composite fibers (vol 16, pg 58, 2004).* Advanced Materials, 2004. **16**(18): p. 1583-1583.

79. Chae, H.G., M.L. Minus, A. Rasheed, and S. Kumar, *Stabilization and carbonization of gel spun polyacrylonitrile/single wall carbon nanotube composite fibers.* Polymer, 2007. **48**(13): p. 3781-3789.

80. Chae, H.G., Y.H. Choi, M.L. Minus, and S. Kumar, *Carbon nanotube reinforced small diameter polyacrylonitrile based carbon fiber.* Composites Science and Technology, 2009. **69**(3-4): p. 406-413.

81. Masson, J.C., *Acrylic fiber technology and applications*, ed. J.C. Masson. 1995, New York :: M. Dekker.

82. Sittig, M., *Acrylic and vinyl fibers, 1972*. Chemical process review. 1972, Park Ridge, N.J.: Noyes Data Corp.

83. Gupta, A.K., D.K. Paliwal, and P. Bajaj, *Acrylic Precursors for Carbon Fibers.* Journal of Macromolecular Science: Reviews in Macromolecular Chemistry & Physics, 1991. **C31**(1): p. 1-89.

84. Devasia, R., C.P.R. Nair, and K.N. Ninan, *Rheological behavior of dope solutions of poly(acrylonitrile-co-itaconic acid) in N,N-dimethylformamide: Effect of polymer molar mass.* Journal of Macromolecular Science Part a-Pure and Applied Chemistry, 2008. **45**(3): p. 248-254.

85. Devasia, R., C.P.R. Nair, and K.N. Ninan, *Temperature and shear dependencies of rheology of poly(acrylonitrile-co-itaconic acid) dope in DMF*. Polymers for Advanced Technologies, 2008. **19**(12): p. 1771-1778.

86. Nam, J.Y., K.J. Ihn, B.G. Min, B.C. Kim, T.W. Son, and D.W. Ihm, *Effect of coagulation temperature on PAN fiber morphology in dry-jet wet spinning.* Polymer-Korea, 1996. **20**(1): p. 69-78.

87. Tan, L.J., H.F. Chen, D. Pan, and N. Pan, *Investigating the spinnability in the dry-jet wet spinning of PAN precursor fiber.* Journal of Applied Polymer Science, 2008. **110**(4): p. 1997-2000.

88. Chae, H.G. and S. Kumar, *MATERIALS SCIENCE: Making Strong Fibers.* Science, 2008. **319**(5865): p. 908-909.

89. Nakajima, T., K. Kajiwara, and J.E. McIntyre, *Advanced fiber spinning technology*, ed. T. Nakajima, K. Kajiwara, and J.E. McIntyre. 1994, Cambridge, England :: Woodhead.

90. Donnet, J.-B., T.K. Wang, S. Rebouillat, and J.C.M. Peng, *Carbon fibers*. 3rd ed., rev. and expanded. ed, ed. J.-B. Donnet. 1998, New York :: Marcel Dekker.

91. Grassie, N. and R. McGuchan, *Pyrolysis of polyacrylonitrile and related polymers--VI. Acrylonitrile copolymers containing carboxylic acid and amide structures.* European Polymer Journal, 1972. **8**(2): p. 257-269.

92. D. C. Gupta, J. P. Agrawal, and R. C. Sharma, *Effect of comonomers on thermal degradation of polyacrylonitrile.* Journal of Applied Polymer Science, 1989. **38**(2): p. 265-270.

93. Guyot, A., M. Bert, A. Hamoudi, I. McNeill, and N. Grassie, *Pyrolysis of acrylonitrile-methacrylic acid copolymers and derivatives.* European Polymer Journal, 1978. **14**(2): p. 101-107.

94. Bajaj, P. and M. Padmanaban, *Thermal behaviour of copolymers of acrylonitrile with haloalkyl acrylates or methacrylates.* European Polymer Journal, 1985. **21**(1): p. 93-96.

95. Om Parkash Bahl, L.M.M., *Shrinkage behaviour of polyacrylonitrile during thermal treatment.* Angewandte Makromolekulare Chemie, 1975. **48**(1): p. 145-159.

96. Fitzer, E., W. Frohs, and M. Heine, *Optimization of stabilization and carbonization treatment of PAN fibres and structural characterization of the resulting carbon fibres.* Carbon, 1986. **24**(4): p. 387-395.

97. Thorne, D.J., *Strong fibres*. Handbook of composites ;, ed. W. Watt and B.V. Perov. 1985, Amsterdam ;: North-Holland ;.

98. Evsyukov, S.E., *Carbyne and carbynoid structures*. Physics and chemistry of materials with low-dimensional structures ;, ed. R.B. Heimann, S.E. Evsyukov, and L. Kavan. 1999, Dordrecht Kluwer Academic. pp. 134.

99. Abdalla, M., D. Dean, D. Adibempe, E. Nyairo, P. Robinson, and G. Thompson, *The effect of interfacial chemistry on molecular mobility and morphology of*

multiwalled carbon nanotubes epoxy nanocomposite. Polymer, 2007. **48**(19): p. 5662-5670.

100. Hong, J.S. and C. Kim, *Extension-induced dispersion of multi-walled carbon nanotube in non-Newtonian fluid.* Journal of Rheology, 2007. **51**(5): p. 833-850.

101. Kim, J.A., D.G. Seong, T.J. Kang, and J.R. Youn, *Effects of surface modification on rheological and mechanical properties of CNT/epoxy composites.* Carbon, 2006. **44**(10): p. 1898-1905.

102. Ma, A.W.K., F. Chinesta, T. Tuladhar, and M.R. Mackley, *Filament stretching of carbon nanotube suspensions.* Rheologica Acta, 2008. **47**(4): p. 447-457.

103. Ma, A.W.K., M.R. Mackley, and S.S. Rahatekar, *Experimental observation on the flow-induced assembly of Carbon nanotube suspensions to form helical bands.* Rheologica Acta, 2007. **46**(7): p. 979-987.

104. Ma, W.K.A., F. Chinesta, A. Ammar, and M.R. Mackley, *Rheological modeling of carbon nanotube aggregate suspensions.* Journal of Rheology, 2008. **52**(6): p. 1311-1330.

105. Oh, J.S., K.H. Ahn, and J.S. Hong, *Dispersion of entangled carbon nanotube by melt extrusion.* Korea-Australia Rheology Journal, 2010. **22**(2): p. 89-94.

106. Seyhan, A.T., F.H. Gojny, M. Tanoglu, and K. Schulte, *Rheological and dynamic-mechanical behavior of carbon nanotube/vinyl ester-polyester suspensions and their nanocomposites.* European Polymer Journal, 2007. **43**(7): p. 2836-2847.

107. Song, Y.S., *Rheological characterization of carbon nanotubes/poly(ethylene oxide) composites.* Rheologica Acta, 2006. **46**(2): p. 231-238.

108. Xu, D.-H., Z.-G. Wang, and J.F. Douglas, *Influence of Carbon Nanotube Aspect Ratio on Normal Stress Differences in Isotactic Polypropylene Nanocomposite Melts.* Macromolecules, 2008. **41**(3): p. 815-825.

109. Khenoussi, N., E. Drean, L. Schacher, D.C. Adolphe, and H. Balard, *Preparation and morphology study of carbon nanotube reinforced polyacrylonitrile nanofibres.* Materials Technology, 2009. **24**(1): p. 36-40.

110. Mikolajczyk, T., G. Szparaga, M. Bogun, A. Fraczek-Szczypta, and S. Blazewicz, *Effect of Spinning Conditions on the Mechanical Properties of Polyacrylonitrile Fibers Modified with Carbon Nanotubes.* Journal of Applied Polymer Science, 2010. **115**(6): p. 3628-3635.

111. Wang, B., J. Li, H. Wang, J. Jiang, and Y. Liu, *Rheological Behavior of Spinning Dope of Multiwalled Carbon Nanotube/Polyacrylonitrile Composites.* Macromolecular Symposia, 2004. **216**(1): p. 189-194.

112. Jain, R., *Ph.D.Thesis, Carbon nanotube reinforced polyacrylonitrile and poly(etherketone) fibers*, in *Polymer, Textile and Fiber Engineering*. 2009, Georgia Institute of Technology: Atlanta.

113. Chae, H.G., *Ph.D.Thesis, Polyacrylonitrile / carbon nanotube composite fibers: reinforcement efficiency and carbonization studies*, in *Polymer, Textile and Fiber Engineering*. 2008, Georgia Institute of Technology: Atlanta.

114. V. F. Holland, S.B.M., W. L. Hunter, P. H. Lindenmeyer,, *Crystal structure and morphology of polyacrylonitrile in dilute solution.* Journal of Polymer Science, 1962. **62**(173): p. 145-151.

115. Colvin, B.G. and P. Storr, *The crystal structure of polyacrylonitrile.* European Polymer Journal, 1974. **10**(4): p. 337-340.

116. Kumamaru, F., T. Kajiyama, and M. Takayanagi, *Formation of single crystals of poly(acrylonitrile) during the process of solution polymerization.* Journal of Crystal Growth, 1980. **48**(2): p. 202-209.

117. Allen, R.A., I.M. Ward, and Z. Bashir, *The variation of the d-spacings with stress in the hexagonal polymorph of polyacrylonitrile.* Polymer, 1994. **35**(19): p. 4035-4040.

118. Allen, R.A., I.M. Ward, and Z. Bashir, *An investigation into the possibility of measuring an [`]X-ray modulus' and new evidence for hexagonal packing in polyacrylonitrile.* Polymer, 1994. **35**(10): p. 2063-2071.

119. Ricardo Diaz-Calleja, E.S., Evaristo Riande, Ligia Gargallo, Deodato Radic,, *Relaxation behavior, intramolecular interactions, and local motions on monosubstituted esters of poly(itaconic acid).* Journal of Polymer Science Part B: Polymer Physics, 1994. **32**(6): p. 1069-1077.

120. Z. Bashir, *Co-crystallization of solvents with polymers: The x-ray diffraction behavior of solvent-containing and solvent-free polyacrylonitrile.* Journal of Polymer Science Part B: Polymer Physics, 1994. **32**(6): p. 1115-1128.

121. A. K. Gupta, R.P.S., *Effect of copolymerization and heat treatment on the structure and x-ray diffraction of polyacrylonitrile.* Journal of Polymer Science: Polymer Physics Edition, 1983. **21**(11): p. 2243-2262.

122. Chae, H.G., M.L. Minus, and S. Kumar, *Oriented and exfoliated single wall carbon nanotubes in polyacrylonitrile.* Polymer, 2006. **47**(10): p. 3494-3504.

123. Abbasi, S., P.J. Carreau, and A. Derdouri, *Flow induced orientation of multiwalled carbon nanotubes in polycarbonate nanocomposites: Rheology, conductivity and mechanical properties.* Polymer, 2010. **51**(4): p. 922-935.

124. Abdalla, M., D. Dean, M. Theodore, J. Fielding, E. Nyairo, and G. Price, *Magnetically processed carbon nanotube/epoxy nanocomposites: Morphology, thermal, and mechanical properties.* Polymer, 2010. **51**(7): p. 1614-1620.

125. Deng, F., T. Ogasawara, and N. Takeda, *Evaluating the orientation and dispersion of carbon nanotubes inside nanocomposites by a focused-ion-beam technique.* Materials Letters, 2007. **61**(29): p. 5095-5097.

126. Dijkstra, D.J., M. Cirstea, and N. Nakamura, *The orientational behavior of multiwall carbon nanotubes in polycarbonate in simple shear flow.* Rheologica Acta, 2010. **49**(7): p. 769-780.

127. Fan, Z.H. and S.G. Advani, *Characterization of orientation state of carbon nanotubes in shear flow.* Polymer, 2005. **46**(14): p. 5232-5240.

128. Fan, Z.H. and S.G. Advani, *Rheology of multiwall carbon nanotube suspensions.* Journal of Rheology, 2007. **51**(4): p. 585-604.

129. Kovacs, J.Z., K. Andresen, J.R. Pauls, C.P. Garcia, M. Schossig, K. Schulte, and W. Bauhofer, *Analyzing the quality of carbon nanotube dispersions in polymers using scanning electron microscopy.* Carbon, 2007. **45**(6): p. 1279-1288.

130. Wang, Q., J.F. Dai, W.X. Li, Z.Q. Wei, and J.L. Jiang, *The effects of CNT alignment on electrical conductivity and mechanical properties of SWNT/epoxy nanocomposites.* Composites Science and Technology, 2008. **68**(7-8): p. 1644-1648.

131. Camponeschi, E., R. Vance, M. Al-Haik, H. Garmestani, and R. Tannenbaum, *Properties of carbon nanotube-polymer composites aligned in a magnetic field.* Carbon, 2007. **45**(10): p. 2037-2046.

132. Fischer, D., P. Potschke, H. Brunig, and A. Janke, *Investigation of the orientation in composite fibers of polycarbonate with multiwalled carbon nanotubes by Raman microscopy.* Macromolecular Symposia, 2005. **230**: p. 167-172.

133. Kordas, K., T. Mustonen, G. Toth, J. Vahakangas, A. Uusimaki, H. Jantunen, A. Gupta, K.V. Rao, R. Vajtai, and P.M. Ajayan, *Magnetic-field induced efficient alignment of carbon nanotubes in aqueous solutions.* Chemistry of Materials, 2007. **19**(4): p. 787-791.

134. Mazinani, S., A. Ajji, and C. Dubois, *Fundamental Study of Crystallization, Orientation, and Electrical Conductivity of Electrospun PET/Carbon Nanotube Nanofibers.* Journal of Polymer Science Part B-Polymer Physics, 2010. **48**(19): p. 2052-2064.

135. Pegel, S., P. Potschke, T. Villmow, D. Stoyan, and G. Heinrich, *Spatial statistics of carbon nanotube polymer composites.* Polymer, 2009. **50**(9): p. 2123-2132.

136. Uchida, T., D. Anderson, M. Minus, and S. Kumar, *Morphology and modulus of vapor grown carbon nano fibers.* Journal of Materials Science, 2006. **41**(18): p. 5851-5856.

137. Liu, T. and S. Kumar, *Quantitative characterization of SWNT orientation by polarized Raman spectroscopy.* Chemical Physics Letters, 2003. **378**(3-4): p. 257-262.

138. Wood, J.R., Q. Zhao, and H.D. Wagner, *Orientation of carbon nanotubes in polymers and its detection by Raman spectroscopy.* Composites Part a-Applied Science and Manufacturing, 2001. **32**(3-4): p. 391-399.

139. T. Takahagi, I.S., M. Fukuhara, K. Morita, A. Ishitani,, *XPS studies on the chemical structure of the stabilized polyacrylonitrile fiber in the carbon fiber production process.* Journal of Polymer Science Part A: Polymer Chemistry, 1986. **24**(11): p. 3101-3107.

140. Chae, H.G., T.V. Sreekumar, T. Uchida, and S. Kumar, *A comparison of reinforcement efficiency of various types of carbon nanotubes in polyacrylonitrile fiber.* Polymer, 2005. **46**(24): p. 10925-10935.

141. Samuels, R.J., *Structured polymer properties: the identification, interpretation, and application of crystalline polymer structure*. 1974, New York: Wiley.

142. Wilchinsky, Z.W., *MEASUREMENT OF ORIENTATION IN POLYPROPYLENE FILM.* Journal of Applied Physics, 1960. **31**(11): p. 1969-1972.

143. Kharchenko, S.B., J.F. Douglas, J. Obrzut, E.A. Grulke, and K.B. Migler, *Flow-induced properties of nanotube-filled polymer materials.* Nat Mater, 2004. **3**(8): p. 564-568.

144. Davis, V.A., L.M. Ericson, A.N.G. Parra-Vasquez, H. Fan, Y.H. Wang, V. Prieto, J.A. Longoria, S. Ramesh, R.K. Saini, C. Kittrell, W.E. Billups, W.W. Adams, R.H. Hauge, R.E. Smalley, and M. Pasquali, *Phase Behavior and rheology of SWNTs in superacids.* Macromolecules, 2004. **37**(1): p. 154-160.

145. Lin-Gibson, S., J.A. Pathak, E.A. Grulke, H. Wang, and E.K. Hobbie, *Elastic flow instability in nanotube suspensions.* Physical Review Letters, 2004. **92**(23).

146. Baek, S.G., J.J. Magda, and R.G. Larson, *RHEOLOGICAL DIFFERENCES AMONG LIQUID-CRYSTALLINE POLYMERS .1. THE 1ST AND 2ND NORMAL STRESS DIFFERENCES OF PBG SOLUTIONS.* Journal of Rheology, 1993. **37**(6): p. 1201-1224.

147. Larson, R.G., *ARRESTED TUMBLING IN SHEARING FLOWS OF LIQUID-CRYSTAL POLYMERS.* Macromolecules, 1990. **23**(17): p. 3983-3992.

148. Sawai, D., T. Kanamoto, H. Yamazaki, and K. Hisatani, *Dynamic Mechanical Relaxations in Poly(acrylonitrile) with Different Stereoregularities.* Macromolecules, 2004. **37**(8): p. 2839-2846.

149. Bahl, O.P., R.B. Mathur, V.K. Matta, and P.S. Ram, *ON THE SHELF-LIFE OF PAN PRECURSOR.* Carbon, 1989. **27**(3): p. 494-495.

150. Bajaj, P., T.V. Sreekumar, and K. Sen, *Structure development during dry-jet-wet spinning of acrylonitrile/vinyl acids and acrylonitrile/methyl acrylate copolymers.* Journal of Applied Polymer Science, 2002. **86**(3): p. 773-787.

151. Gupta, V.B., *Heat setting.* Journal of Applied Polymer Science, 2002. **83**(3): p. 586-609.

152. Qian, B.J., Z.Q. Wu, P.P. Hu, J. Qin, C.X. Wu, and J.X. Zhao, *STUDIES ON MACROMOLECULAR ENTANGLEMENT .2. MODIFICATION OF MACROMOLECULAR ENTANGLEMENTS BY HEAT-TREATMENT.* Journal of Applied Polymer Science, 1993. **47**(10): p. 1881-1895.

153. Sahoo, A., M. Jassal, and A.K. Agrawal, *pH-responsive fibers based on acrylonitrile acrylic acid block copolymers: Effect of spinning conditions and postspinning operations on response and mechanical properties.* Journal of Applied Polymer Science, 2008. **109**(6): p. 3792-3803.

154. Lee, S.H., E. Cho, S.H. Jeon, and J.R. Youn, *Rheological and electrical properties of polypropylene composites containing functionalized multi-walled carbon nanotubes and compatibilizers.* Carbon, 2007. **45**(14): p. 2810-2822.

155. Seo, M.-K. and S.-J. Park, *Electrical resistivity and rheological behaviors of carbon nanotubes-filled polypropylene composites.* Chemical Physics Letters, 2004. **395**(1-3): p. 44-48.

156. *Dynamics of polymeric liquids*. 2nd ed. ed, ed. R.B. Bird. 1987, New York :: Wiley.

157. Cox, W.P. and E.H. Merz, *Correlation of dynamic and steady flow viscosities.* Journal of Polymer Science, 1958. **28**(118): p. 619-622.

158. Macosko, C.W., *Rheology : principles, measurements, and applications*. Advances in interfacial engineering series, ed. R.G. Larson. 1994, New York, NY :: VCH.

159. Lee, S.J., *Rheology and its applications*. 2001, Seoul: The Korean Soceity of Rheology.

160. *Orienting polymers : proceedings of a workshop held at the IMA, University of Minnesota, Minneapolis, March 21-26, 1983*. Lecture notes in mathematics ;, ed. J.L. Ericksen. 1984, Berlin ;: Springer-Verlag.

161. Graessley, W.W., *Linear Viscoelasticity in Entangling Polymer Systems.* The Journal of Chemical Physics, 1971. **54**(12): p. 5143-5157.

162. Guo, J. and K.A. Narh, *Simplified model of stress-induced crystallization kinetics of polymers.* Advances in Polymer Technology, 2002. **21**(3): p. 214-222.

163. Flory, P.J., *Thermodynamics of Crystallization in High Polymers. I. Crystallization Induced by Stretching.* The Journal of Chemical Physics, 1947. **15**(6): p. 397-408.

164. Gaylord, R.J., *THEORY OF STRESS-INDUCED CRYSTALLIZATION OF CROSSLINKED POLYMERIC NETWORKS.* Journal of Polymer Science Part B-Polymer Physics, 1976. **14**(10): p. 1827-1837.

165. Mitchell, J.C. and D.J. Meier, *RAPID STRESS-INDUCED CRYSTALLIZATION IN NATURAL RUBBER.* Journal of Polymer Science Part a-2-Polymer Physics, 1968. **6**(10PA): p. 1689-&.

166. Misra, A. and R.S. Stein, *STRESS-INDUCED CRYSTALLIZATION OF POLY(ETHYLENE-TEREPHTHALATE).* Journal of Polymer Science Part B-Polymer Physics, 1979. **17**(2): p. 235-257.

167. D. I. Bower, *Investigation of molecular orientation distributions by polarized raman scattering and polarized fluorescence.* Journal of Polymer Science: Polymer Physics Edition, 1972. **10**(11): p. 2135-2153.

168. Gurp, M., *The use of rotation matrices in the mathematical description of molecular orientations in polymers.* Colloid & Polymer Science, 1995. **273**(7): p. 607-625.

169. Sawai, D., A. Yamane, T. Kameda, T. Kanamoto, M. Ito, H. Yamazaki, and K. Hisatani, *Uniaxial Drawing of Isotactic Poly(acrylonitrile): Development of Oriented Structure and Tensile Properties.* Macromolecules, 1999. **32**(17): p. 5622-5630.

170. Hu, X., D.J. Johnson, and J.G. Tomka, *Molecular Modelling of the Structure of Polyacrylonitrile Fibres.* Journal of the Textile Institute, 1995. **86**(2): p. 322 - 331.

171. Lao, S.C., C. Wu, T.J. Moon, J.H. Koo, A. Morgan, L. Pilato, and G. Wissler, *Flame-retardant Polyamide 11 and 12 Nanocomposites: Thermal and Flammability Properties.* Journal of Composite Materials, 2009. **43**(17): p. 1803-1818.

172. Alongi, J. and A. Frache, *Poly(ethylene terephthalate)-carbon nanofiber nano composite for fiber spinning; properties and combustion behavior.* E-Polymers, 2010.

173. http://www.chemwide.com/.

174. http://www.toyobo.co.jp/e/seihin/fb/procon/.

175. Francis P. McCullough, J., B.C. Goswami, and S.E. Hill, *NON-LINEAR CARBONACEOUS FIBER*. 1993, The Dow Chemical Company: US5356707.

176. Tsafack, M.J. and J. Levalois-Gruzmacher, *Plasma-induced graft-polymerization of flame retardant monomers onto PAN fabrics.* Surface and Coatings Technology, 2006. **200**(11): p. 3503-3510.

177. Ziabicki, A., *Fundamentals of fibre formation : the science of fibre spinning and drawing*. 1976, London ;: Wiley.

178. Bastiaansen, C.W.M., Y. Ohta, and H. Sugiyama, *PROCESS FOR PREPARING POLYETHYLENE ARTICLES OF HIGH TENSILE STRENGTH AND MODULUS AND LOW CREEP AND ARTICLES THUS OBTAINED*. 1987, Dyneema V.O.F.: US5128415.

179. Lemstra, P.J. and R. Kirschbaum, *Speciality products based on commodity polymers.* Polymer, 1985. **26**(9): p. 1372-1384.

180. Karacan, I., *Molecular structure and orientation of gel-spun polyethylene fibers.* Journal of Applied Polymer Science, 2006. **101**(3): p. 1317-1333.

181. Kalb, B. and A.J. Pennings, *Hot drawing of porous high molecular weight polyethylene.* Polymer, 1980. **21**(1): p. 3-4.

182. Sawai, D., A. Yamane, H. Takahashi, T. Kanamoto, M. Ito, and R.S. Porter, *Development of high ductility and tensile properties by a two-stage draw of poly(acrylonitrile): Effect of molecular weight.* Journal of Polymer Science Part B: Polymer Physics, 1998. **36**(4): p. 629-640.

183. Hurley, R.B. and L.S. Tzentis, *Density of polyacrylonitrile.* Journal of Polymer Science Part B: Polymer Letters, 1963. **1**(8): p. 423-426.

184. Han, L., W. Wu, F.L. Kirk, J. Luo, M.M. Maye, N.N. Kariuki, Y.H. Lin, C.M. Wang, and C.J. Zhong, *A direct route toward assembly of nanoparticle-carbon nanotube composite materials.* Langmuir, 2004. **20**(14): p. 6019-6025.

185. Jain, R., Y.H. Choi, Y. Liu, M.L. Minus, H.G. Chae, S. Kumar, and J.B. Baek, *Processing, structure and properties of poly(ether ketone) grafted few wall carbon nanotube composite fibers.* Polymer, 2010. **51**(17): p. 3940-3947.

186. Lee, H.J., S.J. Oh, J.Y. Choi, J.W. Kim, J. Han, L.S. Tan, and J.B. Baek, *In situ synthesis of poly(ethylene terephthalate) (PET) in ethylene glycol containing terephthalic acid and functionalized multiwalled carbon nanotubes (MWNTs) as an approach to MWNT/PET nanocomposites.* Chemistry of Materials, 2005. **17**(20): p. 5057-5064.

187. Zhang, D.S., L.Y. Shi, J.H. Fang, X.K. Li, and K. Dai, *Preparation and modification of carbon nanotubes.* Materials Letters, 2005. **59**(29-30): p. 4044-4047.

188. Baek, J.B., C.B. Lyons, and L.S. Tan, *Grafting of vapor-grown carbon nanofibers via in-situ polycondensation of 3-phenoxybenzoic acid in poly(phosphoric acid).* Macromolecules, 2004. **37**(22): p. 8278-8285.

189. Banerjee, S., T. Hemraj-Benny, and S. Wong, *Covalent Surface Chemistry of Single-Walled Carbon Nanotubes.* Advanced Materials, 2005. **17**(1): p. 17-29.

190. Dyke, C.A. and J.M. Tour, *Covalent Functionalization of Single-Walled Carbon Nanotubes for Materials Applications.* The Journal of Physical Chemistry A, 2004. **108**(51): p. 11151-11159.

191. Hirsch, A., *Functionalization of Single-Walled Carbon Nanotubes.* Angewandte Chemie International Edition, 2002. **41**(11): p. 1853-1859.

192. Niyogi, S., M.A. Hamon, H. Hu, B. Zhao, P. Bhowmik, R. Sen, M.E. Itkis, and R.C. Haddon, *Chemistry of Single-Walled Carbon Nanotubes.* Accounts of Chemical Research, 2002. **35**(12): p. 1105-1113.

193. Strano, M.S., C.A. Dyke, M.L. Usrey, P.W. Barone, M.J. Allen, H. Shan, C. Kittrell, R.H. Hauge, J.M. Tour, and R.E. Smalley, *Electronic Structure Control of Single-Walled Carbon Nanotube Functionalization.* Science, 2003. **301**(5639): p. 1519-1522.

194. Worsley, K.A., K.R. Moonoosawmy, and P. Kruse, *Long-Range Periodicity in Carbon Nanotube Sidewall Functionalization.* Nano Letters, 2004. **4**(8): p. 1541-1546.

195. Bansal, A., H. Yang, C. Li, K. Cho, B.C. Benicewicz, S.K. Kumar, and L.S. Schadler, *Quantitative equivalence between polymer nanocomposites and thin polymer films.* Nat Mater, 2005. **4**(9): p. 693-698.

196. Krishnamoorti, R., R.A. Vaia, and E.P. Giannelis, *Structure and Dynamics of Polymer-Layered Silicate Nanocomposites.* Chemistry of Materials, 1996. **8**(8): p. 1728-1734.

197. Starr, F.W., T.B. Schroder, and S.C. Glotzer, *Molecular Dynamics Simulation of a Polymer Melt with a Nanoscopic Particle.* Macromolecules, 2002. **35**(11): p. 4481-4492.

198. Vaia, R.A. and E.P. Giannelis, *Polymer Nanocomposites: Status and Opportunities.* MRS bulletin, 2001. **26**(5): p. 394.

199. Vaia, R.A. and H.D. Wagner, *Framework for nanocomposites.* Materials Today, 2004. **7**(11): p. 32-37.

200. Ding, W., A. Eitan, F.T. Fisher, X. Chen, D.A. Dikin, R. Andrews, L.C. Brinson, L.S. Schadler, and R.S. Ruoff, *Direct Observation of Polymer Sheathing in Carbon Nanotube−Polycarbonate Composites.* Nano Letters, 2003. **3**(11): p. 1593-1597.

201. Wei, C., D. Srivastava, and K. Cho, *Structural Ordering in Nanotube Polymer Composites.* Nano Letters, 2004. **4**(10): p. 1949-1952.

202. Coleman, J.N., M. Cadek, K.P. Ryan, A. Fonseca, J.B. Nagy, W.J. Blau, and M.S. Ferreira, *Reinforcement of polymers with carbon nanotubes. The role of an ordered polymer interfacial region. Experiment and modeling.* Polymer, 2006. **47**(26): p. 8556-8561.

203. Fisher, F.T. and L.C. Brinson, *Viscoelastic interphases in polymer-matrix composites: theoretical models and finite-element analysis.* Composites Science and Technology, 2001. **61**(5): p. 731-748.

204. Winey, K.I. and R.A. Vaia, *Polymer Nanocomposites.* MRS bulletin, 2007. **32**(4): p. 314-322.

205. Bisschops, J., *Gelation of concentrated polyacrylonitrile solutions. II.* Journal of Polymer Science, 1955. **17**(83): p. 89-98.

206. Labudzin.A and A. Ziabicki, *EFFECT OF COMPOSITION AND GELATION CONDITIONS ON STRUCTURAL CHANGES ACCOMPANYING GELATION OF PAN, PVA AND GELATIN SOLUTIONS.* Kolloid-Zeitschrift and Zeitschrift Fur Polymere, 1971. **243**(1): p. 21-27.

207. Chiu, H.-T. and J.-H. Wang, *Characterization of the rheological behavior of UHMWPE gels using parallel plate rheometry.* Journal of Applied Polymer Science, 1998. **70**(5): p. 1009-1016.

208. Bercea, M., S. Morariu, C. Ioan, S. Ioan, and B.C. Simionescu, *Viscometric study of extremely dilute polyacrylonitrile solutions.* European Polymer Journal, 1999. **35**(11): p. 2019-2024.

209. Morariu, S., M. Bercea, C. Ioan, S. Ioan, and B.C. Simionescu, *Conformational characteristics of oligo- and polyacrylonitrile in dilute solution.* European Polymer Journal, 1999. **35**(3): p. 377-383.

210. Tanaka, Y., *Viscoelastic properties of polyacrylonitrile gels: Dependence of sol-gel transition on concentration and aging time.* Macromolecular Symposia, 2003. **200**: p. 265-270.

211. Bercea, M., S. Morariu, and C.E. Brunchi, *Rheological Investigation of Thermal-Induced Gelation of Polyacrylonitrile Solutions.* International Journal of Thermophysics, 2009. **30**(4): p. 1411-1422.

212. Brunchi, C.E., M. Bercea, and S. Morariu, *Viscometric and rheological study of polyacrylonitrile solutions.* E-Polymers, 2009.

213. Botelho, E.C., L. Figiel, M.C. Rezende, and B. Lauke, *Mechanical behavior of carbon fiber reinforced polyamide composites.* Composites Science and Technology, 2003. **63**(13): p. 1843-1855.

214. Chen, P.W. and D.D.L. Chung, *Low-drying-shrinkage concrete containing carbon fibers.* Composites Part B-Engineering, 1996. **27**(3-4): p. 269-274.

215. Dong, S. and R. Gauvin, *APPLICATION OF DYNAMIC-MECHANICAL ANALYSIS FOR THE STUDY OF THE INTERFACIAL REGION IN CARBON FIBER/EPOXY COMPOSITE-MATERIALS.* Polymer Composites, 1993. **14**(5): p. 414-420.

216. Fu, S.Y., B. Lauke, E. Mader, C.Y. Yue, and X. Hu, *Tensile properties of short-glass-fiber- and short-carbon-fiber-reinforced polypropylene composites.* Composites Part a-Applied Science and Manufacturing, 2000. **31**(10): p. 1117-1125.

217. Gall, K., M. Mikulas, N.A. Munshi, F. Beavers, and M. Tupper, *Carbon fiber reinforced shape memory polymer composites.* Journal of Intelligent Material Systems and Structures, 2000. **11**(11): p. 877-886.

218. Kim, J.K. and Y.W. Mai, *HIGH-STRENGTH, HIGH FRACTURE-TOUGHNESS FIBER COMPOSITES WITH INTERFACE CONTROL - A REVIEW.* Composites Science and Technology, 1991. **41**(4): p. 333-378.

219. Lamouroux, F., S. Bertrand, R. Pailler, R. Naslain, and M. Cataldi, *Oxidation-resistant carbon-fiber-reinforced ceramic-matrix composites.* Composites Science and Technology, 1999. **59**(7): p. 1073-1085.

220. Soutis, C., F.C. Smith, and F.L. Matthews, *Predicting the compressive engineering performance of carbon fibre-reinforced plastics.* Composites Part a-Applied Science and Manufacturing, 2000. **31**(6): p. 531-536.

221. Stevanović, M.M. and D.R. Pešikan-Sekulić, *Tensile Characteristics of Carbon Fibres.* Materials Science Forum, 2000. **352**: p. 183-188.

222. Bourgain, E. and J.J. Masson, *Deterministic method of describing rupture probability application to the analysis of high-modulus carbon fibres.* Journal of Materials Science, 1992. **27**(7): p. 1811-1817.

223. Yu, W. and J. Yao, *Tensile strength and its variation of PAN-based carbon fibers. I. Statistical distribution and volume dependence.* Journal of Applied Polymer Science, 2006. **101**(5): p. 3175-3182.

224. Naito, K., Y. Tanaka, J.-M. Yang, and Y. Kagawa, *Tensile properties of ultrahigh strength PAN-based, ultrahigh modulus pitch-based and high ductility pitch-based carbon fibers.* Carbon, 2008. **46**(2): p. 189-195.

225. Daniels, H.E., *The Statistical Theory of the Strength of Bundles of Threads. I.* Proceedings of the Royal Society of London. Series A, Mathematical and Physical Sciences, 1945. **183**(995): p. 405-435.

226. Weibull, W., *A statistical Distribution Function of Wide Applicability.* Journal of Applied Mechanics, 1951. **18**: p. 293-297.

227. Trustrum, K. and A.D.S. Jayatilaka, *On estimating the Weibull modulus for a brittle material.* Journal of Materials Science, 1979. **14**(5): p. 1080-1084.

228. Davies, I.J., *Best estimate of Weibull modulus obtained using linear least squares analysis: An improved empirical correction factor.* Journal of Materials Science, 2004. **39**(4): p. 1441-1444.

229. Bourgain, E. and J.J. Masson, *A NEW METHOD OF MODELING STRENGTH DISTRIBUTIONS FOR CERAMIC FIBERS.* Composites Science and Technology, 1992. **43**(3): p. 221-228.

230. Pan, N., H. Chen, J. Thompson, M. Inglesby, S. Khatua, X. Zhang, and S. Zeronian, *The size effects on the mechanical behaviour of fibres.* Journal of Materials Science, 1997. **32**(10): p. 2677-2685.

231. Moreton, R., *The effect of gauge length on the tensile strength of R.A.E. carbon fibres.* Fibre Science and Technology, 1969. **1**(4): p. 273-284.

232. Lu, Q., G. Keskar, R. Ciocan, R. Rao, R.B. Mathur, A.M. Rao, and L.L. Larcom, *Determination of Carbon Nanotube Density by Gradient Sedimentation.* The Journal of Physical Chemistry B, 2006. **110**(48): p. 24371-24376.

233. Gao, G.H., T. Cagin, and W.A. Goddard, *Energetics, structure, mechanical and vibrational properties of single-walled carbon nanotubes.* Nanotechnology, 1998. **9**(3): p. 184-191.